

Pore-scale Visualisation and Geochemical Modelling of Low Salinity Water Flooding as an Enhanced Oil Recovery Method

Tammy Amirian

A thesis submitted in fulfilment of the requirements for the degree of Doctor of Philosophy



THE UNIVERSITY
of ADELAIDE

The University of Adelaide

Faculty of Engineering, Computer and Mathematical Sciences

Australian School of Petroleum

July 2019

Table of Contents

List of Publications:	iii
List of Figures	iv
List of Tables	vi
Abstract.....	vii
Declaration.....	ix
Acknowledgment	x
Chapter 1: Research background and Literature Review	1
1.1 Enhanced oil recovery	1
1.2 Mechanism behind LSE	2
1.3 Low salinity effect in carbonate reservoirs	6
1.4 Microfluidics	8
1.4.1 Microfluidics fabrication	8
1.4.2 Geo-material micromodels	11
1.4.3 Measurements and visualization techniques:	17
1.5 Microfluidics applications in EOR	19
1.6 Application of microfluidics in LSE Research	22
1.7 Surface complexation modelling:	26
1.7.1 Parameters estimation for surface complexation models	28
1.7.2 The Diffuse Layer Model (DLM)	29
Chapter 2: Project Aims and Thesis Outline	31
2.1 Research gap	31
2.2 Research aims and objectives	31
2.3 Thesis Outline	31
2.3.1 Experimental phase	31
2.3.2 Simulation phase	32
2.3.3 Conclusions and recommendations	33
2.3.4 Appendices	33
Chapter 3: Pore Scale Visualization of Low Salinity Water Flooding as an Enhanced Oil Recovery	
Method	34

Chapter 4: Impact of Clay Type and Nature of Cations on Low Salinity Water Injection – Visualisation Approach.....	35
Chapter 5: Geochemical Modelling and Microfluidic Experiments to Analyse Impact of Clay Type and Cations on Low Salinity Water Flooding	36
Chapter 6: Conclusion and Future Work.....	37
6.1 Conclusion	37
6.2 Future works:	38
6.2.1 3D micromodels	38
6.2.2 Measuring the thin brine film	39
6.2.3 Pore-scale modelling of low salinity water injection	39
6.2.4 Molecular simulation of low salinity water injection	40
7 References	41
Appendices.....	46

This thesis is prepared in *publication format* which includes chapters presenting the aim of the research, a comprehensive literature review, conclusions and future directions of the work as well as the related publications. The list of published papers are as follows:

List of Publications:

(1) **Amirian, T.**; Haghghi, M.; Mostaghimi, P., Pore Scale Visualization of Low Salinity Water Flooding as an Enhanced Oil Recovery Method. *Energy & Fuels* **2017**, *31* (12), 13133-13143.

DOI: [10.1021/acs.energyfuels.7b01702](https://doi.org/10.1021/acs.energyfuels.7b01702)

(2) **Amirian, T.**; Haghghi, M., Impact of Clay Type and Water Composition On Low Salinity Water Injection – Visualisation Approach. *The APPEA Journal* 2018, *58* (1), 51-59.

DOI: [10.1071/AJ17076](https://doi.org/10.1071/AJ17076)

(3) **Amirian, T.**; Haghghi, M.; Sun, C.; Armstrong, R. T.; and Mostaghimi, P., “Geochemical Modelling and Microfluidic Experiments to Analyse Impact of Clay Type and Cations on Low Salinity Water Flooding" *Energy & Fuels* 2019, *Article ASA*.

DOI: [10.1021/acs.energyfuels.8b04145](https://doi.org/10.1021/acs.energyfuels.8b04145)

(4) Gerami, A.; Alzahid, Y.; Mostaghimi, P.; Kashaninejad, N.; Kazemifar, F.; **Amirian, T.**; Mosavat, N.; Ebrahimi Warkiani, M.; Armstrong, R. T., Microfluidics for Porous Systems: Fabrication, Microscopy and Applications. *Transp Porous Med* **2018**.

DOI: [10.1007/s11242-018-1202-3](https://doi.org/10.1007/s11242-018-1202-3)

(5) Alzahid, Y. A.; Mostaghimi, P.; Gerami, A.; Singh, A.; Privat, K.; **Amirian, T.**; Armstrong, R. T., Functionalisation of Polydimethylsiloxane (PDMS)- Microfluidic Devices coated with Rock Minerals. *Scientific Reports* **2018**, *8* (1), 15518.

DOI: [10.1038/s41598-018-33495-8](https://doi.org/10.1038/s41598-018-33495-8)

List of Figures

<i>Figure 1. 1: Adsorption of polar component from crude oil onto the surface of clay particles alters the wettability and causes fines to become mixed wet. LSE detaches fines from the pore wall, which leads to the release of oil.</i>	<i>2</i>
<i>Figure 1.2: The reduction in ionic strength led to expansion of double layers (Debye length) of oil and clay, so the screening from the counter ions in the electrolyte becomes weaker, resulting in higher repulsion forces between oil and clay.</i>	<i>4</i>
<i>Figure 1.3: Illustration of non-DLVO interactions between brine/oil and brine/clay edge interfaces.</i>	<i>5</i>
<i>Figure 1.4: Comparison of photolithography and soft lithography techniques. Reproduced from Gerami, et al. ⁴⁸</i>	<i>11</i>
<i>Figure 1.5: Overview of fabrication methods for geomaterial micromodels. (a) Laser etching on real rock surfaces. Reproduced from Gerami, et al. ⁵⁴(b) Silicon/glass/PDMS functionalisation by depositing relevant rock mineral. Reproduced from Song and Kovscek ⁵⁶. (c) Rock slicing. Reproduced form Song, et al. ⁵³</i>	<i>14</i>
<i>Figure 1. 6: Two proposed processes of PDMS functionalisation (a) Layer-by-layer method, reproduced from Zhang, et al. ⁵⁸. (b) Method proposed by Alzahid, et al. ⁵⁹ Reproduced from Gerami, et al. ⁴⁸</i>	<i>15</i>
<i>Figure 1.7: Fabrication process of the functionalised PDMS micromodels. Reproduced from Alzahid, et al. ⁵⁹</i>	<i>17</i>
<i>Figure 1.8: Images generated from various optical techniques. (a) Transmitted microscopy is employed to visualize the gas transport in a coal fracture. Dyes are added to the fluid phase to improve visualization Reproduced from Gerami, et al. ⁷⁰. (b) The displacement of decane oil in a pore network is pictured using direct visualization setup. The injection starts from the center of the chip. (c) The image was taken using confocal laser microscope which was implemented to visualize displacement of fluorescein-dyed buffer by a non-dyed buffer. Reproduced from Singh, et al. ⁵⁷. (d) A dual camera visualization setup was used to capture the images of dyed CO₂ (left) and tracer particle image (right) in a silicon-based micromodel Reproduced from Kazemifar, et al. ⁷¹.</i>	<i>19</i>
<i>Figure 1. 9: The formation of emulsion in three studies. (a) Top view of a T-junction capillary during the injection of the surfactant solution with a co-flowing colored decane under fluorescent light, highlighting the microemulsion formation at optimum salinity during continuous flow. Black represents aqueous phase, red represents micro-emulsion, and brown represents decane. Reproduced from Unsal, et al. ⁷⁴ (b) The image was taken after alkaline flooding. Emulsions are formed in some sections. Reproduced from Pei, et al. ⁷⁵. (c)</i>	

<i>Emulsions after steam-assisted gravity drainage (oil shown in green and water in black). Reproduced from de Haas, et al. ⁸⁵</i>	<i>22</i>
<i>Figure 1.10 :Enlarged images of the clay-coated glass micromodel (a) before and (b) after secondary LSW injections. During the secondary phase, fines detached from the surface, which led to the release of oil attached to them. Reproduced from Barnaji, et al. ⁸⁶</i>	<i>23</i>
<i>Figure 1.11: Images recorded by Song and Kovsky ⁵⁶ after (a) HS brine and(b) LS brine injections. To calculate the residual oil saturation, these images were processed, yielding (b) and (d), respectively. The oil saturation was less for LS brine. Reproduced from Song and Kovsky ⁵⁶</i>	<i>24</i>
<i>Figure 1.12: X-ray images showing the redistribution of fluids after LSW injection. Reproduced from Bartels, et al. ⁹⁵</i>	<i>25</i>
<i>Figure 1.13: Emadi and Sohrabi ⁹³ suggested that formation of water micro dispersion in the oil phase (dark particles in the oil phase) led to a slight change in the fluid redistribution and resultant improved recovery. Reproduced from Emadi and Sohrabi ⁹³</i>	<i>25</i>
<i>Figure 1.14: (1) The fluid distribution in HSW, prior to LS brine injection. The dissolved droplets of HSW in the oil phase are indicated by yellow arrows. (2) During LSW injection, the water-in-oil emulsification started to grow and the aggregation of emulsions displaced the oil ⁹⁴. Reproduced from Fredriksen, et al. ⁹⁴</i>	<i>26</i>
<i>Figure 1.15: Inner-sphere and outer-sphere adsorptions. The inner-sphere adsorption formed surface complexes in which there is no water between the adsorbing ion (Pb) and the surface functional group. However, each outer-sphere adsorption has at least one water molecule between the adsorbing ion (Sr) and the surface functional group.....</i>	<i>28</i>
<i>Figure 1.16: Schematic of the Electrical Double Layer used in the DLM.....</i>	<i>30</i>

List of Tables

Table 1.1: Optimum parameters in glass micromodel fabrication.....10

Abstract

Low salinity water (LSW) injection is a promising technique for improving oil recovery from reservoirs. The salinity ranges from 1000 to 2000 ppm which is significantly less than the salinity of the formation brine. However, the mechanisms underlying the Low Salinity Effect (LSE) are not well understood. To investigate the dynamics of displacement, clean and clay coated micromodels were fabricated and used where the wettability was set to both water-wet and oil-wet. This allows the visualisation of pore-scale displacement mechanisms in the presence and absence of kaolinite and illite.

It is observed that in water-wet systems, in the absence and presence of clays, LSW hinders “snap-off,” perhaps due to the development of a viscoelastic water/oil interface. There was a transition from snap-off to piston-like displacement in much of the volume of each pore and the amount of trapped oil was decreased by almost 10%. The wettability alteration toward water-wetness is also visualised for oil-wet systems which resulted in 15% improved recovery in oil-wet porous medium.

Throughout LSW injection microfluidic experiments after the long-term aging period with oil, fines migration was insignificant. In another set of experiments, when the systems were flushed with LS brine without any delay, fines migration was significant. These observations suggest that the aging time and crude oil composition are contributing factors to fines release.

Also analysed is the impact of type of clay mineral and nature of cations on LSE, using geochemical modelling complemented with visualisation experiments. The models are developed to provide the charge density and electrostatic potential profiles (the ζ -potential) at the brine/mineral interface of illite as a basal-charged clay against an edge-charge dominated kaolinite. Based on the observations and simulation results, it was concluded that since kaolinite has higher density of acid/base reaction sites on its surface (edges) than does illite, the charge development under differing ionic strength and pH was significant. As a result, kaolinite responded well to LSW injection, whereas illite did not. This could elucidate the unlike sensitivities of clays to LSW, such as their extent of being prone to wettability alteration.

The SCM results agree well with the microfluidic results when DLE is considered the mechanism behind LSE. The extent of the ζ -potential calculated by SCMs shows the degree of electrostatic repulsion between adjacent, similarly charged surfaces, that is, the brine–oil and brine–clay interfaces, so the enhanced repulsion forces weakened the oil and clay pinning

points. As a result, wettability altered toward more water-wetness, which is confirmed by contact angle measurements. Once the attraction forces were low enough, the oil was released from the clay surface and replaced by water, as observed in microfluidic experiments.

If the chemical composition of connate water and the content of clay minerals in a particular reservoir can be determined to a degree, the findings of this study will determine the concentration of ions and pH of the injecting water that maximise LSE (wettability alteration) and the resulting oil recovery.

Declaration

I certify that this work contains no material which has been accepted for the award of any other degree or diploma in my name in any university or other tertiary institution and, to the best of my knowledge and belief, contains no material previously published or written by another person, except where due reference has been made in the text. In addition, I certify that no part of this work will, in the future, be used in a submission in my name for any other degree or diploma in any university or other tertiary institution without the prior approval of the University of Adelaide and where applicable, any partner institution responsible for the joint award of this degree.

The author acknowledges that copyright of published works contained within this thesis resides with the copyright holder(s) of those works.

I give permission for the digital version of my thesis to be made available on the web, via the University's digital research repository, the Library Search and also through web search engines, unless permission has been granted by the University to restrict access for a period of time.

Signature:

Date: 04/07/2019

Tammy Amirian

Acknowledgment

I would like to thank my supervisory panel, Assoc. Professor Manouchehr Haghighi (Principal Supervisor) and Dr. Peyman Mostaghimi, for their support, encouragement, and guidance throughout my study. I would also like to thank Delis Hollands for her assistance and advice in matters concerning the experimental setup and procedure.

I extend my gratitude to the MUTRIS group at the University of New South Wales, particularly Dr. Ryan Armstrong, for their support and advice relating to the image processing and analyses.

I would like to thank Jose for his encouragement and support. Without your love, I could not have done it.

Chapter 1: Research background and Literature Review

1.1 Enhanced oil recovery

The current global recovery factor is almost 30% of the original oil in place (OOIP), which means that about 70% of global oil reserves cannot be extracted using conventional techniques. Improving the global oil recovery factor by as little as 1% would yield an additional 88 billion barrels annually, equal to three years of oil production.²

Oil production operations consist of three phases: primary, secondary, and tertiary recovery. In the primary phase, oil recovery from the reservoir relies on its natural energy such as solution gas drive or water drive. The secondary phase, also known as the improved oil recovery phase, often employs waterflooding, in which water is injected to maintain reservoir pressure in addition to displacing oil from pore spaces. These two phases, known as conventional recovery, can recover no more than 30–35% of the oil²⁻⁴.

Tertiary recovery, also known as Enhanced Oil Recovery (EOR), employs techniques such as steam injection, miscible gas flooding, and chemical injection. EOR increases large-scale sweep efficiency, which restores reservoir pressure and improves mobilisation efficiency. EOR design and method selection and the expected recovery depend on several technological and economic factors and considerations, such as oil viscosity and density, and reservoir rock properties. EOR can extract an additional 5–20% of the OOIP, bringing total oil recovery to 50–70%.^{2,3,5}

Low Salinity Water (LSW) injection is a promising oil recovery technique, in which low-salinity brine is used to reduce residual oil saturation. This approach could be applied both onshore and offshore.^{6,7} Improved recovery from LSW is referred to as the Low Salinity Effect (LSE). LSW flooding has attracted great attention over the last two decades, mostly due to its simplicity. The salinity ranges from 1000 to 2000 ppm which is significantly less than the salinity of the formation brine⁸⁻¹⁰. It requires no additional chemicals, which are often costly, although LSW has recently been coupled with other EOR methods such as surfactant or polymer flooding.¹¹ LSE has been observed for both secondary and tertiary phases. In the secondary mode, LS brine was injected into oil saturated reservoirs, while in the tertiary phase, LSW injection was performed after the formation has already been flooded in the secondary mode with brine of a different composition.⁶

1.2 Mechanism behind LSE

Several mechanisms have been suggested to explain LSE but none of them has been accepted as the dominant mechanism. Many of these mechanisms are related to each other. The main mechanisms are as follows.

One such mechanism is fines migration and limited release of mixed-wet clay particles.^{12,13} Suspended clay particles in the aqueous phase are believed to plug smaller pores or throats, thereby reducing permeability. This would divert the flow toward low-permeability zones, thus increasing sweep efficiency. Tang and Morrow¹³ combined the DLVO theory (named after Boris Derjaguin and Lev Landau, Evert Verwey and Theodoor Overbeek) with fines migration and proposed that the attachment of polar components of crude oil to the clay surface gives mixed-wet fines (Figure 1.1). Reduction of ionic strength expands the electrical double layer around particles, which increases fines detachment. The stripped fines combine, so the oil coalesces.

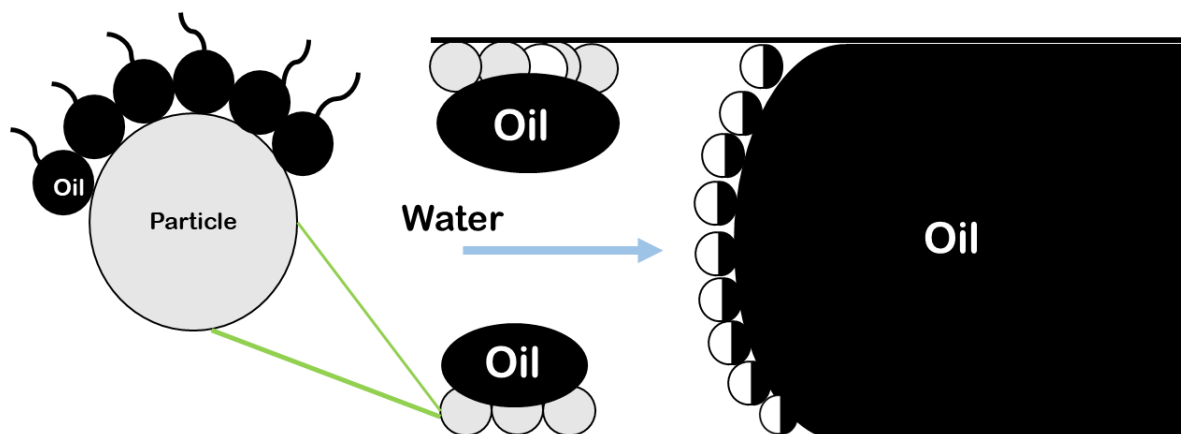


Figure 1.1: Adsorption of polar component from crude oil onto the surface of clay particles alters the wettability and causes fines to become mixed wet. LSE detaches fines from the pore wall, which leads to the release of oil.

Lager, et al.¹⁴ conducted several LSW flooding experiments under lab and reservoir conditions and recorded the increased oil recovery. However, unlike the previous reported experiments, neither fines migration nor significant permeability reduction was observed. Limited fines migration was also reported by Zhang and Morrow¹⁵ but permeability damage was minimal.

Similarly, Zhang, et al. ¹⁶ and Valdy and Fogler ¹⁷ reported EOR following LSW core flooding, although little or no clay was collected in the effluents.

Lager, et al. ¹⁴ proposed the multi-component ionic exchange (MIE) theory as the primary mechanism underlying the improved recovery. They hypothesised that when multivalent cations adsorb on the clay surfaces, they form organometallic complexes through bridging with oil molecules. During LSW injection, uncomplexed cations of the invading brine will replace and remove the organo-metallic complexes or organo-polar compounds from the clay mineral surface. This leads to detachment of oil components and a change in wettability.

MIE implies that for LSW to promote EOR requires multivalent cations such as Ca^{2+} and Mg^{2+} in the connate water. In the absence of divalent cations, no organometallic complexes can be formed. To test MIE, Lager et al. performed tertiary LSW flooding and found no LSE, which they attributed to the divalent cations' having been eliminated from the system. However, LSE has been observed even where no multivalent cations were present in the residential water, or when the injected brine had the same composition as the connate water. Yildiz and Morrow ¹⁸ recorded the highest recovery in their trials when a core that was initially saturated with brine containing 2% Ca^{2+} was flushed successively by brines with 4% Na^+ , 0.5% Ca^{2+} , and 2% Ca^{2+} .

McGuire, et al. ¹⁹ proposed that LSE could be due to the increase in pH and the subsequent reduction in Interfacial tension (IFT) similar to surfactant flooding. This pH increase would result from hydrogen's being exchanged with sodium ions on the clay surface. McGuire et al. proposed that under high pH, organic acid in the crude oil reacts and generates in-situ surfactants, which in turn leads to water-in-oil emulsification due to lower IFT. In contrast, most studies have reported that the pH of the effluents from LSW flooding either remained unchanged or was lower than 7. To generate in-sit surfactants, pH should be greater than 9. The buffering impact of reservoirs should have been taken into account as well. In addition, IFT under low ionic salinity was measured by Zhang and Morrow ²⁰ at 16 dyne/cm, not low enough to be indicative of IFT reduction. Buckley and Fan ²¹ reported 10 mN/m on $\text{pH} < 9$ as well.

Austad, et al. ²² proposed that multivalent cations desorb from the surface in response to decrease in cation concentration. The desorbed cations would be exchanged with protons produced from the hydrolysis of water molecules. This would create a local increase in pH, which induce the acid/base reactions that lead to the release of oil acidic and basic groups from

the surface. The net result is wettability alteration and oil detachment due to breakage of non-DLVO reactions at the water/clay and water/oil interfaces.

One of the simplest, yet effective ways in which low-salinity brine may alter the wettability is Double Layer Expansion (DLE). Counterions in the brine film adsorb to the negatively charged brine/oil and brine/rock interfaces. These ions form an electrical double layer at each interface and screen the electrostatic repulsion forces between the two negatively charged interfaces.²³ When the brine salinity is reduced, double layers around the charged interfaces expand to become more diffuse, thereby weakening the screening. Hence, the two interfaces experience a greater electrostatic repulsion. The expansion destabilizes the oil/clay pinning points; the wettability alters toward a more-water-wetting state, and when the attraction forces are low enough, the oil may be released from the clay surface.

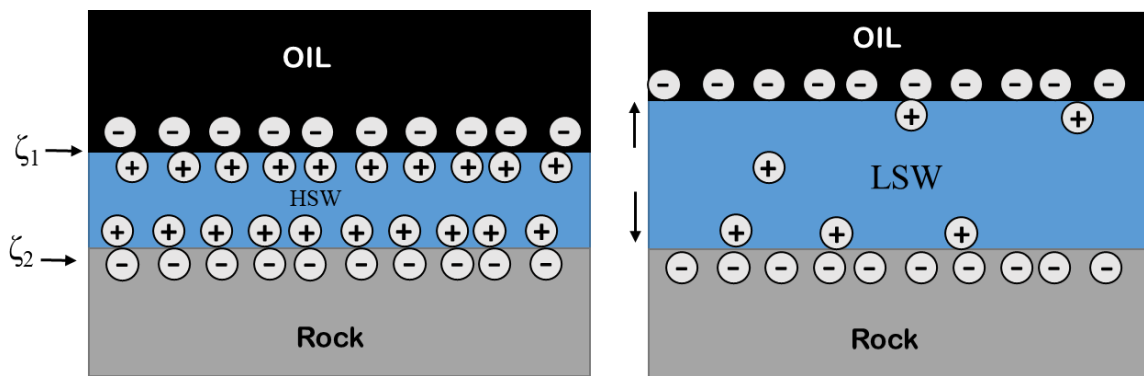


Figure 1.2: The reduction in ionic strength led to expansion of double layers (Debye length) of oil and clay, so the screening from the counter ions in the electrolyte becomes weaker, resulting in higher repulsion forces between oil and clay.

Wettability alteration has been frequently suggested as the main mechanism for LSE. Experiments have shown that LS brine changes the wettability towards more water wet.^{24,25} Vledder, et al.²⁶ found evidence of wettability alteration on a field scale. Wettability alteration is also a by-product of many proposed mechanisms, such as MIE, DLE, and the chemical mechanism proposed by Austad, which are directly related to stability of the thin brine film that wets the reservoir rock surface. Wettability depends upon the interactions between the brine/mineral and brine/oil interfaces. They can be categorised as DLVO and non-DLVO interactions. Electrostatic interactions between the charged interfaces, which are described by DLVO theory, are known as DLVO interactions. There are three types of non-DLVO interactions: (a) Lewis acid/base interactions between acidic charged groups (NH^+) in the oil

phase and negatively charged groups on the rock surface; (b) hydrogen bonding between polar functional groups present in the oil, such as asphaltenes, and polar components on the mineral surface; and (c) formation of organometallic complexes that bridge between divalent cations adsorbed on the surface and charged acidic groups on the oil surface (Figure 1.3).

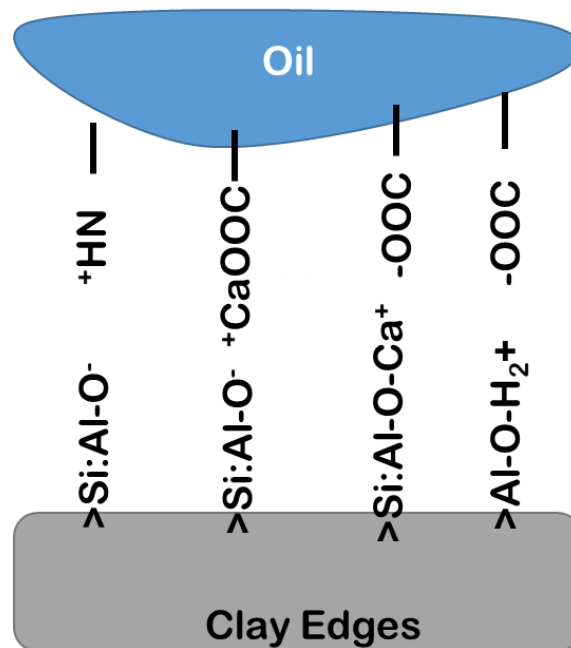


Figure 1.3: Illustration of non-DLVO interactions between brine/oil and brine/clay edge interfaces.

DLE takes into account the DLVO interactions to explain the LSE. In contrast, MIE and the chemical mechanism proposed by Austad consider changes in non-DLVO interactions under LS brine to be the main mechanism for improved recovery. Austad's mechanism could alter the surface charge of the brine/clay interface because the exchange of adsorbed divalent cations makes the clay interface even more negative, which in turn enhances the DLE. MIE and the Austad's mechanism initially proposed to happen on the clay surface only. However, recent findings suggest that these two mechanisms could occur on the clay-free quartz surfaces as well. Silica can undergo cation exchange, and the formation of molecular complexes on the silica surface has been reported.²⁷

It has been suggested that these three mechanisms occur together during LSW injection. Researchers^{28,29} have sought to compare the significance of DLE and MIE.^{28,29} Ligthelm, et al.²⁸ designed core flooding experiments where in the secondary mode, they flushed the

sandstone with formation HS brine containing both monovalent and divalent cations. Then, during tertiary mode, they injected HS NaCl at the same ionic strength as in the formation brine, resulting in 3% additional recovery. In tertiary recovery, MIE might have been a factor because Na could have exchanged with divalent complexes, but DLE could not have been, because the salinity was not lowered.

The HS NaCl injection then was followed by LS NaCl solution, which recovered an additional 6%. The improved recovery cannot be attributed to MIE since during HS NaCl injections all divalent cations were flushed out effectively. Although, DLE probably had a significant role and resulted in much larger recovery. Hence, they all concluded that DLE is more significant than MIE.

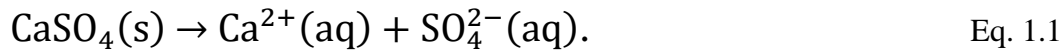
The salt-in effect is a proposed mechanism³⁰ for LSE in which reducing salinity lower than a critical concentration and corresponding ionic strength increase the solubility of organic materials. In Sandengen, et al.³¹ EOR attained through LS brine injection was attributed to osmosis: the difference between the chemical potential in LSW and oil causes water to migrate from LSW to the oil, where the oil acts as a semi-permeable membrane. Diffusion of water into oil forms water-in-oil emulsions, and the expansion of water-in-oil emulsions mobilises the oil phase.

1.3 Low salinity effect in carbonate reservoirs

Carbonates mainly contain calcite (CaCO_3), but they can also contain other minerals such as dolomite [$\text{CaMg}(\text{CO}_3)_2$], anhydrite (CaSO_4), and aragonite (another form of CaCO_3). Two common types of rock found in carbonate oil reservoirs are dolostone, which mainly contains dolomite, and limestone (e.g., chalk). Laboratory studies such as imbibition tests, core flooding experiments, and contact angle measurements have shown a positive LSE for carbonates. The positive impact of LSW on oil recovery in carbonates was first observed by Yousef, et al.²⁵ in which cores obtained from a carbonate reservoir were injected with six brines: formation brine, seawater brine, and seawater brines diluted by 2, 10, 20 and 100 times. They reported improved oil recovery from tertiary LSW flooding, which was consistent with their observation that the contact angle between oil drops and the flat surfaces of carbonates decreased in LS brines, which was indicative of wettability alteration.

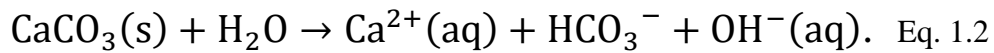
DLE and a chemical mechanism by Austad, et al.³² have been proposed to explain incremental oil recovery under LSW conditions. Austad's theory involves the production of $(\text{SO}_4)_2^{2-}$ due to

the dissolution of anhydrite. Sulphate ions are produced as anhydrite dissolves in LSW through the chemical reaction



According to Austad's mechanism, the sulphate ions adsorbed to the mineral surface, which results in co-adsorption of multivalent ions such as Ca^{2+} and Mg^{2+} . The adsorbed Ca^{2+} reacts with crude oil carboxylic groups initially attached to the carbonate surface. This breaks the bonds and releases the oil. Austad, et al. ³² also suggested that at sufficiently high temperature, Mg^{2+} can exchange with the Ca^{2+} initially present in the system which forms bridges with the acidic group in the oil phase. This substitution further improves oil recovery.

DLE has been extended to explain the incremental recovery during LS brine injection. According to this mechanism, lowering the ionic strength disturbs the thermodynamic balance between ions present in the system, which in turn induces the dissolution of calcite and anhydrite to compensate for the reduced concentration of ions in the aqueous phase. Calcite dissolves in water following the chemical reaction below, which may increase the pH



The above chemical reactions' effects such as increasing the pH and the production of and consequent adsorption of SO_4^{2-} ions make the brine/carbonate interface more negative. Hence, lowering the ionic strength expands the electric double layer around the charged interfaces, which reduces the screening potential from counter ions, so that the brine film thickens, and the surface becomes water wet. DLE theory in carbonates has been supported by zeta potential measurements, which have been reported to decrease even more under high temperature.

Many studies suggest that to achieve LSE in carbonate reservoirs does not necessarily require low salinity.²⁹ Even at salinity 35,000–45,000 ppm, tuning injection brine chemistry and concentration of active ions can aid oil recovery. These studies emphasised the need for appropriate concentrations of potential-determining ions such as SO_4^{2-} , Ca^{2+} , and Mg^{2+} in LSE. The ions that are responsible for the surface charge are the potential-determining ions. Al-Attar, et al. ³³ and Austad, et al. ³² suggested that there is an optimum combination of these divalent cations.

Al-Shalabi, et al. ³⁴ developed a thermodynamic model to simulate the wettability alteration reported in Yousef, et al. ²⁵ experiments. Al-Shalabi, et al. ³⁴ concluded that wettability

alteration in Yousef, et al. ²⁵ was strongly correlated to the change in surface potential as opposed to the anhydrite dissolution. They cautioned that this conclusion cannot be generalised to all systems.

1.4 Microfluidics

The combination of micromodels and advanced microscopy technology allow the direct visualisation platforms of fluid transport inside porous media in static as well as dynamic conditions. Microfluidic experiments can be conducted at both macro and pore scale. Direct visualization is particularly valuable for studying the multiphase flow in subsurface porous media. Pore-scale observations helps in formulating hypotheses regarding the underlying mechanisms of fluid transport phenomena and help in constructing quantitative and qualitative models. The modelling could be upscaled using mathematical techniques, enabling the simulation results to be substantiated against macroscale experimental results.

1.4.1 Microfluidics fabrication

Micromodels are fabricated primarily out of silicon. However, disadvantages include opacity and high cost. Substitutes for silicon include polymeric materials, such as polystyrene (PS), polymethylmethacrylate (PMMA), polycarbonate (PC) and the most commonly used material, polydimethylsiloxane (PDMS), as well as glass. Irrespective of the materials used, most microfabrication processes involve two main steps: lithography and shaping. Lithography is the transfer of a predesigned geometric image from a photomask to a photoresist layer on the substrate. Shaping physically alters the micromodel material to conform to the image, through replica moulding, etching, or hot embossing.

Lithography begins by using a high-resolution printer to generate a photomask that depicts a predesigned geometric pattern. The most common method of then transferring the image from the photomask to the substrate is photolithography, consisting of three steps. First, the substrate is coated with a light-sensitive material called photoresist. Second, the substrate is placed in an oven to remove the volatile solvents in the photoresist, which is termed “prebaking” or “soft baking.” Third, the photoresist layer is exposed to UV light through the mask, which changes the properties of the exposed material. More details regarding photolithography are provided Stevenson and Gundlach ³⁵; Berkowski, et al. ³⁶.

Shaping involves three stages: thin-film deposition, etching, and bonding. In the first stage, thin films such as silicon dioxide, polysilicon, silicon nitride, and metal are deposited onto the surface of the silicon wafer. This is usually accomplished through Physical Vapor Deposition

(PVD), in which the silicon wafer is placed in a vacuum or low-pressure gaseous environment where condensed vapor of the desired materials is deposited on the surface. An alternative is Chemical Vapor Deposition (CVD). The second stage involves removing the material not protected by the photoresist. Selecting an etching method depends on the structures being etched, the type of silicon wafer, and the aspect ratio of the channels that are to be etched. Methods include wet etching (using chemical solutions) and dry etching (using plasma). Wet etching can be isotropic (same etching rate in all directions) or anisotropic (etching rate varies by direction).^{37,38} Dry etching includes reactive ion etching (RIE) and deep reactive ion etching (DRIE). The details of etching techniques can be found in Schwartz and Schaible³⁹, Laerme, et al.⁴⁰, Wu, et al.⁴¹. The third stage involves bonding the substrate to an enclosure. The material of the fusing piece determines the bonding technique: fusion bonding for silicon to silicon, and anodic bonding for silicon to glass.⁴²⁻⁴⁵

Microfluidic devices can also be fabricated from glass alone or from glass and silicon. Glass micromodels go through photolithography and can be patterned by wet or dry etching or laser ablation. Another technique is sandblasting. Glass is fused to silicon through anodic bonding, to PDMS through plasma treatment, or to another blank glass by thermal bonding.⁴⁶

This study's flow visualization experiments used glass microfluidic devices that were fabricated using sandblasting. The microchannel pattern was taken from thin sections of actual porous rock representing heterogenous media. In this method, the pattern was first turned into photonegative image using image J and then printed onto a transparent plastic film.

Afterwards, the image was exposed to UV light and transferred to a UV light-sensitive photoresist film. This study used a 4-mm photoresist film, Rapid Mask, and an IKONICS UV-exposure unit. The cylindrical frame of the unit keeps the pattern and the photoresist at the same position, ensuring uniform exposure to UV light. Plasma treatment makes the white-assigned areas in the photonegative image brittle. The UV-exposure time was 60 seconds, beyond which the unwanted area might have also become brittle.

Next, the photoresist film was deposited on a piece of glass. The substrate was then placed in a sandblaster containing Zircon sand, which was propelled at the glass in order to etch where the photoresist film is brittle. To ensure uniform etching, an optimum pressure was also required. The parameters used in this study to fabricate the microfluidic device are listed in Table 1.1.

Table 1.1: Optimum parameters in glass micromodel fabrication

Parameter	Value
Photoresist film thickness	4 mm
Time of UV exposure on the photoresist film	1 min.
Sand grain size	150 micron
Pressure of sandblasting	30-35 psi
Exposure time of sand on the glass pate	4-6 sec/cm

Last, to enclose the device, a plain glass plate was fused to the etched plate using a thermal technique. They were placed in an oven and heated to 800°C for 10–20 mins. The fusing was performed in a programmable Labecs CEMLL Muffle (France). Prior to fusing, a sensitivity study was conducted, since temperature and soaking time are so crucial. Over-fusing can block the pores, and under-fusing leaves an unstable bond between the two pieces of glass. When the oven was turned off, the micromodel was left inside for 10–15 hours to cool down.

For polymer-based microfluidic devices, soft lithography is often used. First, a master mould on a silicon wafer is generated using photolithography. The master silicon wafer is then salinized with trichlorosilane to render the surface less hydrophobic prior to the PDMS coating. PDMS is made by mixing prepolymer with a curing agent. The master mould is then coated with the mix, degassed in a vacuum chamber, and cured. The pattern then is peeled off the mould and treated with oxygen plasma. The main advantages of using soft lithography are rapid prototyping, ease of fabrication, and not requiring expensive equipment.⁴⁷

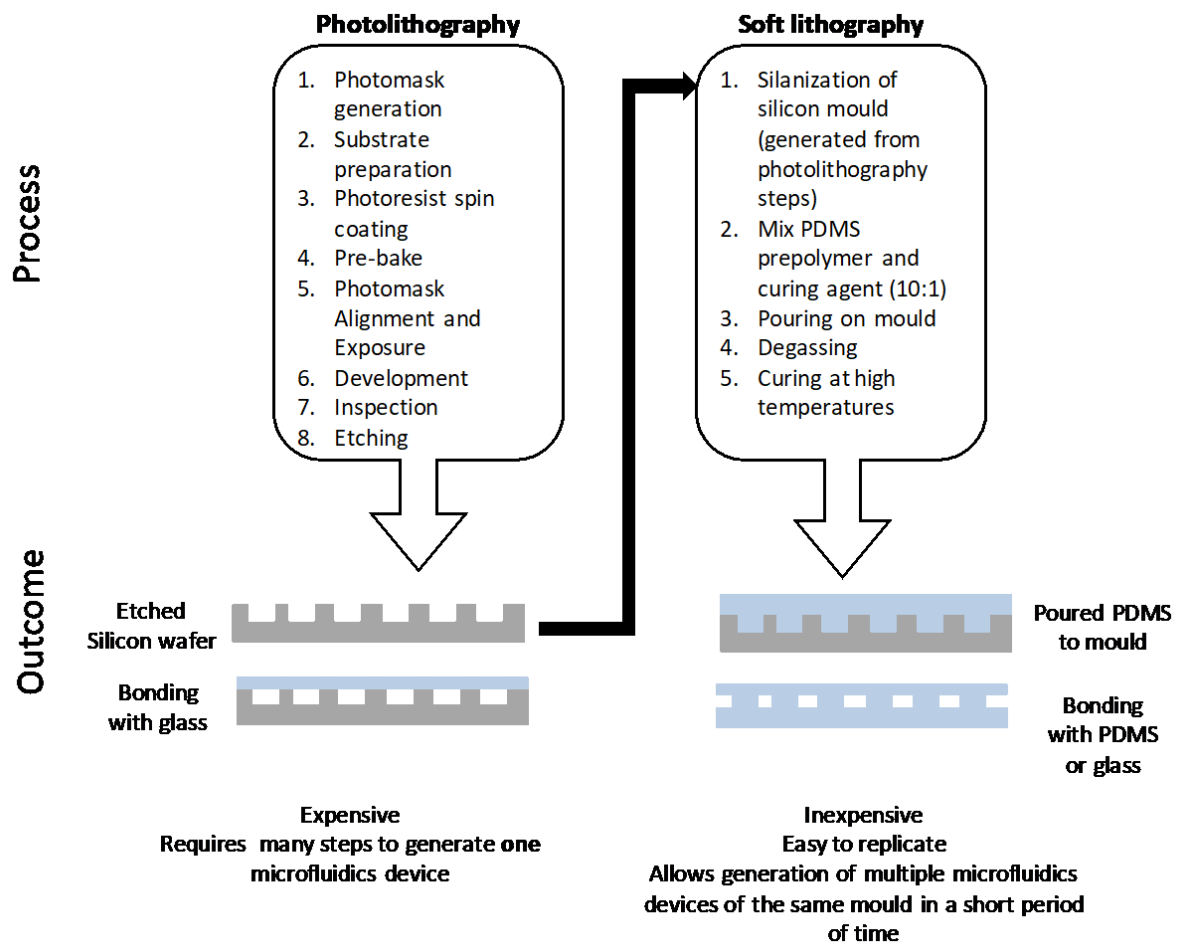


Figure 1.4: Comparison of photolithography and soft lithography techniques. Reproduced from Gerami, et al. ⁴⁸

Recent advances in the customization and development of PDMS micromodels including the integration of fiber optic pressure sensor into a PDMS chip in order to measure the pore pressure under transient multiphase flow ⁴⁹. Another example is a procedure to make a hydrophobic PDMS micromodel as demonstrated by Karadimitriou, et al. ⁵⁰. Gerami, et al. ⁵¹ fabricated a dual-wettability PDMS device for studying flow in regions with parallel and adjacent wettability⁵¹.

1.4.2 Geo-material micromodels

Traditional micromodels cannot accurately represent surface heterogeneity and surface chemistry that dictate pore-scale flow dynamics. Hence, they cannot demonstrate the geochemical and physical interactions between fluid/rock that are expected in natural porous media, nor can they depict heterogeneous wettability.

To address this, microfabrication techniques have been developed such as fabrication of real-rock models or functionalization of glass, silicon, and PDMS micromodels. To investigate the gradual dissolution of carbonate rock as a result of hydrochloric acid flow in conditions relevant to acidizing processes for reservoir stimulation, Porter, et al.⁵², used laser-etched rock to develop experimental systems involving geo-material micromodels made of cement, shale, siltstone, and sandstone. The experiments were conducted at pressures and temperatures consistent with conditions encountered in EOR, hydraulic fracturing, and geothermal operations. Song, et al.⁵³ established a method to etch microchannels into a natural calcite crystal. They first cut a calcite crystal into 3 mm-thick wafers, which were then dipped into 150°C beeswax and left to solidify. The desired microfluidic patterns were laser-etched into the wax, and the wafer and wax were immersed in hydrochloric acid, resulting in the inscription of the microfluidics channels on the calcite crystal. Last, the chip was bonded to a glass slide. The method was established in order to investigate the dissolution of carbonate rock over time as a result of hydrochloric acid flow in conditions relevant to acidizing processes for reservoir stimulation.

Gerami, et al.⁵⁴ fabricated a geo-material coal micromodel. The cleat structure pattern was based on the images obtained from coal micro-computed tomography (micro-CT). The CAD drawing of the coal cleat structure was imported into the laser machine micro STRUCT-C (3DMicromac, Chemnitz, Germany) and was etched on a flat coal surface. The cleat structure pattern was based on the images obtained from coal micro-computed tomography (micro-CT). The CAD drawing of the coal cleat structure was imported into the laser machine micro STRUCT-C (3DMicromac, Chemnitz Germany) and was etched on a flat coal surface. Wang, et al.⁵⁵ designed and executed a method for achieving more realistically simulated carbonate rock. They coated a glass micromodel with layers of CaCO₃ nanocrystal by adding a silane agent, followed by ions of Ca²⁺ and CO₃²⁻. To ensure a uniform thickness of CaCO₃ nanocrystals on the inner surface of channels, the process was monitored using dispersive X-ray spectroscopy (EDS), scanning electron microscopy (SEM) imaging, and Raman spectroscopy.

To investigate LSE in sandstone reservoirs, Song and Kovscek⁵⁶ developed a method to functionalise a silicon microfluidic device by depositing kaolinite into the micromodels. The clay functionalised model provided a tool with characteristic pore-geometry and realistic surface interactions between the reservoir fluids and the formation rock. A mixture of kaolinite and HSW was injected into the micromodel. After the dislodgement of throat-plugging

kaolinite with air, they followed two approaches, to create distinct systems. In one porous medium, the clays might be mobilised in response to the change in the ionic strength, whereas in the other one, clays were firmly adhered to the pore surface and fines were immobile for all salinities. To create a system for the clay detachment study, the microfluidic system with mobile clay particles was re-injected with the initial brine in order to remove the loose particles that were not attached to the silicon surface. The injection of HSW was continued until no further change in the deposited clay was observed. Then they tested the impact of ionic strength on clay detachment using various concentrations and compositions of brine. For wettability alteration studies during LSW injection, the system with immobile clay particles was used. The clay-saturated micromodel was first vacuum-dried. Then, the microfluidic chip was heated gradually to 120°C and maintained there for 25 minutes. The micromodel was initially drained of water in order to avoid its breaking due to the rapid volume expansion and subsequent pressure build-up during heating.

In another attempt to study the reactive transport in more realistically simulated porous media, Singh, et al.⁵⁷ designed and constructed a microfluidic setup called the Real Rock Microfluidic Flow Cell (RR-MFC). The microfluidic chip consists of a 500 µm-thick rock wafer from a subsurface reservoir inserted into a PDMS microfluidic channel, then it was sealed by plasma bonded PDMS, and equipped with inlet and outlet ports.

**Geo-material Microfluidics
Device Fabrication Method**

Illustration

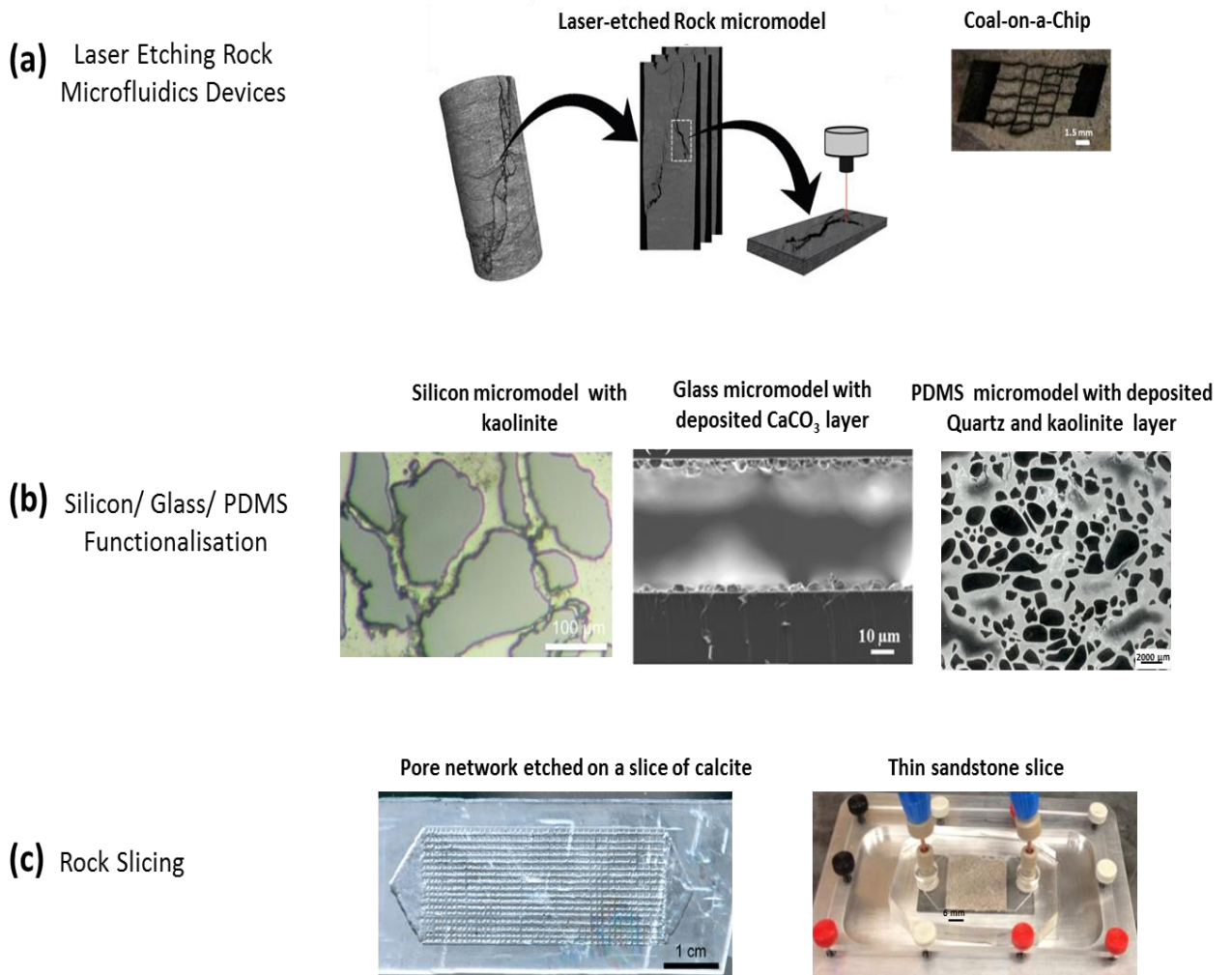


Figure 1.5: Overview of fabrication methods for geomaterial micromodels. (a) Laser etching on real rock surfaces. Reproduced from Gerami, et al. ⁵⁴(b) Silicon/glass/PDMS functionalisation by depositing relevant rock mineral. Reproduced from Song and Kovscek ⁵⁶. (c) Rock slicing. Reproduced form Song, et al. ⁵³

Recent studies demonstrated new methods to functionalise PDMS micromodels as well. Zhang, et al. ⁵⁸ introduced a method in which PDMS microfluidic devices are clay-coated layer-by-layer (LbL). First, PDMS containing the porous medium was exposed to plasma, then injected by poly (diallyldimethylammonium chloride) (PDDA) solution and by clay suspension. PDDA is a commonly used polyelectrolyte for LbL assembly. After each step, the device was dried, rinsed with DI water to remove loosely attached particles, and dried again before the next

deposition. The cycle was repeated until achieving the desired thickness of mineral covering the channels.

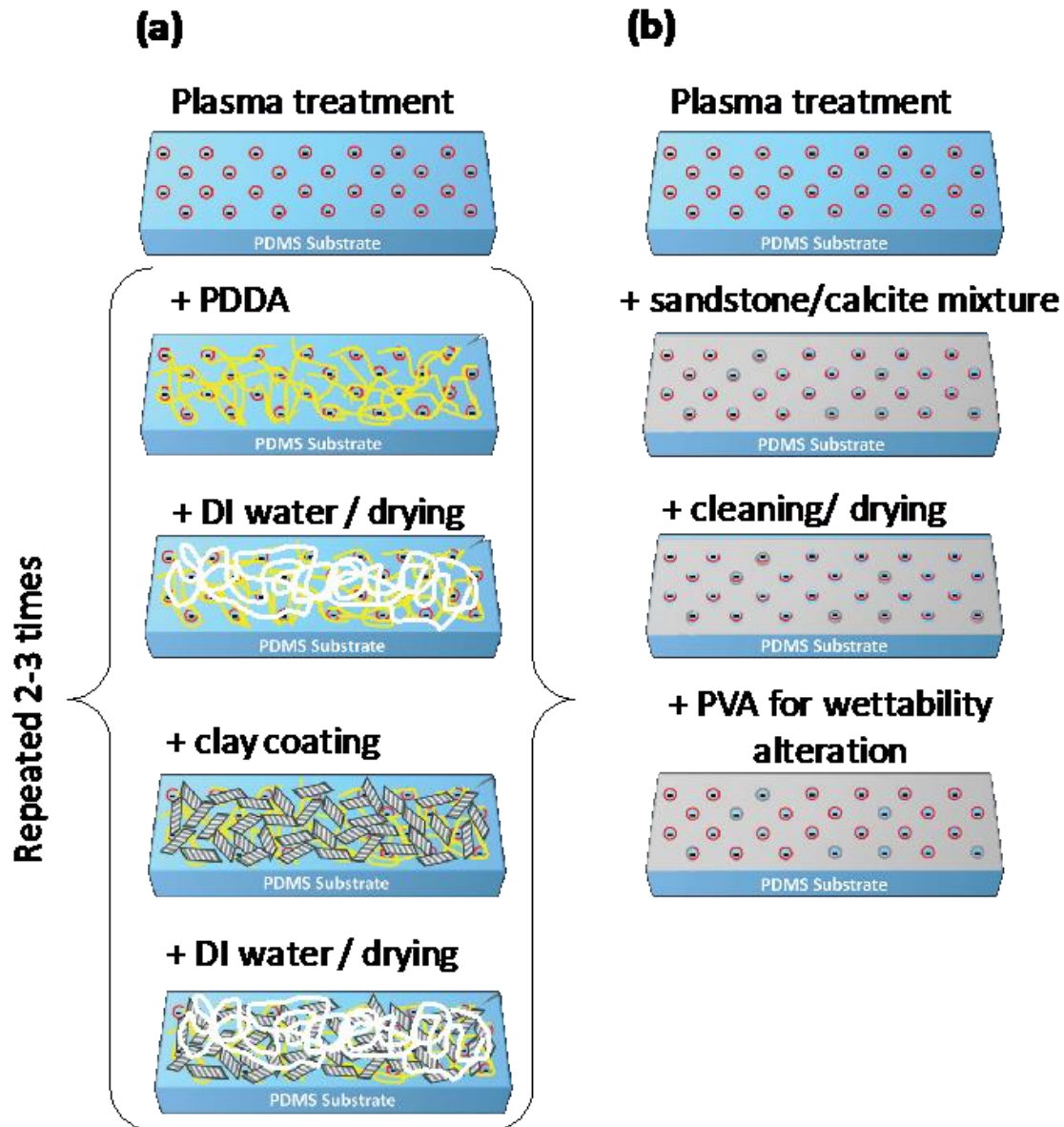


Figure 1.6: Two proposed processes of PDMS functionalisation (a) Layer-by-layer method, reproduced from Zhang, et al. ⁵⁸. (b) Method proposed by Alzahid, et al. ⁵⁹ Reproduced from Gerami, et al. ⁴⁸

Another method was developed by Alzahid, et al. ⁵⁹ to create geo-material micromodels that are representative of sandstone and carbonate reservoir rocks. Slurries of minerals were

prepared by mixing quartz and kaolinite, as well as carbonates with DI water. Mixing kaolinite and quartz formed silicic acid (SiOH_4) and kaolinite gibbsite (AlOH_3). However, the calcium carbonate precipitated out of the DI water as soon as it was left stagnant, but some Ca^{2+} ions attached with the silanol groups in subsequent steps.

Alzahid et al. used the lithography technique discussed earlier to transfer a predesigned random pore network from a photomask to a photoresist layer on a silicon mould. The mould then was etched with deep reactive ion etching (DRIE) technique to create 10 μm -depth pore networks. The mould then salinised and coated with degassed PDMS, followed by curing for 4 hours at 65°C. The PDMS slide containing the pattern was then peeled off the mould and exposed to oxygen plasma for 4 minutes and 15 seconds before being coated with 1 ml of the slurry of minerals and DI water. The plasma treatment caused oxygen to attach to the surface, which made it temporarily water wet, then the silanol groups bonded with silicic acid and kaolinite gibbsite in the sandstone mixture and calcium hydroxide in the carbonate mixture.

Then, the chips were air-dried and cleaned by ethanol. To ensure there were no particles on top of the PDMS pillars, the devices were inspected with a stereo microscope (PSB X2-4, Saxon). Such particles might have weakened the bonding between the cover and the chip containing the porous media. The slice containing the microchannels and minerals was bonded to a blank PDMS through a second plasma treatment. The second PDMS cover was left blank because the silanol groups on the PDMS are required for permanent bonding between the blank cover and the pillars of the PDMS with minerals.

Through SEM, EDS, contact angle measurements, and a surface profilometer, the functionalised PDMS micromodels were compared against carbonate and sandstone rocks. By comprehensively analysing micromodel features, it was concluded that the micromodels' wettability, contact angle, and roughness were comparable to those of sandstone and carbonate. In addition, semi variograms showed that mineral deposition across the different geo-material devices was nearly isotropic. At the end, visualisation experiments revealed multiphase flow phenomena such as snap-off and corner flow mechanisms, equivalent to those occurring in reservoir rocks. The workflow for fabrication of the geo-material PDMS microfluidic device is presented in Figure 1.7.

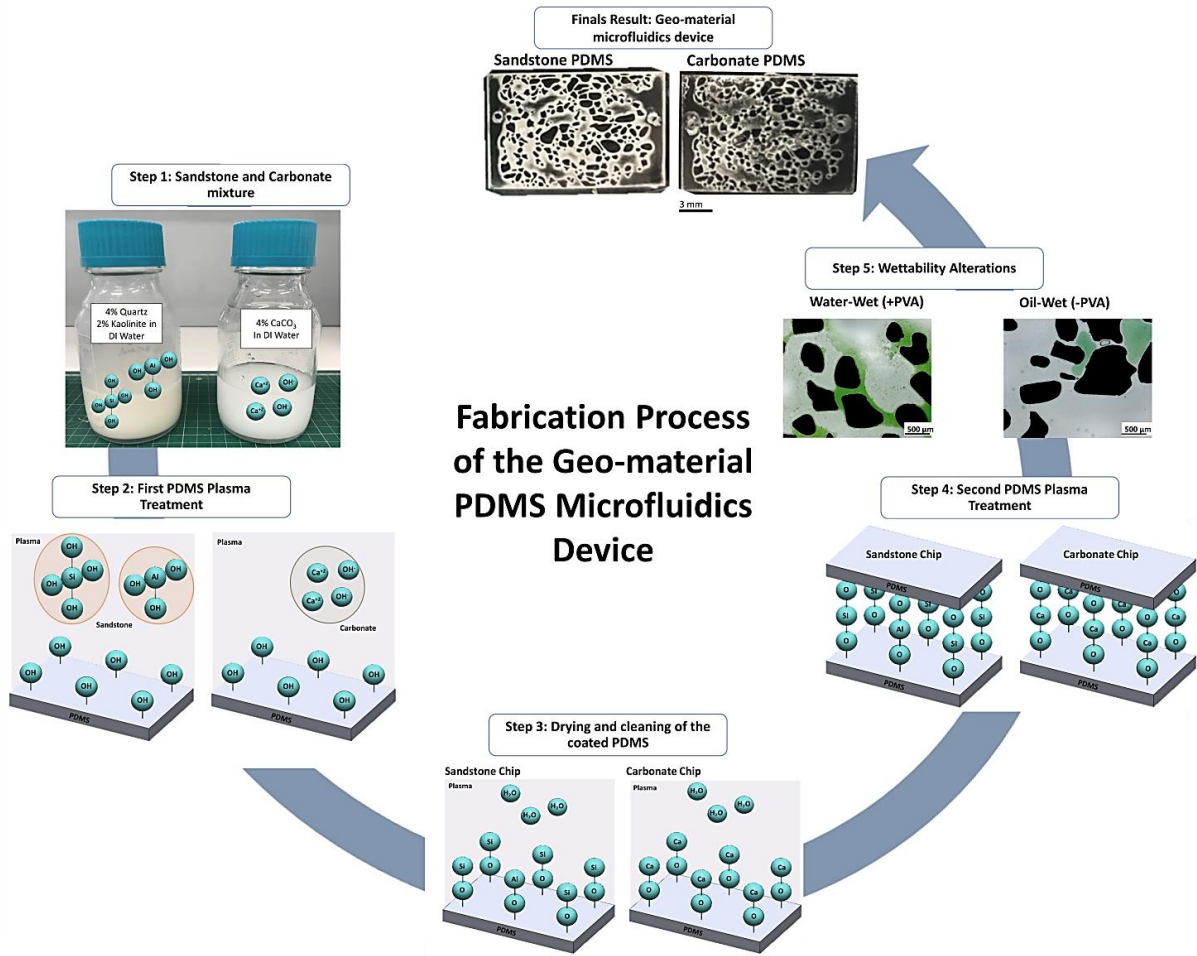


Figure 1.7: Fabrication process of the functionalised PDMS micromodels. Reproduced from Alzahid, et al. ⁵⁹

1.4.3 Measurements and visualization techniques:

1.4.3.1 Transmitted and reflected microscopy

Transmitted and reflected microscopy often employs a camera coupled to a microscope ⁶⁰⁻⁶² to visualise the flow system at microscale. This is one of most effective approaches for when the focus is on a particular area in the micromodel at high resolution ($<1 \mu\text{m}$), being able to measure parameters like interfacial curvature and contact angle. ⁶³ Rapid events can be studied by incorporating a high-speed camera. ⁶⁴ Reflected microscopy is suitable for transparent chips and for dark, solid, or opaque microfluidic devices if the light source and the optical access are on the same side of the chip. Transmitted microscopy can be employed even where the light source and optical access are on opposite sides of the chip.

1.4.3.2 Raman spectroscopy

Raman spectroscopy identifies molecule-specific information by measuring their vibrational modes.⁶⁵ Chrimes, et al.⁶⁵ discusses the technique in detail. Raman spectroscopy coupled with microfluidic experiments could be applied for analyzing miscible and immiscible fluids. They can provide information on fluid transport, which helps with identifying chemical pathways and structures, understanding thermodynamics and intrinsic kinetics, and improving the accuracy of mass transport coefficients.

1.4.3.3 Confocal microscopy

Confocal microscopy is used for three-dimensional (3D) imaging and for microfluidic experiments with high-resolution requirements ($< 1 \mu\text{m}$). This setup can be implemented to visualise rather slow fluid transport and displacements that occur over a length scale less than the optical diffraction limit. Confocal Laser Scanning Microscopy (CLSM) is an optical imaging technique for increasing contrast and optical resolution. It scans and captures multiple two-dimensional (2D) images at different depths in a sample and then reconstructs the 3D structure of the object using those planar images.

1.4.3.4 Fluorescent microscopy

Fluorescent microscopy distinguishes phases in porous media by adding dyes to the fluid phases⁶⁶, so the change in the light intensity can be monitored⁶⁷. Alternatively, fluids can be seeded with fluorescent particles⁶⁸. After the solution is tagged with a fluorescent dye, a light source is employed to excite the fluorescent particles. The particles emit light at a lower wavelength than does the light source, which is called the Stokes shift.⁶⁹ Then, the long-pass-filtered light is captured with a digital camera. Figure 1.8 shows images generated using different optical microscopes and techniques described briefly in this section.

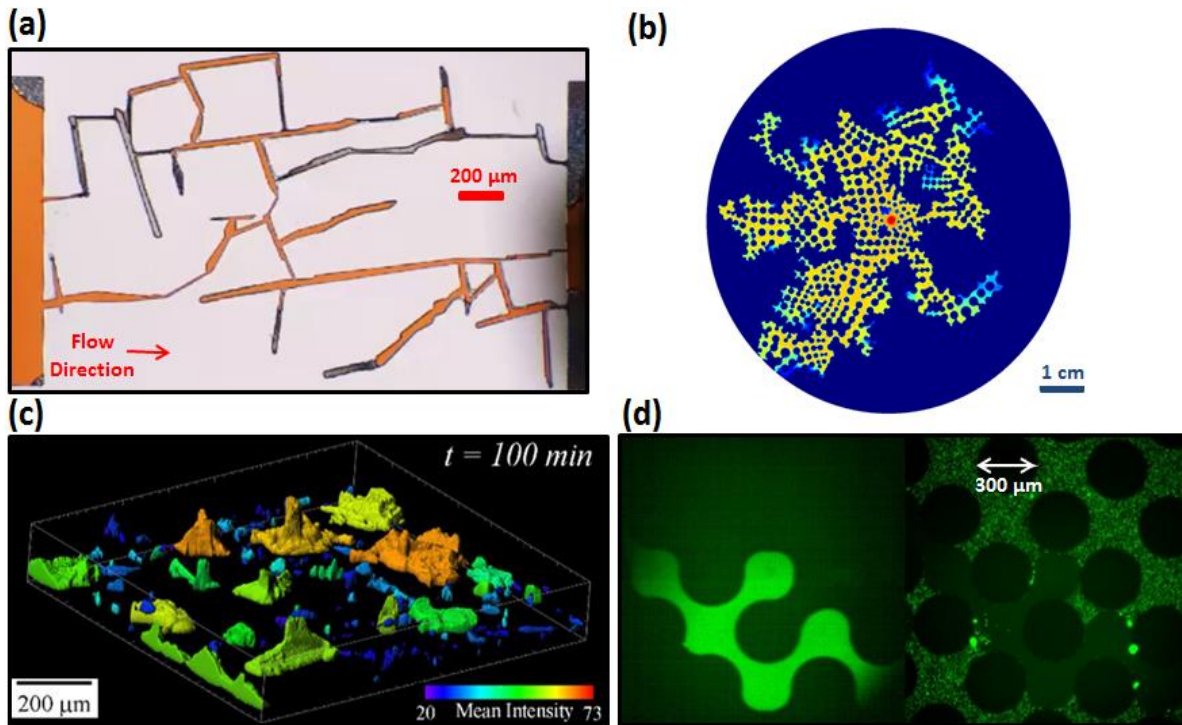


Figure 1.8: Images generated from various optical techniques. (a) Transmitted microscopy is employed to visualize the gas transport in a coal fracture. Dyes are added to the fluid phase to improve visualization. Reproduced from Gerami, et al. ⁷⁰. (b) The displacement of decane oil in a pore network is pictured using direct visualization setup. The injection starts from the center of the chip. (c) The image was taken using confocal laser microscope which was implemented to visualize displacement of fluorescein-dyed buffer by a non-dyed buffer. Reproduced from Singh, et al. ⁵⁷. (d) A dual camera visualization setup was used to capture the images of dyed CO₂ (left) and tracer particle image (right) in a silicon-based micromodel. Reproduced from Kazemifar, et al. ⁷¹.

1.5 Microfluidics applications in EOR

EOR processes in general involve the flow and transport of chemical species and the resulting phase behaviour in porous media. In chemical and thermal recovery in particular, microfluidic chips are implemented as a platform to assess pore-scale chemical or thermal recovery processes. These devices can be adjusted to accommodate a testing reservoir fluid at reservoir conditions.

He, et al. ⁷² used “Reservoir-on-a-chip” setup to compare the recovery efficiencies of non-emulsifying surfactants and weakly-emulsifying surfactants (WES). Using The “oil-wet” micromodels, He, et al. ⁷² produced experimental results that confirmed higher efficiency of the stimulation fluid with WES surfactant. Another study⁷³, investigated the effect of

wettability patterns on fluid displacement, using UV-initiated graft polymerization of polyacrylic acid to alter pore wettability. This revealed that rise in wettability heterogeneity significantly improved recovery. It was suggested that neither topology nor dimensions of the system influenced the observed phase behaviour.

Unsal, et al. ⁷⁴ investigated the effect of wettability patterns on fluid displacement, using UV-initiated graft polymerization of polyacrylic acid to alter pore wettability. This revealed that rise in wettability heterogeneity significantly improved recovery. It was suggested that neither topology nor dimensions of the system influenced the observed phase behavior.

Pei, et al. ⁷⁵, visualised the displacement mechanism in alkaline flooding using glass- etched micromodels. They observed emulsions in some sections of the glass micromodel (Figure 1.9b). For heavy oil displacements, they reported two pore-scale displacement mechanisms: formation of water-in-oil emulsions as well as partial wettability alteration, and formation of oil-in-water emulsions due to the surfactant. Song, et al. ⁵³ used an imaginative method to study the acidizing process in carbonate reservoirs. A crystal of calcite was etched to replicate the pore structure of a carbonate formation. This model was used to study the effects of acid brine flow (HCl+NaCl) and the resultant etching of the porous rock. Acidic brine solutions were injected into the model, and dissolution kinetics were recorded using optical microscopy. Several glass micromodels with varying fracture systems were used to study the impact of fracture characteristics (i.e., length, orientation, and number of fractures) on heavy oil recovery ⁷⁶.

It has been suggested that floods consisting of water mixed with nanoparticles could yield exceptional oil recovery. One nanoparticle that has been tried is colloidal silica, which has particle diameters in the range of 5–10 nm. Nilsson, et al. ⁷⁷ applied soft lithology to replicate actual sandstone profiles in PDMS micromodels. They investigated the effect of surfactants and nanoparticles on oil recovery. Li ⁷⁸ implemented glass micromodels to study the mechanisms behind improved recovery with nanofluids. Their visualisation approach enabled them to discern whether recovery was due to colloidal silica particles or silica nanoparticles. They suggested that although colloidal silica reduced the interfacial tension and enhanced forming water-in-oil emulsions, nanoparticles had the same impact on the interfacial tension, promote break-up of oil into smaller droplets forming oil-in-water emulsion.

Foams have higher viscosity than do normal solutions, which better allows them to flow into the higher permeability regions and render them less permeable. This diverts the flow to areas

with lower permeability, thereby improving sweep efficiency. Ma, et al. ⁷⁹ implemented a PDMS chip with regions of low and high permeability. By injecting gas into a co-flowing surfactant solution, foam was generated. Their results confirmed that surfactant-stabilised foams improve sweep efficiency from both areas more than does gas-only injection.

Following the same approach, Conn, et al. ⁸⁰ designed a glass model with a central fracture that was surrounded by the high- and low-permeability regions. It was visualised that foam increased the flow resistance in permeable regions and the fracture and diverts the flow into zones of low permeability, which improves oil extraction from those areas. Using a dual-porosity system to replicate the pore structure of a particular carbonate reservoir rock, they confirmed the effectiveness of foam injection at diverting gas flow from high-permeability regions to low-permeability regions.

In recovering heavy oil, thermal EOR techniques such as Steam-Assisted Gravity Drainage (SAGD) are frequently used. Glass microfluidic devices have been applied in order to comprehensively study conventional SAGD and hybrid SAGD processes (n-pentane and n-hexane additives).^{81,82} Microscale visualizations helped explain microscale flow, microscale displacement, and residual oil trapping mechanisms, including layered drainage flow perpendicular to the nominal oil-gaseous mixture interface, and coexistence of water-in-oil and solvent-in-water emulsification at the interface.

de Haas, et al. ⁸³ used “steam-on-a-chip” setup to compare the efficiency of bitumen recovery using steam with additive alkaline against that of pure steam recovery. To achieve high resolution, they exploited bitumen's inherent fluorescence in order to quantify the efficiency of an alkaline additive (Figure 1.9c). This additive reduced the mean characteristic size of oil-in-water emulsions formed during SAGD, which improved recovery by ~50%. To further analyse SAGD with and without the additive, infrared and optical pore-scale imaging were conducted on the same micromodel ⁸⁴. Microscale flow and high-resolution temperature analysis provided insight into pore-scale phenomena and assisted in identifying and understanding the link among the rapid temperature drop at the steam chamber interface, drainage modes, efficiency, and ultimate recovery achieved in SAGD.

de Haas, et al. ⁸³, investigated the performance of SAGD with alkaline and alcohol-based additives as well. Fluorescent microscopes were used to differentiate mechanisms associated with these additives. It was concluded that although alcohol-based additives provided a minor

change on the steam chamber growth, alkaline-based additives expanded the chamber significantly, which led to much greater improvement in recovery.

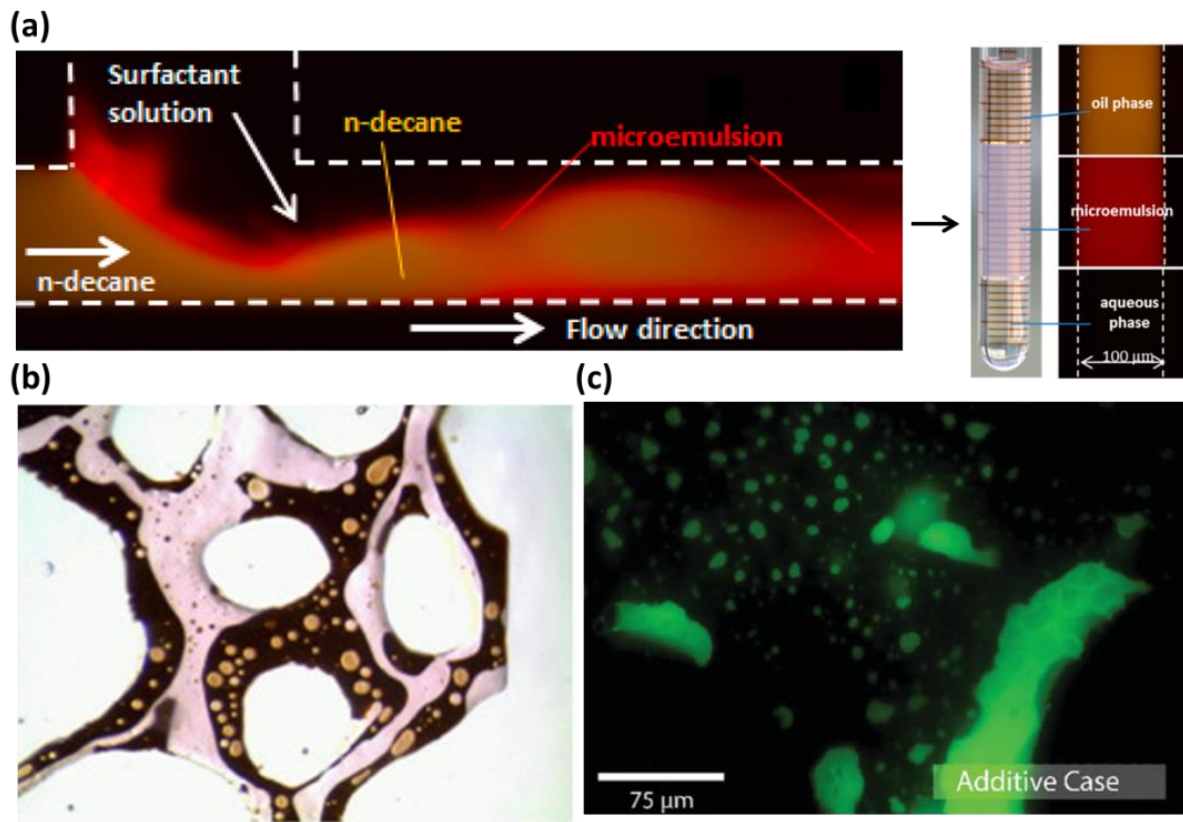


Figure 1.9: The formation of emulsion in three studies. (a) Top view of a T-junction capillary during the injection of the surfactant solution with a co-flowing colored decane under fluorescent light, highlighting the microemulsion formation at optimum salinity during continuous flow. Black represents aqueous phase, red represents micro-emulsion, and brown represents decane. Reproduced from Unsal, et al. ⁷⁴ (b) The image was taken after alkaline flooding. Emulsions are formed in some sections. Reproduced from Pei, et al. ⁷⁵. (c) Emulsions after steam-assisted gravity drainage (oil shown in green and water in black). Reproduced from de Haas, et al. ⁸⁵

1.6 Application of microfluidics in LSE Research

Although LSW flooding often leads to improved oil recovery, the experimental evidence has seldom provided an explanation. To address this, several researchers ⁸⁶⁻⁹⁰ have sought visual pore-scale evidence for the underlying mechanisms.

Morin, et al. ⁹⁰ introduced a microfluidic device to assess the effects of chemically mediated interfacial properties between oil and brine upon snap-off at the pore level. The device formed oil drops through extensional flows and allowed the aging of crude oil against brines having

different salinities, hence assessing the role of salinity in snap-off. LS brine was found to result in the development of dynamic interfacial viscoelasticity, thereby suppressing pore-level snap-off events.

Berg, et al. ⁸⁷ and Mahani, et al. ⁸⁹ used very similar setups to monitor the effect of LS brine on crude oil droplets attached to clay particles that were adhered to a glass substrate. The glass substrate was placed in a transparent flow cell. The researchers introduced LS brine and then monitored the amount of oil recovered as well as the change in the oil droplet contact angle. Barnaji, et al. ⁸⁶ used clay-coated glass micromodels and determined the oil recovery factor from micromodel images taken before and after LSW injection. They also monitored fines migration. Barnaji, et al. ⁸⁶ concluded that LSW in the secondary phase increased oil recovery and that the initial wettability of the porous formation is mixed-wet due to adsorption of polar compounds of oil onto the clay minerals (Figure 1.10).

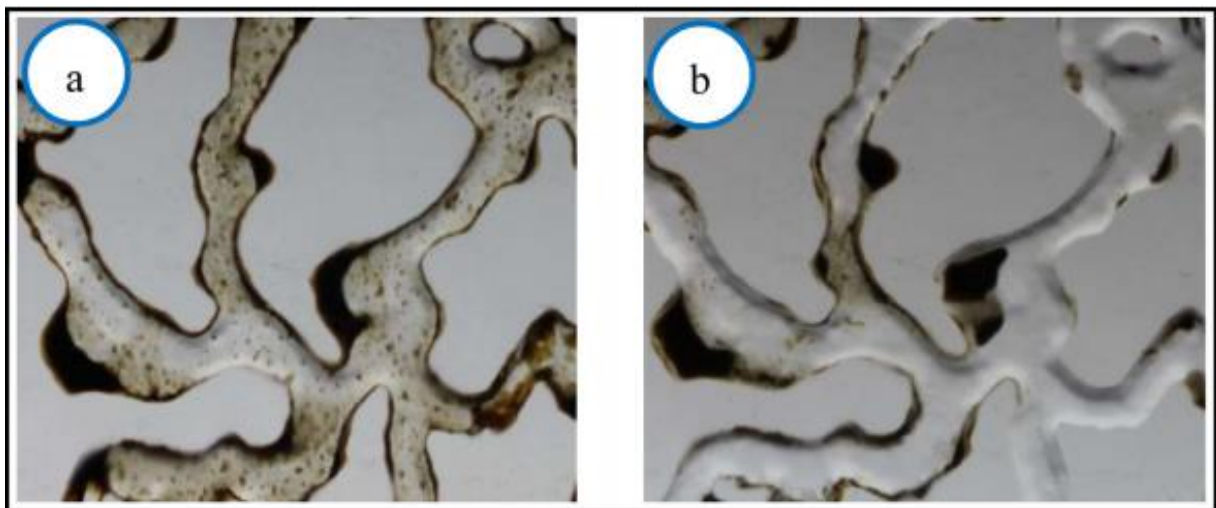


Figure 1.10 :Enlarged images of the clay-coated glass micromodel (a) before and (b) after secondary LSW injections. During the secondary phase, fines detached from the surface, which led to the release of oil attached to them. Reproduced from Barnaji, et al. ⁸⁶.

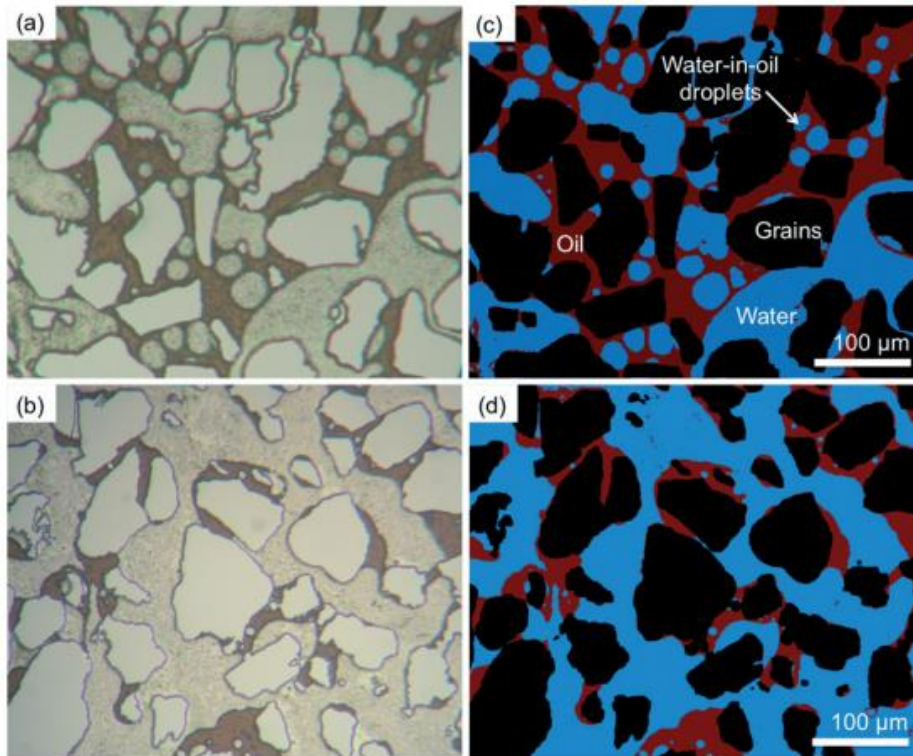


Figure 1.11: Images recorded by Song and Kovscek⁵⁶ after (a) HS brine and (b) LS brine injections. To calculate the residual oil saturation, these images were processed, yielding (c) and (d), respectively. The oil saturation was less for LS brine. Reproduced from Song and Kovscek⁵⁶.

Song and Kovscek⁵⁶ functionalised the micromodels and injected HS and LS brines in series, and image processing was applied to quantify the LSE on improved recovery (Figure 1.11). They have reported 14% improved recovery after initial HSW injection.

A few studies, reported fluid distribution and the micromechanism of displacement throughout LSW injection⁹¹⁻⁹⁴. Bartels, et al.⁹² used single-channel clay-functionalised micromodels, where a change in the oil contact angle was considered a positive response to LSW. Bartels, et al.⁹⁵ conducted dynamic experiments in natural rock and fluid systems instead of models and applied X-ray micro-CT to image the redistribution of fluids when LS brine was injected. They reported the occurrence of an additional oil/water structure (microemulsion) in the porous media.

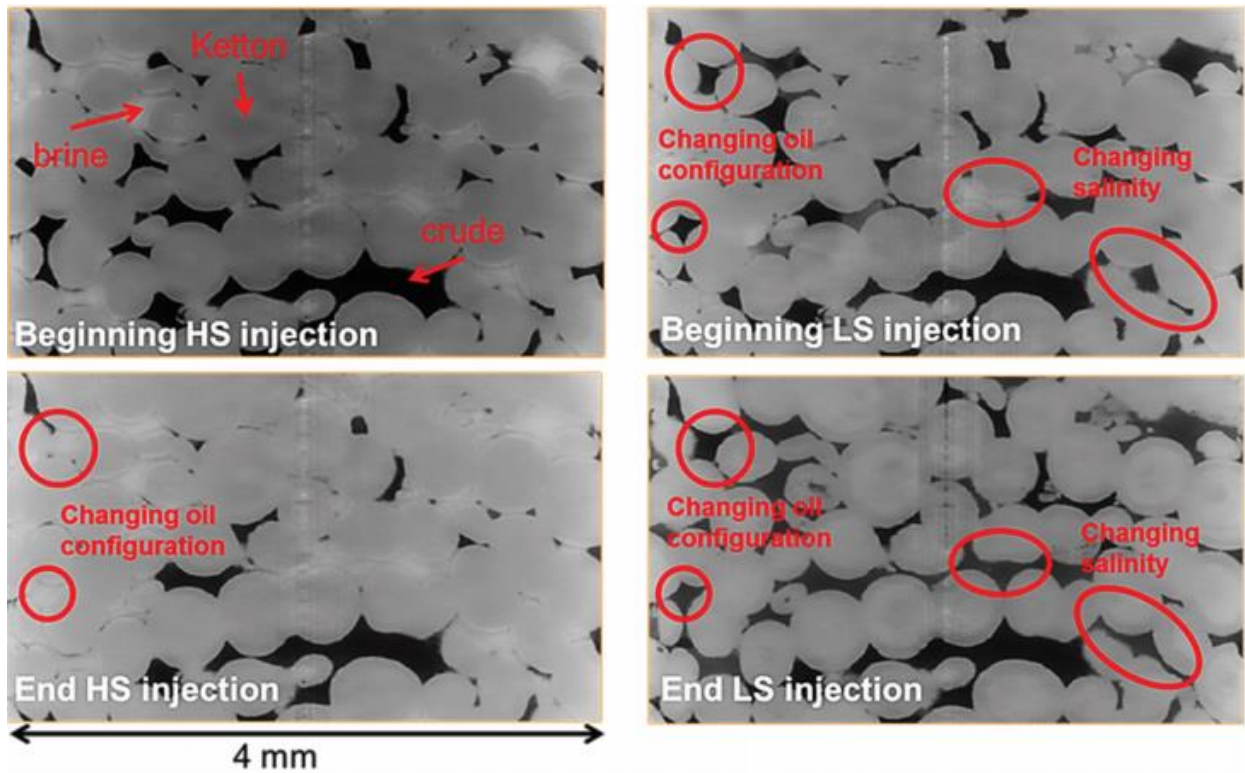


Figure 1.12: X-ray images showing the redistribution of fluids after LSW injection. Reproduced from Bartels, et al. ⁹⁵.

Emadi and Sohrabi ⁹³ used mixed-wet clean micromodels to visualize the mechanism of the LS brine effect. They suggested that the formation of water micro dispersion in oil phase led to a slight change in the fluid redistribution that led to improved recovery.

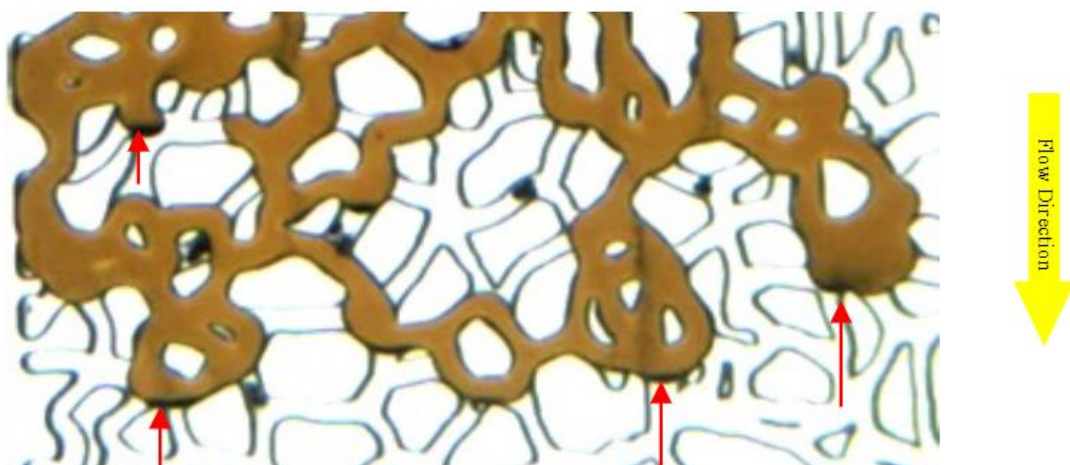


Figure 1.13: Emadi and Sohrabi ⁹³ suggested that formation of water micro dispersion in the oil phase (dark particles in the oil phase) led to a slight change in the fluid redistribution and resultant improved recovery. Reproduced from Emadi and Sohrabi ⁹³

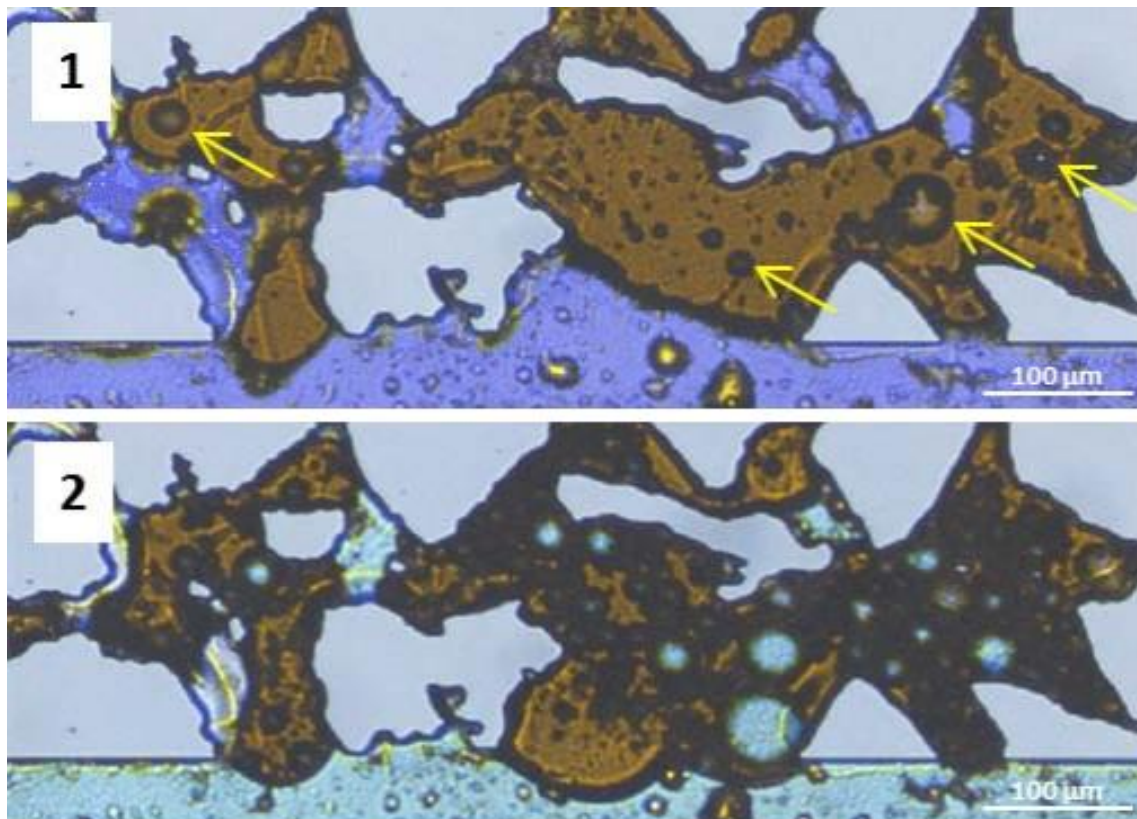


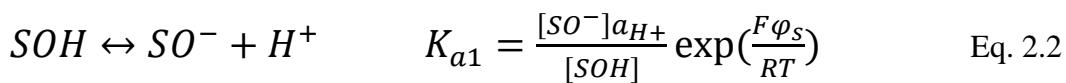
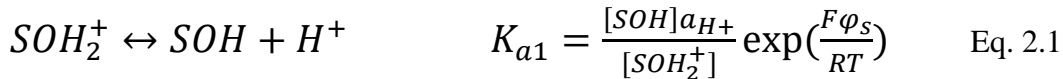
Figure 1.14: (1) The fluid distribution in HSW, prior to LS brine injection. The dissolved droplets of HSW in the oil phase are indicated by yellow arrows. (2) During LSW injection, the water-in-oil emulsification started to grow and the aggregation of emulsions displaced the oil ⁹⁴. Reproduced from Fredriksen, et al. ⁹⁴.

Fredriksen, et al. ⁹⁴ identified osmosis as the oil mobilisation mechanism during LS brine injection. They implemented capillary tubes and micromodels having different wetting properties. They reported that osmosis led to formation of water-in-oil emulsions and that the expanding emulsions displaced the oil phase. Osmotic oil mobilisation was observed under both oil-wet and water-wet conditions.

1.7 Surface complexation modelling:

Metal ions, through interactions with solid phases, can be removed from solutions. Adsorption is one of the most common interactions between metal ions in an aqueous phase and a solid phase present in the system. Adsorption is a surface process that leads to transfer of a molecule from a fluid bulk to solid surface. This can occur because of physical forces or by chemical bonds. It is simulated using a surface complexation model (SCM), which is a thermodynamic-based approach. An SCM depicts the interactions of components in the solution with the reactive surface, through solute-surface functional groups complexations or ion-pair

association. SCMs also integrate a description of the EDL formed around charged particles, which is used to adjust the activity coefficients for each surface species.⁹⁶ SCMs depict the extent to which chemical interactions between protons (hydrogen ions), surface functional groups, and metal ions results in the development of surface charge. Hydrogen ions are considered to be potential-determining ions at the mineral/water interface of oxide surfaces and are associated with the development of surface acidity. The following reactions are used to describe protonation/deprotonation reactions at the surface:



where $[]$ terms are concentrations, a_{H^+} is the activity of H^+ , ϕ_s is surface potential, T is absolute temperature, and R is the gas constant. SOH_2^+ , SO^- , and SOH represent the positively charged, negatively charged, and neutral surface sites, respectively. K_{a1} and K_{a2} are equilibrium constants, and F is the Faraday constant.

In SCMs, inner and outer-sphere surface complexes are developed between the metal ions and the reactive surface. Inner-sphere complexes are formed when no water of hydration exists between the adsorbing ion and the surface functional group. When at least one water molecule resides between the reactive surface and the adsorbed ion, the complex formed is termed as an outer-sphere complex.

Inner- and outer-sphere surface complexes are formed through interactions between adsorbed multivalent ions (e.g., Me^{2+}) and surface hydroxyls ($\equiv SOH$). For a divalent metal ion, these reactions can be described by the following equations:



Figure 1.15 illustrates the inner-sphere (Eq. 2.3) and outer-sphere (Eq. 2.4) surface complexation of divalent metal cations to an iron oxide.

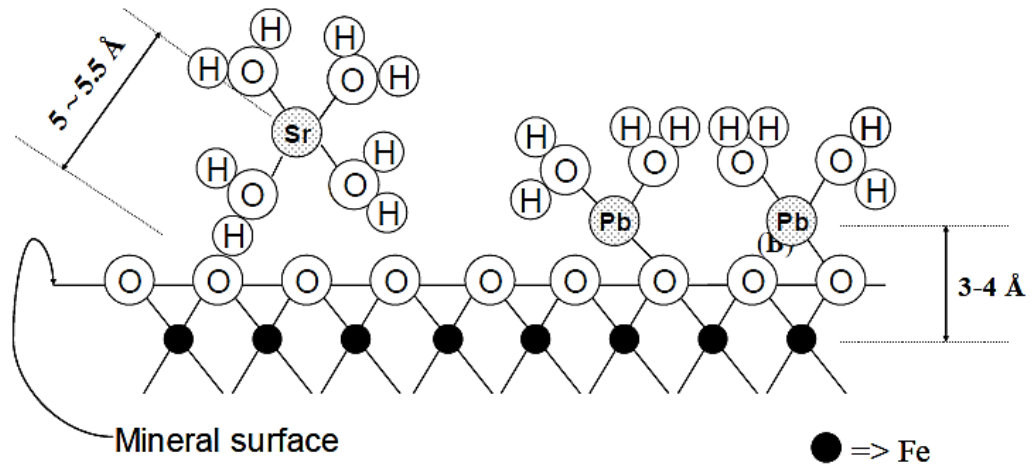


Figure 1.15: Inner-sphere and outer-sphere adsorptions. The inner-sphere adsorption formed surface complexes in which there is no water between the adsorbing ion (Pb) and the surface functional group. However, each outer-sphere adsorption has at least one water molecule between the adsorbing ion (Sr) and the surface functional group.

1.7.1 Parameters estimation for surface complexation models

SCMs have a several number of input parameters, such as surface site density, surface area, interfacial capacitances as well as surface equilibrium constants. To determine the model parameters, theoretical or experimental methods are required. In this modelling approach, it is essential to minimise the number of adjustable parameters as much as possible. When the value of input parameters is optimised using mathematical and theatrical techniques, instead of being measures directly, the accuracy of modelling will suffer. Hence, it is crucial to determine as many of these data experimentally as possible in order to improve the chemical significance of SCMs.

Although the most reliable method of evaluating the model parameters is to measure it directly, direct experimental methods are not available except for total site concentration ⁹⁷. As an alternative, the values of model parameters are often selected as a set of values and evaluated based on their ability to simulate experimental titration data adequately. For oxide minerals, the total site concentration (moles/litre) can be calculated from measured values for surface area (m²/g), site density (site/m²), and solids concentration (g/L):

$$\text{Total site concentration} = \text{Surface area} \times \text{Site density} \times \text{Solid concentration} \times 1.66 \times 10^{-6}$$

Site density and surface area can be determined experimentally from tritium exchange measurements and BET surface area, respectively. The value of site density for oxides ranges from 2 to 20 sites/nm².⁹⁷⁻⁹⁹

As mentioned above, acid-base titration data are required to estimate surface equilibrium constants. Titration is an analytical chemistry technique that determines an unknown volume and concentration of an analyte (the titrand) by reacting it with a known volume and concentration of a standard solution (called the titrant). Titrations are typically used for acid-base reactions and redox reactions. There exist various mathematical methods for parameter estimation from titration data. The two common approaches for determining the surface complexation constants from titration data are objective curve fitting and graphical extrapolation.⁹⁷⁻⁹⁹

SCM complexity varies according to a model's ability to predict surface ionisation and adsorption. The more parameters a model contains, the more closely it can fit the data. Nevertheless, the capability of the model to predict data more accurately comes at an expense. An inclusive model requires many parameters to describe the adsorption process and surface ionisation. Fortunately, for numerous cases, metal ion adsorption behaviour can be adequately described using simpler models.

1.7.2 The Diffuse Layer Model (DLM)

The Diffuse Layer Model (DLM) was first developed by Huang and Stumm¹⁰⁰ and refined by Dzombak¹⁰¹. The DLM is one of the simplest electrostatic models, as it requires only three parameters: two surface equilibrium constants (K_{a1} and K_{a2}), and the number of surface sites (N_s). The inner sphere is considered the adsorption mechanism as well. The impact of ionic strength on adsorption is accounted for through the direct relationship between surface charge (δ_s) and ionic strength (I), as seen in Eq. 2.5. Therefore, DLM can be applied to systems with low and variable ionic strength conditions. The double layer surface potential is linked to the surface charge by

$$\sigma_s^2 = 8000 \varepsilon \varepsilon_0 R I T \left[\sinh \left(\frac{F \varphi_s}{2RT} \right) \right] \quad \text{Eq. 2.5}$$

where I is the ionic strength of the electrolyte, T is the absolute temperature, R is the ideal gas constant, ε is the vacuum permittivity, and ε_0 is the dielectric constant of pure water. A schematic of the diffuse double layer used in DLM is presented in Figure 1.16. A diffuse double layer is formed by the ions from the background electrolyte. This double layer is to balance the

surface charge, which is the result of adsorption and desorption of potential determining ions in the system.

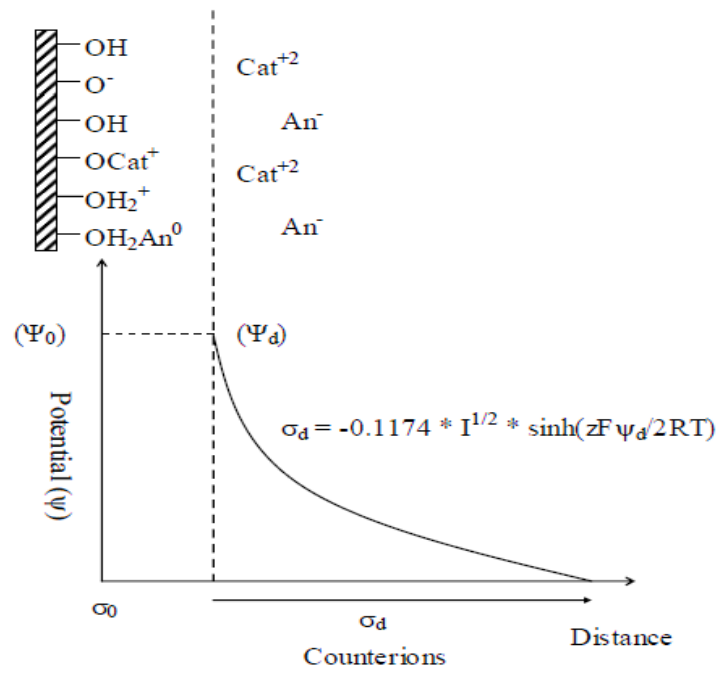


Figure 1.16: Schematic of the Electrical Double Layer used in the DLM.

Chapter 2: Project Aims and Thesis Outline

2.1 Research gap

Although LSW flooding has been shown to improve oil recovery, reported results have been inconsistent and sometimes conflicting. The mechanisms associated with the LSE are still debatable, and conditions for LSW flooding to work are still unclear. For each mechanism or explanation there are several experimental counterexamples published in the literature, and this is the challenge of defining the primary mechanism of LSW flooding and the main research gap. Even though some necessary prerequisites or working conditions for the Low Salinity (LS) injection are known, they are not yet sufficient to guarantee the success of LS brine flooding. In some cases, where the necessary prerequisites were met, no LSE was observed or vice versa^{12,102}.

2.2 Research aims and objectives

The main aim of this research is to study the LSE at the fundamental and microscopic level, so as to assess the relative influence of the major parameters and phenomena involved in the process, the major objectives are listed below:

- To directly visualise the impact of LSW on dynamics of displacement and measure the recovery factor
- To analyse the impact of clay minerals type;
- To investigate the fines migration and its contribution to LSE;
- To analyse the effect of chemical composition of residential and injectate brines;
- To study the impact of potential determining ions such as Ca^{2+} ;
- To assess the impact of initial wettability status on the process.

Another aim is to develop a geochemical model for predicting the degree of wettability alteration for different clay types and ion concentrations. Fundamental understanding of the mechanism behind LSE and its controlling factors would contribute significantly to the EOR method design and reservoir selection for LSW treatment.

2.3 Thesis Outline

2.3.1 Experimental phase

Chapter 1 presents a comprehensive literature review of LSW flooding, its significance as an EOR method, and the mechanisms proposed to explain the LSE. It also discusses the

fabrication of micromodels, the experimental setups, visualisation and measurement techniques, functionalisation of microfluidic devices, new advances in fabrication of geomicromodels, and the history of microfluidic applications in EOR. In the current chapter (chapter 2) the aims and objectives of this research are presented.

Chapter 3 consists of a paper titled, “Pore Scale Visualization of Low Salinity Water Flooding as an Enhanced Oil Recovery Method,” which presents the experimental phase of this study, including the detailed experimental procedure, the visualisation results, and related discussions. The micromodels are functionalised by depositing clay minerals into the micromodels in order to create a surface that represents the surface heterogeneities and surface chemistry that dictate pore-scale flow dynamics in reservoirs. The wettability status was also set to both water-wet and oil-wet.

In order to investigate the controlling factors for the LSE, such as clay type and brine composition, micromodels are functionalised with kaolinite and illite to visualise the performance of each clay during LSW injection. A variety of brine concentrations and compositions are used as the injecting and injectate waters to study the impact of water composition on LSE. An automated measurement is also conducted using an algorithm that determines contact angles from pore-space images. Details of the sensitivity analysis experiments and contact angle measurements, in addition to the results, are discussed in papers titled, “Impact of Clay Type and Nature of Cations on Low Salinity Water Injection – Visualisation Approach” and "Geochemical Modelling and Microfluidic Experiments to Analyse Impact of Clay Type and Cations on Low Salinity Water Flooding,” given as Chapters 4 and 5.

2.3.2 Simulation phase

Following pore scale visualisation, a surface complexation model is developed to extend our electrokinetic analysis of wettability alteration during LSW injection. The thermodynamic model is developed to predict clay mineral surface charge distributions for different fluid compositions and concentrations that could occur during LSW injection. The numerical model is tested by comparing modelling results against microfluidic observations. Based on the observations and the simulation results, as well as the geochemistry and chemical structure, the unlike sensitivities of clays to LSW which in turn leads to different extents of wettability alteration has been elucidated. These are coupled with the geochemistry and chemical structure

to determine the sensitivities of clays to LSW and the resulting extent of wettability alteration. The above are presented in Chapter 5.

2.3.3 Conclusions and recommendations

Chapter 6 summarises the conclusions of this research and suggests future work.

2.3.4 Appendices

The appendices contain two papers: “Microfluidics for Porous Systems: Fabrication, Microscopy and Applications” and “Functionalisation of Polydimethylsiloxane (PDMS)-Microfluidic Devices Coated with Rock Minerals.”

The first paper discusses traditional fabrication techniques for microfluidics devices and recent techniques that use three-dimensional printing; geomaterials and biomaterials; and multiphase transport in subsurface porous media and can be applied to hydrology and petroleum engineering. It also covers the application of microfluidics to study membrane systems in biomedical science and particle sorting. Last, it explores how synergies across disciplines can lead to innovations in the oil exploration field. It highlights a number of problems that have been resolved, topics that are under investigation, and cutting-edge applications. The second paper presents a new fabrication process for creating geo-material micromodels, by attaching rock minerals to Polydimethylsiloxane (PDMS). The functionalised micromodels are compared to carbonate and sandstone rocks, using energy dispersive X-ray spectroscopy.

Chapter 3: Pore Scale Visualization of Low Salinity Water Flooding as an Enhanced Oil Recovery Method

Statement of Authorship

Title of Paper	Pore scale visualization of low salinity water flooding as an enhanced oil recovery method.
Publication Status	<input checked="" type="checkbox"/> Published <input type="checkbox"/> Accepted for Publication <input type="checkbox"/> Submitted for Publication <input type="checkbox"/> Unpublished and Unsubmitted work written in manuscript style
Publication Details	Tammy Amirian, Manouchehr Haghighi, and Peyman Mostaghimi. "Pore scale visualization of low salinity water flooding as an enhanced oil recovery method." <i>Energy & Fuels</i> 2017, 31(12) (2017): 13133-13143.

Principal Author

Name of Principal Author (Candidate)	Tammy Amirian		
Contribution to the Paper	Conducted the experiments, performed data analysis, interpreted data, wrote the manuscript and acted as the corresponding author.		
Overall percentage (%)	65%		
Certification:	This paper reports on original research I conducted during the period of my Higher Degree by Research candidature and is not subject to any obligations or contractual agreements with a third party that would constrain its inclusion in this thesis. I am the primary author of this paper.		
Signature		Date	27/03/19

Co-Author Contributions

By signing the Statement of Authorship, each author certifies that:

- i. the candidate's stated contribution to the publication is accurate (as detailed above);
- ii. permission is granted for the candidate to include the publication in the thesis; and
- iii. the sum of all co-author contributions is equal to 100% less the candidate's stated contribution.

Name of Co-Author	Manouchehr Haghighi		
Contribution to the Paper	Developed the concept of the work, supervised development of the work, helped in data interpretation and manuscript evaluation.		
Signature		Date	02/04/2019

Name of Co-Author	Peyman Mostaghimi		
Contribution to the Paper	Helped to evaluate and edit the manuscript.		
Signature		Date	27/3/19

Pore Scale Visualization of Low Salinity Water Flooding as an Enhanced Oil Recovery Method

Tammy Amirian,^{*,†} Manouchehr Haghighi,[†] and Peyman Mostaghimi[‡]

[†]Australian School of Petroleum, Faculty of Engineering, Computer and Mathematical Sciences, The University of Adelaide, Adelaide, SA 5000, Australia

[‡]School of Petroleum Engineering, The University of New South Wales, Sydney, NSW 2052, Australia

S Supporting Information

ABSTRACT: The controlling mechanisms behind low salinity water flooding (LSWF) as an Enhanced Oil Recovery (EOR) method are not well understood. So far, a limited number of researchers have tried to provide visual and direct evidence of the underlying mechanisms behind the LS effect. In this paper, to investigate the dynamics of displacement throughout LSWF, clean and clay-coated two-dimensional glass micromodels were used, with the wettability status set at both water-wet and oil-wet conditions. Hence, pore-scale displacement mechanisms in the presence and absence of clay, as well as in the drainage and imbibition-dominated two-phase flow, were studied. In water-wet systems, in the absence and presence of clays, LSW hindered “snap-off” perhaps due to the development of a viscoelastic water–oil interface. The wettability alteration toward more water wetness was observed for oil-wet systems. The observations are discussed in terms of the expansion of the Electrical Double Layer (EDL). Fines migration played an insignificant role in our observations.

1. INTRODUCTION

The low salinity effect on improved recovery was first reported by Bernard,¹ although most of the modern work on this topic began in the 1990s. In 1996, Yildiz and Morrow² advanced the research started by Jadhunandan,³ and published their paper on the influence of brine composition on oil recovery. They showed that not only the physical properties of the injection water, i.e., density and viscosity, matter, but also its chemical properties, such as brine composition, are of great importance for determining the ultimate level of oil recovery from a reservoir. Since then several researchers have conducted laboratory experiments and field trials to investigate the low salinity water (LSW) effect.^{4–9} They have confirmed that performing a secondary or tertiary LSW, with salinity in the range 1000–2000 ppm, results in enhanced oil recovery.

Based on the experimental observations, several mechanisms of low salinity water flooding (LSWF) have been proposed. Among them wettability alteration is the most frequently suggested mechanism in the literature.^{10–12} Many other mechanisms could lead to wettability alteration. Fines migration and double layer effect are among the mechanisms which could result in wettability alteration. A number of authors suggested that, in a complete water-wet system, LSW could lead to the reduction of snap-off and consequently to enhanced oil recovery. There is no general agreement over the main mechanism, and none of the suggested mechanisms to date have been generally accepted as the true mechanism.^{10,12–16} For each mechanism or explanation there are several experimental counterexamples published in the literature, and this is the challenge of defining the primary mechanism of LSWF. Most likely, different mechanisms work under different conditions. Even though some necessary prerequisites or working conditions for the low salinity flooding (LSF) are known, they are not yet sufficient to guarantee the success of

LSF recovery. In some cases, where the necessary prerequisites were met, no low salinity effect was observed or vice versa.^{10,16} Therefore, more research is needed to identify the true mechanism and sufficient conditions for the low salinity effect to work, so that its field performance can be predicted accurately.

Most experimental evidence of the improved oil recovery associated with LSWF is indirect and macroscopic, that is, in the form of an increase in the produced oil. Limited numbers of researchers^{17–20} took a different approach in order to study LSWF and tried to provide visual and direct evidence underlying mechanisms of the LS effect at pore scale. Berg et al.¹⁸ and Mahani et al.²⁰ in very similar setups have monitored the effect of low salinity brine on crude oil droplets attached to clay particles adhered to a glass substrate that was placed in a transparent flow cell. They monitored the amount of oil recovered as well as the change in the oil droplet contact angle after LS brine was introduced to the system. Song and Kovscek²¹ and Barnaji et al.¹⁷ used clay-coated glass micromodels and measured the oil recovery factor based on the micromodel images taken before and after LSW injection. They also monitored fines migrations.

In a few studies, fluid distribution and the micromechanism of displacement throughout LSWF have been reported.^{22–25} Emadi and Sohrabi²⁴ used mixed-wet clean micromodels to visualize the micromechanism of the LS brine effect. They suggested that the formation of water microdispersion in oil phase led to a slight change in the fluid redistribution and resultant improved recovery. Another experimental study²⁵ identified osmosis as an oil mobilization mechanism during low

Received: June 16, 2017

Revised: October 26, 2017

Published: October 31, 2017

salinity water flooding using capillary tubes and micromodels with different wetting properties. Bartels et al.²³ used single channel clay-functionalized micromodels and a change in the oil contact angle was considered as the positive response to LSW. In another study,²² they conducted dynamic experiments in natural rock and fluid systems instead of models and applied a X-ray micro-CT technique to image the redistribution of fluids when low salinity brine was injected. They reported the occurrence of an additional oil/water structure (micro-emulsion) in the porous media. However, such observations need to be further assessed to evaluate the existing hypotheses on the influence of LSW on fluid distribution and the micromechanism of displacement for systems (porous media) with a variety of statuses in wettability, fluid properties, and lithology.

Herein, a microfluidic approach is developed to understand micromechanisms of displacement under LSWF at the pore scale level (micrometers to millimeters) using glass micromodels. The micromodels provide direct visualization of the controlling mechanism of LSWF. To investigate the dynamics of displacement in a variety of conditions throughout LSWF, clean and clay-coated micromodels were used, with the wettability status set at both water-wet and oil-wet. Different micromechanisms of displacement were observed for water-wet and oil-wet conditions. These observations have been discussed in terms of expansion of the electrical double layer (EDL).

2. MATERIALS AND METHODS

2.1. Test Fluid. Deionized water was used to make different concentrations of saline water (NaCl solutions) as the aqueous phases. The saline water properties are listed in Table 1. The crude oil was

Table 1. Basic Properties of Brine Solutions^a

component (salt)	HSW/connate water (pH 7)	LSW (pH 7)
concentration (ppm)	30 000	0–6000
viscosity (cP)	1.2	1.1
density (g/cm ³)	1.01	1
interfacial tension (mN/m)	23	23

^aHSW, high salinity water; LSW, low salinity water.

obtained from Cooper Basin in South Australia and used as the oil phase. The crude oil physical properties are listed in Table 2. The interfacial tension (IFT) of crude oil/water was measured using a Kruss spinning drop tensiometer, and is included in Table 1.

Table 2. Basic Properties of the Crude Oil Used in This Study

API gravity at 60 °F	53.2
density at 60 °F	0.76
viscosity (cSt) at 40 °C	3.2
acid number (mg of KOH/g)	<0.1

2.2. Clay Minerals. Clay minerals were deposited on the solid surfaces of the glass micromodel to create a visualization platform with more representative surface interactions between the reservoir fluids and the reservoir rock. The clay mineral used in the experiments was kaolinite. The kaolinite was supplied by The Clay Minerals Society (www.clayminerals.org) and was used without any purification or alteration. Kaolinite, Al₂Si₂O₅(OH)₄, is a typical 1:1-type clay mineral and consists of alternating silica (SiO₄) tetrahedral and aluminum hydroxide (Al(OH)₃) octahedral sheets. In the octahedral sheet, each aluminum atom is coordinated by two oxygen atoms of the tetrahedral sheet and shares four hydroxyls with neighboring

aluminum atoms. The hydrogen bonds between the hydroxyl ions of the octahedral sheet of one bilayer and the tetrahedral oxygen atoms of the adjacent silica sheet of the next bilayer hold the kaolinite layers together.

2.3. Clay-Coating Procedure. Clay minerals are always present in sandstone reservoirs, from 2 to 15%.²⁶ To coat the micromodel with clays, a slurry made of clay particles and high salinity brine water (30 000 ppm NaCl) was made and injected into the system. Prior to injection, to obtain a homogeneous solution, the mixture was stirred for 15 min followed by sonication for 1/2 h to prevent flocculation from occurring. The slurry was injected into the micromodels using a syringe pump at a very high rate of 20 m/day for several pore volumes to avoid clay settlement and clogging. During several practical tests, the optimized concentration of the clay content in the suspension (20 wt %) and the flow rate were selected both to prevent the pore plugging and to ensure a quasi-homogeneous distribution of clay in the micromodel.

For the clay-coating purposes, in the majority of the reported experiments in the literature, after clay injection, the micromodels have been heated in ovens for at least 72 h at 80 °C.^{27,28} As a result, the water of the suspension evaporated and dried clay adhered to the pore walls. Heat drying clay minerals can lead to irreversible clay coating, which means that the clay left on the surface of throats and grains would be immobile and unresponsive to any change in the salinity. Exposure of micromodels to extreme heat would induce chemical degradation of the clay minerals. To address this issue, the models were air-dried while they were placed on a hot (80 °C) plate. The micromodel was hot-air-dried for 2 h. Very strong interfacial tensions between the air and water phases would also dislodge the blocked throats and the moderate temperature of the hot plate would assist with the drying procedure. The whole process was monitored using the microscope setup. The images were taken from evenly distributed parts of the micromodel after deposition and analyzed to ensure a quasi-homogeneous distribution of clay in the micromodel pores. The clay deposition was characterized mostly as pore lining, and for very small parts of the model, a pore bridging structure was observed.

A very similar approach was employed by Song and Kovscek,²¹ but their procedure for clay deposition was further optimized to be applicable to the methodology employed in the current study. Song and Kovscek²¹ only air-dried (no heating was involved) the micromodel to study the LS brine effect on the clay detachment in single phase flow. However, to study the wettability alteration throughout LS brine injection for two phase flow analysis, they heated the micromodel up to 120 °C for 25 min.

Moreover, to make the system oil-wet, the pH of the clay suspension was modified. Kaolinite is always (even after drying) covered with a thin water film which originates from the capillary condensation in small pores between clay aggregates as well as from the air humidity. The wettability of kaolinite depends on the stability of the thin brine film, which is influenced by the salinity and pH of the liquid phase, as well as the aging time.²⁹ This thin film is increasingly prone to rupture, to allow adhesion and deposition of oil, if the concentration of sodium is decreased and/or brine pH is decreased. The kaolinite had already been saturated in high salinity (HS) brine, so the presence of salt in high concentrations did not contribute to the adhesion of the oil. Lowering the pH of the slurry by almost 20% contributes to the rupture of the thin film and, as a result, the adhesion of oil to the surface during the inadequate time allowed for aging. The pH reduction (of only 20%) is not considered a drastic modification since the pH is still well above the zero point of charge (ZPC) of kaolinite and the surface remains negative. The stability of the water film will be discussed in more detail in Section 4.2. Figure 1 shows microscopic images of the micromodel before and after injecting the slurry and air drying. As seen in Figure 1, grains and throats are evenly coated with a sufficient amount of kaolinite.

2.4. Microfluidic Setup. The microfluidic setup includes a pump to inject water, a glass micromodel, and a microscope equipped with a camera, which is connected to a computer. A schematic of the experimental system is provided in Figure 2. Flow and transport within the micromodel were visualized using a BH12 fluorescence microscope

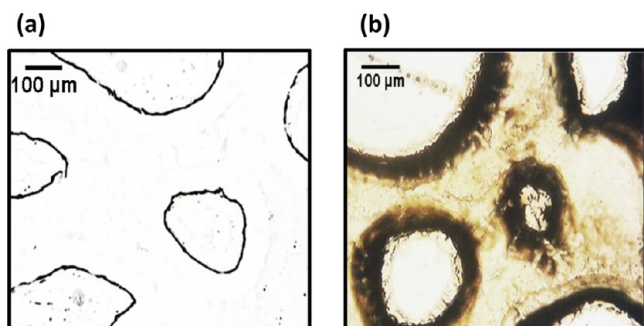


Figure 1. (a) Clean micromodel; (b) clayey micromodel after air drying.

(Olympus, Tokyo, Japan). The microscope was equipped with a camera (Moticam 580, China). The camera captures 5 megapixel, 2560×1920 images and records videos at 1080P (full HD) using the Motic Images Plus software package.

3. VISUALIZATION EXPERIMENTS

The visualization experiments were divided into two categories: (1) LSWF in the absence of clays; (2) LSWF in the presence of clays

3.1. LSWF in the Absence of Clay. At this stage, a clean micromodel was continuously flushed with several pore volumes of brine with a salinity level close to the initial formation brine (30 000 ppm NaCl). Once the micromodel was fully saturated with brine, crude oil was injected for several pore volumes at a constant rate of 30 m/day. The water saturation was monitored over time, and continued until it became invariant. After the microfluidic system was aged (3 weeks), low salinity solutions were injected at a constant rate until no incremental increase in water saturation was observed. The injection rate was set at a rate which corresponds to a domain velocity of 10 m/day. Deionized water was used to make the NaCl solutions with different concentrations. Salt concentrations in the reduced salinity saltwater ranged from 6000 to 0 ppm NaCl (fresh water) in decrements of 2000 ppm. The pH of the brines was neutral.

3.2. LSWF in the Presence of Clay. Following the clay-coating procedure discussed in section 2.3, high salinity brine

(30 000 ppm NaCl) and oil were introduced into the system to replicate the initial reservoir condition. After a delay which took 3 weeks, LS brine was injected at a flow rate of 10 m/day. Similar to LSWF in the absence of clay, the LS brines were NaCl solutions at concentrations spanning the range 6000–0 ppm (fresh water) and with pH 7. The LSW injection was continued until the water saturation plateaued. To investigate LSW effects and their possible contribution to enhanced oil recovery (EOR) comprehensively, the wettability status of the microfluidic devices was set at water-wet and oil-wet conditions. To make the system oil-wet, the glass micromodel was saturated with oil and then aged for almost 3 weeks. The presence of salt in connate water increases the hydrophilicity of clay minerals significantly,³⁰ which leads to an extremely water-wet system, so the micromodel was saturated with oil only. In addition, slight pH modification ($5 < \text{pH} < 6$) on the clay slurry was performed because, even in the absence of the connate water, the oil-saturated porous medium behaves as a water-wet system. Even after 3 weeks of aging with oil, the thin brine film was visible around the grains under the microscope, which is indicative of a fully water-wet system.

4. RESULTS AND DISCUSSION

4.1. LSWF in the Presence of Clay Minerals (Water-Wet Porous Media)

A mixture of kaolinite and brine with a salinity of 30 000 ppm NaCl was injected into the micromodel. Afterward, the micromodel was hot-air-dried and the clay-coated model was saturated first with high salinity water (30 000 ppm NaCl) and then crude oil. The initial water saturation (S_{wi}) was almost 3%. The porous medium was completely water-wet since kaolinite is highly hydrophilic and the presence of salt enhances the water wettability considerably. As mentioned in section 2.2, kaolinite has two different basal surfaces: a siloxane surface (SiO_2) and a hydroxylated surface (O–H). The strong water affinity may be attributed to the formation of hydrogen bonds (HBs). The Si–O–Si on the siloxane surface can serve as HB acceptors, while the O–H groups on the hydroxylated surface act as both HB acceptors and donors. The formation of HBs determines the surface wettability of clays. More HBs and more intense HBs result in the stronger water affinity of the clay basal surface. The

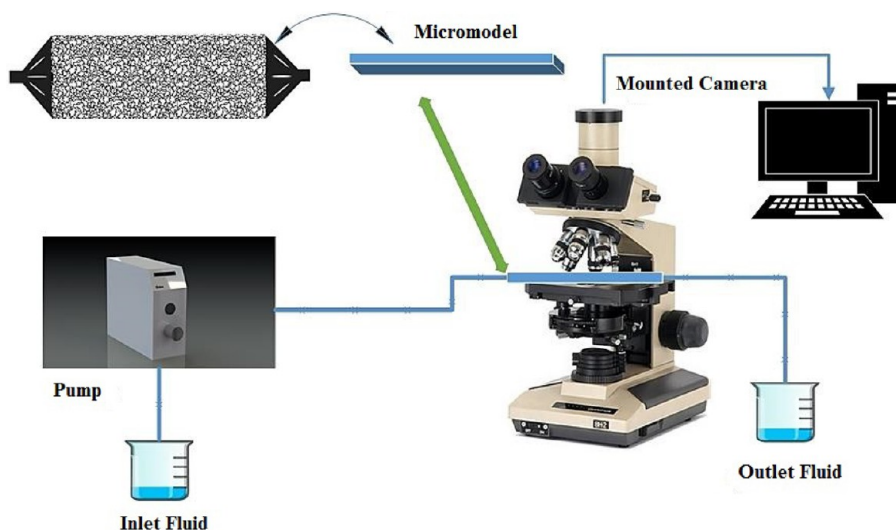


Figure 2. Laboratory setup.

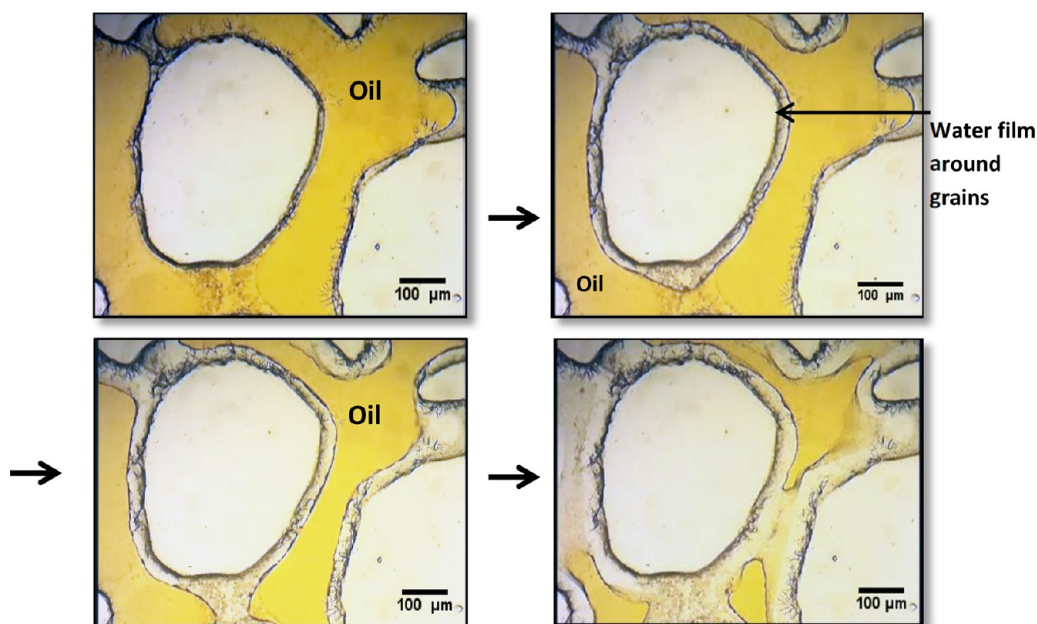


Figure 3. Sequence of snapshots from the video recorded when the water-wet system was flushed with saline water. During imbibition, water flows through thin layers coating the solid, pinching off threads of oil in the narrow channels.

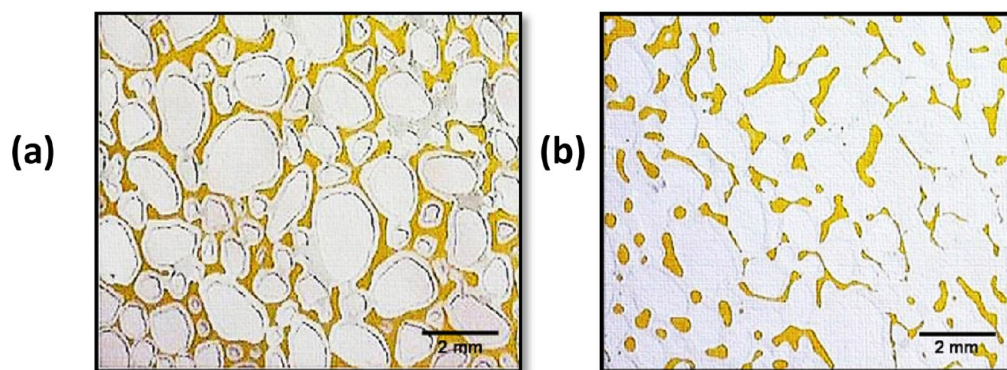


Figure 4. Water-wet micromodel after (a) HSWF and (b) LSWF.

addition of salts contributes considerably to the formation of a strong HB network at the interfaces and makes basal surfaces of kaolinite completely hydrophilic.³⁰

After aging, the micromodel was flushed with LSW (0–6000 ppm NaCl). The different concentrations of LS brines used in this study produced parallel results. The experiment was also repeated with saline water, with the salinity close to the formation brine, so a comparison could be made between the results. During the visualization experiments, videos were recorded to provide visual evidence of displacement mechanisms. In addition, images were taken at a variety of locations which were distributed evenly throughout the micromodel and qualitative/quantitative analysis of the images was performed using image analysis techniques with ImageJ. The images were segmented to differentiate between different phases, and then they were binarized and analyzed to find the oil and water saturations ($S_{oil} = A_{oil}/(A_{total} - A_{grains})$ and $S_w = A_{water}/(A_{total} - A_{grains})$).

As illustrated in Figure 3, the dynamics of two-phase flow and the details of the displacement mechanism were clearly visualized during the brine injection. In the water-wet porous medium, during imbibition, the wetting fluid (water) flows

through thin layers coating the solid surfaces of the medium, pinching off threads of oil in the narrow channels. This nonlocal flow forms disconnected oil ganglia, some of which remain trapped within the medium (refer to Video 1 in the Supporting Information). This phenomenon is called “snap-off”.^{17,31} Oil trapped in forms of ganglia after both LS and HS brine injections is pictured and presented in Figures 4 and 5.

Generally, in water-wet systems, there are two mechanisms that control fluid displacement at the pore scale: snap-off and pistonlike displacement. If the invading fluid can completely sweep the receding fluid in a pore element, the displacement is referred to as pistonlike movement. If the capillary number is small, snap-off is dominant, and with the increase in capillary number, the possibility of snap-off decreases.³² In the current study, the displacement was dominated by capillary forces when high salinity (HS) brine was the invading phase (Figure 5a). After switching to LS brine, snap-off was not dominant in the whole system and there was a transition from snap-off to pistonlike displacement in relatively considerable parts of the pores (Figure 5b). In other words, as shown in Video 2, in LS brine snap-off was reduced in some parts and the amount of trapped oil was decreased by almost 10%.

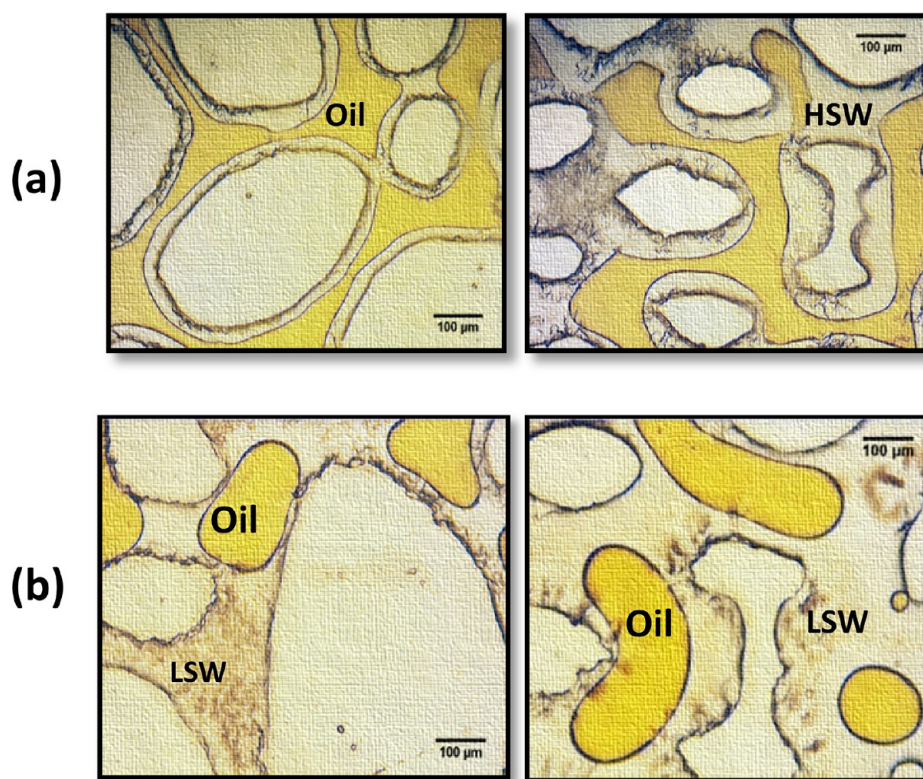


Figure 5. Microscopic images after the model was flushed with (a) HSW and (b) LSW.

In general, the snap-off mechanism can be suppressed by decreasing the capillary forces in comparison with viscous forces.³² Thus, by increasing the capillary number, lessening the interfacial tension, and changing the wettability, the snap-off probability can be reduced and consequently the residual saturation will be declined. However, no evidence of wettability alteration was observed and the system remained water-wet. The interfacial tension was nearly constant with the salt concentration as well. Accordingly, the capillary number ($N_{ca} \cong 1.5 \times 10^{-5}$) stayed in the range over which, according to the work of Chatzis and Morrow,³³ capillary displacement is predominant ($N_{ca} < 10^{-5} - 10^{-4}$). This conflicts with what we observed, since in LS brine snap-off was not dominant in the whole system and there was a transition from snap-off to pistonlike displacement in large sections of the pores. In other words, the change from interfacial tension (thermodynamic property) alone does not describe improved oil recovery from LS brine injection. To explain the snap-off suppression in LS brine, a theory has been proposed in recent studies. It has been suggested that polar components of crude oil, in contact with a brine phase, form highly elastic films and this process is aggravated under LS brine conditions.^{34,35} The increased viscoelasticity of the water/oil interface hinders snap-off of the oil into small droplets dispersed in the brine. As a result, the oil phase is more continuous and mobile (easier to extract) in LS than in HS water flooding. Therefore, the viscoelastic and rigid (rheological property) fluid–fluid interface may make a critical contribution to the enhanced oil recovery.

A number of authors have studied crude oil–water interfacial rheology in relation to the stability of water-in-oil emulsions. These authors relate the elasticity of the fluid–fluid interface to the stability of the emulsion due to the formation of interfacial

structures from amphiphilic molecules in the crude oil in relation to the salt concentration in the aqueous phase.^{36–41}

The time dependency of interfacial viscoelasticity development during crude oil–brine contact has been rheologically characterized previously, and it has been confirmed that the rheological properties of crude oil/water interface are sensitive to aging time.^{34,40} To investigate the kinetics of the formation of the viscoelastic interface, after injecting 4 pore volumes (PV) of LSW, the injection was stopped for almost 1 h, and then continual injection up to breakthrough led to a further 2% improved recovery. Extended the aging time for more than an hour did not result in an additional increase in recovery. The kinetics of the formation of the elastic interface is dependent on the crude oil compositions. In some cases, the interface is elastic at all times, which corresponds with the time scale of continuous water flooding, while in others the interface viscoelasticity may take longer to develop.³⁴ The impact of aging time on enhanced recovery after shutting down can be due to other potential reasons, including redistribution of fluids due to the equilibrium of pressure gradients in the system during the shutdown period. However, repeating the visualization experiment with HSW as the displacing phase results in a negligible improved recovery after short-term shutdown ($\ll 1\%$). Hence, it can be concluded that the production of extra oil can be associated with the development of a viscoelastic interface.

As the interfacial tension for crude oil–brine systems displayed no salinity dependence, and due to the visualized invariable wettability status and impact of aging time on improved recovery, it is presumed that this resistance to snap-off could be attributed to the enhanced viscoelasticity. The rheological property has been shown to develop when crude oil

systems containing polar components come in contact with low salinity brine.

It has been also hypothesized that the effect of low salinity on the formation of the polar component network on the interface and the resultant viscoelasticity can be explained in terms of the expansion of the EDL.³⁴ The part of the water film that is closest to the charged surface forms an electrical double layer: excess charges on the surface are countered by electrolyte ions of the opposite charge. The first layer of water with these ions is static, and the second layer exchanges ions with the bulk water. The diffuse layer of charge and the surface charge form an ionic structure known as the EDL, which was first described by Helmholtz in 1879. The EDL is electrically neutral. A schematic

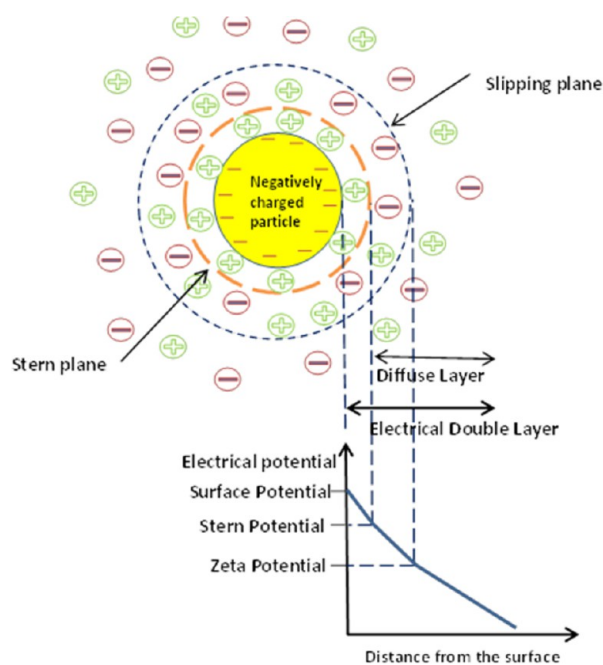


Figure 6. Schematic of the electrical double layer around a charged particle.

of a charged particle and the double layer is shown in Figure 6. A characteristic length of EDL is the Debye length κ^{-1} given by

$$\kappa^{-1} = \left(\frac{\epsilon_r \epsilon_0 k_B T}{2 N_A e^2 I} \right)^{1/2} \quad (1)$$

where ϵ_r is the relative permittivity (dielectric constant) of the brine, ϵ_0 is the permittivity of free space, k_B is the Boltzmann constant, T is temperature, N_A is Avogadro's number, e is the charge of an electron, and the ionic strength I is

$$I = \frac{1}{2} \sum_{i=1}^n c_i z_i^2 \quad (2)$$

where n is the number of ionic species, c_i is the molar concentration of i , and z_i is the charge of i . When the brine salinity is lowered, the Debye length increases since the ionic strength decreases. The double layers expand to become more diffuse, and the screening becomes weaker.⁴²

The expansion of the EDL in LS brine may be the reason for the high amount of oil polar components at the oil–water interface in LS brine compared with the HS brine. In LS brine,

since the diffuse layer is very broad, the screening from the counterions in the electrolyte is weaker; the polar components of the oil experience higher electrostatic attraction toward the interface and are adsorbed and organized at the interface. On the other hand, in HS brine, the double layers are thin, and counterions in the electrolyte screen off the charge on the interface, which results in a decrease in the attraction of the polar components to the interface.³⁴

Throughout LSWF, fines migration was insignificant and an inconsiderable degrees of fines release were observed in those systems which had been aged for almost 3 weeks. However, in another set of experiments, when the water-wet systems were flushed with LS brine without any delay, the extent of fines migration was significant. These observations are suggestive that the aging time is a contributing factor to fines release.

4.2. LSWF in the Presence of Clay Minerals (Oil-Wet Porous Media). The procedure of the experiment was similar to the water-wet system with two exceptions. First, the slurry of kaolinite and brine was modified in terms of pH (the pH was reduced by 20%). Second, the micromodel was initially saturated with crude oil only. It should be emphasized that the initial state of the clay is, strictly speaking, not dry because clay always contains the clay-bound water, adsorbed water, and capillary condensation in small pores between the clay aggregates from the air humidity.²⁰ In the clay-coating procedure no excessive drying that would remove adsorbed or even clay-bound water was used, so the surface of kaolinite is coated by a film of the water phase.

The wettability of the reservoir rock depends on the stability of the thin brine film that wets its surface. The film's stability is influenced by interactions between its brine/oil and brine/rock interfaces such as electrostatic interactions between charged groups on the oil surface of the brine/oil interface and charges on the mineral surface of the brine/rock interface; this interaction is described by classical DLVO theory.¹¹ When clay/water and water/oil interfaces are in proximity, the forces acting to keep them separated or draw them closer together include van der Waals, structural, or solvation interactions and double layer forces. Double layer forces occur between charged objects across liquids. This force acts over distances that are comparable to the Debye length, which is in the order of 1 nm to a few tenths of nanometers. The strength of these forces increases with the magnitude of the surface charge density (or the electrical surface potential). The potentials at the two interfaces can be estimated by measuring the zeta potentials, ζ . The zeta potential is the electric potential in the EDL at the location of the slipping plane relative to a point in the bulk fluid away from the interface. The magnitude of the zeta potential indicates the degree of electrostatic repulsion between adjacent, similarly charged surfaces. Double layer forces along with other electrostatic interactions described by DLVO theory, and non-DLVO forces contribute to a quantity referred to as disjoining pressure. The stability of the water film depends on the disjoining pressure $\Pi(h)$. The disjoining pressure in the film depends on its thickness h .^{43,44} Attractive interactions between the two interfaces produce negative contributions to Π that cause the film to collapse, decreasing h . Repulsive interactions produce positive contributions to Π that stabilize the film and increase h . The composition of the crude oil, the pH, the composition of the brine, along with the aging time all influence the disjoining pressure.⁴⁵ Stable, thick brine films are indicative of a water-wet state.

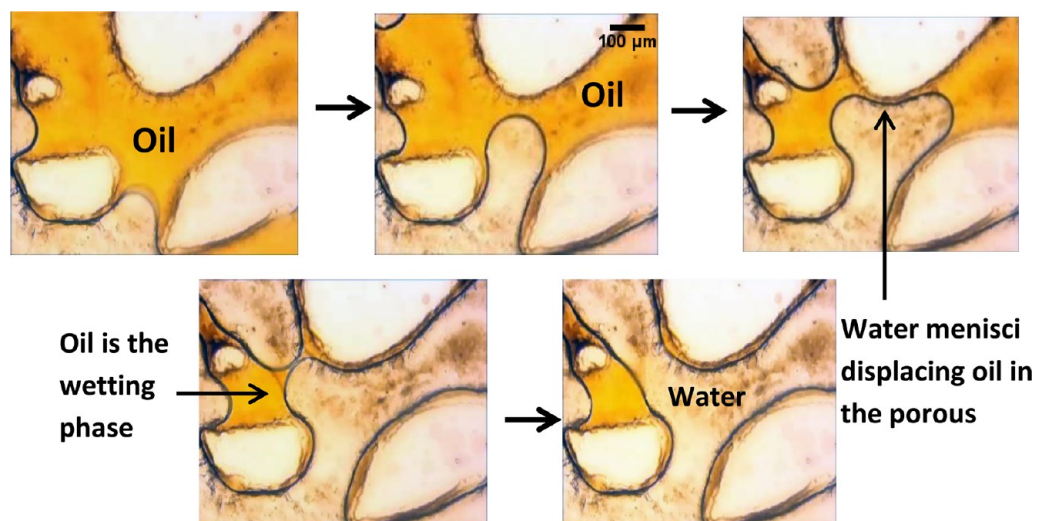


Figure 7. Sequence of snapshots taken during HSFW, showing that the wetting phase (oil) was displaced by the nonwetting (water) phase in a meniscus moving mechanism. The wetting phase (oil) stuck to the surface and did not flow.

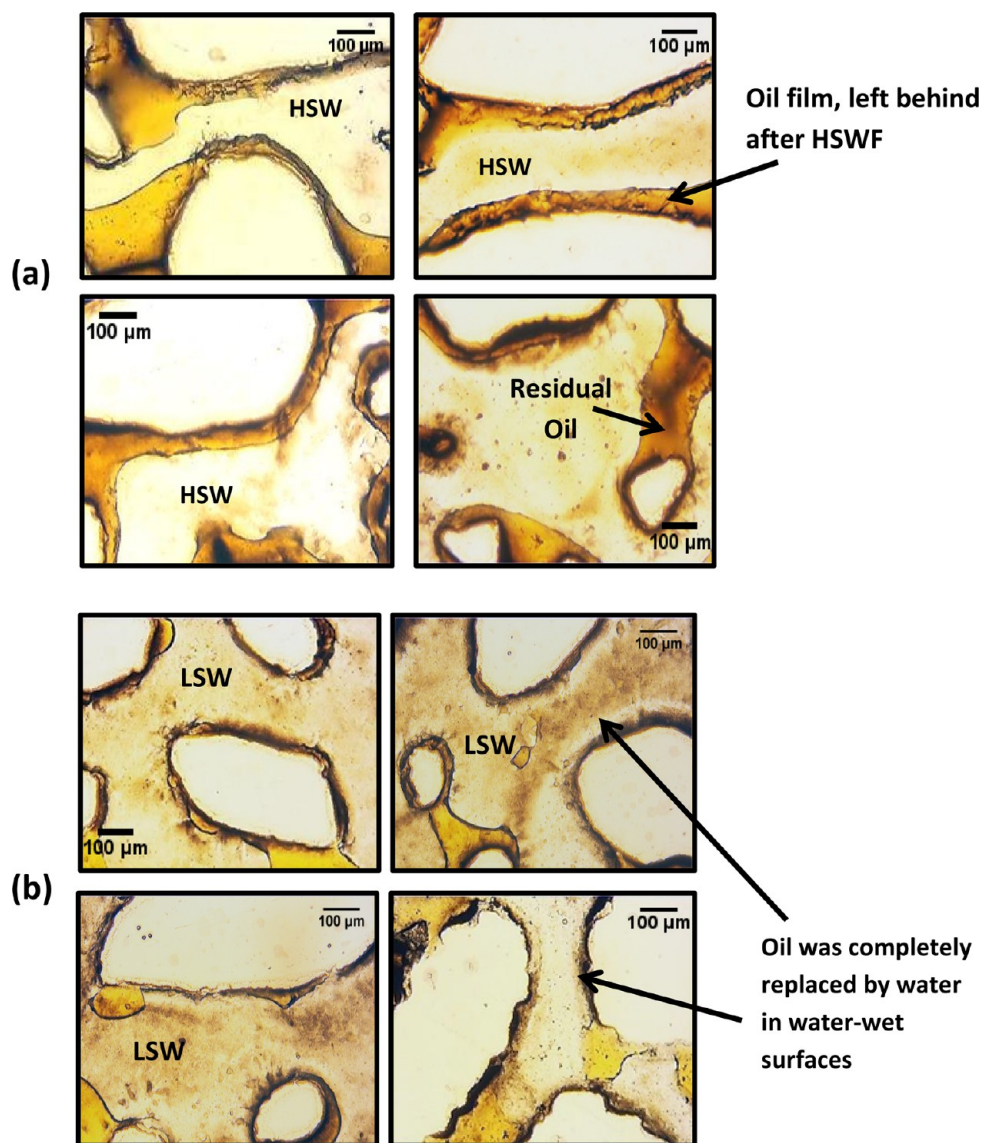


Figure 8. Microscopic images after (a) HSFW and (b) LSWF. Wettability alteration was observed throughout LSWF.

When kaolinite and oil came in contact with HS brine (since the clay was initially saturated with HS brine), the surface charge of the clay and the oil was screened off by oppositely charged ions present in the HS brine. Accordingly, the double layers became thin and the double layer repulsion forces between the interfaces were reduced; consequently the disjoining pressure declined. When the film destabilized, the polar components of the crude oil could adhere to the surface and make the surface more oil-wetting. After oil saturation and aging, the system was flushed with LSW (0–6000 ppm). The experiment was also repeated with HSW. For both HSWF and LSWF, the meniscus moving mechanism was observed, as shown in Figure 7. During HSWF, in most parts of the medium, the oil phase stuck to the surface and did not flow (Figure 8a and Video 3). The thick oil film was visible around the majority of grains. This resulted in poor oil recovery efficiency. However, throughout LSWF, a mixed-wet system was visualized. As seen in Figure 8b and Video 4, although the advancement of the stable water front left behind an oil film near the oil-wet pore walls, in water-wet surfaces, the interface moves toward the grain surfaces and replaces the oil film. In Figure 9, improved oil displacement efficiency is evident

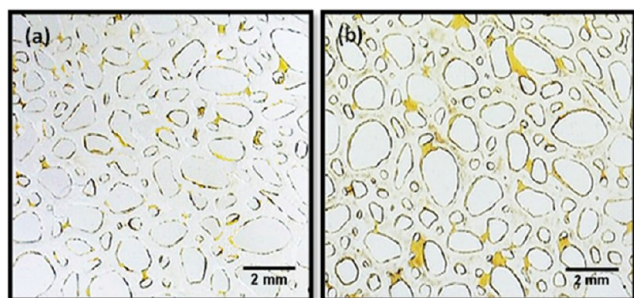


Figure 9. Micromodel images after (a) LSWF and (b) HSWF. Less residual oil remained on the pore walls after LSWF.

through LS brine injection, because the wettability was modified toward more water-wet conditions. Image analysis of the recorded images showed that wettability alteration due to LS brine led to 15% improved recovery.

The mechanism behind the wettability alteration can be described in terms of the expansion of the EDL. In HS brine, the electrical double layers of oil and clay are thin, and the negative surface charge of oil and clay is screened off, counteracting the repulsion between oil and clay. Therefore, the disjoining pressure is very low and the attraction DLVO and non-DLVO forces keep the oil connected to the surface, resulting in an oil-wet porous medium. After exposure to LSW, the HSW is gradually refreshed. Mahani et al.²⁰ theorized that the transport of ions is limited by diffusion and the ion-exchange capacity by the clay substrate and the thermodynamics of double layers. The reduction in ionic strength caused by this transport process led to expansion of double layers (Debye length) of oil and clay, so the screening from the counterions in the electrolyte becomes weaker, resulting in higher repulsion forces between oil and clay. This expansion destabilized the oil/clay pinning points; the wettability moved toward a more-water-wetting state and, when the attraction forces were low enough, the oil was released from the clay surface and replaced by water.

Our observations could be described in terms of the expansion of the EDL. Decreasing the water salinity results in decreasing the surface charges of all types of sandstones and clay particles (the charges became more negative in the clay/water interface). Many studies have provided evidence for it through measuring zeta potentials.^{46–48} Figure 10 shows the surface charges, using the zeta potential technique, of different types of clays and sandstones with brines at salinity levels very similar to those used in this paper.⁴⁶ Regarding the oil/water interface, the zeta potential of crude oil droplets dispersed in brine are dependent on the pH and ionic strength of the brine.⁴⁷ Crude oils are normally positively charged at a low pH, but as the pH increases the oil charge decreases until it reaches zero at the isoelectric point (IEP) and then becomes strongly negative at a high pH. In our experiment the pH of the LSW was around 7, so the oil/water interface was negative.

Fines migration was not visualized in the course of LSWF in the oil-wet system; however, it cannot be completely ruled out as one of the primary mechanisms behind the wettability alteration due to the type of test fluids (polar crude oil), methodology, and procedure implemented in this study. As was mentioned in the methodology, the pH of the slurry, made of

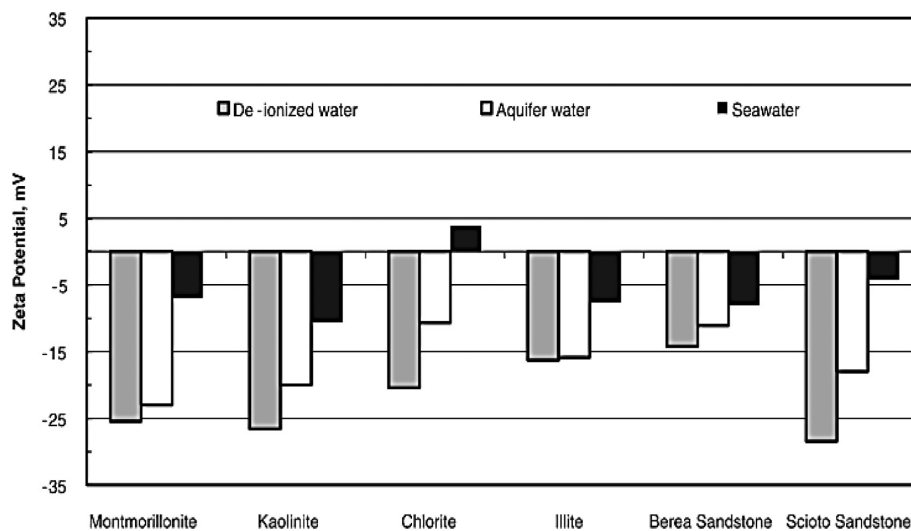


Figure 10. Zeta potential variation for different clays and sandstone particles.⁴⁶

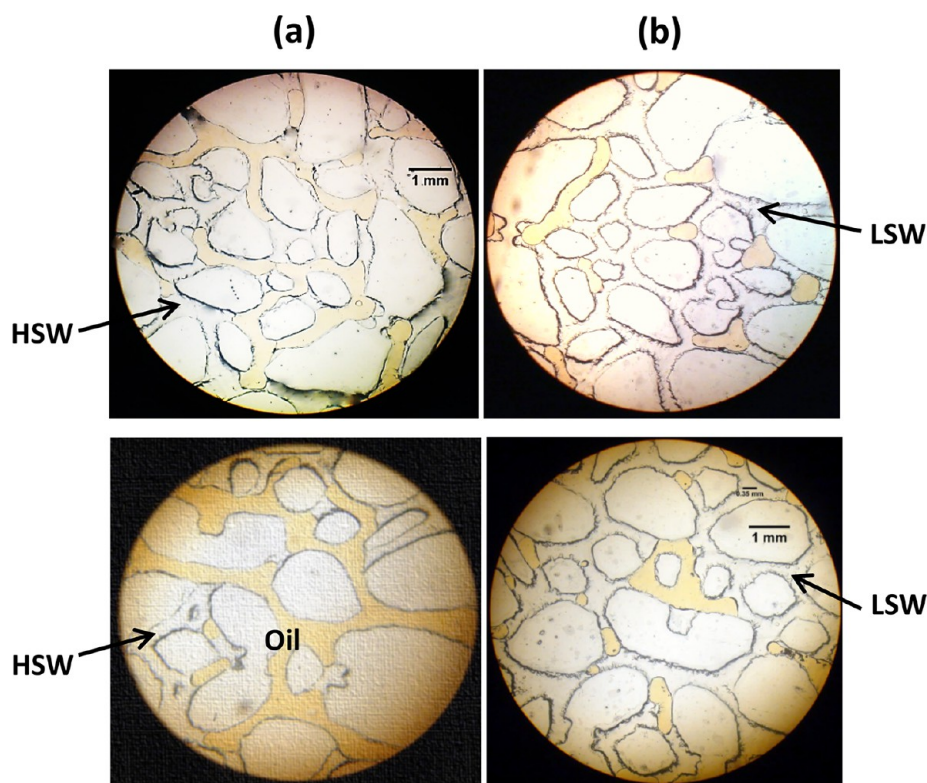


Figure 11. (a) HWS and (b) LSW were injected in the absence of clay minerals. The reduction in snap-off is evident.

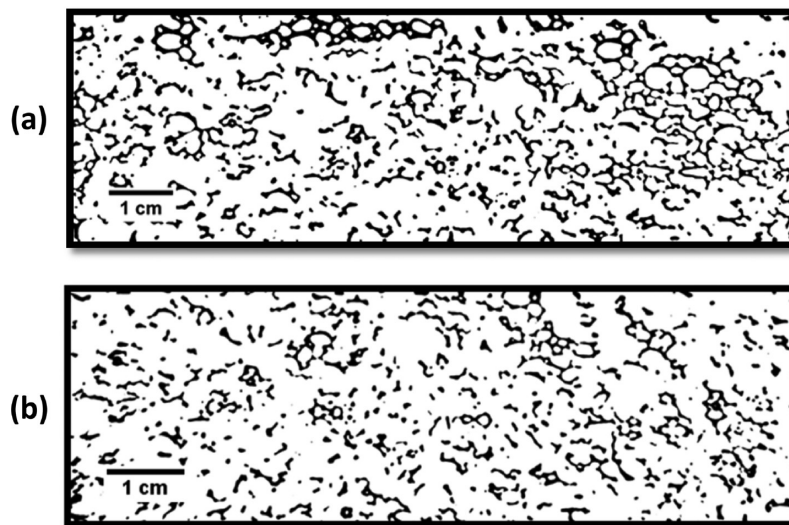


Figure 12. (a) HWS and (b) LSW were injected in the absence of clay minerals. The binarized images taken after the injection show the snap-off was clearly reduced.

kaolinite and saline water, was slightly changed to create an oil-wet system. Reducing the pH might have an influence on clay detachment and subsequent fines migration. However, in the water-wet porous medium where the pH of the slurry was not altered, fines migration was insignificant as well. Sarkar and Sharma⁴⁹ studied the effect of polar crude oil on fines migration experimentally. The presence of polar crude oil slowed down the fines release process due to adsorption of the polar components but did not prevent it. The adsorption of polar ends to the rock surface is a slow process. Over geologic time at reservoir temperatures and pressures, this process may cause fines to become immobile by adsorbing on them. For the short

contact time allowed in our experiments (3 weeks), the release of fines occurred but at a very slow rate. As a result, the concentration of particles was not sufficient to be clearly visible, have a noticeable effect on oil recovery, and to form bridges in the pore throats (cause a permeability reduction).

4.3. LSWF in the Absence of Clay Minerals. The microfluidic device was first saturated with connate water (30 000 ppm NaCl) and then flushed with crude oil to form connate water and initial oil saturations. The initial water saturation (S_{wi}) was almost 4%. Visualization experiments were performed by injecting brines with different concentrations (0–6000 ppm). Different concentrations of LS brine produced very

similar results. Through the recorded videos and images, it was evident that snap-off was reduced while injecting LSW (Figures 11 and 12) and the recovery factor was increased by almost 10%. The system was water-wet, and during the injection of LS brine, the wettability remained invariant.

The observations were very similar to those observed in clay-coated water-wet systems. Aging micromodels in LS for 1 h also led to a further 3% improved recovery. Hence, it is hypothesized that the LS effect in water-wet systems, in the presence and absence of clay minerals, could be solely attributed to the formation of a highly elastic oil–water interface. Many researchers have studied crude oil–water interfacial rheology in the past, and they confirmed the dependency of the interfacial structure on the salt concentration of the aqueous phase.^{40,41,50}

As mentioned in sections 4.1 and 4.2, in clay-coated micromodels, the aging time had a considerable effect particularly on fines migration and wettability alteration. However, in clean micromodels a significant impact on wettability and fluid distribution was not visualized when compared with those that did not age for 3 weeks.

5. CONCLUSION

In this study, pore scale displacement studies in the presence and absence of clay minerals, as well as in the drainage and imbibition dominated two-phase flow, were performed. The outcome of this study helps to explain and understand the mechanism behind the LSW effect in petroleum reservoirs. The results can provide greater insight into the LSWF effect and will contribute to the development of universal and inclusive guidelines for optimized field applications. The significant observations are listed below:

- In water-wet systems, in the presence and absence of kaolinite, LS brine clearly hindered the snap-off.
- It is hypothesized that the reduction in snap-off could be linked to the formation of a highly elastic oil/water interface. Formation of a highly elastic interface in LS brine could be described in terms of the expansion of the EDL.
- The wettability alteration was observed after injecting LSW into oil-wet systems. The wettability status was altered toward more water-wet systems. The wettability alteration could be explained in terms of the expansion of the EDL as well.
- Fines migration had an insignificant role in our observations.

The results of this paper are based on fully water-wet or fully oil-wet systems, and further experiments are recommended to analyze transport in models with a distribution of wettability.

■ ASSOCIATED CONTENT

Supporting Information

The Supporting Information is available free of charge on the ACS Publications website at DOI: 10.1021/acs.energyfuels.7b01702.

Video 1, recorded when the water-wet system was flushed with saline water (AVI)

Video 2, recorded when the model was flushed with LSW (AVI)

Video 3, recorded during HSW injection, when the oil phase stuck to the surface and did not flow (AVI)

Video 4, recorded during LSW injection, when a mixed-wet system was visualized (AVI)

Glass micromodels' method of fabrication (PDF)

■ AUTHOR INFORMATION

Corresponding Author

*E-mail: Tammy.Amirian@adelaide.edu.au.

ORCID

Tammy Amirian: 0000-0003-3857-0300

Notes

The authors declare no competing financial interest.

■ ACKNOWLEDGMENTS

The authors would like to thank Santos, Ltd., Australia, for providing crude oil and Delise Hollands for her assistance and advice in matters concerning the experimental setup and procedure.

■ REFERENCES

- (1) Bernard, G. G. Effect of Floodwater Salinity on Recovery Of Oil from Cores Containing Clays. In *SPE California Regional Meeting, Oct 26–27, Los Angeles, CA, USA*; Society of Petroleum Engineers: 1967. DOI: 10.2118/1725-MS.
- (2) Yildiz, H. O.; Morrow, N. R. Effect of brine composition on recovery of Moutray crude oil by waterflooding. *J. Pet. Sci. Eng.* **1996**, *14* (3–4), 159–168.
- (3) Jadhunandan, P. P. *Effects of Brine Composition, Crude Oil and Aging Conditions on Wettability and Oil Recovery*; New Mexico Institute of Mining and Technology: Socorro, NM, 1990.
- (4) Mahani, H.; Sorop, T.; Ligthelm, D. J.; Brooks, D.; Vledder, P.; Mozahem, F.; Ali, Y. Analysis of field responses to low-salinity waterflooding in secondary and tertiary mode in Syria. In *SPE EUROPEC/EAGE Annual Conference and Exhibition, Vienna, Austria*; Society of Petroleum Engineers: 2011. DOI: 10.2118/142960-MS.
- (5) McGuire, P. L.; Chatham, J. R.; Paskvan, F. K.; Sommer, D. M.; Carini, F. H. Low Salinity Oil Recovery: An Exciting New EOR Opportunity for Alaska's North Slope. In *SPE Western Regional Meeting, Irvine, CA*; Society of Petroleum Engineers: 2005. DOI: 10.2118/93903-MS.
- (6) Soraya, B.; Malick, C.; Philippe, C.; Bertin, H. J.; Hamon, G. Oil Recovery by Low-Salinity Brine Injection: Laboratory Results on Outcrop and Reservoir Cores. In *SPE Annual Technical Conference and Exhibition, New Orleans, LA*; Society of Petroleum Engineers: 2009. DOI: 10.2118/124277-MS.
- (7) Vledder, P.; Gonzalez, I. E.; Carrera Fonseca, J. C.; Wells, T.; Ligthelm, D. J. Low Salinity Water Flooding: Proof Of Wettability Alteration On A Field Wide Scale. In *SPE Improved Oil Recovery Symposium, Tulsa, OK, USA*; Society of Petroleum Engineers: 2010. DOI: 10.2118/129564-MS.
- (8) Zhang, Y.; Morrow, N. R. Comparison of Secondary and Tertiary Recovery With Change in Injection Brine Composition for Crude-Oil/Sandstone Combinations. In *SPE/DOE Symposium on Improved Oil Recovery, Tulsa, OK, USA*; Society of Petroleum Engineers: 2006. DOI: 10.2118/99757-MS.
- (9) Zhang, Y.; Xie, X.; Morrow, N. R. Waterflood Performance By Injection Of Brine With Different Salinity For Reservoir Cores. In *SPE Annual Technical Conference and Exhibition, Anaheim, California, USA*; Society of Petroleum Engineers: 2007. DOI: 10.2118/109849-MS.
- (10) Morrow, N.; Buckley, J. Improved Oil Recovery by Low-Salinity Waterflooding. *JPT, J. Pet. Technol.* **2011**, *63* (05), 106–112.
- (11) Myint, P. C.; Firoozabadi, A. Thin liquid films in improved oil recovery from low-salinity brine. *Curr. Opin. Colloid Interface Sci.* **2015**, *20* (2), 105–114.
- (12) Sheng, J. J. Critical review of low-salinity waterflooding. *J. Pet. Sci. Eng.* **2014**, *120*, 216–224.
- (13) Mahani, H.; Keya, A. L.; Berg, S.; Bartels, W.-B.; Nasralla, R.; Rossen, W. Driving Mechanism of Low Salinity Flooding in Carbonate Rocks. In *EUROPEC 2015, Madrid, Spain*; Society of Petroleum Engineers: Madrid, Spain, 2015. DOI: 10.2118/174300-MS.

- (14) Nasralla, R. A.; Alotaibi, M. B.; Nasr-El-Din, H. A. Efficiency of Oil Recovery by Low Salinity Water Flooding in Sandstone Reservoirs. In *SPE Western North American Region Meeting, Anchorage, AK, USA*; Society of Petroleum Engineers: 2011. DOI: [10.2118/144602-MS](https://doi.org/10.2118/144602-MS).
- (15) Nasralla, R. A.; Nasr-El-Din, H. A. Impact of Electrical Surface Charges and Cation Exchange on Oil Recovery by Low Salinity Water. In *SPE Asia Pacific Oil and Gas Conference and Exhibition, Jakarta, Indonesia*; Society of Petroleum Engineers: 2011. DOI: [10.2118/147937-MS](https://doi.org/10.2118/147937-MS).
- (16) Suijkerbuijk, B.; Hofman, J.; Ligthelm, D. J.; Romanuka, J.; Brussee, N.; van der Linde, H.; Marcelis, F. Fundamental Investigations into Wettability and Low Salinity Flooding by Parameter Isolation. In *SPE Improved Oil Recovery Symposium, Tulsa, OK, USA*; Society of Petroleum Engineers: 2012. DOI: [10.2118/154204-MS](https://doi.org/10.2118/154204-MS).
- (17) Barnaji, M. J.; Pourafshary, P.; Rasaie, M. R. Visual investigation of the effects of clay minerals on enhancement of oil recovery by low salinity water flooding. *Fuel* **2016**, *184*, 826–835.
- (18) Berg, S.; Cense, A. W.; Jansen, E.; Bakker, K. Direct Experimental Evidence of Wettability Modification by Low Salinity. *Petrophysics* **2010**, *51* (05), No. SPWLA-2010-v51n5a3.
- (19) Lee, S. Y.; Webb, K. J.; Collins, I.; Lager, A.; Clarke, S.; O'Sullivan, M.; Routh, A.; Wang, X. Low Salinity Oil Recovery: Increasing Understanding of the Underlying Mechanisms. In *SPE Improved Oil Recovery Symposium, Tulsa, OK, USA*; Society of Petroleum Engineers: 2010. DOI: [10.2118/129722-MS](https://doi.org/10.2118/129722-MS).
- (20) Mahani, H.; Berg, S.; Ilic, D.; Bartels, W.-B.; Joekar-Niasar, V. Kinetics of Low-Salinity-Flooding Effect. *SPE J.* **2015**, *20* (01), 8–20.
- (21) Song, W.; Kovscek, A. R. Functionalization of micromodels with kaolinite for investigation of low salinity oil-recovery processes. *Lab Chip* **2015**, *15* (16), 3314–3325.
- (22) Bartels, W. B.; Rücker, M.; Berg, S.; Mahani, H.; Georgiadis, A.; Fadili, A.; Brussee, N.; Coorn, A.; van der Linde, H.; Hinz, C.; Jacob, A.; Wagner, C.; Henkel, S.; Enzmann, F.; Bonnin, A.; Stampanoni, M.; Ott, H.; Blunt, M.; Hassanizadeh, S. M. Fast X-Ray Micro-CT Study of the Impact of Brine Salinity on the Pore-Scale Fluid Distribution During Waterflooding. *Petrophysics* **2017**, *58* (01), No. SPWLA-2017-v58n1a4.
- (23) Bartels, W.-B.; Mahani, H.; Berg, S.; Menezes, R.; van der Hoeven, J. A.; Fadili, A. Oil Configuration Under High-Salinity and Low-Salinity Conditions at Pore Scale: A Parametric Investigation by Use of a Single-Channel Micromodel. *SPE J.* **2017**, *22* (05), 1362.
- (24) Emadi, A.; Sohrabi, M. Visual Investigation of Oil Recovery by Low Salinity Water Injection: Formation of Water Micro-Dispersions and Wettability Alteration. In *SPE Annual Technical Conference and Exhibition, New Orleans, LA*; Society of Petroleum Engineers: 2013. DOI: [10.2118/166435-MS](https://doi.org/10.2118/166435-MS).
- (25) Fredriksen, S. B.; Rognmo, A. U.; Sandengen, K.; Fernø, M. A. Wettability Effects on Osmosis as an Oil-Mobilization Mechanism During Low-Salinity Waterflooding. *Petrophysics* **2017**, *58* (01), No. SPWLA-2017-v58n1a3.
- (26) Muecke, T. W. Formation Fines and Factors Controlling Their Movement in Porous Media. *JPT, J. Pet. Technol.* **1979**, *31* (02), 144.
- (27) Lebedeva, E. V.; Fogden, A. Adhesion of Oil to Kaolinite in Water. *Environ. Sci. Technol.* **2010**, *44* (24), 9470–9475.
- (28) Bondino, I.; Doorwar, S.; Ellouz, R.; Hamon, G. Visual microscopic investigations about the role of pH, salinity and clay on oil adhesion and recovery. Presented at the International Symposium of the Society of Core Analysts, NAPA Valley, CA, Sept 16–19, 2013.
- (29) Lebedeva, E. V.; Fogden, A.; Senden, T. J.; Knackstedt, M. A. Kaolinite Wettability—The Effect of Salinity, pH and Calcium. Presented at the 24th International Symposium of Core Analysts, Halifax, NS, Canada, Oct 4–7, 2010.
- (30) Zhang, L.; Lu, X.; Liu, X.; Yang, K.; Zhou, H. Surface Wettability of Basal Surfaces of Clay Minerals: Insights from Molecular Dynamics Simulation. *Energy Fuels* **2016**, *30* (1), 149–160.
- (31) Krummel, A. T.; Datta, S. S.; Münster, S.; Weitz, D. A. Visualizing multiphase flow and trapped fluid configurations in a model three-dimensional porous medium. *AIChE J.* **2013**, *59* (3), 1022–1029.
- (32) Joekar-Niasar, V.; Hassanizadeh, S. M. Analysis of Fundamentals of Two-Phase Flow in Porous Media Using Dynamic Pore-Network Models: A Review. *Crit. Rev. Environ. Sci. Technol.* **2012**, *42* (18), 1895–1976.
- (33) Chatzis, I.; Morrow, N. R. Correlation of capillary number relationships for sandstone. *SPEJ, Soc. Pet. Eng. J.* **1984**, *24* (05), 555–562.
- (34) Chávez-Miyauchi, T. E.; Firoozabadi, A.; Fuller, G. G. Nonmonotonic Elasticity of the Crude Oil–Brine Interface in Relation to Improved Oil Recovery. *Langmuir* **2016**, *32* (9), 2192–2198.
- (35) Morin, B.; Liu, Y.; Alvarado, V.; Oakey, J. A microfluidic flow focusing platform to screen the evolution of crude oil-brine interfacial elasticity. *Lab Chip* **2016**, *16* (16), 3074–3081.
- (36) Gawel, B.; Nourani, M.; Tichelkamp, T.; Øye, G. Influence of the wettability of particles on the morphology and stability of crude oil–particle aggregates in synthetic produced water. *J. Pet. Sci. Eng.* **2016**, *139*, 198–204.
- (37) Abdel-Raouf, M. E.-S. Factors affecting the stability of crude oil emulsions. In *Crude Oil Emulsions - Composition Stability and Characterization*; InTech: 2012.
- (38) Sjöblom, J.; Hemmingsen, P. V.; Kallevik, H. The Role of Asphaltenes in Stabilizing Water-in-Crude Oil Emulsions. In *Asphaltenes, Heavy Oils, and Petroleomics*; Mullins, O. C., Sheu, E. Y., Hammami, A., Marshall, A. G., Eds.; Springer New York: New York, NY, 2007; pp 549–587.
- (39) Xia, L.; Lu, S.; Cao, G. Stability and demulsification of emulsions stabilized by asphaltenes or resins. *J. Colloid Interface Sci.* **2004**, *271* (2), 504–506.
- (40) Spieker, P. M.; Kilpatrick, P. K. Interfacial Rheology of Petroleum Asphaltenes at the Oil–Water Interface. *Langmuir* **2004**, *20* (10), 4022–4032.
- (41) Quintero, C. G.; Noik, C.; Dalmazzone, C.; Grossiord, J. L. Formation Kinetics and Viscoelastic Properties of Water/Crude Oil Interfacial Films. *Oil Gas Sci. Technol.* **2009**, *64* (5), 607–616.
- (42) Derjaguin, B. V.; Churaev, N. V.; Müller, V. M. *Surface Forces*; Consultants Bureau: New York, 1987. Translated from the Russian by V. I. Kisin; translation edited by J. A. Kitchener.
- (43) Hirasaki, G. J. Wettability: Fundamentals and Surface Forces. *SPE Form. Eval.* **1991**, *6* (02), 217–226.
- (44) Tokunaga, T. K. DLVO-Based Estimates of Adsorbed Water Film Thicknesses in Geologic CO₂ Reservoirs. *Langmuir* **2012**, *28* (21), 8001–8009.
- (45) Buckley, J. S.; Takamura, K.; Morrow, N. R. Influence of Electrical Surface Charges on the Wetting Properties of Crude Oils. *SPE Reservoir Eng.* **1989**, *4* (03), 332.
- (46) Alotaibi, M. B.; Nasralla, R. A.; Nasr-El-Din, H. A. Wettability Studies Using Low-Salinity Water in Sandstone Reservoirs. *SPE Reservoir Eval. Eng.* **2011**, *14* (06), 713.
- (47) Farooq, U.; Tweheyo, M. T.; Sjöblom, J.; Øye, G. Surface characterization of model, outcrop, and reservoir samples in low salinity aqueous solutions. *J. Dispersion Sci. Technol.* **2011**, *32* (4), 519–531.
- (48) Nasralla, R. A.; Nasr-El-Din, H. A. Double-Layer Expansion: Is It a Primary Mechanism of Improved Oil Recovery by Low-Salinity Waterflooding? *SPE Reservoir Evaluation & Engineering* **2014**, *17* (01), 49–59.
- (49) Sarkar, A. K.; Sharma, M. M. Fines Migration in Two-Phase Flow. *JPT, J. Pet. Technol.* **1990**, *42* (05), 646.
- (50) Alvarado, V.; Moradi Bidhendi, M.; Garcia-Olvera, G.; Morin, B.; Oakey, J. S. Interfacial visco-elasticity of crude oil-brine: An alternative EOR mechanism in smart waterflooding. In *SPE Improved Oil Recovery Symposium, Tulsa, OK, USA*; Society of Petroleum Engineers: 2014. DOI: [10.2118/169127-MS](https://doi.org/10.2118/169127-MS).

Chapter 4: Impact of Clay Type and Nature of Cations on Low Salinity Water Injection – Visualisation Approach

Statement of Authorship

Title of Paper	Impact of clay type and water composition on low salinity water injection–visualisation approach.
Publication Status	<input checked="" type="checkbox"/> Published <input type="checkbox"/> Accepted for Publication <input type="checkbox"/> Submitted for Publication <input type="checkbox"/> Unpublished and Unsubmitted work written in manuscript style
Publication Details	Tammy Amirian and Manouchehr Haghighi. "Impact of clay type and water composition on low salinity water injection–visualisation approach." <i>The APPEA Journal</i> 58.1 (2018): 51-59.

Principal Author

Name of Principal Author (Candidate)	Tammy Amirian		
Contribution to the Paper	Conducted the experiments, performed data analysis, interpreted data, wrote the manuscript and acted as the corresponding author.		
Overall percentage (%)	75%		
Certification:	This paper reports on original research I conducted during the period of my Higher Degree by Research candidature and is not subject to any obligations or contractual agreements with a third party that would constrain its inclusion in this thesis. I am the primary author of this paper.		
Signature		Date	27/03/19

Co-Author Contributions

By signing the Statement of Authorship, each author certifies that:

- i. the candidate's stated contribution to the publication is accurate (as detailed above);
- ii. permission is granted for the candidate to include the publication in the thesis; and
- iii. the sum of all co-author contributions is equal to 100% less the candidate's stated contribution.

Name of Co-Author	Manouchehr Haghighi		
Contribution to the Paper	Developed the concept of the work, supervised development of the work, helped in data interpretation and manuscript evaluation.		
Signature		Date	02/04/2019

Impact of clay type and water composition on low salinity water injection – visualisation approach

Tammy Amirian^{A,B} and Manouchehr Haghighi^A

^AAustralian School of Petroleum, Faculty of Engineering, Computer and Mathematical Sciences, The University of Adelaide, Adelaide, SA 5005, Australia.

^BCorresponding author. Email: Tammy.Amirian@adelaide.edu.au

Abstract. Low salinity water (LSW) injection as an enhanced oil recovery method has attracted much attention in the past two decades. Previously, it was found that the presence of clay such as kaolinite and water composition like the nature of cations affect the enhancement of oil recovery under LSW injection. In this study, a pore-scale visualisation approach was developed using a 2D glass micromodel to investigate the impact of clay type and water composition on LSW injection. The glass micromodels were coated by kaolinite and illite. A meniscus moving mechanism was observed and the oil–water interface moved through narrow throats to large bodies, displacing the wetting phase (oil phase). In the presence of kaolinite, the effect of LSW injection was reflected in the change to the wettability with a transition towards water-wetness in the large sections of the pore walls. The advance of the stable water front left behind an oil film on the oil-wet portions of pore walls; however, in water-wet surfaces, the interface moved towards the surface and replaced the oil film. As a result of wettability alteration towards a water-wet state, the capillary forces were not dominant throughout the system and the water–oil menisci displaced oil in large portions of very narrow channels. This LSW effect was not observed in the presence of illite. With regard to the water composition effect, systems containing divalent cations like Ca^{2+} showed the same extent of recovery as those containing only monovalent ions. The observation indicates a significant role of cation exchange in wettability alteration. Fines migration was insignificant in the observations.

Keywords: cation exchange, clay minerals, EOR, fines migration, LSW injection, wettability.

Received 5 December 2017, accepted 29 January 2018, published online 28 May 2018

Introduction

Low salinity water (LSW) injection is an emerging oil recovery technique. Injecting LSW into sandstone reservoirs can increase the oil recovery by 8–12%, and up to 40% on secondary recovery (Lager *et al.* 2008b). However, the main challenge of LSW injection is to comprehend how this process works in the oil production process. Various mechanisms have been proposed to explain the effect. Wettability alteration is the most frequently proposed mechanism in the literature (Shalabi *et al.* 2014; Sheng 2014). It has been proposed that lowering the salt concentration alters the wettability towards a more water-wet state which is more favourable for oil recovery.

The impact of clay minerals on oil recovery under LSW injection has been investigated previously and it has been mostly a reflection of the reduction in contact angle (Romanuka *et al.* 2012; Sina and Andrés Delgado 2015; Rezaei Gomari and Joseph 2017). The reduction from 48° to 29° for a carbonate rock caused by a reduction of salinity from 50 000 to 10 000 ppm in the

injection brine was reported by Romanuka *et al.* (2012). Sina and Andrés Delgado (2015) investigated the individual performance of clay materials (type and content of clay) on the alteration of carbonate rock surface-wettability using three different brines, from high to low salinity concentration. They studied the impact of two clay types including illite and kaolinite. Rezaei Gomari and Joseph (2017) studied the effect of kaolinite and montmorillonite on LSW injection in sandstone reservoirs. The extent of wettability alteration caused by three LSW treatments on oil-wet sandstone samples containing varying clay contents and types of clay (kaolinite or montmorillonite) were analysed through measuring the contact angle.

It has been proposed that the wettability alteration is induced by chemical mechanisms such as double-layer expansion (DLE) (Ligthelm *et al.* 2009; Lee *et al.* 2010; Nasralla and Nasr-El-Din 2014). The DLE is described by classical Derjaguin–Landau–Verwey–Overbeek (DLVO) theory (Ligthelm *et al.* 2009; Lee *et al.* 2010). In DLE, injection of LSW increases

the electrostatic repulsion between the water film's brine–oil and brine–clay interfaces via the expansion of two electrical double layers, one formed at each of the two interfaces. Consequently, the film becomes thicker and more stable, resulting in a more water-wet rock. The extent of the DLE is affected by the composition of LSW (e.g. whether the brine contains divalent or monovalent cations) and the brine pH (Farooq *et al.* 2011; Nasralla and Nasr-El-Din 2014). The film thickness measurements by Lee *et al.* (2010) showed that DLE was more sensitive to salinity in brines with larger monovalent cations.

Wettability alteration may occur due to the non-DLVO interactions between the water–oil and water–rock interfaces (Lager *et al.* 2008a). Crude oil forms organometallic complexes with divalent cations adsorbed on the clay surface. In LSW, multicomponent cation exchange (MIE) occurs so that the complex cations are replaced with noncomplex cations from the brine film, leading to the release of organometallic complexes and oil recovery.

Based on experimental observations, Tang and Morrow (1999) described the alteration in wettability due to fines migration. They developed a theory based on the assumption that heavy polar components in crude oil adsorb on clay particles at the pore walls to give mixed-wet fines. During the course of LSW, fine particles would be mobilised, so oil droplets attached to the mobilised fines would be released from the pore wall. As a result, there is a transition towards a water-wet surface alongside incremental oil recovery.

In this paper, the microfluidic approach was developed to visualise the individual performance of clay minerals (type and content of clay) and water composition on wettability alteration during LSW injection.

Materials and methods

Test fluid

Deionised water was used to make different concentrations of saline water (NaCl and CaCl₂) as the aqueous phases. The saline water properties are listed in Table 1. The crude oil was obtained from the Cooper Basin in South Australia and used as the oil phase. The crude oil's physical properties are listed in Table 2.

Clay minerals

Clay minerals were deposited on the solid surfaces of the glass micromodel to create a visualisation platform with more

representative surface interactions between the reservoir fluids and the reservoir rock. The clay minerals used in the experiments were illite and kaolinite. The clay minerals were supplied by the Clay Minerals Society (www.clays.org) and were used without any purification or alteration.

Microfluidic set-up

The microfluidic set-up included a pump to inject water, a glass micromodel and a microscope equipped with a camera, which was connected to a computer. A schematic of the experimental system is provided in Fig. 1. The water was pumped by an Optos (Eldex, Napa, USA) metering pump. Flow and transport within the micromodel were visualised using a BH12 fluorescence microscope (Olympus, Tokyo, Japan). The microscope was equipped with a Chinese Moticam 580 camera capturing 5-megapixel (2560 × 1920) images and recording videos at 1080P (full HD) using the Motic Images Plus software package.

Clay coating procedure

To deposit clays into the micromodel, slurry made of clay and high salinity water (HSW) was injected into the microfluidic device. Then, the micromodel was air-dried for almost 2 h by placing it on a hot plate (80°C). Very strong interfacial tensions between the air and the water phases would dislodge the blocked throats (Song and Kovscek 2015) and the moderate temperature of the hot plate would assist with the drying procedure. To prevent pore plugging and to ensure a quasi-homogeneous distribution of clay in the micromodel, the clay content concentration in the slurry, the flow rates and hot plate temperature were optimised through several practical tests. The whole process was monitored using the microscope set-up. Images were taken from evenly distributed parts of the micromodel after deposition and analysed to ensure a quasi-homogeneous distribution of clay in the micromodel pores. The clay deposition was characterised mostly as pore lining and, for very small parts of the model, a pore bridging structure was observed. Fig. 2 shows microscopic images of the micromodel before and after injecting the slurry and air-drying and demonstrates that the grains and throats were evenly coated with a sufficient amount of clay minerals.

Visualisation experiments

Following the clay coating process, the micromodel was saturated with oil and then aged for almost 3 weeks. The presence of salt (dissolved in saline water) increases the hydrophilicity of clay minerals significantly (Zhang *et al.* 2016) and results in an extremely water-wet system, therefore the micromodel was saturated with oil only. In addition, the pH of the clay slurry was slightly modified (reduced by almost 20%) before injection because, even after a month of aging with oil, the thin brine film was still visible around grains, indicating a fully water-wet system. The change in the pH value was minor and the pH was still well above the zero point of charge of clays, so the clay surface remained highly negative. After the aging period, the micromodel was flushed with LSW of neutral pH. The experiments were repeated with HSW so the results could be compared and analysed. During the visualisation experiments, images were taken at evenly distributed locations in the micromodel and qualitative and quantitative analyses of the

Table 1. Salt components of brines

Component (salt)	HSW/Connate water (ppm)	LSW (ppm)
NaCl	30 000	0–6000
CaCl ₂	22 000	NA

Table 2. Basic properties of the crude oil

API gravity @ 60°F	53.2
Density (g/cm ³) @ 60°F	0.76
Viscosity (cSt) @ 40°C	3.2
Acid number (mg KOH/g)	<0.1

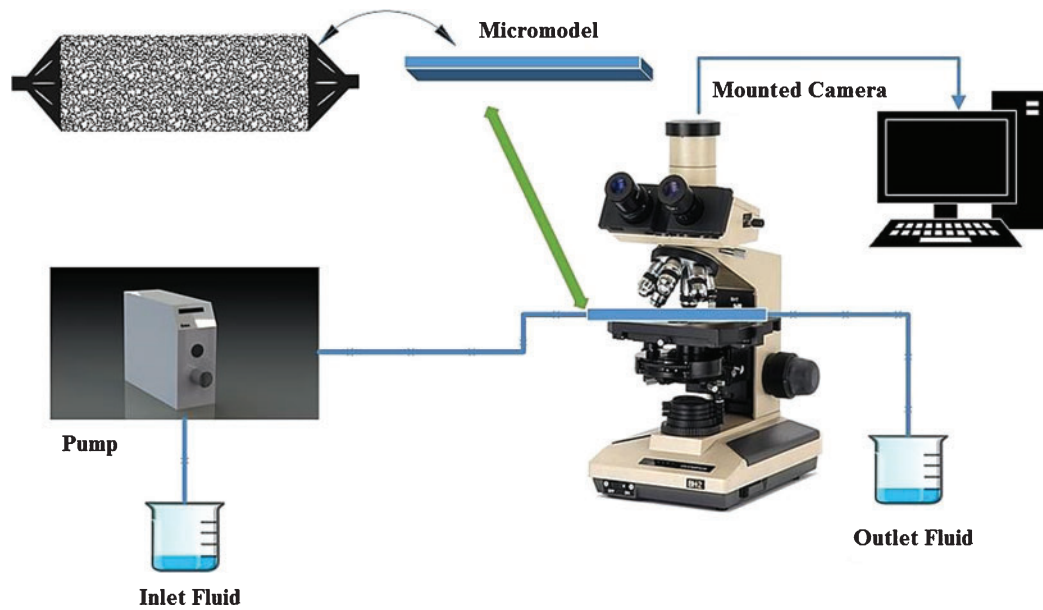


Fig. 1. Schematic of the laboratory set-up (Amirian *et al.* 2017).

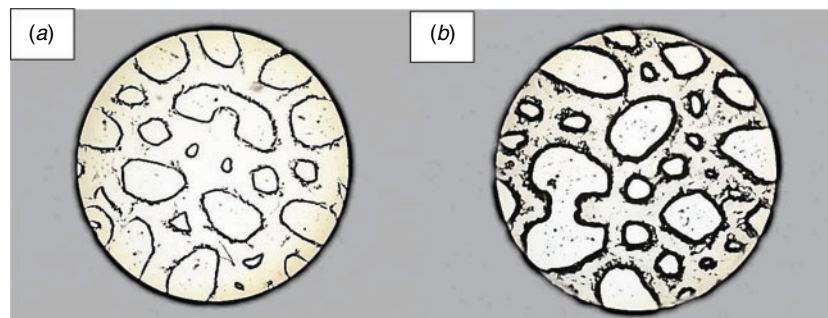


Fig. 2. (a) Clean and (b) clay-coated micromodels.

images were performed using image analysis techniques with ImageJ (Schindelin *et al.* 2015). The images were segmented to differentiate between different phases, and then they were binarised and analysed to find the oil and water saturations using the following equation (A denotes area):

$$S_{\text{oil}} = \frac{A_{\text{oil}}}{(A_{\text{total}} - A_{\text{grains}})}$$

$$S_{\text{w}} = \frac{A_{\text{water}}}{(A_{\text{total}} - A_{\text{grains}})}$$

Results and discussion

The visualisation results are presented in the following subsection including impacts of kaolinite, illite, water composition and fines migration.

Impact of kaolinite

Details of two-phase interface displacement and its interactions with the solid surfaces under drainage were clearly visualised (Fig. 3). During the injection of both HSW and LSW, the

meniscus moving mechanism was observed and the oil–water interface moved through narrow throats to large bodies, displacing the wetting phase (oil phase).

During HSW injection, the system was strongly oil-wet and the oil phase near the pore wall stuck to the surface and did not flow, which resulted in poor oil recovery efficiency (Figs 3 and 4). The micromechanism of displacement could be best described as menisci flow through the centres of pore and throats, leaving a wetting layer of oil attached to the oil-wet surface of the grains. In addition, the system was dominated by capillary force. Due to the capillary forces, menisci could not enter some narrow throats and as a result a considerable amount of oil (the wetting phase) was bypassed by the displacing phase (Figs 4 and 5).

However, throughout LSW injection, there was a transition towards water-wetness in the large sections of the pore walls. Fig. 6 shows that although the advance of the stable water front left behind an oil film on the oil-wet portions of the pore walls, in water-wet surfaces, the interface moved towards the surface and replaced the oil film. Because of wettability alteration towards a water-wet state, the capillary forces were not dominant

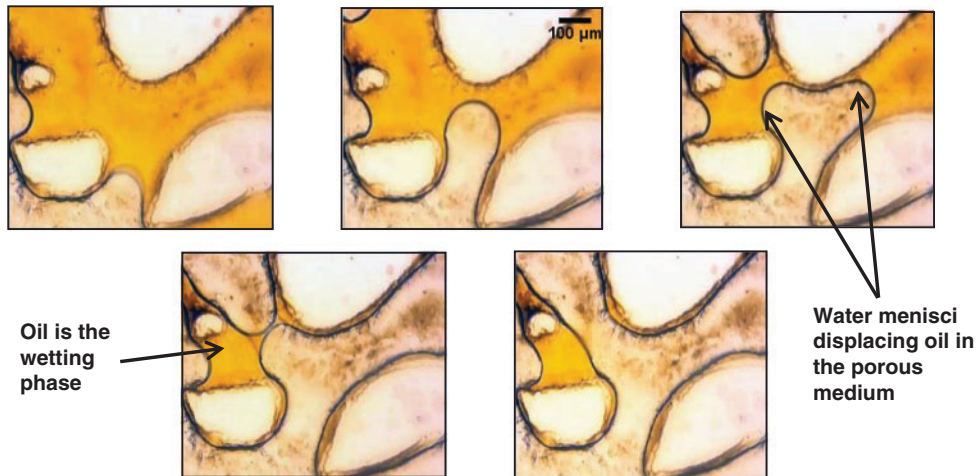


Fig. 3. Clay-coated, oil-wet micromodel during HSW injection (Amirian *et al.* 2017).

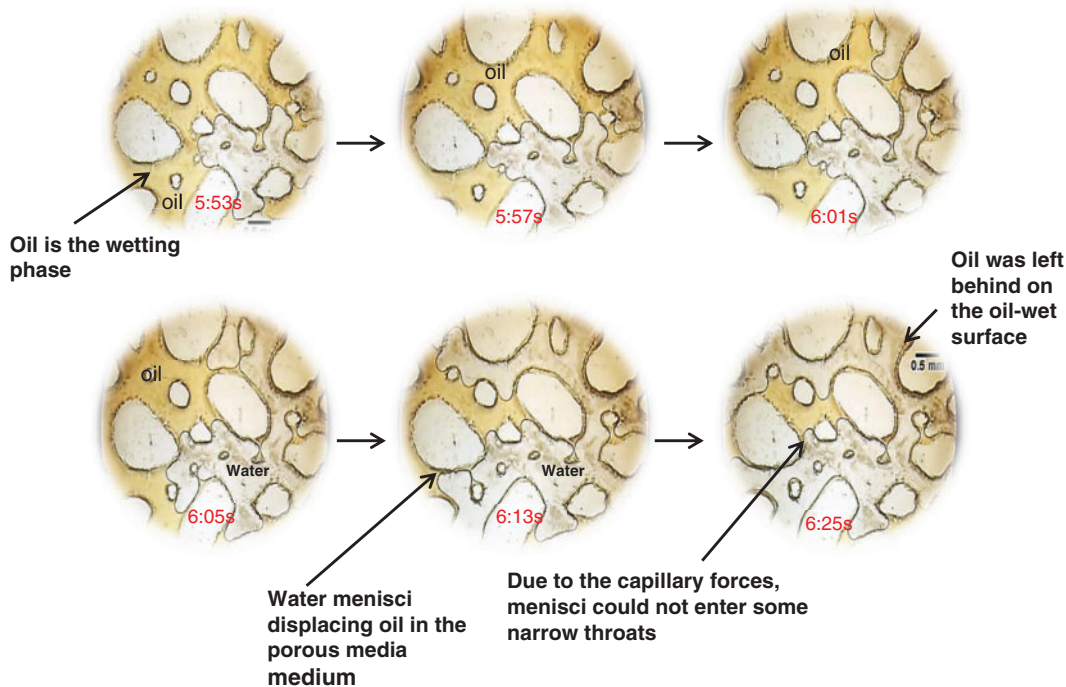


Fig. 4. Kaolinite-coated micromodel during HSW injection.

throughout the system and the water–oil menisci displaced oil in large portions of very narrow channels. In Figs 7 and 8, improved oil displacement efficiency is evident during LSW injection. Image analysis of the recorded images showed that wettability alteration due to LSW led to a 15% improved recovery. The different concentrations of LSW (0–6000 ppm) produced comparable results.

The mechanism behind the wettability alteration can be described in terms of DLE. The part of the water film closest to the charged surface forms an electrical double-layer and excess charges on the surface are countered by electrolyte ions of the opposite charge. The first layer of water with these ions is static, and the second layer exchanges ions with the bulk water. The

diffuse layer of charge and the surface charge form an ionic structure known as an electrical double-layer.

First, it should be emphasised that the initial state of the clay was, strictly speaking, not dry because clay always contains clay-bound water, adsorbed water and capillary condensation in small pores between the clay aggregates from the air humidity (Mahani *et al.* 2015). In the clay coating procedure, no excessive drying that would remove adsorbed or even clay-bound water was used, so the surface of the kaolinite was coated by a film from the water phase.

So, when clay and oil contacted the HSW (as the clay was initially saturated with HSW), the electric double layers of oil and clay were thin, and the negative surface charge of oil

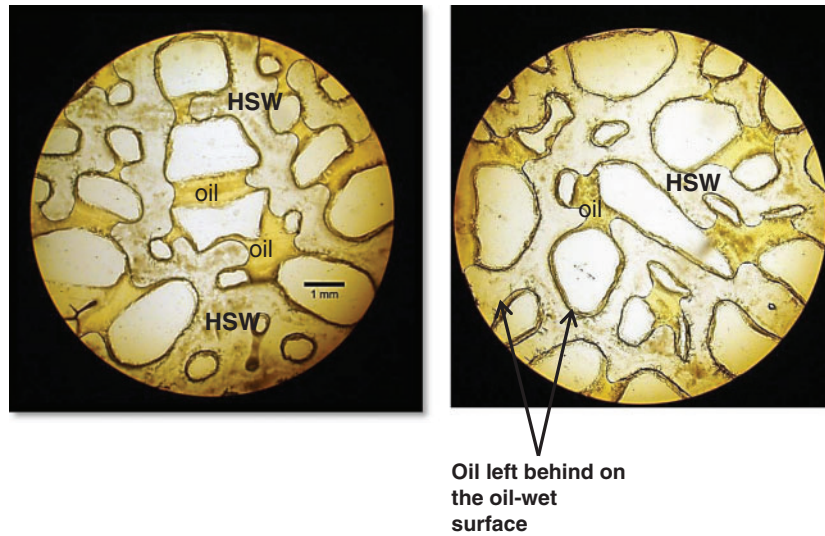


Fig. 5. Kaolinite-coated micromodel after HSW injection.

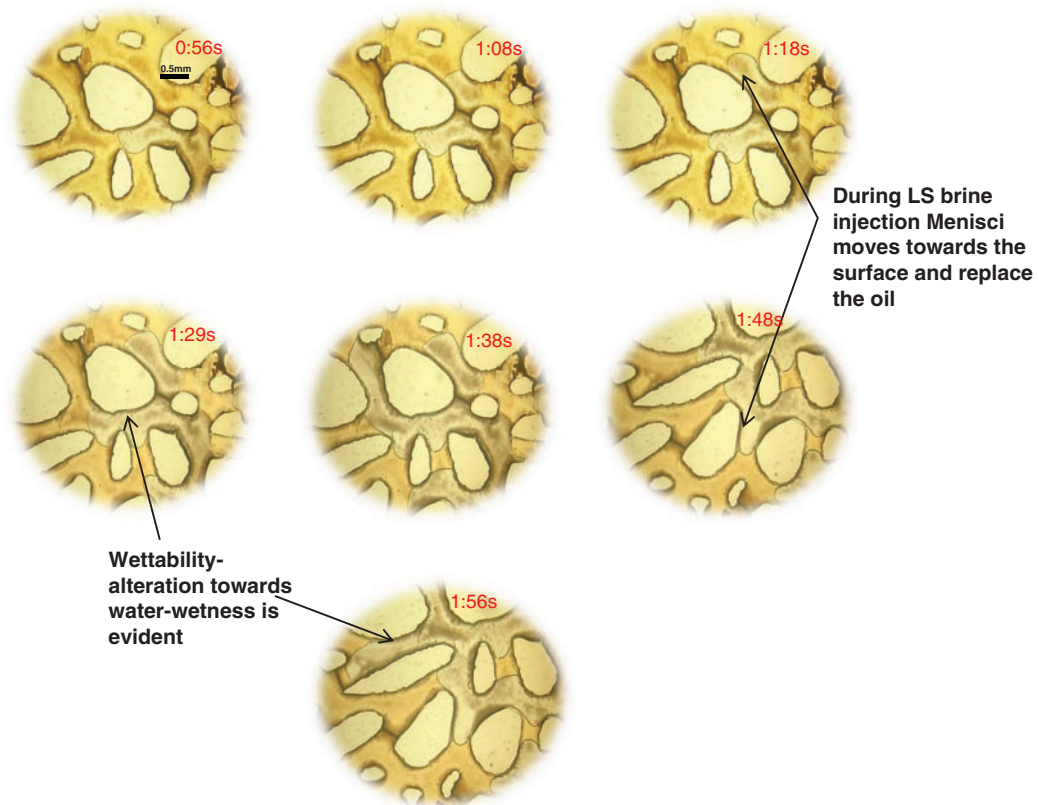


Fig. 6. Kaolinite-coated micromodel during LSW injection.

and clay was screened off, counteracting the repulsion between oil and clay. The attraction forces, then, kept the oil connected to the surface, resulting in an oil-wet porous medium. After exposure to LSW, the HSW was gradually refreshed. The reduction in ionic strength led to DLE of oil and clay, so the screening from the counter ions in the

electrolytes became weaker, resulting in higher repulsion forces between oil and clay. This expansion destabilised the oil-clay pinning points and the wettability moved toward a more water-wetting state and, when the attraction forces were low enough, oil was released from the clay surface and replaced by water.

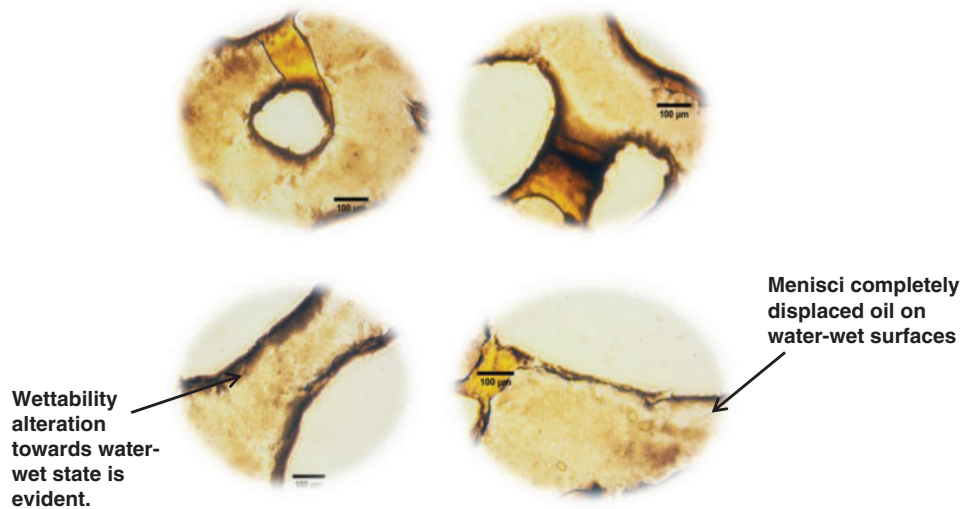


Fig. 7. Kaolinite-coated micromodel after LSW injection. Wettability alteration is evident.

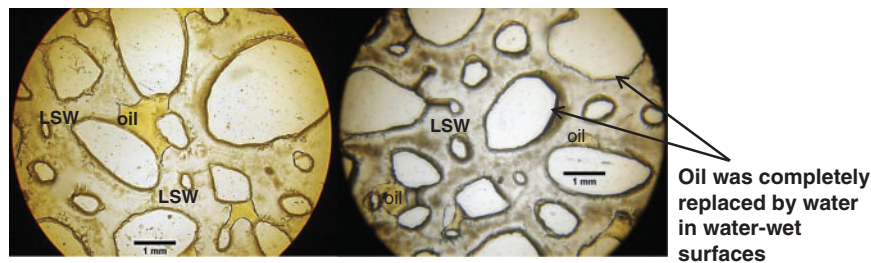


Fig. 8. Kaolinite-coated micromodel after LSW injection. The oil phase was completely replaced by water on water-wet surfaces but the layer of the wetting phase was left on oil-wet surfaces.

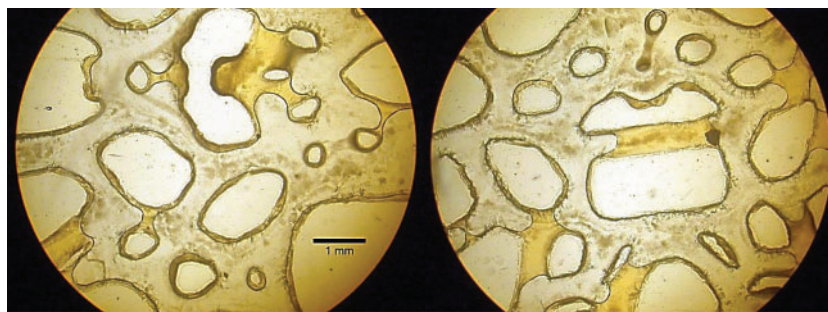


Fig. 9. Illite-coated micromodels after LSW injection. The LSW effect was not visualised.

Impact of illite

Visualisation experiments were also performed with illite. Similar to kaolinite, in the oil-wet porous medium, meniscus movement was the dominant micromechanism for displacement; however, wettability alteration and the resultant enhanced oil recovery (EOR) was not observed after switching to LSW (Fig. 9). Experimental results suggest that kaolinite might be more sensitive to variation in salinity than illite, so the effect was only observed for the micromodel functionalised with kaolinite. These results are in agreement with the LSW coreflooding

experiments performed before the visualisation experiments. The EOR was not achieved when an unconsolidated sandstone core sample containing illite was flushed with LSW. The recovery was only improved in samples containing kaolinite.

It is well established that, in oil-saturated sandstones, kaolinites are preferentially wetted by oil whereas illite and other minerals are essentially wetted by water. The wettability contrast of clays is characteristic of their crystalline structures and chemical compositions. The structures of kaolinite and illite are described in the literature (Worden and Morad 2009). In general, kaolinite has a large concentration of hydroxyl groups on its

surface. Due to the hydroxyl groups, kaolinite is inclined to contact with asphaltenes, so in oil-saturated sandstone, the presence of kaolinite will produce an oil-wet preference for the reservoir (Lebedeva and Fogden 2010). However, in oil-saturated sandstone, illite is characteristically preferentially wetted by water. This hydrophilic characteristic of illite results from the presence of cations in the clay surface.

The surfaces of illite and kaolinite differ, and these structural differences may explain the behaviour of the clays toward oil in the presence of water. Based on the observations during LSW injection, however, the wettability alteration from oil-wet to mixed-wet occurred only in the micromodels coated by kaolinite. This is despite the fact that illite has more affinity towards water-wetness. The results suggest that kaolinite could be more sensitive to modification by LSW than illite.

The visualisations are consistent with the conclusions of Sina and Andrés Delgado (2015). They investigated the impact of illite and kaolinite in calcium carbonate systems and sandstones. Stronger alteration towards water-wetness was reported for modified calcium carbonate mixes with kaolinite treated with LSW compared with samples containing illite.

Impact of water composition (nature of cations)

To evaluate the impact of cations initially present in the system, visualisation experiments were performed in the kaolinite-coated micromodels where Ca^{2+} cations were present in high concentration (22 000 ppm). The Ca^{2+} was introduced into the system through clay coating and aging. Then, the results were compared with the case in which only monovalent cations (Na^+) were present. The image analysis results showed that the LSW resulted in almost 15% recovery enhancement in both systems. This was despite Ca^{2+} having the reputation of making sandstones extremely oil-wet and the extent of recovery enhancement under LSW being expected to be less than the Na^+ -saturated micromodels. The result might indicate the considerable impact that divalent cations, already present in water, and the cation exchange mechanism have on the LSW effect.

The impact of divalent cations on wettability alteration cannot be explained by DLE, because divalent cations like Ca^{2+} , due to their double valency, compress the electrical double layers of oil and clay and lead to weaker repulsive double-layer forces between oil and clay. So, the attraction forces keep the oil connected to the surface. If the DLE was the primary mechanism behind the wettability alteration during LSW injection, the extent of recovery enhancement was estimated to be lower than when only monovalent cations were present.

The positive impact of Ca^{2+} can be elucidated by the cation exchange or MIE mechanism. The adsorbed Ca^{2+} on the clay surface bridged with oil molecules to form organo-metallic complexes. During LSW injection, these complex molecules are exchanged by monovalent cations like Na^+ from the brine film. The MIE improves oil recovery because it removes the bridging interactions of the water–oil and water–rock interfaces of the film, leading to a more water-wet state. This conclusion, however, needs to be further assessed and the investigation is in progress.

Fines migration

Although fines migration was not visualised in the visualisation experiments in clay-coated micromodels in response to the change in salinity and cation type, it cannot be completely disregarded as one primary mechanism behind the wettability alteration. As mentioned previously, to create an oil-wet system, the pH of the clay and saline water slurry was modified slightly, before injection into the microfluidic device. Reducing the pH value might affect clay detachment and fines migration. Fines migrations, however, has not been reported for clay-coated, water-wet micromodels during LSW injection in which pH was not modified (Amirian *et al.* 2017). According to Amirian *et al.* (2017), in water-wet clay functionalised systems, aging time had a substantial impact on fines detachment. Sarkar and Sharma (1990) experimentally studied the effect of polar crude oil on fines migration. The adsorption of polar components of crude oil reduced the fines release process but did not prevent it. The adsorption of polar ends to the rock surface is a slow process. Over geologic time at reservoir temperatures and pressures, this process may cause fines to become immobile by adsorbing on them. For the short aging period in the experiments (3 weeks), the release of fines happened at a very slow rate. As a result, the concentration of particles was not sufficient to be clearly visible, and had no noticeable effect on resultant oil recovery (i.e. caused a permeability reduction).

Conclusion

In the current study, a visualisation approach was applied to investigate the impact of clay type and water composition on the performance of LSW injection as an EOR method. Clay-coated two-dimensional glass micromodels were used, with the wettability status set at oil-wet condition. During HSW and LSW injection, the micromechanism of displacement was the meniscus moving. The effect of clay type was reflected in the change to wettability of the porous medium because, in the presence of kaolinite, wettability alteration was observed from oil-wet to mixed-wet conditions; however, the presence of illite had no considerable effect on the wettability status. With regard to the effect of water composition and nature of ions present in the aqueous phase, we observed a positive impact on enhanced recovery of the Ca^{2+} cations initially present in the system. In addition, fines migration was not visualised while flushing clay-coated micromodels with LSW.

Conflicts of interest

The authors declare no conflicts of interest.

Acknowledgement

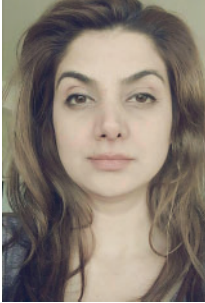
The authors would like to thank Santos Ltd, Australia, for providing the crude oil.

References

- Amirian, T., Haghghi, M., and Mostaghimi, P. (2017). Pore scale visualization of low salinity water flooding as an enhanced oil recovery method. *Energy & Fuels* **31**, 13133–13143. doi:10.1021/acs.energyfuels.7b01702

- Farooq, U., Tweheyo, M. T., Sjöblom, J., and Øye, G. (2011). Surface characterization of model, outcrop, and reservoir samples in low salinity aqueous solutions. *Journal of Dispersion Science and Technology* **32**, 519–531. doi:10.1080/01932691003756936
- Lager, A., Webb, K. J., Black, C. J. J., Singleton, M., and Sorbie, K. S. (2008a). Low salinity oil recovery – an experimental investigation 1. *Petrophysics* **49**, 28–35.
- Lager, A., Webb, K. J., and Collins, I. R. and Richmond, D. M. (2008b). LoSal enhanced oil recovery: evidence of enhanced oil recovery at the reservoir scale. In ‘SPE Symposium on Improved Oil Recovery’. Tulsa, Oklahoma, USA, 20–23 April. (Society of Petroleum Engineers)
- Lebedeva, E. V., and Fogden, A. (2010). Adhesion of oil to kaolinite in water. *Environmental Science & Technology* **44**, 9470–9475. doi:10.1021/es102041b
- Lee, S. Y., Webb, K. J., Collins, I., Lager, A., and Clarke, S., O’Sullivan, M., Routh, A., Wang, X. (2010). Low salinity oil recovery: increasing understanding of the underlying mechanisms. In ‘SPE Improved Oil Recovery Symposium’. Tulsa, Oklahoma, USA, 24–28 April. (Society of Petroleum Engineers)
- Ligthelm, D. J., Gronsveld, J., Hofman, J., Brussee, N., Marcelis, F., and van der Linde, H. (2009). Novel waterflooding strategy by manipulation of injection brine composition. In ‘EUROPEC/EAGE Conference and Exhibition’. Amsterdam, The Netherlands, 8–11 June. (Society of Petroleum Engineers)
- Mahani, H., Berg, S., Ilic, D., Bartels, W.-B., and Joekar-Niasar, V. (2015). Kinetics of low-salinity-flooding effect. *SPE Journal* **20**, 8–20. doi:10.2118/165255-PA
- Nasralla, R. A., and Nasr-El-Din, H. A. (2014). Double-layer expansion: is it a primary mechanism of improved oil recovery by low-salinity waterflooding? *SPE Reservoir Evaluation & Engineering* **17**, 49–59. doi:10.2118/154334-PA
- Rezaei Gomari, S., and Joseph, N. (2017). Study of the effect of clay particles on low salinity water injection in sandstone reservoirs. *Energies* **10**, 322. doi:10.3390/en10030322
- Romanuka, J., Hofman, J., Ligthelm, D. J., Suijkerbuijk, B., Marcelis, F., Oedai, S., Brussee, N., van der Linde, H., Aksulu, H., and Austad, T. (2012). Low salinity EOR in carbonates. In ‘SPE Improved Oil Recovery Symposium’. Tulsa, Oklahoma, USA, 2012/1/1/. (Society of Petroleum Engineers)
- Sarkar, A. K., and Sharma, M. M. (1990). Fines migration in two-phase flow. *Journal of Petroleum Technology* **42**, 646–652. doi:10.2118/17437-PA
- Schindelin, J., Rueden, C. T., Hiner, M. C., and Eliceiri, K. W. (2015). The ImageJ ecosystem: an open platform for biomedical image analysis. *Molecular Reproduction and Development* **82**, 518–529. doi:10.1002/mrd.22489
- Shalabi, E. W. A., Sepehrmoori, K., and Delshad, M. (2014). Mechanisms behind low salinity water injection in carbonate reservoirs. *Fuel* **121**, 11–19. doi:10.1016/j.fuel.2013.12.045
- Sheng, J. J. (2014). Critical review of low-salinity waterflooding. *Journal of Petroleum Science Engineering* **120**, 216–224. doi:10.1016/j.petrol.2014.05.026
- Sina, R.-G., and Andrés Delgado, A. (2015). Study of the effect of illite and kaolinite on low salinity water injection. *International Journal of Engineering Research and Applications* **5**, 16–22.
- Song, W., and Kovscek, A. R. (2015). Functionalization of micromodels with kaolinite for investigation of low salinity oil-recovery processes. *Lab on a Chip* **15**, 3314–3325. doi:10.1039/C5LC00544B
- Tang, G. Q., and Morrow, N. R. (1999). Influence of brine composition and fines migration on crude oil/brine/rock interactions and oil recovery. *Journal of Petroleum Science Engineering* **24**, 99–111. doi:10.1016/S0920-4105(99)00034-0
- Worden, R. H., and Morad, S. (Eds) (2009). Clay minerals in sandstones: controls on formation, distribution and evolution. In ‘Clay Mineral Cements in Sandstones’. pp. 1–41. (Blackwell Publishing Ltd.: Oxford, UK.)
- Zhang, L., Lu, X., Liu, X., Yang, K., and Zhou, H. (2016). Surface wettability of basal surfaces of clay minerals: Insights from molecular dynamics simulation. *Energy & Fuels* **30**, 149–160. doi:10.1021/acs.energyfuels.5b02142

The authors



Tammy Amirian is a PhD candidate at the Australian School of Petroleum. She has experience in the mining sector in Western Australia. She holds a Master's degree in petroleum engineering with specialisation in reservoir engineering and a BSc degree in Mining engineering. Her research interests are fundamental processes in multiphase flow, reactive transport in porous media, solid-fluid interaction and their implication for enhanced oil recovery methods, and modelling and simulation of fluid flow in porous media. Currently, Tammy is conducting a research on low salinity water flooding as an emerging EOR technique. Member: SPE.



Manouchehr (Manny) Haghighi is an associate professor of petroleum engineering. His research and teaching focus is on unconventional reservoirs, reservoir simulation, well testing, and formation evaluation. He has supervised more than 40 MSc and 10 PhD students. Before joining the University of Adelaide in 2009, Manouchehr was associate pro-fessor of petroleum engineering at the University of Tehran (Iran). During 2000–07, he was the head of the petroleum engineering program at the University of Tehran. In 2000, Manouchehr established Simtech, a consulting company for integrated reservoir simulation in which he has been project director of several full-field simulation projects for oil and gas reservoirs. Manouchehr has published more than 100 articles in peer-reviewed journals or presented in international conferences. He has served as a reviewer for various journals including the Journal of Petroleum Science and Engineering. Member: SPE.

**Chapter 5: Geochemical Modelling and Microfluidic Experiments
to Analyse Impact of Clay Type and Cations on Low Salinity
Water Flooding**

Statement of Authorship

Title of Paper	Geochemical Modelling and Microfluidic Experiments to Analyse Impact of Clay Type and Cations on Low Salinity Water Flooding.
Publication Status	<input checked="" type="checkbox"/> Published <input type="checkbox"/> Accepted for Publication <input type="checkbox"/> Submitted for Publication <input type="checkbox"/> Unpublished and Unsubmitted work written in manuscript style
Publication Details	Tammy Amirian, Manouchehr Haghghi, Chenhao Sun, Ryan T Armstrong and Peyman Mostaghimi. " Geochemical Modelling and Microfluidic Experiments to Analyse Impact of Clay Type and Cations on Low Salinity Water Flooding" <i>Energy & Fuels</i> , 2019.

Principal Author

Name of Principal Author (Candidate)	Tammy Amirian		
Contribution to the Paper	Developed the model, Conducted the experiments, performed data analysis, interpreted data, wrote the manuscript and acted as the corresponding author.		
Overall percentage (%)	60%		
Certification:	This paper reports on original research I conducted during the period of my Higher Degree by Research candidature and is not subject to any obligations or contractual agreements with a third party that would constrain its inclusion in this thesis. I am the primary author of this paper.		
Signature		Date	27/03/19

Co-Author Contributions

By signing the Statement of Authorship, each author certifies that:

- i. the candidate's stated contribution to the publication is accurate (as detailed above);
- ii. permission is granted for the candidate to include the publication in the thesis; and
- iii. the sum of all co-author contributions is equal to 100% less the candidate's stated contribution.

Name of Co-Author	Manouchehr Haghghi		
Contribution to the Paper	Developed the concept of the work, Supervised development of the work, helped in data interpretation and manuscript evaluation.		
Signature		Date	02/04/2019

Name of Co-Author	Chenhao Sun		
Contribution to the Paper	Helped in image analysis and developing the algorithm.		
Signature		Date	22/03/2019

Name of Co-Author	Ryan T Armstrong		
Contribution to the Paper	Helped in data interpretation and manuscript evaluation.		
Signature		Date	27-3-19

Name of Co-Author	Peyman Mostaghimi		
Contribution to the Paper	Supervised development of the work and helped to evaluate and edit the manuscript.		
Signature		Date	27/3/19

Geochemical Modeling and Microfluidic Experiments To Analyze Impact of Clay Type and Cations on Low-Salinity Water Flooding

Tammy Amirian,^{*,†} Manouchehr Haghghi,[†] Chenhao Sun,[‡] Ryan T. Armstrong,[‡] and Peyman Mostaghimi[‡]

[†]Australian School of Petroleum, The University of Adelaide, Adelaide, SA 5005, Australia

[‡]School of Minerals and Energy Resources Engineering, The University of New South Wales, Sydney, NSW 2052, Australia

ABSTRACT: The types of clay minerals and cations are the factors controlling improved recovery from low-salinity water (LSW) injection. In this paper, a surface complexation model was developed to predict the clay surface charge that develops for different brine compositions and salinities. It was followed by microfluidic experiments to visualize the individual performances of illite, kaolinite, and brine compositions and salinities during LSW injection. An automated measurement was conducted using an algorithm that determines contact angles from pore-space images. Our model results were substantiated against microfluidic observations. Based on the observations coupled with the simulation results, it is concluded that in kaolinite as an edge-charge-dominated clay, the charge development is significant under differing pH and ionic strengths. Accordingly, it responded well to LSW in the system under study, whereas illite as a basal-charged clay did not. This could elucidate the unlike sensitivities of clays to LSW, which in turn leads to different extents of wettability alteration.

1. INTRODUCTION

Low-salinity water (LSW) injection is a developing enhanced oil recovery (EOR) technique. Based on the experimental observations, several mechanisms have been proposed that occur during this process. Wettability alteration has been considered as one of the main mechanisms in the literature.^{1–3} It has been proposed that wettability alteration is induced by chemical mechanisms such as double-layer expansion (DLE).^{4–6} In DLE, injection of LSW enhanced the electrostatic repulsion between the brine–oil and brine–clay interfaces via the expansion of electrical double layers formed at each of the two interfaces. Once the attraction forces are low enough, the oil is released from the clay surface and replaced by water.

The impact of clay type on wettability alteration and the resulting oil recovery under LSW injection has been previously reported, and it has been mostly a reflection of the reduction in the contact angle.^{7–9} Collins et al.¹⁰ suggest that LSW works best at high temperatures (~ 100 °C), near pH 5, and when the clays are kaolinite (9–30% by volume). Clay minerals especially but not exclusively kaolinite were identified as a necessary component by a number of researchers.^{11–14} Sina and Andrés Delgado⁹ investigated the individual performances of illite and kaolinite (type and content of clay) on the alteration of carbonate rock surface-wettability. The strong alteration toward water wetness has been reported from samples with 10% kaolinite treated with the lowest salinity concentration. However, in the context of low-salinity effect (LSE), an explanation has been rarely suggested so far, which clarifies why different clay minerals have different sensitivities to the change of salinity and ionic composition of brines, which in turn leads to different extents of wettability alteration. Only very recently, Jelavić et al.¹⁵ used cryogenic X-ray photoelectron spectroscopy to observe the composition in the clay mineral–brine interface region on illite and chlorite in $MgCl_2$

and $CaCl_2$ electrolytes over a range of concentrations. They concluded that since during LSW injection the concentration of $(Ca^{2+} + Mg^{2+})$ dropped from 69 to 4 mM, a mineral with a threshold concentration of $(Ca^{2+} + Mg^{2+})$ that lies between 4 and 69 mM would then respond to lowering of the ionic strength. The response would be the additional release of negative charge, which is anionic organic molecules (oil molecules). This indicates that chlorite has a potential for responding to LSW, whereas illite does not.

There are contradictory views over the impact of multivalent cations on LSE as well. Lager et al.¹⁴ suggested that the presence of multivalent cations in the connate water is necessary. They hypothesized that when multivalent cations adsorb on the clay surfaces, they form organometallic complexes through bridging with oil molecules. During LSW injection, these complexes are exchanged with uncomplexed cations such as Na^+ . This leads to detachment of the oil phase and change of wettability. However, LSE has also been reported in systems where only monovalent cations were present, which led researchers to conclude that DLE is more important than multicomponent ionic exchange (MIE).^{1,5,16}

In this study, a surface complexation model (SCM) was developed to extend our previous electrokinetic analyses of wettability alteration during LSW injection.^{17,18} The SCM predicts the interface charge distributions for individual surface species using thermodynamic parameters like equilibrium constants. SCMs for clay minerals,^{19,20} calcite, and dolomite²¹ have been suggested. In the context of EOR, temperature-dependent SCMs were used by Brady and Krumhansl²² to study the reactions at the brine–oil and brine–kaolinite interfaces. Following the same approach and considering non-

Received: November 28, 2018

Revised: March 5, 2019

Published: March 13, 2019

Table 1. Surface Complexation Reactions as well as Cation-Exchange Reactions and Their Intrinsic Stability Constants on a Clay Surface^{b,c20,22,63–65}

reactions	log K_{in} at 25 °C				
		kaolinite		illite	
edge reactions	Si-OH	Al-OH	Si-OH	Al-OH	
$>SOH + H^+ \rightleftharpoons >SOH_2^+$		3		4	
$>SOH \rightleftharpoons >SO^- + H^+$	-3.8		-7		-6.2
$>SOH + Ca^{2+} \rightleftharpoons >SOCa^+ + H^+$	-9.7		-9.7		-5.9
$>SOH + CaOH^+ \rightleftharpoons >SOCaOH + H^+$		-4.5			NA ^a
					selectivity coefficient (log K_C)
basal surface reactions					kaolinite
$2 >X - Na^+ + Ca^{2+} \rightleftharpoons >X_2 - Ca + 2Na^+$					illite
					0.8
					1.04

^aNot available. ^bCation-exchange capacity for illite = 210 meq/kg.²⁰ ^cCation-exchange capacity for kaolinite = 40 meq/kg.⁶⁶

DLVO interactions between oil and the mineral surface, researchers concluded that low salinity increases oil adhesion in illite-containing reservoirs but decreases oil adhesion in kaolinite-containing reservoirs. They concluded that this might be the direct result of the different oil sorption characteristics of clay basal planes vs clay edges.^{23–26} Chen et al.²⁷ also performed a geochemical study considering the double-layer diffuse theory. They hypothesize that in the presence of basal-charged clays, LSW enables ion exchange. Ion exchange stimulates a pH increase, which in turn decreases the bridges between oil and minerals, and subsequently, oil films lift off from pore surfaces. Lately, Mahani et al.²⁸ developed an SCM for calcite to elucidate the effect of sulfate concentration on the ζ -potential at the water–calcite interface.

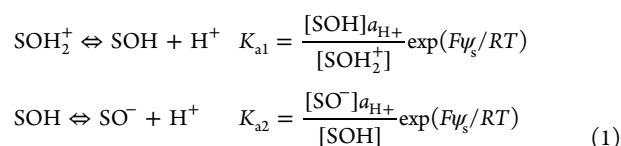
Herein, a model is constructed by developing submodels for kaolinite and illite edge surface charge and multivalent cation (Ca^{2+}) adsorption to clay–water interfaces. The models were developed to predict clay mineral surface charge distributions for different fluid compositions and concentrations that could occur during LSW injection. In addition, microfluidic experiments were developed to visualize wettability alteration during LSW injection with different clay minerals and water compositions. The simulation results were compared with microfluidic observations to substantiate the numerical model. In the end, based on clays' electrochemistry and structural differences, we concluded that kaolinite as an edge-charged clay has a significant potential to respond to LSW, and it responded well in the system under study, whereas illite as a basal-charged clay did not. This could elucidate why different clay minerals have unlike sensitivities to the change of salinity and ionic composition of brines, which in turn leads to different extents of wettability alteration.

2. MATERIALS AND METHODS

2.1. Model Description. The chemistry of mineral surfaces in sandstone reservoirs is a combination of quartz, feldspar, and clay.²⁹ The surface reactivity of clays dominates due to high specific surface areas and a high concentration of unsatisfied bonds especially at the edges.

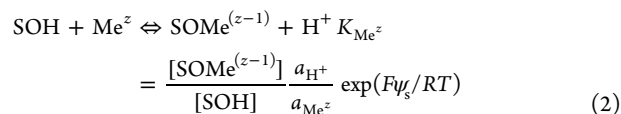
The thermodynamic model includes surface complexation and cation-exchange modeling. SCM describes amphoteric reactions (acid/base reactions) on the edge sites (i.e., broken surfaces) under differing pH and ionic compositions. The cation-exchange modeling has been considered due to the impact it might have on the pH and subsequently on the surface complexation reactions and the resultant charge development. The model is solved using PHREEQC (www.usgs.gov/software/phreeqc). The systems of equations are presented as described next.

2.1.1. Protonation and Deprotonation Reactions. The pH-dependent charge at the edge sites is determined by the following acid/base reaction:

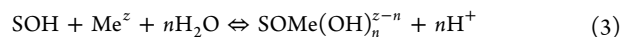


where [] terms are concentrations, a_{H^+} is the activity of H^+ , ψ_s is surface potential, T is absolute temperature, and R is the gas constant. SOH_2^+ , SO^- , and SOH represent, respectively, the positively charged, negatively charged, and neutral surface sites. K_{a1} and K_{a2} are equilibrium constants, and F is the Faraday constant.

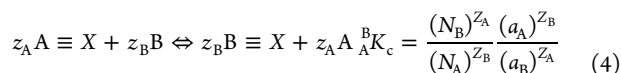
A surface complexation reaction representing the sorption of a metal, Me , of valency, Z , on edge sites can be represented by the following reaction:



Surface complexes can also be formed by hydrolyzed species



2.1.2. Cation Exchange. Clay minerals possess a permanent negative charge due to the substitution of silica (Si^{4+}) by aluminum (Al^{3+}) in the mineral lattice (so-called isomorphous substitution). This negative charge on the surfaces binds with cations, but allows them to exchange with other cations present in the solution. The cation exchange between cation B with charge Z_B , which exists in the aqueous phase, and cation A with charge Z_A at the clay surface ($\equiv X$) is defined by



where a_A and a_B are the activities and N_s are the equivalent fractional occupancies. N_Y is defined as the equivalents of cation Y adsorbed per unit mass divided by the cation-exchange capacity (CEC). CEC is defined as the amount of positive charge that can be exchanged per mass of clay (expressed in eq/g)

$$N_Y = \frac{eq(Y)_{ads}/g_{solid}}{CEC} \quad (5)$$

For illite and kaolinite, surface reactions and their intrinsic stability constants have been presented in Table 1.

A simple double-layer model was used to determine the charge and potential on the surfaces. The total surface charge σ_s can be calculated by summing the charges of all surface complexes

$$\sigma_s = F \sum_i m_{si} \nu_{si} \quad (6)$$

where ν_{si} and m_{si} , respectively, are the charge of the complex (si) and the surface concentration. The double-layer surface potential ψ_s is linked to the surface charge by the following equation:

$$\sigma_s^2 = 8000 \epsilon \epsilon_0 RT I \left[\sinh \left(\frac{F \psi_s}{2RT} \right) \right] \quad (7)$$

where I is the ionic strength of the electrolyte, T is the absolute temperature, and R is the ideal gas constant. ϵ_0 is the vacuum permittivity and ϵ is the dielectric constant of pure water. In the diffuse double-layer model, it is assumed that all surface reactions occur on the 0-plane. This implies that the ζ -potential and the potential at the surface of the clays are equivalent.

Some parameters of the solids must be defined in the model. PHREEQC uses the number of surface sites, the specific surface area, and ion-exchange capacities in the calculation run during surface complexation modeling. Bradbury and Baeyens²⁰ recommend a value of 2×10^{-3} mol/kg for the concentration of surface sites (i.e., SOH) for illite. The specific surface area used for illite was $83.0 \text{ m}^2/\text{g}$.³⁰ For kaolinite the surface density of surface hydroxyl (-SOH) sites is equal to $1.92 \text{ } \mu\text{mol}/\text{m}^2$ (1.92 for Si-OH and Al-OH each) and the specific surface area is $23 \text{ m}^2/\text{g}$.²²

2.2. Microfluidic Experiments. A variety of concentrations of NaCl and CaCl_2 were used as the aqueous phases. The crude oil came from the Cooper Basin in South Australia. The properties of the saline waters and crude oil are listed in Tables 2 and 3. The clay minerals of illite and kaolinite were obtained from the Source Clay Minerals Repository (The Clay Minerals Society).

Table 2. Brine Compositions

component (salt)	HSW/connate water (pH = 7) (mol/L)	LSW (pH = 7)
NaCl	1	deionized water
CaCl_2	0.01–0.2	NA

Table 3. Crude Oil Properties

API gravity @ 60 °F	53.2
density @ 60 °F	0.76
viscosity (cSt) @ 40 °C	3.2
acid number (mg KOH/g)	<0.1

2.2.1. Experimental Procedure. The experimental setup consists of a pump, a microscope equipped with a digital camera, which was connected to a computer, and a glass micromodel. The pore pattern and dimensions of the micromodel have been presented in Figure 1. A slurry made of HSW and clay (20 wt %) was injected into the microfluidic device. Then, the clay-saturated micromodel was air-dried while it had been placed on a hot plate. To set the wettability oil wet, the pH of the slurry before injection was reduced by almost one unit and the micromodel was aged only with oil for 3–4 weeks. Even after drying, clays are always coated with a thin water film originating from the adsorbed water and capillary condensation. The wettability of clays depends upon the stability of the thin brine film, which is subject to the pH and salinity of the liquid phase, as well as the aging time.^{24,31,32} In the microfluidic experiments, HSW did not contribute to the adhesion of the oil for both kaolinite and illite. Lowering the pH of the slurry by almost 1 unit induced the rupture of the thin film and, consequently, the adhesion of oil to the surface during the insufficient aging time. The reduction of pH values is not considered an extreme modification since the pH was still well above the isoelectronic point of the kaolinite and illite ≤ 4 .³³ The details about the clay coating procedure can be found elsewhere.¹⁷

Then, the clay-coated, oil-wet micromodel was flushed with LSW. The LS brine was deionized water with pH 7. The injection rate was set at a velocity of 10 m/day, resulting in a capillary number of 10^{-6} . The water saturation was monitored continuously, and the LSW injection was continued until water saturation remained constant. To compare the results, the microfluidics were flushed with high-salinity water. While conducting microfluidic experiments, images were collected at evenly distributed locations in the micromodel, and image analyses were performed. Using ImageJ, the images were filtered to reduce the noise and then segmented to distinguish different phases. Then, they were binarized to measure the oil and water saturations before and after injection. A_{phase} denotes the area saturated by the phase.

$$S_{\text{water}} = \frac{A_{\text{water}}}{(A_{\text{total}} - A_{\text{grains}})}$$

$$S_{\text{oil}} = \frac{A_{\text{oil}}}{(A_{\text{total}} - A_{\text{grains}})} \quad (8)$$

2.2.2. Measuring the Contact Angles. An automatic contact angle measurement was conducted in this study. An algorithm was developed to extract and measure contact angles from pore-space images automatically. The automated measurement was applied since there were a substantial number of angles to be measured. This

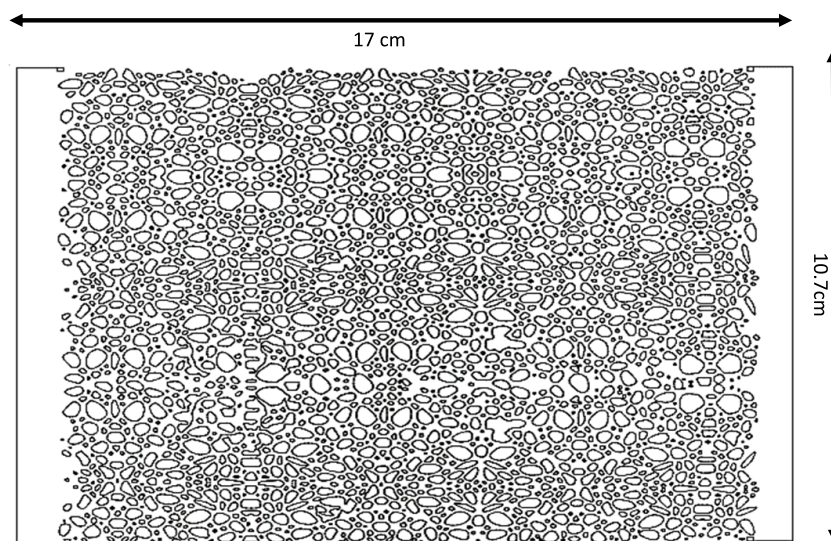


Figure 1. Pore network pattern of the glass micromodel.

method provides a rapid process to provide an accurate characterization of pore-scale wettability.^{34,35} The images were filtered and segmented using image analysis tools like Aviso 9.0 and Adobe Photoshop. The images were filtered using a nonlocal means filter to remove noise and improve demarcation between phases, which was followed by segmentation using the seeded watershed method. Then, three-phase contact points were automatically detected from the images, which can be defined as a pixel that has two other phases as neighbors. To estimate the effective contact angle, linear regression was applied to fit the grain surface. In addition, a constant fluid–fluid interface was assumed under equilibrium, which enabled us to fit a circle at the interface. The tangent line to the circle, which passed through the three-phase contact point, was identified as well. Consequently, the contact angle was measured as the angle between the surface straight line and the tangent line. The whole process has been schematically presented in Figure 2.

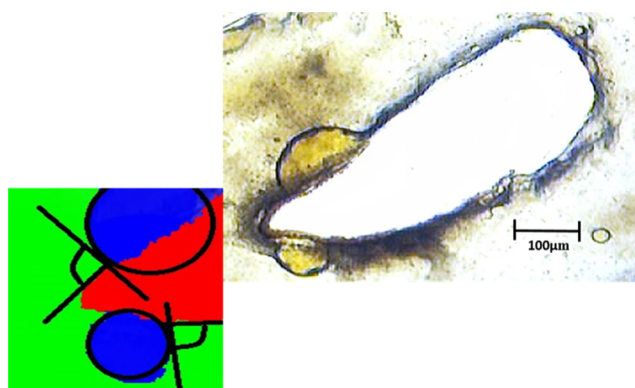


Figure 2. The original image on the right was segmented into three phases (RGB) as schematically has been shown on the left. The green phase is water, blue is the oil, and red is the grain surface. A circle was fitted at the fluid–fluid interface. The contact angle was measured as the angle between the tangent line passing through the three-phase point and the fitted line on the grain surface.

3. SCM RESULTS

The surface charge development of kaolinite and illite as a function of pH and concentration of brine is presented in Figure 3. In the models, after defining the surface, the surface was equilibrated with HS brine before mixing with lower-salinity brine. As seen in Figure 3, an incomplete mixing of the injectate (LSW) and residential (HSW) fluids has been considered; hence, a variety of mixing fractions in the modeling approach has been applied, for instance, 90/10 refers to 90:10 mixing of LSW/connate water (HSW). In heterogeneous systems, complete mixing occurs at late times. For reactive and nonreactive systems, the coupling between chemical reaction and transport or so-called reactive transport modeling has also been shown to give inaccurate predictions of experimental results considering the complete mixing of the resident and injectate fluids.^{36,37}

The results suggest that the kaolinite surface charge is quantitatively different from illite under the same condition (pH and ionic strength). The trend is the same, but in kaolinite, the ζ potential spans between almost -3 and -27 mV, whereas in illite it goes from -0.02 to -0.3 mV. More importantly, lowering the brine concentration from HS to LS has a substantial impact on the surface charge of kaolinite. For instance, at pH values around 7, the ζ potential decreases from almost -3 mV in HSW to -14 mV considering 90/10 mixing

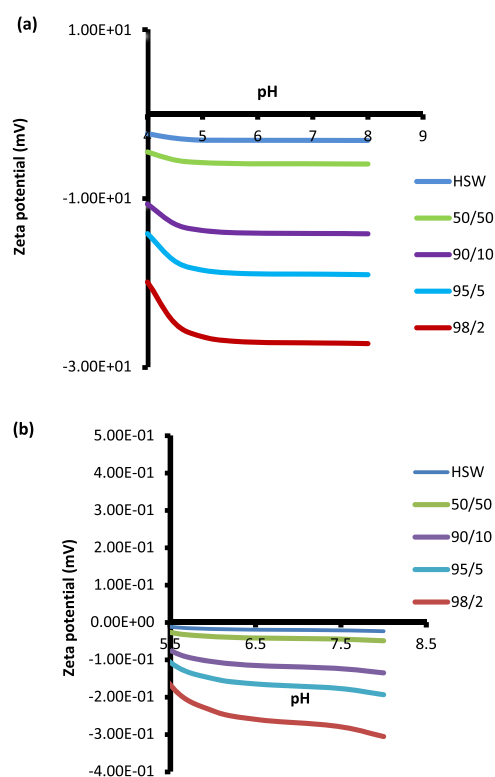


Figure 3. ζ Potential as a function of pH and ionic strength for (a) illite and (b) kaolinite.

of LSW/HSW. In illite, however, under the same chemical condition, the change in ζ potential is less than 0.1 mV.

Impact of Ca^{2+} cations in the residential water on the surface potential has been modeled for illite- and kaolinite-coated micromodels, and some results are presented in Figure 4. In all cases, Ca^{2+} reduced the quantity of the negative charges on the surface. In kaolinite, the ζ potential was reduced by less than 3 mV when more than 100 mM of Ca^{2+} was present in the connate water. The change was less than 2 mV when the Ca^{2+} concentration was lower than 50 mM. For illite, the maximum reduction was less than 2 mV.

4. MICROFLUIDIC RESULTS

4.1. Impact of Kaolinite. During the visualization experiments, details of two-phase interface displacement and its interactions with the solid surface were clearly visualized. As seen in Figure 5, throughout the injection of both HSW and LSW, the oil–water interface advanced through pores and throats, displacing the wetting phase (oil phase). During HSW injection, the system was strongly oil wet, and the oil phase near the pore wall remained attached to the surface and did not flow. To describe the mechanism of displacement, it was the menisci channeling through the centers of pores and throats, leaving behind a layer of oil attached to the oil-wet surface of the grains. Moreover, the flow was dominated by the capillary forces, and a substantial amount of oil (wetting phase) in narrow throats was bypassed by the displacing phase (water). However, throughout LSW injection, the wettability alteration was observed in the larger sections of the pore walls. The advance of the oil–water interface replaced the oil film on the water-wet grain surfaces. Because of wettability alteration toward a water-wet state, the water–oil menisci displaced oil in large portions of even very narrow channels. As seen in Figure

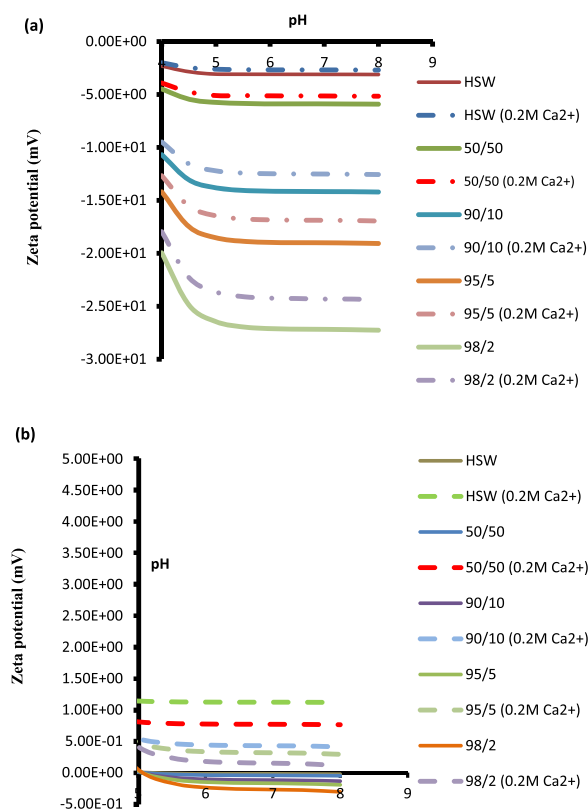


Figure 4. ζ Potentials as a function of ionic strength and ionic composition (the presence of Ca^{2+} in the resident and pH values) for (a) illite and (b) kaolinite.

6, improved oil mobilization efficiency is apparent during the injection of LSW. To determine the improved oil recovery, the entire chip was imaged after injections, followed by image analysis to differentiate between the phases; then, using eq 8, oil saturations were measured. The oil recovery showed 15% improvement after switching to LSW.

4.2. Impact of Illite. Visualization experiments were also performed with illite. Similar to kaolinite, in the oil-wet porous medium, meniscus movement was the pore-scale mechanism for displacement. However, wettability alteration and the resultant increased oil recovery were not observed after switching to LSW. Figure 5 shows the aftermath of LSW injection in the kaolinite-coated and illite-coated micromodels. The wettability alteration and enhanced recovery are evident only in the presence of kaolinite. In a series of microfluidic experiments that were performed in the absence of clay minerals, LSE was observed as well. LS brine clearly hindered the snap-off, which further investigation linked it to the formation of the highly elastic oil–brine interface. The details have been discussed in Amirian et al.¹⁷

4.3. Impact of Ca^{2+} in the Resident Water on LSE. To study the impact of multivalent cations on LSE, the concentration of Ca^{2+} in the connate water was set at various values from 10 up to 200 mM while the injecting water contained no Ca^{2+} cations. In the presence of kaolinite, LSE was observed in all experimental cases, but the recovery factor did not change. In the illite-coated micromodel, Ca^{2+} cations did not induce a change in the wettability status, and the oil recovery was not improved.

4.4. Fines Migration. Fines migration was not visualized while injecting LSW. However, due to the type of test fluids (polar crude oil) and methodology applied for microfluidic experiments, it cannot be completely disregarded as one of the primary mechanisms behind LSE. It has been reported that the presence of polar crude oil³⁸ slows down the fines release process due to adsorption of the polar components but does not prevent it. Over geologic time and at reservoir pressure and temperature, very slow process of adsorption may cause fines to become immobile. For the short aging time in our experiments (3–4 weeks), fines detachment perhaps occurred but at a very slow rate. Accordingly, the concentration of particles was not sufficient to be clearly visible or have an impact on permeability and oil recovery.

Clay swelling was not observed as well. There are two mechanisms behind clay swelling: crystalline swelling and osmotic swelling.^{15,39–43} Crystalline swelling happens in all types of clay minerals, especially in the smectite group (montmorillonite). Montmorillonite, which has a large basal exchange capacity (90–150 meq/100 g), will readily adsorb Na^+ and other hydrating cations. The hydration of cations by water increases the distance between the layers of clay. In the osmotic swelling process, if the cation concentration in the interlayer areas is higher than that in the water nearby, water molecules enter the area to dilute the concentration of cations and restore the cationic balance. This process leads to expansion of the layers and swelling of clay.⁴⁴ Illite contains interlayer potassium (K^+), and the strong electrostatic bonds exerted by potassium ions link the unit layers together. Therefore, as a result of strongly bonded layers as well as having a much smaller cation-exchange capacity (20–30 meq/100 g), the layers do not expand due to addition of water.⁴³

In kaolinite, the small number of exchangeable cations (2–5 meq/100 g) associated with the clay structure is presumed to be held by broken bonds on the edges of the sheets. Even though kaolinite is more highly ionized than montmorillonite and illite, this greater ionization, because of the small number of cations present and their location on the edges of the sheets, cannot pry the units apart or leave the sheets sufficiently charged to cause the mineral to exhibit the phenomenon of swelling.^{43,45,46}

4.5. Contact Angle Distribution. For the region of interest, a set of spatially distributed values of the effective contact angle could be measured. Hence, the distribution of

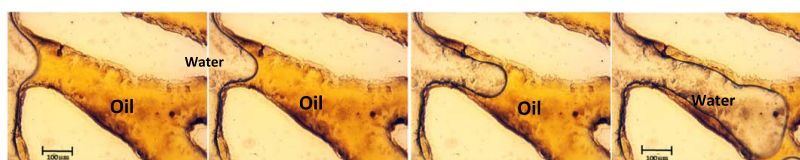


Figure 5. Images taken during HSW injection. The menisci channel through the center of the pore and throat leaving behind a layer of oil attached to the surface.

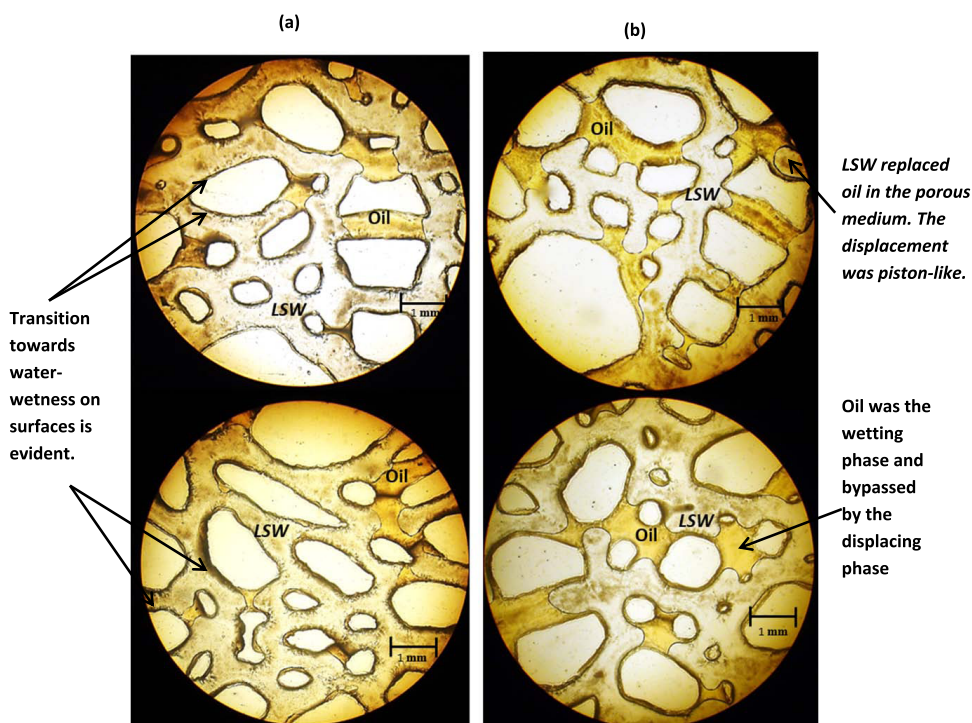


Figure 6. (a) Porous medium after LSW injection in the oil-wet, kaolinite-coated micromodels. (b) Images captured after LSW injection in the oil-wet, illite-coated micromodels. In the presence of kaolinite, wettability altered toward water wetness in some surfaces; however, in the presence of illite, the wettability status remained constant.

the contact angle can be obtained for the whole system. As shown in Figure 7, the most common contact angle value is

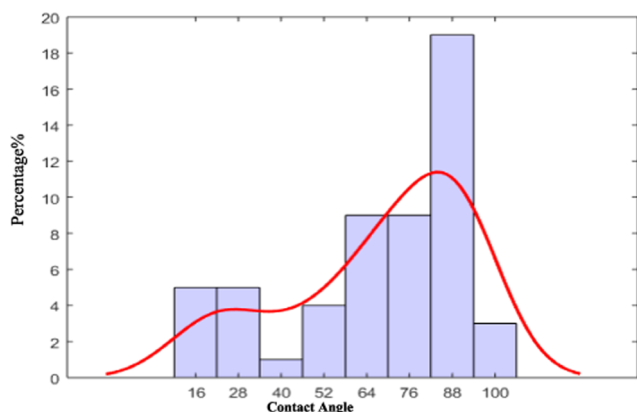


Figure 7. Distribution of the contact angle and the probability density of contact angle values.

approximately 87°. The distribution of contact angle can be understood as the result of the multiple contributing factors such as surface heterogeneity and small fitting errors due to the low resolution of the images. Furthermore, the data was inferred and interpreted by a probabilistic framework. Here, we apply a kernel density estimation to fit the probability density function of measured contact angles.

$$f_h(x) = \frac{1}{n} \sum_{i=1}^n K_h(x - x_i) = \frac{1}{nh} \sum_{i=1}^n K\left(\frac{x - x_i}{h}\right) \quad (9)$$

where K is kernel and h is a smoothing parameter. From Figure 7, it is seen that the average values of contact angle are in the range of 80–90° and most likely to be 88°. The nonuniform

clay coverage of the surface in the micromodel might be the reason behind the bimodal distribution of the contact angle. This might be glass regions that have lost clay or never had clay attached in the first place.

It should be emphasized that the contact angle measurement was performed for the porous media after LSW injection. As discussed earlier, after HSW injection, the system remained mostly oil wet and the layer of oil remained attached to the surface. In other words, contact angle distribution was not observed.

5. DISCUSSION

The SCM results agree well with the microfluidic results when DLE is considered the mechanism behind LSE. The extent of the ζ -potential shows the degree of electrostatic repulsion between adjacent, similarly charged surfaces, that is, the brine–oil and brine–clay interfaces, so the enhanced repulsion forces weakened the oil and clay pinning points. As a result, wettability altered toward more water-wetness, which is confirmed by contact angle measurements. Once the attraction forces were low enough, the oil was released from the clay surface and replaced by water, as observed in microfluidic experiments.

The change in wettability was not observed on the surface of the device, which was coated by illite. The model also calculates less than 1 mV change in the ζ -potential under the experimental condition. In the case of illite, SCM results suggest that the surface potential did not undergo a considerable change, so the oil remained attached to the surface due to DLVO and non-DLVO forces.

The impact of multivalent cations like Ca^{2+} , initially present in the system, on the surface charge of illite and kaolinite was modeled and experimentally investigated as well. Although the surface potential underwent some degrees of change

(maximum of 3 mV for kaolinite), this change did not translate into variation in the oil recovery and the wettability status as observed in the visualization experiments. The change was less than 2 mV for illite.

The impact of divalent cations on surface potential can be explained by DLE because divalent cations like Ca^{2+} , due to their double valency, compress the electrical double layers formed at the interfaces. This leads to weaker repulsive double-layer forces between oil and clay. This effect is manifested in the reduction in the ζ -potential but perhaps was not sufficient to induce significant change in the wettability status.

To explain the higher sensitivity of kaolinite surface charge compared to illite, which led to a significant extent of wettability alteration in kaolinite, an understanding of clays' electrochemistry and structural differences is ultimately of assistance.

Clay minerals are silicates with basic structural units consisting of a silica tetrahedron and an alumina octahedron, which are schematically presented in Figure 8A. These basic

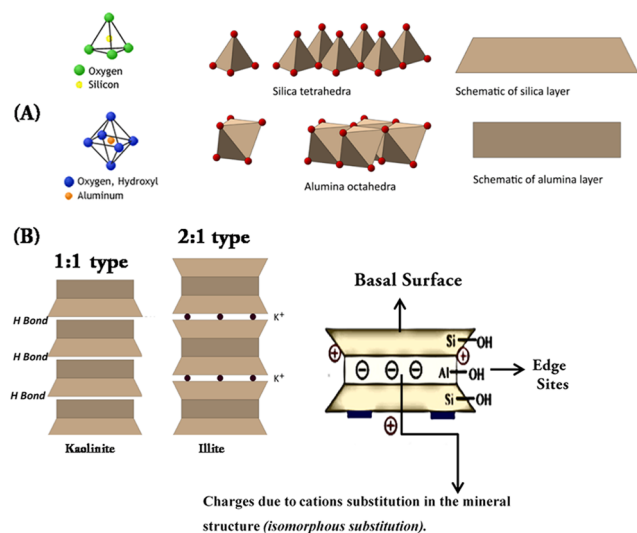


Figure 8. Clay minerals' molecular structure (from Knappett⁶²). (A) Basic structural components of clay minerals; a single eight-sided octahedron and a single four-sided tetrahedron. These basic units are combined by sharing oxygens to form silica tetrahedra and alumina octahedra. (B) Illite is a 2:1-type clay mineral consisting of an octahedral sandwiched by two tetrahedral sheets, whereas kaolinite as a 1:1-type clay mineral consists of one tetrahedral sheet attached to an octahedral sheet.

units are combined to form sheet structures. Then, these layers are combined to form the crystal structure of clay minerals. In general, there are two major types of structural layers: 1:1 type and 2:1 type. In the 1:1 type, the structural layer consists of an octahedral sheet attached to a tetrahedral sheet, whereas in the 2:1 type, it comprises an octahedral sheet sandwiched by two tetrahedral sheets⁴⁷ as shown in Figure 8B. Because of the layered structure of clay minerals, there are two types of surfaces: basal surfaces (interlayer surfaces) and edge surfaces (broken surfaces)⁴⁸ as schematically presented in Figure 8B. Basal charge due to exchange of cations in the mineral lattice is permanent, but the amount of negative charge on the edges and the exposed basal hydroxyls (if present) depends on pH and other ion concentrations.

The structural layers combine to form clay particles. The number of stacked layers in a single particle depends on the

nature of the clay mineral. The number of layers stacked to form the kaolinite particle can range from 10 to more than 200,⁴⁹ and thicknesses fall in the range of 40–70 nm.⁵⁰ So, kaolinite particles are relatively thick, and their edges account for a considerable proportion (between 20 and 34%) of the surface area. It has been also suggested that kaolinite has high density of pH-dependent reaction sites at the particle edges, which could be easily accommodated by the structure at the edges of these particles. Hence, the electrostatic charge developed on the surface of kaolinite results from acid/base reactions, which changes with pH and ionic strength. Considering the high density of these reaction sites in kaolinite and the resultant surface charge, the substantial sensitivity of surface charge distribution toward ionic strength is acceptable. In addition, kaolinite has two basal surfaces: hydroxyl and siloxane. Siloxane surfaces behave as adsorbing sites for external molecules like cations and water; however, kaolinite possesses one of the lowest CEC among clay minerals.^{51,52} The –OH units of hydroxyl surfaces have negligible chemical reactivity and nearly have no contribution to the acid–base chemistry of kaolinite.^{53–55}

On the other hand, illite particles typically consist of 5–20 stacked layers;^{49,56} the thickness of illite particles is often of only a few unit cells, and it tends to fall in the range of 8–20 nm as reported in the literature. Therefore, edges often account for ~1% of their surface area.^{50,57} It has been also proposed that illite possesses low density of pH-dependent reaction sites consistent with the structure at the edges of these particles.^{19,22,49,58} As a result, the development of surface charge on the clay edges, under LSW conditions, is significantly lower than kaolinite. Low surface potential values that have been reported for illite so far support the theory that the basal surface of this mineral is free of pH-dependent charge and that protonation/deprotonation interactions at its edge surfaces do not result in the development of a significant charge.^{47,59,60} In addition, the basal surfaces of illite have a low affinity or selectivity toward cation exchange although it has a high CEC.⁶¹ Hence, considering the chemical structure of illite, insignificant surface charge development on the clay edges under differing ionic strengths and pH in the SCM model is justifiable.

6. CONCLUSIONS

A study was performed to investigate the impact of different types of clay minerals and nature of cations on LSE by using microfluidics and geochemical modeling. The key impact of this study is the coupling between visualization experiments and surface complexation modeling when the observations substantiated the simulation results. Based on the results, it is concluded that in kaolinite as an edge-charge dominated clay, the charge development is significant under differing chemical circumstances (pH and ionic strength). Accordingly, it responded well to LSW in the current system, whereas illite did not. Surface charge (the edges) of illite as a basal-charged clay did not undergo a significant change under differing ionic strengths as well as pH. The basal surfaces of illite also have a low affinity or selectivity toward cation exchange, whereas it has a high CEC. However, we should emphasize that this conclusion is based on the observations and modeling of the system under study. LSE is a very complicated phenomenon, so illite might respond to LSE through a different mechanism under different circumstances.

Understanding of the clay surface behavior and its controlling factors like ionic strength and composition would contribute significantly to the EOR method design and reservoir selection for the LSW treatment. If the chemical composition of connate water and the content of clay minerals in the reservoir are known to some extent, the findings of this study would assist in determining the optimized concentration for ions and pH of the injecting water to maximize LSE (wettability alteration) in a reservoir. The following are the main conclusions from this work.

- According to the SCM model, in kaolinite, the negative surface potential increased significantly with gradual reduction in the ionic strength; however, for illite the change was insignificant.
- Microfluidic experiments and the subsequent automated contact angle measurements confirmed that the change in the ionic strengths under LSW injection leads to wettability alteration in kaolinite. No major wettability alteration was observed for illite.
- Clays' electrochemistry and structural differences between kaolinite and illite were discussed as the reason behind the unlike sensitivity of the clays' surface charge toward the change in ionic strength and ionic composition.
- In our microfluidic experiments, Ca^{2+} cations present in the residential water did not have an impact on LSE as observed in the visualization experiments. The numerical model also predicted insignificant change in the ζ -potential under experimental conditions.
- Fines migration was not visualized in the experiments.

AUTHOR INFORMATION

Corresponding Author

*E-mail: Tammy.Amirian@adelaide.edu.au.

ORCID

Tammy Amirian: 0000-0003-3857-0300

Ryan T. Armstrong: 0000-0001-6431-7902

Peyman Mostaghimi: 0000-0002-2071-6247

Notes

The authors declare no competing financial interest.

REFERENCES

- (1) Myint, P. C.; Firoozabadi, A. Thin liquid films in improved oil recovery from low-salinity brine. *Curr. Opin. Colloid Interface Sci.* **2015**, *20*, 105–114.
- (2) Bartels, W.-B.; Mahani, H.; Berg, S.; Menezes, R.; van der Hoeven, J. A.; Fadili, A. Oil Configuration Under High-Salinity and Low-Salinity Conditions at Pore Scale: A Parametric Investigation by Use of a Single-Channel Micromodel. *SPE J.* **2017**, *22*, 1362–1373.
- (3) Bartels, W. B.; Mahani, H.; Berg, S.; Hassanizadeh, S. M. Literature review of low salinity waterflooding from a length and time scale perspective. *Fuel* **2019**, *236*, 338–353.
- (4) Lee, S. Y.; Webb, K. J.; Collins, I.; Lager, A.; Clarke, S.; Sullivan, M.; Routh, A.; Wang, X. Low Salinity Oil Recovery: Increasing Understanding of the Underlying Mechanisms. In *SPE Improved Oil Recovery Symposium*; Society of Petroleum Engineers: Tulsa, Oklahoma, 2010.
- (5) Ligthelm, D. J.; Gronsveld, J.; Hofman, J.; Brussee, N.; Marcelis, F.; van der Linde, H. Novel Waterflooding Strategy By Manipulation Of Injection Brine Composition. In *EUROPEC/EAGE Conference and Exhibition*, Society of Petroleum Engineers: Amsterdam, The Netherlands, 2009.
- (6) Nasralla, R. A.; Nasr-El-Din, H. A. Double-Layer Expansion: Is It a Primary Mechanism of Improved Oil Recovery by Low-Salinity Waterflooding? *SPE Reservoir Eval. Eng.* **2014**, *17*, 49–59.
- (7) Rezaei Gomari, S.; Joseph, N. Study of the effect of clay particles on low salinity water injection in sandstone reservoirs. *Energies* **2017**, *322*.
- (8) Romanuka, J.; Hofman, J.; Ligthelm, D. J.; Suijkerbuijk, B.; Marcelis, F.; Oedai, S.; Brussee, N.; van der Linde, H.; Aksulu, H.; Austad, T. Low Salinity EOR in Carbonates. In *SPE Improved Oil Recovery Symposium*; Society of Petroleum Engineers: Tulsa, Oklahoma, 2012.
- (9) Sina, R.-G.; Andrés Delgado, A. Study of the effect of Illite and Kaolinite on low salinity water injection. *Int. J. Eng. Res. Ind. Appl.* **2015**, *5*, 16–22.
- (10) Collins, I. R.; Jerauld, G. R.; Lager, A.; McGuire, P. L.; Webb, K. Hydrocarbon recovery process. Google Patents, 2013.
- (11) Al-adasani, A.; Bai, B.; Wu, Y.-S. Investigating Low-Salinity Waterflooding Recovery Mechanisms in Sandstone Reservoirs. In *SPE Improved Oil Recovery Symposium*; Society of Petroleum Engineers: Tulsa, Oklahoma, 2012.
- (12) Skrettingland, K.; Holt, T.; Tveheyo, M. T.; Skjevraak, I. Snorre Low-Salinity-Water Injection–Coreflooding Experiments and Single-Well Field Pilot. *SPE Reservoir Eval. Eng.* **2011**, *14*, No. 182.
- (13) Zhang, Y.; Xie, X.; Morrow, N. R. Waterflood Performance By Injection Of Brine With Different Salinity For Reservoir Cores. *SPE Annual Technical Conference and Exhibition*; Society of Petroleum Engineers: Anaheim, California, 2007.
- (14) Lager, A.; Webb, K. J.; Black, C. J. J.; Singleton, M.; Sorbie, K. S. Low Salinity Oil Recovery - An Experimental Investigation I. *Petrophysics* **2008**, *49*, 28–35.
- (15) Jelavić, S.; Nielsen, A. R.; Stipp, S. L. S.; Bovet, N. Composition in the Interface between Clay Mineral Surfaces and Divalent Cation Electrolytes. *Langmuir* **2018**, *34*, 7011–7020.
- (16) Xie, Q.; Liu, Y.; Wu, J.; Liu, Q. Ions tuning water flooding experiments and interpretation by thermodynamics of wettability. *J. Pet. Sci. Eng.* **2014**, *124*, 350–358.
- (17) Amirian, T.; Haghighi, M.; Mostaghimi, P. Pore Scale Visualization of Low Salinity Water Flooding as an Enhanced Oil Recovery Method. *Energy Fuels* **2017**, *31*, 13133–13143.
- (18) Amirian, T.; Haghighi, M. Impact of clay type and water composition on low salinity water injection – visualisation approach. *APPEA J.* **2018**, *58*, 51–59.
- (19) Bradbury, M. H.; Baeyens, B. A mechanistic description of Ni and Zn sorption on Na-montmorillonite Part II: modelling. *J. Contam. Hydrol.* **1997**, *27*, 223–248.
- (20) Bradbury, M. H.; Baeyens, B. Sorption modelling on illite Part I: Titration measurements and the sorption of Ni, Co, Eu and Sn. *Geochim. Cosmochim. Acta* **2009**, *73*, 990–1003.
- (21) Pokrovsky, O. S.; Mielczarski, J. A.; Barres, O.; Schott, J. Surface Speciation Models of Calcite and Dolomite/Aqueous Solution Interfaces and Their Spectroscopic Evaluation. *Langmuir* **2000**, *16*, 2677–2688.
- (22) Brady, P. V.; Krumhansl, J. L. A surface complexation model of oil–brine–sandstone interfaces at 100 °C: Low salinity waterflooding. *J. Pet. Sci. Eng.* **2012**, *81*, 171–176.
- (23) Brady, P. V.; Bryan, C. R.; Thyne, G.; Li, H. Altering wettability to recover more oil from tight formations. *J. Unconv. Oil Gas Resour.* **2016**, *15*, 79–83.
- (24) Lebedeva, E. V.; Fogden, A. Wettability alteration of kaolinite exposed to crude oil in salt solutions. *Colloids Surf., A* **2011**, *377*, 115–122.
- (25) RezaeiDoust, A.; Puntervold, T.; Austad, T. In *A Discussion of the Low-Salinity EOR Potential for a North Sea Sandstone Field*; SPE Annual Technical Conference and Exhibition; Society of Petroleum Engineers, 2010.
- (26) Brady, P. V.; Krumhansl, J. L. Surface Complexation Modeling for Waterflooding of Sandstones. *SPE J.* **2013**, *18*, 214–218.

- (27) Chen, Y.; Xie, Q.; Pu, W.; Saeedi, A. Drivers of pH increase and implications for low salinity effect in sandstone. *Fuel* **2018**, *218*, 112–117.
- (28) Mahani, H.; Keya, A. L.; Berg, S.; Nasralla, R. Electrokinetics of Carbonate/Brine Interface in Low-Salinity Waterflooding: Effect of Brine Salinity, Composition, Rock Type, and pH on ζ -Potential and a Surface-Complexation Model. *SPE J.* **2017**, 53–68.
- (29) Liu, M.; Shabaninejad, M.; Mostaghimi, P. Impact of mineralogical heterogeneity on reactive transport modelling. *Comput. Geosci.* **2017**, *104*, 12–19.
- (30) Macht, F.; Eusterhues, K.; Pronk, G. J.; Totsche, K. U. Specific surface area of clay minerals: Comparison between atomic force microscopy measurements and bulk-gas (N₂) and-liquid (EGME) adsorption methods. *Appl. Clay Sci.* **2011**, *53*, 20–26.
- (31) Lebedeva, E. V.; Fogden, A. Adhesion of Oil to Kaolinite in Water. *Environ. Sci. Technol.* **2010**, *44*, 9470–9475.
- (32) Lebedeva, E. V.; Fogden, A.; Senden, T. J.; Knackstedt, M. A. In *Kaolinite Wettability—The Effect of Salinity, pH and Calcium*, 24th International Symposium of Core Analysts, 2010.
- (33) Kosmulski, M. The pH dependent surface charging and points of zero charge. VII. Update. *Adv. Colloid Interface Sci.* **2018**, *251*, 115–138.
- (34) AlRatrou, A.; Raeini, A. Q.; Bijeljic, B.; Blunt, M. J. Automatic measurement of contact angle in pore-space images. *Adv. Water Resour.* **2017**, *109*, 158–169.
- (35) Andrew, M.; Bijeljic, B.; Blunt, M. J. Pore-scale contact angle measurements at reservoir conditions using X-ray microtomography. *Adv. Water Resour.* **2014**, *68*, 24–31.
- (36) Alhashmi, Z.; Blunt, M. J.; Bijeljic, B. Predictions of dynamic changes in reaction rates as a consequence of incomplete mixing using pore scale reactive transport modeling on images of porous media. *J. Contam. Hydrol.* **2015**, *179*, 171–181.
- (37) Karadimitriou, N. K.; Joekar-Niasar, V.; Brizuela, O. G. Hydrodynamic Solute Transport under Two-Phase Flow Conditions. *Sci. Rep.* **2017**, *7*, No. 6624.
- (38) Sarkar, A. K.; Sharma, M. M. Fines Migration in Two-Phase Flow. *J. Pet. Technol.* 646 652. DOI: 10.2118/17437-PA.
- (39) Fink, D.; Rich, C.; Thomas, G. Determination of internal surface area, external water, and amount of montmorillonite in clay-water systems. *Soil Sci.* **1968**, *105*, 71–77.
- (40) Krishna Mohan, K.; Reed, M. G.; Scott Fogler, H. Formation damage in smectitic sandstones by high ionic strength brines. *Colloids Surf., A* **1999**, *154*, 249–257.
- (41) Norrish, K. The swelling of montmorillonite. *Discuss. Faraday Soc.* **1954**, *18*, 120–134.
- (42) Zhang, Z. Z.; Low, P. F. Relation between the heat of immersion and the initial water content of Li-, Na-, and K-montmorillonite. *J. Colloid Interface Sci.* **1989**, *133*, 461–472.
- (43) Tan, K. H. *Principles of Soil Chemistry*; CRC Press, 2010.
- (44) Sharifipour, M.; Pourafshary, P.; Nakhaee, A. Study of the effect of clay swelling on the oil recovery factor in porous media using a glass micromodel. *Appl. Clay Sci.* **2017**, *141*, 125–131.
- (45) Hensen, E. J. M.; Smit, B. Why Clays Swell. *J. Phys. Chem. B* **2002**, *106*, 12664–12667.
- (46) Foster, M. D. The relation between composition and swelling in clays. *Clays Clay Miner.* **1954**, *3*, 205–220.
- (47) Jeans, C. V. F. Bergaya, B. K. G. Theng & G. Lagaly(eds) 2006. Handbook of Clay Science. Developments in Clay Science Series Volume 1. xxi + 1224 pp. Amsterdam: Elsevier. Price £105, US \$165, Euros 150 (hard covers). ISBN 0 08 044183 1. *Geol. Mag.* **2008**, *145*, 444.
- (48) Schoonheydt, R. A.; Johnston, C. T.; Bergaya, F.; Theng, B. K. G.; Lagaly, G. *Handbook of Clay Science*; Elsevier: Amsterdam, 2006.
- (49) Sayed Hassan, M.; Villieras, F.; Gaboriaud, F.; Razafitianamaharavo, A. AFM and low-pressure argon adsorption analysis of geometrical properties of phyllosilicates. *J. Colloid Interface Sci.* **2006**, *296*, 614–623.
- (50) Brady, P. V.; Cygan, R. T.; Nagy, K. L. Molecular Controls on Kaolinite Surface Charge. *J. Colloid Interface Sci.* **1996**, *183*, 356–364.
- (51) Ma, C.; Eggleton, R. A. Cation exchange capacity of kaolinite. *Clays Clay Miner.* **1999**, *47*, 174–180.
- (52) Vasconcelos, I. F.; Bunker, B. A.; Cygan, R. T. Molecular Dynamics Modeling of Ion Adsorption to the Basal Surfaces of Kaolinite. *J. Phys. Chem. C* **2007**, *111*, 6753–6762.
- (53) Gupta, V.; Hampton, M. A.; Stokes, J. R.; Nguyen, A. V.; Miller, J. D. Particle interactions in kaolinite suspensions and corresponding aggregate structures. *J. Colloid Interface Sci.* **2011**, *359*, 95–103.
- (54) Ma, X.; Bruckard, W. J.; Holmes, R. Effect of collector, pH and ionic strength on the cationic flotation of kaolinite. *Int. J. Miner. Process.* **2009**, *93*, 54–58.
- (55) Yavuz, Ö.; Altunkaynak, Y.; Güzel, F. Removal of copper, nickel, cobalt and manganese from aqueous solution by kaolinite. *Water Res.* **2003**, *37*, 948–952.
- (56) Tournassat, C.; Steefel, C. I. Ionic Transport in Nano-Porous Clays with Consideration of Electrostatic Effects. *Rev. Mineral. Geochem.* **2015**, *80*, 287–329.
- (57) Nadeau, P. The physical dimensions of fundamental clay particles. *Clay Miner. Clay Miner.* **1985**, *20*, 499.
- (58) Pivovarov, S. Physico-chemical modeling of heavy metals (Cd, Zn, Cu) in natural environment. *Encycl. Surf. Colloid Sci.* **2004**, 468–93.
- (59) Lagaly, G.; Ogawa, M.; Dékány, I. Clay Mineral Organic Interactions. In *Developments in Clay Science*; Bergaya, F., Theng, B. K. G., Lagaly, G., Eds.; Elsevier, 2006; Chapter 7.3; Vol. 1, pp 309–377.
- (60) Zhang, L.; Lu, X.; Yang, K.; Zhou, H. Surface Wettability of Basal Surfaces of Clay Minerals: Insights from Molecular Dynamics Simulation. *Energy Fuels* **2016**, *30*, 149–160.
- (61) Wick, S.; Baeyens, B.; Marques Fernandes, M.; Voegelin, A. Thallium Adsorption onto Illite. *Environ. Sci. Technol.* **2018**, *52*, 571–580.
- (62) Knappett, J. *Craig's Soil Mechanics*; Spon Press: London, UK, 2012; Vol. 8.
- (63) Bradbury, M. H.; Baeyens, B. Sorption modelling on illite. Part II: Actinide sorption and linear free energy relationships. *Geochim. Cosmochim. Acta* **2009**, *73*, 1004–1013.
- (64) Srivastava, P.; Singh, B.; Angove, M. Competitive adsorption behavior of heavy metals on kaolinite. *J. Colloid Interface Sci.* **2005**, *290*, 28–38.
- (65) Argent, J.; Torkzaban, S.; Hubbard, S.; Le, H.; Amirianshoja, T.; Haghighi, M. Visualization of Micro-Particle Retention on a Heterogeneous Surface Using Micro-models: Influence of Nanoscale Surface Roughness. *Transp. Porous Med.* **2015**, 239.
- (66) Olin, M.; Puhakka, E.; Lehtikoinen, J.; Puukko, E.; Hakanen, M.; Lindberg, A. *Characterisation of Kaolinite and Adsorption of Europium on Kaolinite*; Posiva Oy, 2007.

Chapter 6: Conclusion and Future Work

6.1 Conclusion

This thesis has presented an experimental and simulation study that investigated the mechanism underlying the improved recovery from LS brine. Because microfluidics can provide real time, pore-scale evidence of LSE and its controlling mechanism, glass micromodels were developed to understand the dynamics of displacement under LSW injection.

A method was applied to functionalise glass microfluidic devices depositing clay minerals into the micromodels. The functionalised micromodels provided an implement for pore-scale, real-time visualization of fluid/solid interactions with representative pore-geometry and realistic surface interactions between the reservoir fluids and the formation rock. Wettability status was set to both water-wet and oil-wet. In water-wet systems, regardless of the clay presence, the displacement was dominated by capillary forces when HS brine was injected. After switching to LS brine, snap-off was not dominant in the whole system and there was a transition from snap-off to piston-like displacement in much of the volume of each pore and the amount of trapped oil was decreased by almost 10%.

In oil-wet conditions, during HSW injection, in most parts of the medium, the oil phase stuck to the surface and did not flow which resulted in poor oil recovery efficiency. However, throughout LSW injection, a mixed-wet system was visualized. For oil-wet surfaces, advancement of the stable waterfront left behind an oil film near the oil-wet pore walls while for water-wet surfaces, the interface moves toward the grain surfaces and replaces the oil film. LSE was resulted in 15% improved recovery in oil-wet porous medium.

Throughout LSW injection in all microfluidic experiments, fines migration was insignificant, particularly after the long-term aging period with oil. In another set of experiments, when the systems were flushed with LS brine without any delay, fines migration was significant. These observations suggest that the aging time and crude oil composition are contributing factors to fines release.

Wettability alteration and decrease in snap-off were both discussed in terms of the expansion of electrical double layers. This study provides direct pore-scale visualisation evidence of LSE under various conditions such as imbibition and drainage-dominated displacement in presence and absence of clay minerals. The outcome of this study can help significantly to explain the mechanism behind the LSE at the fundamental level.

Also analysed was the impact of type of clay mineral and nature of cations on LSE, using geochemical modelling complemented with visualisation experiments. The models were developed to provide the charge density and electrostatic potential profiles at the brine/mineral interface of illite as a basal-charged clay against an edge-charge dominated kaolinite. Based on the observations and simulation results, I concluded that since kaolinite as an edge-charge dominated clay has higher density of acid/base reaction sites on its surface (edges) than does illite, the charge development under differing ionic strength and pH was significant. As a result, kaolinite responded well to LSW injection, whereas illite did not. This could elucidate the unlike sensitivities of clays to LSW, such as their extent of being prone to wettability alteration. The experimental results and automated contact angle measurement also confirmed the wettability alteration under LSW injection only in kaolinite.

Understanding of the clay surface behaviour and its controlling factors like ionic strength and composition would contribute significantly to the EOR method design and reservoir selection for LSW treatment. If the chemical composition of connate water and the content of clay minerals in the reservoir is known to some extent, the findings of this study would assist in determining the optimised concentration for ions and pH of the injecting water in order to maximise LSE.

6.2 Future works:

6.2.1 3D micromodels

Although, this study employed geo-material glass micromodels, greater understanding of LSE might be obtained from 3D micromodels coupled with advanced optical measurement. 3D micromodels and conducting microfluidic experiments in an environment consistent with the condition encountered in reservoirs, the temperature to be specific. Temperature has been shown to significantly affect the oil/brine/mineral interactions at the pore-scale multiphase flow in porous media.

In addition, 3D micromodels can be implemented through dynamic imaging with high temporal resolution, enabling the visualisation of mechanisms that can be seen only in 3D, such as trapping. Advanced microscopic equipment could directly observe and analyse the chemical interaction between brine/oil and brine/mineral interfaces. Cryogenic x-ray photoelectron spectroscopy could be used to observe the composition in the interfacial regions, for instance. 3D micromodels using laser-etched rocks coupled with dynamic micro CT-scan imaging would

best reflect the actual pore-scale environment, heterogeneities in wettability, and chemical interactions.

Moreover, geo-material PDMS microfluidic devices, whose fabrication was summarised in the second chapter, is a proper alternative to glass micromodels. They could be implemented to observe the impact of LS brine in carbonates. Microfluidics has seldom been used to elucidate the impact of LSW on carbonates, which presents another opportunity.

6.2.2 Measuring the thin brine film

This thesis focused on expansion of the double layer as a possible mechanism behind LSE. More water film thickness measurements are required to better understand how this mechanism is affected by ionic strength, brine composition, pH, and temperature. Brine film thickness measurements are analogous to zeta potential measurements, which are relatively common in the literature. In the context of LSW flooding, only one study has obtained brine thickness measurements on sandstone¹⁰³ by means of physical chemistry techniques such as Small Angle Scattering using neutrons and x-rays. These techniques are capable of measuring the thickness of any water layer at the mineral surface down to the Angstrom. According to the literature, brine film measurement has yet to be conducted on carbonates.

Beside wettability alteration, other mechanisms could contribute to the improved recovery from LS brine injection. One promising topic is the enhanced viscoelasticity of the oil/brine interfaces, as it was found in the current study to be associated with improved recovery. More research is required to confirm the impact of LSW on the elasticity of the brine/oil in addition to analysing the significance of its contribution to LSE.

6.2.3 Pore-scale modelling of low salinity water injection

Modelling of LSE at the pore-scale is classified as reactive transport modelling in porous media in which the geochemical reactions taking place at the water/mineral interface can influence wettability. Therefore, a model to simulate reactive transport during LSW injection should include a numerical model to account for dynamic wettability alteration induced by surface complexations. One of the major advantages of SCM is that it considers the charges on both the adsorbing ion and the solid adsorbent surface.¹⁰⁴ Hence, SCM can provide the link between water composition and change of surface potential.

There seems to be no established modelling approach to link SCMs with wettability alteration. Recently, Maes and Geiger¹⁰⁵ developed a numerical model that includes two-phase flow, solute reactive transport, and dynamic wettability change induced by surface complexations.

However, the link between wettability alteration and surface charge distribution and its gradual change was portrayed using a linear model resulting from a simple fitting of data from one study. Hence, for modelling LSE, wettability alteration to be specific, a scientific approach is required to mathematically link the wettability variation with the change in the surface potential.

6.2.4 Molecular simulation of low salinity water injection

Molecular simulation provides valuable information about the brine/oil/rock interactions, such as film thickness, charge density, and electrostatic potential profile at the interface as well as the disjoining pressure in the film. In addition, experimental variables that are difficult to control in real laboratory settings tend to be easier to control in simulations. Dynamic molecular simulation has not been applied directly to thin brine film in LS brine injection, but it has been used to study the formation of thin brine film on the surface of gas hydrates¹⁰⁶. Dynamic molecular simulations can be complemented with thermodynamic models, which provide information about the oil/brine/rock interfaces at a more macroscopic level.

7 References

- 1 Amirian, T., Haghghi, M. & Mostaghimi, P. Pore Scale Visualization of Low Salinity Water Flooding as an Enhanced Oil Recovery Method. *Energy & Fuels* **31**, 13133-13143, doi:10.1021/acs.energyfuels.7b01702 (2017).
- 2 Sheng, J. *Enhanced oil recovery field case studies*. (Gulf Professional Publishing, 2013).
- 3 Kokal, S. & Al-Kaabi, A. Enhanced oil recovery: challenges & opportunities. *World Petroleum Council: Official Publication* **64** (2010).
- 4 Derkani, M. *et al.* Low Salinity Waterflooding in Carbonate Reservoirs: Review of Interfacial Mechanisms. *Colloids and Interfaces* **2**, 20 (2018).
- 5 Lake, L. W., Johns, R. T., Rossen, W. R. & Pope, G. A. Fundamentals of enhanced oil recovery. (2014).
- 6 Myint, P. C. & Firoozabadi, A. Thin liquid films in improved oil recovery from low-salinity brine. *Current Opinion in Colloid & Interface Science* **20**, 105-114, doi:<http://dx.doi.org/10.1016/j.cocis.2015.03.002> (2015).
- 7 Sheng, J. J. Critical review of low-salinity waterflooding. *Journal of Petroleum Science and Engineering* **120**, 216-224, doi:<http://dx.doi.org/10.1016/j.petrol.2014.05.026> (2014).
- 8 Batias, J., Hamon, G., Lalanne, B. & Romero, C. in *Paper SCA2009-01 presented at the 23rd international symposium of the society of core analysts, Noordwijk aan Zee, The Netherlands*. 27-30.
- 9 Lager, A., Webb, K. J., Black, C., Singleton, M. & Sorbie, K. S. Low salinity oil recovery-an experimental investigation1. *Petrophysics* **49** (2008).
- 10 McGuire, P., Chatham, J., Paskvan, F., Sommer, D. & Carini, F. in *SPE western regional meeting*. (Society of Petroleum Engineers).
- 11 Shaker Shiran, B. & Skauge, A. Enhanced Oil Recovery (EOR) by Combined Low Salinity Water/Polymer Flooding. *Energy & Fuels* **27**, 1223-1235, doi:10.1021/ef301538e (2013).
- 12 Morrow, N. & Buckley, J. Improved Oil Recovery by Low-Salinity Waterflooding. *Journal of Petroleum Technology* **63**, 106 - 112, doi:10.2118/129421-JPT (2011).
- 13 Tang, G. Q. & Morrow, N. R. Influence of brine composition and fines migration on crude oil/brine/rock interactions and oil recovery. *Journal of Petroleum Science and Engineering* **24**, 99-111, doi:[http://dx.doi.org/10.1016/S0920-4105\(99\)00034-0](http://dx.doi.org/10.1016/S0920-4105(99)00034-0) (1999).
- 14 Lager, A., Webb, K. J., Black, C. J. J., Singleton, M. & Sorbie, K. S. Low Salinity Oil Recovery - An Experimental Investigation1. *Petrophysics* **49**, 28-35 (2008).
- 15 Zhang, Y. & Morrow, N. R. in *SPE/DOE Symposium on Improved Oil Recovery* (Society of Petroleum Engineers, Tulsa, Oklahoma, USA, 2006).
- 16 Zhang, Y., Xie, X. & Morrow, N. R. in *SPE annual technical conference and exhibition*. (Society of Petroleum Engineers).
- 17 Valdya, R. & Fogler, H. Fines migration and formation damage: influence of pH and ion exchange. *SPE production engineering* **7**, 325-330 (1992).
- 18 Yildiz, H. O. & Morrow, N. R. Effect of brine composition on recovery of Moutray crude oil by waterflooding. *Journal of Petroleum Science and Engineering* **14**, 159-168, doi:[http://dx.doi.org/10.1016/0920-4105\(95\)00041-0](http://dx.doi.org/10.1016/0920-4105(95)00041-0) (1996).
- 19 McGuire, P. L., Chatham, J. R., Paskvan, F. K., Sommer, D. M. & Carini, F. H. in *SPE Western Regional Meeting* (Society of Petroleum Engineers, Irvine, California, 2005).
- 20 Zhang, Y. & Morrow, N. R. in *SPE/DOE symposium on improved oil recovery*. (Society of Petroleum Engineers).
- 21 Buckley, J. S. & Fan, T. Crude Oil/Brine Interfacial Tensions1. **48** (2007).
- 22 Austad, T., Rezaeidoust, A. & Puntervold, T. in *SPE Improved Oil Recovery Symposium* (Society of Petroleum Engineers, Tulsa, Oklahoma, USA, 2010).

- 23 Nasralla, R. A. & Nasr-El-Din, H. A. Double-Layer Expansion: Is It a Primary Mechanism of Improved Oil Recovery by Low-Salinity Waterflooding? *SPE Reservoir Evaluation & Engineering* **17**, 49 - 59, doi:10.2118/154334-PA (2014).
- 24 Nasralla, R. A., Bataweel, M. A. & Nasr-El-Din, H. A. in *Offshore Europe* (Society of Petroleum Engineers, Aberdeen, UK, 2011).
- 25 Yousef, A. A., Al-Saleh, S. H., Al-Kaabi, A. & Al-Jawfi, M. S. Laboratory Investigation of the Impact of Injection-Water Salinity and Ionic Content on Oil Recovery From Carbonate Reservoirs. *SPE Reservoir Evaluation & Engineering* **14**, 578-593, doi:10.2118/137634-PA (2011).
- 26 Vledder, P., Gonzalez, I. E., Carrera Fonseca, J. C., Wells, T. & Ligthelm, D. J. in *SPE Improved Oil Recovery Symposium* (Society of Petroleum Engineers, Tulsa, Oklahoma, USA, 2010).
- 27 Wang, X. *et al.* Cation Bridging Studied by Specular Neutron Reflection. *Langmuir* **29**, 5520-5527, doi:10.1021/la400767u (2013).
- 28 Ligthelm, D. J. *et al.* in *EUROPEC/EAGE conference and exhibition*. (Society of Petroleum Engineers).
- 29 Xie, Q., Liu, Y., Wu, J. & Liu, Q. Ions tuning water flooding experiments and interpretation by thermodynamics of wettability. *Journal of Petroleum Science and Engineering* **124**, 350-358, doi:<https://doi.org/10.1016/j.petrol.2014.07.015> (2014).
- 30 RezaeiDoust, A., Puntervold, T., Strand, S. & Austad, T. Smart Water as Wettability Modifier in Carbonate and Sandstone: A Discussion of Similarities/Differences in the Chemical Mechanisms. *Energy & Fuels* **23**, 4479-4485, doi:10.1021/ef900185q (2009).
- 31 Sandengen, K., Kristoffersen, A., Melhuus, K. & Jøsang, L. O. Osmosis as mechanism for low-salinity enhanced oil recovery. *SPE-169101-PA* **21**, 1,227-221,235 (2016).
- 32 Austad, T., Shariatpanahi, S. F., Strand, S., Black, C. J. J. & Webb, K. J. Conditions for a Low-Salinity Enhanced Oil Recovery (EOR) Effect in Carbonate Oil Reservoirs. *Energy & Fuels* **26**, 569-575, doi:10.1021/ef201435g (2012).
- 33 Al-Attar, H. H., Mahmoud, M. Y., Zekri, A. Y., Almehaideb, R. & Ghannam, M. Low-salinity flooding in a selected carbonate reservoir: Experimental approach. *J Petrol Explor Prod Technol* **3**, 139-149, doi:10.1007/s13202-013-0052-3 (2013).
- 34 Al-Shalabi, E. W., Sepehrnoori, K. & Pope, G. Geochemical interpretation of low-salinity-water injection in carbonate oil reservoirs. *SPE-169101-PA* **20**, 1,212-211,226 (2015).
- 35 Stevenson, J. T. M. & Gundlach, A. M. The application of photolithography to the fabrication of microcircuits. *Journal of Physics E: Scientific Instruments* **19**, 654 (1986).
- 36 Berkowski, K. L., Plunkett, K. N., Yu, Q. & Moore, J. S. Introduction to Photolithography: Preparation of Microscale Polymer Silhouettes. *Journal of Chemical Education* **82**, 1365, doi:10.1021/ed082p1365 (2005).
- 37 Franssila, S. Anisotropic Wet Etching. *Introduction to Microfabrication*, doi:doi:10.1002/9781119990413.ch2010.1002/9781119990413.ch20 (2010).
- 38 Madou, M. J. *Fundamentals of microfabrication: the science of miniaturization*. (CRC press, 2002).
- 39 Schwartz, G. & Schaible, P. Reactive ion etching of silicon. *Journal of Vacuum Science and Technology* **16**, 410-413 (1979).
- 40 Laerme, F., Schilp, A., Funk, K. & Offenber, M. in *Micro Electro Mechanical Systems, 1999. MEMS'99. Twelfth IEEE International Conference on*. 211-216 (IEEE).
- 41 Wu, B., Kumar, A. & Pamarthy, S. High aspect ratio silicon etch: A review. *Journal of applied physics* **108**, 9 (2010).
- 42 Schmidt, M. A. Wafer-to-wafer bonding for microstructure formation. *Proceedings of the IEEE* **86**, 1575-1585 (1998).
- 43 Tsao, C.-W. & DeVoe, D. L. Bonding of thermoplastic polymer microfluidics. *Microfluidics and Nanofluidics* **6**, 1-16 (2009).

- 44 Iliescu, C., Taylor, H., Avram, M., Miao, J. & Franssila, S. A practical guide for the fabrication of microfluidic devices using glass and silicon. *Biomicrofluidics* **6**, 016505-016505-016516, doi:10.1063/1.3689939 (2012).
- 45 Lu, C., Lee, L. J. & Juang, Y. J. Packaging of microfluidic chips via interstitial bonding technique. *Electrophoresis* **29**, 1407-1414 (2008).
- 46 Silverio, V. & de Freitas, S. C. in *Complex Fluid-Flows in Microfluidics* 25-51 (Springer, 2018).
- 47 Anbari, A. *et al.* Microfluidic Model Porous Media: Fabrication and Applications. *Small* **0**, 1703575, doi:doi:10.1002/smll.201703575 (2018).
- 48 Gerami, A. *et al.* Microfluidics for Porous Systems: Fabrication, Microscopy and Applications. *Transp Porous Med*, doi:10.1007/s11242-018-1202-3 (2018).
- 49 Zarikos, I. M., Hassanizadeh, S. M., van Oosterhout, L. M. & van Oordt, W. Manufacturing a Micro-model with Integrated Fibre Optic Pressure Sensors. *Transport in Porous Media*, doi:10.1007/s11242-018-1000-y (2018).
- 50 Karadimitriou, N. K. *et al.* On the fabrication of PDMS micromodels by rapid prototyping, and their use in two-phase flow studies. *Water Resources Research* **49**, 2056-2067, doi:10.1002/wrcr.20196 (2013).
- 51 Gerami, A. *et al.* Microscale insights into gas recovery from bright and dull bands in coal. *Journal of Petroleum Science and Engineering*, doi:<https://doi.org/10.1016/j.petrol.2018.08.072> (2018).
- 52 Porter, M. L. *et al.* Geo-material microfluidics at reservoir conditions for subsurface energy resource applications. *Lab on a Chip* **15**, 4044-4053, doi:10.1039/C5LC00704F (2015).
- 53 Song, W., de Haas, T. W., Fadaei, H. & Sinton, D. Chip-off-the-old-rock: the study of reservoir-relevant geological processes with real-rock micromodels. *Lab on a Chip* **14**, 4382-4390 (2014).
- 54 Gerami, A. *et al.* Coal-On-a-Chip: visualizing flow in coal fractures. *Energy & Fuels* **31**, 10393-10403 (2017).
- 55 Wang, W., Chang, S. & Gizzatov, A. Toward Reservoir-on-a-Chip: Fabricating Reservoir Micromodels by in Situ Growing Calcium Carbonate Nanocrystals in Microfluidic Channels. *ACS Applied Materials & Interfaces* **9**, 29380-29386, doi:10.1021/acsami.7b10746 (2017).
- 56 Song, W. & Kavscek, A. R. Functionalization of micromodels with kaolinite for investigation of low salinity oil-recovery processes. *Lab on a Chip* **15**, 3314-3325, doi:10.1039/C5LC00544B (2015).
- 57 Singh, R. *et al.* Real rock-microfluidic flow cell: A test bed for real-time in situ analysis of flow, transport, and reaction in a subsurface reactive transport environment. *Journal of Contaminant Hydrology* **204**, 28-39, doi:<https://doi.org/10.1016/j.jconhyd.2017.08.001> (2017).
- 58 Zhang, Y., Sanati-Nezhad, A. & Hejazi, S. Geo-material surface modification of microchips using layer-by-layer (LbL) assembly for subsurface energy and environmental applications. *Lab on a Chip* **18**, 285-295 (2018).
- 59 Alzahid, Y. A. *et al.* Functionalisation of Polydimethylsiloxane (PDMS)- Microfluidic Devices coated with Rock Minerals. *Scientific Reports* **8**, 15518, doi:10.1038/s41598-018-33495-8 (2018).
- 60 Xu, W., Ok, J. T., Xiao, F., Neeves, K. B. & Yin, X. Effect of pore geometry and interfacial tension on water-oil displacement efficiency in oil-wet microfluidic porous media analogs. *Physics of Fluids* **26**, 093102, doi:10.1063/1.4894071 (2014).
- 61 Gunda, N. S., Bera, B., Karadimitriou, N. K., Mitra, S. K. & Hassanizadeh, S. M. Reservoir-on-a-chip (ROC): a new paradigm in reservoir engineering. *Lab on a Chip* **11**, 3785-3792, doi:10.1039/c1lc20556k (2011).
- 62 Rangel-German, E. & Kavscek, A. A micromodel investigation of two-phase matrix-fracture transfer mechanisms. *Water resources research* **42** (2006).
- 63 Karadimitriou, N. K. & Hassanizadeh, S. M. A Review of Micromodels and Their Use in Two-Phase Flow Studies. *Vadose Zone Journal* **11**, doi:10.2136/vzj2011.0072 (2012).

- 64 Armstrong, R. T. & Berg, S. Interfacial velocities and capillary pressure gradients during Haines jumps. *Physical Review E* **88**, 043010 (2013).
- 65 Chrimes, A. F., Khoshmanesh, K., Stoddart, P. R., Mitchell, A. & Kalantar-zadeh, K. Microfluidics and Raman microscopy: current applications and future challenges. *Chemical Society Reviews* **42**, 5880-5906, doi:10.1039/C3CS35515B (2013).
- 66 Yadali Jamaloei, B. & Kharrat, R. Analysis of Microscopic Displacement Mechanisms of Dilute Surfactant Flooding in Oil-wet and Water-wet Porous Media. *Transport in Porous Media* **81**, 1, doi:10.1007/s11242-009-9382-5 (2009).
- 67 Chapman, E. M., Yang, J., Crawshaw, J. P. & Boek, E. S. Pore Scale Models for Imbibition of CO₂ Analogue Fluids in Etched Micro-model junctions Using Micro-fluidic Experiments and Direct Flow Calculations. *Energy Procedia* **37**, 3680-3686, doi:<http://dx.doi.org/10.1016/j.egypro.2013.06.262> (2013).
- 68 Kazemifar, F., Blois, G., Kyritsis, D. C. & Christensen, K. T. Quantifying the flow dynamics of supercritical CO₂-water displacement in a 2D porous micromodel using fluorescent microscopy and microscopic PIV. *Advances in Water Resources* **95**, 352-368, doi:<https://doi.org/10.1016/j.advwatres.2015.05.011> (2016).
- 69 Albani, J. R. *Structure and dynamics of macromolecules: absorption and fluorescence studies*. (Elsevier, 2011).
- 70 Gerami, A., Mostaghimi, P., Armstrong, R. T., Zamani, A. & Warkiani, M. E. A microfluidic framework for studying relative permeability in coal. *International Journal of Coal Geology* **159**, 183-193 (2016).
- 71 Kazemifar, F., Blois, G., Kyritsis, D. C. & Christensen, K. T. A methodology for velocity field measurement in multiphase high-pressure flow of CO₂ and water in micromodels. *Water Resources Research* **51**, 3017-3029, doi:10.1002/2014WR016787 (2015).
- 72 He, K. *et al.* in *SPE Improved oil recovery symposium*. (Society of Petroleum Engineers).
- 73 Schneider, M. H. & Tabeling, P. Lab-on-chip methodology in the energy industry: wettability patterns and their impact on fluid displacement in oil reservoir models. *American Journal of Applied Sciences* **8**, 927 (2011).
- 74 Unsal, E., Broens, M. & Armstrong, R. T. Pore Scale Dynamics of Microemulsion Formation. *Langmuir* **32**, 7096-7108, doi:10.1021/acs.langmuir.6b00821 (2016).
- 75 Pei, H., Zhang, G., Ge, J., Jin, L. & Ma, C. Potential of alkaline flooding to enhance heavy oil recovery through water-in-oil emulsification. *Fuel* **104**, 284-293, doi:<https://doi.org/10.1016/j.fuel.2012.08.024> (2013).
- 76 Sedaghat, M., Mohammadzadeh, O., Kord, S. & Chatzis, I. Heavy oil recovery using ASP flooding: A pore-level experimental study in fractured five-spot micromodels. *The Canadian Journal of Chemical Engineering* **94**, 779-791, doi:10.1002/cjce.22445 (2016).
- 77 Nilsson, M. A. *et al.* Effect of fluid rheology on enhanced oil recovery in a microfluidic sandstone device. *Journal of Non-Newtonian Fluid Mechanics* **202**, 112-119, doi:<https://doi.org/10.1016/j.jnnfm.2013.09.011> (2013).
- 78 Li, S. An experimental Investigation of Enhanced Oil Recovery Mechanisms in Nanofluid Injection Process. (2016).
- 79 Ma, K., Lontas, R., Conn, C. A., Hirasaki, G. J. & Biswal, S. L. Visualization of improved sweep with foam in heterogeneous porous media using microfluidics. *Soft Matter* **8**, 10669-10675 (2012).
- 80 Conn, C. A., Ma, K., Hirasaki, G. J. & Biswal, S. L. Visualizing oil displacement with foam in a microfluidic device with permeability contrast. *Lab on a Chip* **14**, 3968-3977 (2014).
- 81 Mohammadzadeh, O. & Chatzis, I. Analysis of the heat losses associated with the SAGD visualization experiments. *Journal of Petroleum Exploration and Production Technology* **6**, 387-400 (2016).

- 82 Mohammadzadeh, O., Rezaei, N. & Chatzis, I. Pore-level investigation of heavy oil and Bitumen recovery using solvent- aided steam assisted gravity drainage (SA-SAGD) process. *Energy & Fuels* **24**, 6327-6345 (2010).
- 83 de Haas, T. W., Fadaei, H., Guerrero, U. & Sinton, D. Steam-on-a-chip for oil recovery: the role of alkaline additives in steam assisted gravity drainage. *Lab on a Chip* **13**, 3832-3839 (2013).
- 84 Syed, A. H. *et al.* A combined method for pore-scale optical and thermal characterization of SAGD. *Journal of Petroleum Science and Engineering* **146**, 866-873 (2016).
- 85 de Haas, T. W., Fadaei, H., Guerrero, U. & Sinton, D. Steam-on-a-chip for oil recovery: the role of alkaline additives in steam assisted gravity drainage. *Lab on a Chip* **13**, 3832-3839, doi:10.1039/c3lc50612f (2013).
- 86 Barnaji, M. J., Pourafshary, P. & Rasaie, M. R. Visual investigation of the effects of clay minerals on enhancement of oil recovery by low salinity water flooding. *Fuel* **184**, 826-835, doi:<http://dx.doi.org/10.1016/j.fuel.2016.07.076> (2016).
- 87 Berg, S., Cense, A. W., Jansen, E. & Bakker, K. Direct Experimental Evidence of Wettability Modification By Low Salinity. *Petrophysics* **51** (2010).
- 88 Lee, S. Y. *et al.* in *SPE Improved Oil Recovery Symposium* (Society of Petroleum Engineers, Tulsa, Oklahoma, USA, 2010).
- 89 Mahani, H., Berg, S., Ilic, D., Bartels, W.-B. & Joekar-Niasar, V. Kinetics of Low-Salinity-Flooding Effect. *SPE Journa* **20**, 8 - 20, doi:10.2118/165255-PA (2015).
- 90 Morin, B., Liu, Y., Alvarado, V. & Oakey, J. A microfluidic flow focusing platform to screen the evolution of crude oil-brine interfacial elasticity. *Lab on a Chip* **16**, 3074-3081, doi:10.1039/C6LC00287K (2016).
- 91 Bartels, W. B. *et al.* Fast X-Ray Micro-CT Study of the Impact of Brine Salinity on the Pore-Scale Fluid Distribution During Waterflooding. **58** (2017).
- 92 Bartels, W.-B. *et al.* Oil Configuration Under High-Salinity and Low-Salinity Conditions at Pore Scale: A Parametric Investigation by Use of a Single-Channel Micromodel. doi:10.2118/181386-PA (2017).
- 93 Emadi, A. & Sohrabi, M. (Society of Petroleum Engineers, 2013).
- 94 Fredriksen, S. B., Rognmo, A. U., Sandengen, K. & Fernø, M. A. Wettability Effects on Osmosis as an Oil-Mobilization Mechanism During Low-Salinity Waterflooding. **58** (2017).
- 95 Bartels, W.-B. *et al.* Oil Configuration Under High-Salinity and Low-Salinity Conditions at Pore Scale: A Parametric Investigation by Use of a Single-Channel Micromodel. *SPE-169101-PA* **22**, 1362-1373, doi:10.2118/181386-PA (2017).
- 96 Goldberg, S. in *Advances in agronomy* Vol. 47 233-329 (Elsevier, 1992).
- 97 Hayes, K. F., Redden, G., Ela, W. & Leckie, J. O. Surface complexation models: an evaluation of model parameter estimation using FITEQL and oxide mineral titration data. *Journal of colloid and interface science* **142**, 448-469 (1991).
- 98 Goldberg, S. Application of surface complexation models to anion adsorption by natural materials. *Environmental toxicology and chemistry* **33**, 2172-2180 (2014).
- 99 Lutzenkirchen, J. *Surface complexation modelling*. Vol. 11 (Elsevier, 2006).
- 100 Huang, C.-P. & Stumm, W. Specific adsorption of cations on hydrous γ -Al₂O₃. *Journal of Colloid and Interface Science* **43**, 409-420, doi:[https://doi.org/10.1016/0021-9797\(73\)90387-1](https://doi.org/10.1016/0021-9797(73)90387-1) (1973).
- 101 Dzombak, D. A. *Surface complexation modeling: hydrous ferric oxide*. (John Wiley & Sons, 1990).
- 102 Suijkerbuijk, B. *et al.* in *SPE Improved Oil Recovery Symposium* (Society of Petroleum Engineers, Tulsa, Oklahoma, USA, 2012).
- 103 Lee, S. Y. *et al.* in *SPE Improved Oil Recovery Symposium*. (Society of Petroleum Engineers).
- 104 Goldberg, S. in *Reference Module in Earth Systems and Environmental Sciences* (Elsevier, 2013).

- 105 Maes, J. & Geiger, S. Direct pore-scale reactive transport modelling of dynamic wettability changes induced by surface complexation. *Advances in Water Resources* **111**, 6-19, doi:<https://doi.org/10.1016/j.advwatres.2017.10.032> (2018).
- 106 Jiménez-Ángeles, F. & Firoozabadi, A. Induced Charge Density and Thin Liquid Film at Hydrate/Methane Gas Interfaces. *The Journal of Physical Chemistry C* **118**, 26041-26048, doi:10.1021/jp507160s (2014).

Appendices

Statement of Authorship

Title of Paper	Microfluidics for porous systems: fabrication, microscopy and applications
Publication Status	<input checked="" type="checkbox"/> Published <input type="checkbox"/> Accepted for Publication <input type="checkbox"/> Submitted for Publication <input type="checkbox"/> Unpublished and Unsubmitted work written in manuscript style
Publication Details	Gerami, Alireza, Yara Alzahid, Peyman Mostaghimi, Navid Kashaninejad, Farzan Kazemifar, Tammy Amirian, Nader Mosavat, Majid Ebrahimi Warkiani, and Ryan T. Armstrong. "Microfluidics for porous systems: fabrication, microscopy and applications." <i>Transport in Porous Media</i> (2018): 1-28.

Co-Author

Name of Co-Author (Candidate)	Tammy Amirian		
Contribution to the Paper	Wrote the parts that are directly related to the subject of the PhD research like microfluidics applications in EOR research and LSE. Helped to evaluate and edit the manuscript.		
Overall percentage (%)	10%		
Signature		Date	27/03/19

Co-Author Contributions

By signing the Statement of Authorship, each author certifies that:

- the candidate's stated contribution to the publication is accurate (as detailed above);
- permission is granted for the candidate to include the publication in the thesis; and
- The sum of all co-author contributions is equal to 100% less the candidate's stated contribution.

Name of Co-Author	Alireza Gerami		
Contribution to the Paper	First Author of the paper. Wrote the petroleum engineering applications of microfluidics and organized with co-authors to put together the whole review paper. Edited the manuscript and replied to reviewers.		
Signature		Date	27/03/19

Name of Co-Author	Yara Alzahid		
Contribution to the Paper	Co-first author. Wrote the introduction, fundamentals of fabrication and geomaterial microfluidics. Helped with gathering parts from other co-authors. Edited the manuscript and replied to reviewers.		
Signature		Date	1/4/2019

Name of Co-Author	Peyman Mostaghimi		
Contribution to the Paper	Provided very helpful insights to enhance the overall structure of the review paper. Critically evaluated and edited the manuscript.		
Signature		Date	27/3/19

Name of Co-Author	Navid Kashaninejad		
Contribution to the Paper	Wrote the application of microfluidics in heavy oil research.		
Signature		Date	

Name of Co-Author	Farzan Kazemifar		
Contribution to the Paper	Wrote the application of microfluidics in CO ₂ sequestration. Helped to edit the manuscript.		
Signature		Date	

Name of Co-Author	Nader Mosavat		
Contribution to the Paper	Wrote the application of microfluidics in biomedical research.		
Signature		Date	

Name of Co-Author	Majid Ebrahimi Warkiani		
Contribution to the Paper	Wrote the application of microfluidics in biomedical research. Helped in writing the abstract.		
Signature		Date	27/03/19

Name of Co-Author	Ryan T. Armstrong	
Contribution to the Paper	Edited the paper and replied to reviewers' comments.	
Signature	Date	27-3-19

Statement of Authorship

Title of Paper	Microfluidics for porous systems: fabrication, microscopy and applications Publication
Publication Status	<input checked="" type="checkbox"/> Published <input type="checkbox"/> Accepted for Publication <input type="checkbox"/> Submitted for Publication <input type="checkbox"/> Unpublished and Unsubmitted work written in manuscript style
Publication Details	Gerami, Alireza, Yara Alzahid, Peyman Mostaghimi, Navid Kashaninejad, Farzan Kazemifar, Tammy Amirian, Nader Mosavat, Majid Ebrahimi Warkiani, and Ryan T. Armstrong. "Microfluidics for porous systems: fabrication, microscopy and applications." Transport in Porous Media (2018): 1-28.

Principal Author

Name of Co-author (Candidate)	Tammy Amirian		
Contribution to the Paper	Wrote the parts that are directly related to the subject of the PhD research like microfluidics applications in EOR research and LSE. Helped to evaluate and edit the manuscript.		
Overall percentage (%)	10%		
Certification:	This paper reports on original research I conducted during the period of my Higher Degree by Research candidature and is not subject to any obligations or contractual agreements with a third party that would constrain its inclusion in this thesis. I am the primary author of this paper.		
Signature		Date	

Co-Author Contributions

By signing the Statement of Authorship, each author certifies that:

- i. the candidate's stated contribution to the publication is accurate (as detailed above);
- ii. permission is granted for the candidate to include the publication in the thesis; and
- iii. the sum of all co-author contributions is equal to 100% less the candidate's stated contribution.

Name of Co-Author	Alireza Gerami		
Contribution to the Paper	First Author of the paper. Wrote the petroleum engineering applications of microfluidics and organized with co-authors to put together the whole review paper. Edited the manuscript and replied to reviewers.		
Signature		Date	

Name of Co-Author	Yara Alzahid		
Contribution to the Paper	Co-first author. Wrote the introduction, fundamentals of fabrication and geomaterial microfluidics. Helped with gathering parts from other co-authors. Edited the manuscript and replied to reviewers.		

Signature		Date	
-----------	--	------	--

Please cut and paste additional co-author panels here as required.

Name of Co-Author	Peyman Mostaghimi		
Contribution to the Paper	Provided very helpful insights to enhance the overall structure of the review paper. Critically evaluated and edited the manuscript.		
Signature		Date	

Name of Co-Author	Navid Kashaninejad		
Contribution to the Paper	Wrote the application of microfluidics in biomedical research (Section 2.3 & Section 4.3).		
Signature		Date	10 July 2019

Name of Co-Author	Farzan Kazemifar		
Contribution to the Paper	Wrote the application of microfluidics in CO2 sequestration. Helped to edit the manuscript.		
Signature		Date	03/28/2019

Name of Co-Author	Nader Mosavat		
Contribution to the Paper	Wrote the application of microfluidics in heavy oil research.		
Signature		Date	9-07-2019

Name of Co-Author	Majid Ebrahimi Warkiani		
Contribution to the Paper	Wrote the application of microfluidics in biomedical research.		
Signature		Date	

Name of Co-Author	Ryan T. Armstrong		
Contribution to the Paper	Edited the paper and replied to reviewers' comments.		
Signature		Date	



Microfluidics for Porous Systems: Fabrication, Microscopy and Applications

Alireza Gerami¹ · Yara Alzahid¹ · Peyman Mostaghimi¹ · Navid Kashaninejad² · Farzan Kazemifar³ · Tammy Amirian⁴ · Nader Mosavat⁵ · Majid Ebrahimi Warkiani^{2,6} · Ryan T. Armstrong¹

Received: 29 May 2018 / Accepted: 15 November 2018
© Springer Nature B.V. 2018

Abstract

No matter how sophisticated the structures are and on what length scale the pore sizes are, fluid displacement in porous media can be visualized, captured, mimicked and optimized using microfluidics. Visualizing transport processes is fundamental to our understanding of complex hydrogeological systems, petroleum production, medical science applications and other engineering applications. Microfluidics is an ideal tool for visual observation of flow at high temporal and spatial resolution. Experiments are typically fast, as sample volume is substantially low with the use of miniaturized devices. This review first discusses the fabrication techniques for generating microfluidics devices, experimental setups and new advances in microfluidic fabrication using three-dimensional printing, geomaterials and biomaterials. We then address multiphase transport in subsurface porous media, with an emphasis on hydrology and petroleum engineering applications in the past few decades. We also cover the application of microfluidics to study membrane systems in biomedical science and particle sorting. Lastly, we explore how synergies across different disciplines can lead to innovations in this field. A number of problems that have been resolved, topics that are under investigation and cutting-edge applications that are emerging are highlighted.

Keywords Microfluidics · Porous media · Flow visualization · On-a-chip applications · Lab-on-a-chip · Micromodels

Alireza Gerami and Yara Alzahid have contributed equally to this manuscript.

✉ Alireza Gerami
a.gerami@unsw.edu.au

¹ School of Minerals and Energy Resources Engineering, University of New South Wales, Sydney, Australia

² School of Biomedical Engineering, University Technology Sydney, Sydney, Australia

³ Department of Mechanical Engineering, California State University Sacramento, Sacramento, CA, USA

⁴ Australian School of Petroleum, University of Adelaide, Adelaide, Australia

⁵ Faculty of Engineering and Technology, Muscat University, Muscat, Oman

⁶ Institute of Molecular Medicine, Sechenov First Moscow State University, Moscow, Russia

1 Introduction

The flow and transport of phases and components through porous media is central to subsurface engineering applications, biological engineering technologies, energy-related research and many other disciplines. A complete understanding of the physiochemical mechanisms regarding flow and transport that occur at the length scale of micrometers is essential to the success of these technologies. In particular, the ability to manipulate fluids at the micrometer length scale is paramount. Microfluidics provides a platform to facilitate these efforts. Microfluidics deals with the study of fluids at the microscale (10^{-6} – 10^{-3} m) by utilizing miniaturized devices. It is primarily used to study the science of fluid flow and transport phenomena in microstructures. The concept of microfluidic devices originated from technologies developed by the field of micro-electromechanical systems (MEMS) (Atencia and Beebe 2005; Verpoorte and De Rooij 2003). There are vast applications of microfluidics, some of which include drug screening, biomedical analyses, genetics, proteomics and energy conversion (Kjeang et al. 2009; Sinton 2014). Advantages of microfluidics include: small sample and reagent volumes, high-resolution analysis and small footprint for analytical devices (Davies et al. 2015; Trietsch et al. 2011; Whitesides 2006a). Interest in microfluidics is dated since the late 1950s, and in the last 30 years, the numbers of publications on microfluidics have rapidly increased, reaching a total of approximately 6650 journal articles since 1991 (obtained from a refined search in Google Scholar). Nowadays, advanced fabrication methods, experimental setups and applications are continuously evolving and will continue into the unforeseeable future.

This review highlights microfluidic fabrication techniques and focuses on recent advances, such as geospatial and membrane-based microfluidics. We also cover common visualization methods and experimental setups and emphasize different microscopic techniques that are currently available. We then discuss recent innovations relevant to porous media research across different disciplines, such as petroleum engineering and environmental engineering with a focus on hydrocarbon recovery and CO₂ sequestration, and biomedical engineering in regard to cell sorting and tissue engineering. The study of microfluidics is a vast field with over 6650 journal articles since 1991. Thus, it is neither possible nor instructive to cover all of these great works. As such, we provide a more detailed review of applications from a range of different disciplines to highlight the utility of microfluidics for porous media research. This review is intended for researchers and scientists who are new to the field of microfluidics. It introduces existing fabrication and visualization options and then illustrates examples of specific applications.

2 Fabrication Techniques

Silicon has been the primary material used for fabricating microfluidics devices with well-established processing and fabrication methods for various applications. Other materials have been used to circumvent the drawbacks from using silicon, such as the high cost and opaque nature (Gravesen et al. 1993; Haeberle and Zengerle 2007; Kim et al. 2008b; McDonald et al. 2000; Whitesides 2006b). These materials include glass and polymeric materials, such as polymethylmethacrylate (PMMA), polystyrene (PS), polycarbonate (PC) and, the most commonly used material, polydimethylsiloxane (PDMS), due to its flexibility in molding, optical transparency and biocompatibility (Lei 2015). Depending on the material being used, one of two primary methods is used to generate a microfluidics device: photolithography or

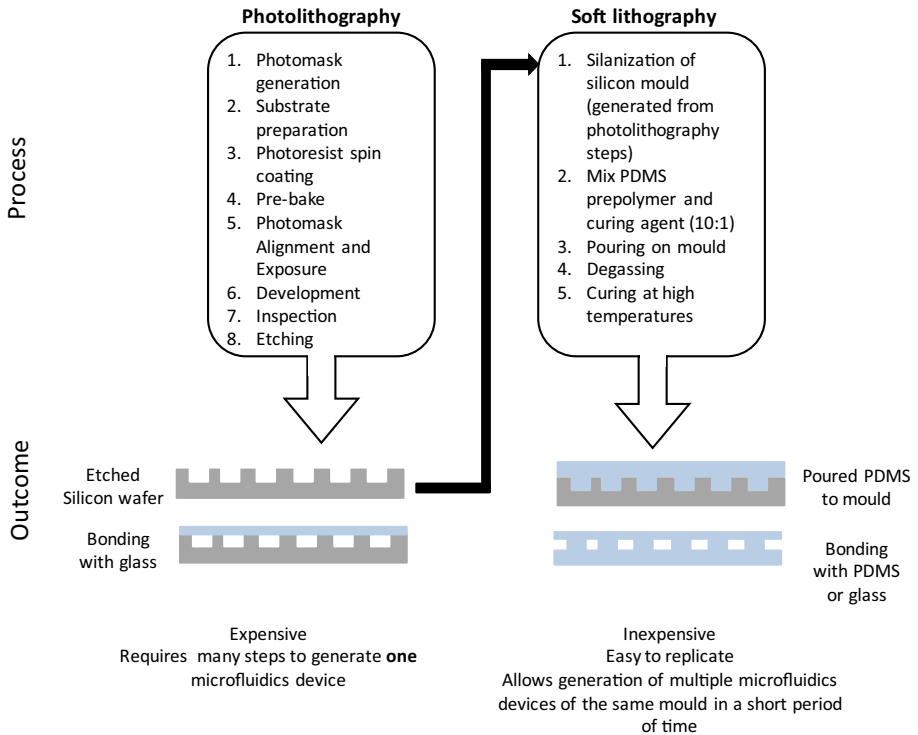


Fig. 1 Comparison of photolithography and soft lithography techniques. Photolithography undergoes many steps in order to create one microfluidics device, whereas soft lithography uses a master mold created by photolithographic methods

soft lithology, as summarized in Fig. 1. With photolithography, the microfluidic pattern is etched into a solid substrate, typically, silicon-based devices, while for soft lithology, which is used for PDMS devices, a negative mold is created in which a liquid agent is poured and then cured.

2.1 Silicon-, Glass- and Polymer-Based Microfluidics

Microfabrication using silicon as the substrate includes the following processes: photolithography, thin-film deposition, etching and bonding. Photolithography results in the transfer of a pattern from a photomask to a silicon wafer, or substrate, that is initially coated with a light-sensitive material called photoresist. This process is performed by employing ultra-violet (UV) light, the details of which are provided in Berkowski et al. (2005); Stevenson and Gundlach (1986). In order to achieve nanometer features on the photoresist, electron beam lithography (EBL) can be used (Chen 2015). Thin-film deposition refers to a process of adding thin films, such as silicon dioxide, polysilicon, silicon nitride and metal onto the surface of a silicon wafer. Physical vapor deposition (PVD) and chemical vapor deposition (CVD) are two techniques used for thin-film deposition; however, PVD is most commonly used. PVD uses a condensable vapor of the desired material to deposit a thin film onto a substrate through a vacuum or low-pressure gaseous environment. Etching of the substrate can

be performed with wet etching (using chemical solutions) and dry etching (plasma) methods. Choosing which type of etching to use for a microfabrication process depends highly on the structures being etched, type of silicon wafer used and the aspect ratio of the channels that are to be etched. In wet etching, isotropic and anisotropic etching can be achieved, which refers to equal or unequal etching rate in all directions, respectively (Franssila 2010; Madou 2002). As for dry etching methods, it includes reactive ion etching (RIE) and deep reactive ion etching (DRIE). The detailed mechanism of etching can be found in Laerme et al. (1999), Schwartz and Schaible (1979) and Wu et al. (2010). Lastly, to create an enclosed microfluidic device, the substrate is bounded to a cover. The type of bonding technique employed depends on the material being bonded to silicon. For instance, silicon-to-silicon bonding can be achieved via fusion bonding; however, silicon-to-glass bonding can be achieved via anodic bonding techniques (Iliescu et al. 2012; Lu et al. 2008; Schmidt 1998; Tsao and DeVoe 2009).

Glass is another material that can be used in combination with silicon, or as an alternative material, which can allow for direct visualization to the fluids in the microfluidics device. The most common glass used is borosilicate glass (Albaugh 1991; Lei 2015). Borosilicate glass has a similar thermal expansion coefficient to that of silicon, resulting in low residual stress after bonding. Also, the chemical composition of borosilicate glass helps the bonding process (Albaugh 1991). Similar to silicon, glass goes through photolithographic steps and can be patterned by wet or dry etching techniques or laser ablation. Glass can bond to silicon through anodic bonding, PDMS through plasma treatment or itself by thermal bonding (Silverio and de Freitas 2018).

For polymer-based microfluidic devices, soft lithography is commonly used, which is based on replica molding for micro- and nanofabrication (Kalkandjiev et al. 2010; Karadimitriou and Hassanizadeh 2012; Kim et al. 2008b; Stephan et al. 2007). Photolithography is first used to generate the so-called master mold, typically on a silicon wafer. This is a negative image of the desired pattern to be created. The master silicon wafer is then silanized, typically using trichlorosilane (HSiCl_3) to create a hydrophobic surface on the master mold for successful PDMS coating. PDMS is then prepared by mixing PDMS monomer and curing agent. By pouring the PDMS mixture into the master mold, followed by degassing in a vacuum chamber, and curing, the channel structures are fabricated. The pattern is then peeled from the master mold and sealed to a substrate, typically glass or PDMS, by various methods, such as plasma treatment (Brian and Ellis 2016; Friend and Yeo 2010; Jahanshahi et al. 2013; Li et al. 2013; Nan et al. 2015; Shiu et al. 2008; Tan et al. 2010; Wong and Ho 2009; Yaozhong et al. 2014). Other bonding methods are discussed in Karadimitriou et al. (2013). The main advantage of using soft lithography is rapid prototyping and requires less equipment, which translates into less expense associated with this type of lithography (Anbari et al. 2018). Although creating the master silicon mold can be expensive, creating several PDMS devices from that master mold makes this option cost-efficient. Hence, PDMS-based microfluidic devices are continuously utilized, customized and developed. For instance, Zarikos et al. (2018) integrated fiber optic pressure sensors into a PDMS micromodel to measure pore pressure under specific transient two-phase flow conditions, Karadimitriou et al. (2013) developed a procedure for making uniformly and stably hydrophobic PDMS micromodels, and Gerami et al. (2018) fabricated a dual-wettability PDMS device for studying flow in regions with different wettabilities. Similar to PDMS, PMMA is another transparent thermoplastic polymer (i.e., hardens at high temperatures) that is used for microfluidic purposes. PS and PC are also other thermoplastic polymers that have gained interest in cell culture microfluidics, due to their hydrophilic nature and biocompatibility (Lei 2015). Hot embossing, microinjection molding (μIM) and micromilling are the most commonly used techniques to create microstructures from PS or PC (Giboz et al. 2007; Guckenberger et al. 2015).

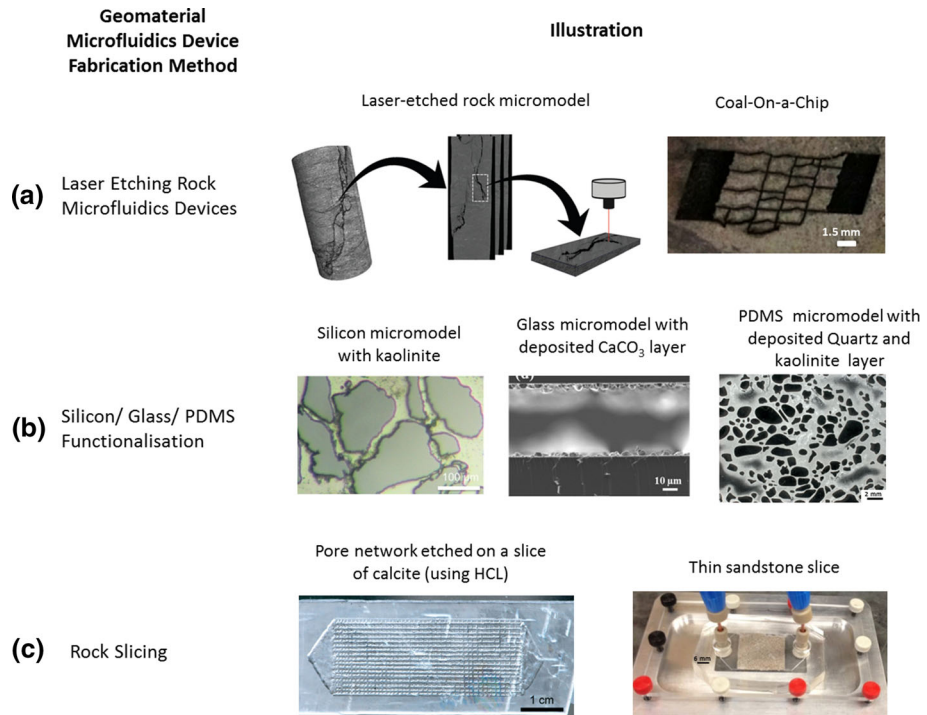


Fig. 2 Overview of geomaterial microfluidics device fabrication methods. **a** Laser etching on real rock surfaces. Reproduced with permission from Gerami et al. (2017) and Porter et al. (2015a). **b** Silicon/glass/PDMS functionalization by attaching relevant rock minerals. Reproduced with permission from Song and Kovscek (2015) and Wang et al. (2017). **c** Rock slicing. Reproduced with permission from Song et al. (2014) and Singh et al. (2017). Images are representatives of each technique

2.2 Geomaterial Microfluidics

Fabrication of geomaterial microfluidics has received attention in the fields of hydrology and petroleum engineering, in which pore-scale flow and/or transport is often dictated by surface chemistry (Bowden et al. 2016; Gerami et al. 2017; Mahoney et al. 2015, 2017; Morais et al. 2016; Oh et al. 2017; Porter et al. 2015b; Song et al. 2014; Tanino et al. 2018; Wang et al. 2017; Zhang et al. 2018). In Fig. 2, we provide an overview of the different geomaterial microfluidics chips that have been reported in the literature.

A laser-etched rock substrate was first employed by Porter et al. (2015b) in microfluidic experiments to provide a tool for more realistic and comprehensive flow visualization. Geomaterial chips have the advantage of mimicking the chemical and physical properties of natural porous media. This is of importance, particularly for unconventional reservoirs, due to their heterogeneity, unique fracture system and specific mechanisms such as swelling and shrinkage, which affects flow and transport (Britt and Schoeffler 2009; Liu et al. 2017). Gerami et al. (2017) used an image of a coal fracture obtained from micro-computed tomography (micro-CT) for fabrication of a coal geomaterial microfluidic chip. The fracture pattern was imported to a CAD drawing, which was then etched on a flat coal surface using the laser machine microSTRUCT-C (3DMicromac, Chemnitz, Germany).

Song et al. (2014) developed a method to etch microchannels into calcite rock. This method includes firstly cutting a calcite crystal into 3-mm-thick wafers and secondly dipping the calcite wafer into molten beeswax heated to 150 °C and left to solidify. The desired microfluidics patterns were then etched via laser into the wax, and lastly, the wax and calcite were immersed in hydrochloric acid, resulting in the inscription of the microfluidics channels into the calcite crystal. This process allowed for the study of acid injection and dissolution in natural calcite rock, which can provide insights into pore-level geochemistry. Wang et al. (2017) used a simple glass micromodel, which was composed of a simple channel, and coated a layer of CaCO₃ nanocrystal. The purpose of their study is to create a realistic representation of carbonate rock. This was achieved by first functionalizing the inner wall of the microfluidic channel by adding a silane agent and then adding Ca²⁺ and CO₃²⁻ ions to attach to the multiple COO⁻ sites, resulting in a uniform thickness of CaCO₃ nanocrystal layer on the inner surface of the microfluidic silica channels. Scanning electron microscopy (SEM) imaging, energy-dispersive X-ray spectroscopy (EDS) and Raman spectroscopy were performed to visualize the presence of CaCO₃ nanocrystals.

Song and Kovscek (2015) developed a functionalized silicon microfluidic device coated with clay minerals, mimicking a sandstone pore surfaces. This approach allows pore-scale visualization of fluid–solid interactions in a sandstone pore geometry. The authors used this design to analyze the effect of low-salinity brine injection to the detachment of clay (Song and Kovscek 2016). Singh et al. (2017) designed a microfluidic platform called the real rock-microfluidic flow cell (RRMFC). This approach involves mounting a 500- μ m sandstone rock section between two PDMS covers. The authors investigated the mineralogy and geochemistry of the microfluidic platform using several microscopic approaches, such as transmitted, cathodoluminescence (CL) and confocal laser microscopy.

Other than glass functionalization, work has been done to functionalize PDMS microfluidics devices (Alzahid et al. 2018; Zhang et al. 2018). Zhang et al. (2018) introduce the concept of layer-by-layer (LbL) coating of PDMS microfluidics devices. Their LbL process requires subjecting PDMS to plasma, followed by injection of poly(diallyldimethylammonium chloride) (PDDA) solution and clay suspension alternately. DI water is injected between the two steps (PDDA and clay suspension injection) to remove any loose particles, in addition to drying the microfluidic device in each step. This cycle is repeated 2–3 times to get the desired minerals thickness. Alzahid et al. (2018) developed another approach to functionalizing PDMS and used two different rock minerals to obtain sandstone and carbonate microfluidic devices. Their method involved plasma treating PDMS, followed by injection of minerals solution, and the PDMS containing the minerals was then dried, cleaned and subjected to another plasma treatment to bond it to the PDMS cover. Finally, polyvinyl alcohol (PVA) was injected immediately after the second plasma treatment to make the PDMS geomaterial microfluidic device water wet. As mentioned previously, these geomaterial approaches are novel tools to capture rock–fluid subsurface phenomena, such as snap-off, wettability and dissolution. Figure 3 shows a schematic illustration of the two PDMS functionalization methods.

2.3 Membrane-Based Microfluidics

For biomedical research, the attachment of cells to surfaces depends on two important factors: the chemistry and physical structure of the microfluidic device. For organ-on-a-chip devices, a semipermeable porous membrane is sandwiched between upper and lower channels. Epithelial cells (e.g., lung, liver) are cultured on the top side of the membrane, while

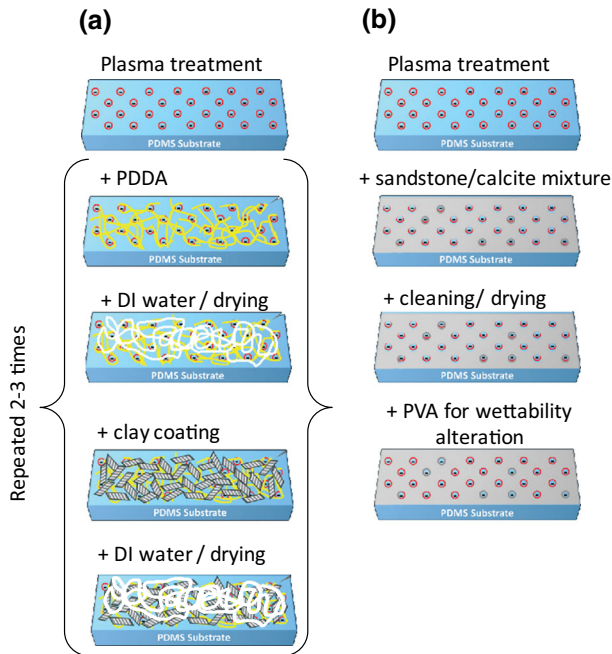


Fig. 3 Proposed methods of PDMS functionalization. **a** Explains the process of layer-by-layer, reproduced from Zhang et al. (2018). The yellow and white lines indicate PDPA and water, respectively. Clay is indicated as the irregular shapes in black dashed lines. Reproduced with permission from (Zhang et al. 2018). **b** Explains the functionalization method proposed by Alzahid et al. (2018). The gray color indicates the sandstone or the calcite mixture attached to the PDMS

endothelial cells (which represent blood capillaries) are cultured on the other side. The culture medium flows from the lower channel, and air passes through the epithelial cells from the upper channel. Accordingly, the nutrients and waste materials are exchanged using a porous membrane, and physicochemical signaling between tissues is facilitated in a shear-free co-culture environment. Figure 4 represents a typical microfluidic device for organ-on-a-chip.

To better recapitulate physicochemical properties and provide a microenvironment, similar to *in vivo* conditions, the incorporation of a micro-/nanoporous membrane in these organ-on-a-chip devices is essential. To become a suitable for organ-on-a-chip platform, the porous membrane needs to entail several characteristics. First, the membrane should be biocompatible and have properties similar to those of the native extracellular matrix (ECM). Second, the membrane should be thin enough to allow rapid mass transport and the size of the pores should be controlled systematically. Finally, the membrane should be mechanically robust and optically transparent for *in situ* or off-chip analysis. For a conventional migration assay, the commercially available polyester and polycarbonate membranes are widely used. For most organ-on-a-chip platforms, polymer membranes mainly fabricated from (PDMS) are utilized, which provides complete optical access, secure sealing and strong bonding. However, these synthetic PDMS membranes have several disadvantages. First, the fabrication for such membranes is relatively time-consuming and expensive. Second, since the surfaces of these PDMS membranes are totally flat, after cell seeding inside the microfluidic device, the cells grow in a two-dimensional (2D) monolayer structure. Although the cells are in a

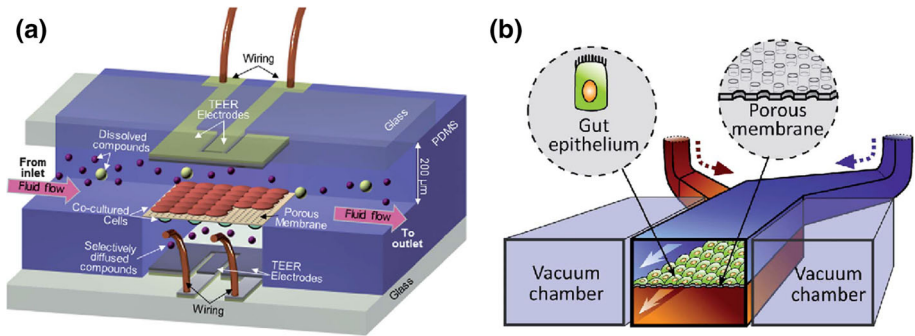


Fig. 4 Schematic representation of the application of membrane-based microfluidic devices in organ-on-a-chip platforms. **a** Various components of blood–brain barrier-on-a-chip with embedded electrodes trans-endothelial electrical resistance. Reproduced with permission from Booth and Kim (2012). **b** Gut-on-a-chip platform with porous PDMS membrane which allowed compartmentalization of the system coated with ECM and seeded by human gut epithelial cells. Reproduced with permission from Kim et al. (2012b). The PDMS membrane is irreversibly bound to the top PDMS microchannel using plasma treatment. To facilitate the bonding, the PDMS membrane and the microchannel are heated at 80 °C overnight. Before plasma bonding these components to the lower PDMS channel, some parts of the membrane are torn using forceps to generate the hollow structures acting as vacuum channels. The vacuum channels could mimic the movement of small intestine by applying the cyclic suction

dynamic and perfusion microbioreactor, 2D monolayer cell culture cannot indeed recapitulate *in vivo* cell signaling.

Considering the aforementioned limitations of polymer membranes, nanofibrous membrane fabricated using electrospinning (Ahmed et al. 2015) can be considered a better candidate for applications in cell culture and tissue engineering (Wang et al. 2013a; Moghadas et al. 2017a). This technique has been used to fabricate a cost-effective and robust scaffold for three-dimensional (3D) cell cultures (Moghadas et al. 2017a). As shown in Fig. 4a, b, by increasing the PDMS mass ratio during electrospinning, the porosity and hydrophobicity of the membrane can be controlled (Moghadas et al. 2017a). Seeded epithelial lung cancer cells were aggregated into 3D multicellular spheroids on such electrospun membranes (Moghadas et al. 2017a). The only limitation of using these nanofibrous electrospun membranes is their opacity. The non-transparent properties of the electrospun membrane make further analysis with bright-field microscopy difficult. Nanofilm-based membranes fabricated by various nanofabrication techniques, such as layer-by-layer assembly (Jiang and Tsukruk 2006), are also an attractive alternative for the microfluidic organ-on-a-chip application. Using a transparent and biocompatible polymer, poly(lactic acid) (PLLA) nanofilms, Pensabene et al. (2016) fabricated a dynamic microfluidic cell culture platform by embedding PLLA ultrathin membrane inside the device, as shown in Figs. 4d and 5c (Pensabene et al. 2016). In addition, the reproducibility limitations and fragile nature of such an ultrathin membrane may affect its widespread use.

3 Visualizations and Measurements

A basic microfluidic setup consists of a pump, microfluidic device, pressure controllers and visualization system. The fluid is injected into the chip pattern through the inlet tube where it displaces/interacts with resident fluid. By utilizing syringe pumps, high-pressure

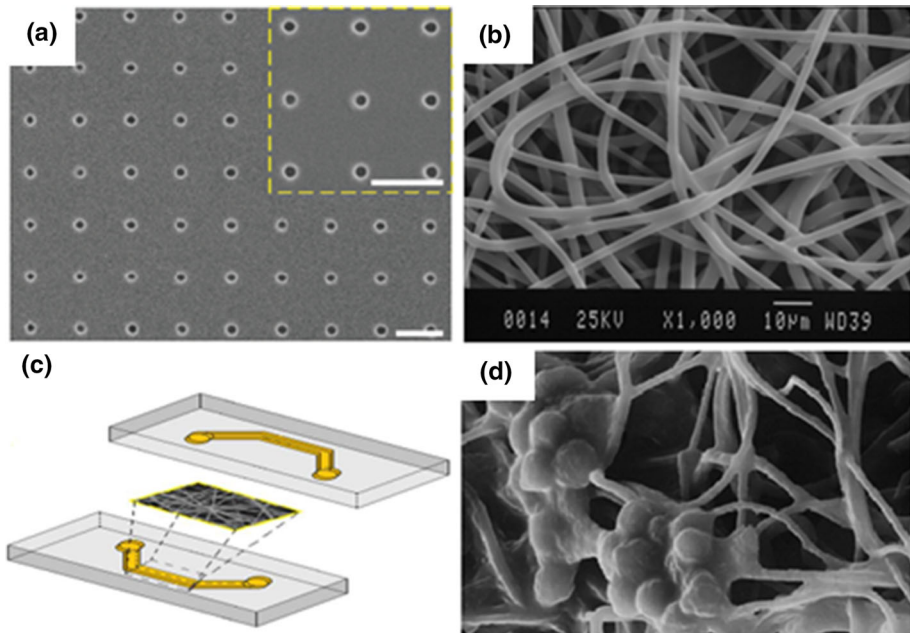


Fig. 5 Characterization of porous membrane used for cell culture applications. **a** Scanning electron microscopy (SEM) free-standing PDMS through-hole membrane. Such membrane is smooth. The scale bars are 5 μm . Reproduced with permission from Le-The et al. (2018). **b** SEM image of PDMS electrospun membrane. Reproduced with permission from Moghadas et al. (2017a). Unlike the smooth PDMS membrane, the electrospun membrane has 3D structures. **c** The electrospun membrane was imbedded between two PDMS microchannels. **d** SEM images of human lung cancer epithelial cells cultured on the electrospun membrane integrated into the microchip. Due to the 3D structure of the membrane, the cells are formed in a 3D cluster. Reproduced with permission from Moghadas et al. (2018)

pumps, pressure transducers, flow sensors, pressure cells, heaters, etc., the setup can be modified for specific applications (Karadimitriou and Hassanizadeh 2012). Overall, the real-time visualization, quantification and/or control of flow and/or transport in the micromodel are considered a significant advantage of microfluidic studies and applications. In particular, the visualization method is critical for a successful microfluidic experiment and can be used as both a qualitative and quantitative tool. For instance, relative permeability data of water and gas flow in coal fractures are measured based on the images obtained from the microfluidic experiments (Gerami et al. 2016) (Fig. 6a). 3D observation of a non-dyed buffer displacing a fluorescein-dyed buffer (Fig. 6c) (Singh et al. 2017) and the transport of decane (Fig. 6b) and dyed CO_2 (Fig. 6d) (Kazemifar et al. 2015) are other examples of visualizations obtained by microfluidic experiments.

3.1 Transmitted and Reflected Microscopy

A camera coupled to a microscope is commonly employed for the visualization of microfluidic experiments (Gunda et al. 2011; Rangel-German and Kovscek 2006; Xu et al. 2014). This setup is effective for focusing on a specific area in the micromodel at high resolution ($> 1 \mu\text{m}$) and for the measurement of parameters, such as contact angle and interfacial curvature (Karadimitriou and Hassanizadeh 2012). In addition, high-speed cameras can be

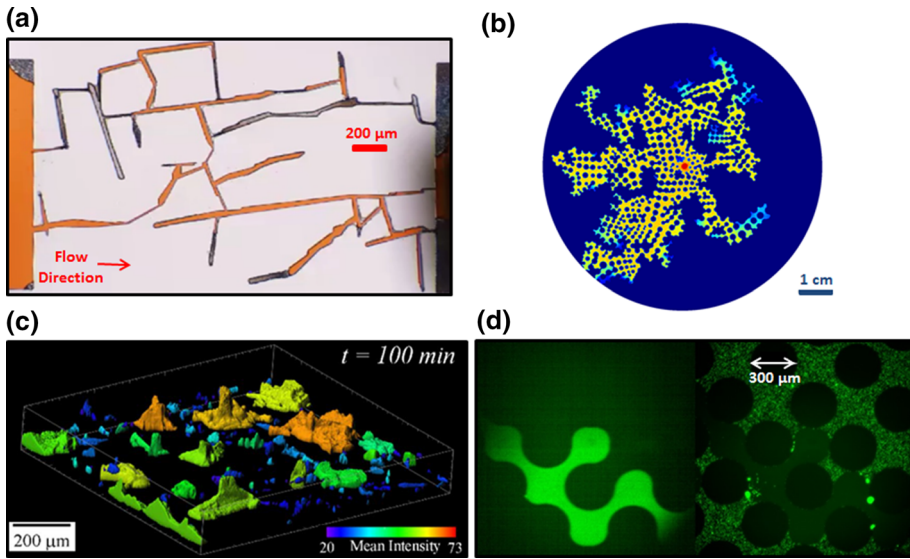


Fig. 6 **a** Dyed colored fluid displacing gas within coal fractures. Transmitted microscopy is utilized to visualize the flow transport. Reproduced with permission from Gerami et al. (2016). **b** Direct visualization is employed to observe the displacement of decane oil in a random pore network model developed by PDE tool in MATLAB. The injection starts from the center of the circle. **c** Confocal laser microscope is utilized to observe the displacement of fluorescein-dyed buffer by a non-dyed buffer at 100 min after the injection. Reproduced with permission from Singh et al. (2017). **d** Sample images of dyed CO₂ (left) and tracer particle image (right) in a silicon-based micromodel using a dual-camera imaging setup. Reproduced with permission from Kazemifar et al. (2015)

incorporated to study rapid events (Armstrong and Berg 2013; Moebius and Or 2012, 2014). For microfluidic chips with one opaque side, the light source and the optical access have to be on the same side of the chip (such as reflected microscopes). For transparent porous media, either a transmitted microscope (light source and optical access are at the opposite side of the chip) or a reflected microscope can be employed.

A setup of camera(s) without a standard microscope is utilized for experiments that require a larger field of view (e.g., flow visualization over time) or for experiments with high acquisition rates (Alzahid et al. 2017; Hematpour et al. 2011; Moebius and Or 2012). With these setups, cameras are placed at flexible distances from the micromodel at any suitable orientation, to capture images and videos from the flow. Because no microscope is coupled to the camera, generally lower-resolution images are obtained for the given camera objective. Karadimitriou et al. (2012) built a customized setup by utilizing a prism between the light source and the objective lens. A beam-splitter box was utilized to produce identical images of the micromodel sections in different directions, and cameras were placed around the box to visualize all of the projected images. Hence, they could capture high spatial and temporal resolutions of the entire micromodel. This setup was utilized for studying flow in elongated micromodels (Karadimitriou et al. 2014) and was then extended to reflected microscopy following the same visualization principles (Godinez-Brizuela et al. 2017). In other setups, a long-distance microscope objective is employed to focus the emitted light from the flow, onto the detector of a camera. This allows for relatively low magnification ($\sim 3\times$, translating to $\sim 2 \mu\text{m}/\text{pixel}$) and a sufficient field of view ($8.8 \text{ mm} \times 5.5 \text{ mm}$) to cover the entire microfluidic chip as employed for the fluorescence imaging setup in Chen et al. (2017) and

Fakhari et al. (2018). Although a conventional epifluorescence microscope can accommodate a low-magnification objective, the large working space of a long-distance microscope provides additional flexibility and space for setting up the experiment.

3.2 Confocal Microscopy

Confocal microscopy is used for three-dimensional (3D) imaging and for microfluidic experiments with high-resolution requirements ($< 1 \mu\text{m}$). This setup can observe relatively slow displacements that occur over a length scale less than the optical diffraction limit (Karadimitriou and Hassanizadeh 2012). This setup can also provide images over the depth of the chip up to a total depth of around $250 \mu\text{m}$. For instance, Zhang et al. (2013) utilized confocal microscopy to monitor colloids transport during two-phase flow in a microfluidic device. Datta et al. (2013) captured the single-phase flow in a 3D packed glass bead porous model via a confocal laser scanning microscope, and in a subsequent publication, they analyzed two-phase fluid flow using the same method in a porous medium (Datta et al. 2014). Zevi et al. (2005) utilized this visualization technique to measure water meniscus shape and water film thickness on sand grains in an unsaturated horizontal chamber. In addition, numerous researchers have used confocal laser scanning microscopy (CLSM) to visualize the growth of biofilms in microfluidics devices. They studied bacteria producing a green fluorescent protein, and different fluorescent staining procedures are utilized (Leis et al. 2005; Rodríguez and Bishop 2007). Concerning flow and transport in porous media, the prominent application of CLMS is the tracking of particles to measure local velocities.

3.3 Fluorescent Microscopy

To distinguish between fluid phases during flow, a fluid can be mixed with dye (Yadali Jamaloei and Kharrat 2009), light intensity changes can be monitored (Chapman et al. 2013), or fluorescent particles can be added to the flow (Kazemifar et al. 2016). In fluorescent visualization, the solution is tagged with a fluorescent dye, and a light source is utilized to excite the fluorescent molecules. The fluorescence signal is at a longer wavelength with respect to the incident (excitation) wavelength, commonly called the Stokes shift (Albani 2011), and a digital camera captures the long-pass-filtered light.

Fluorescence detection methods are convenient because of the simplicity and low detection limit (Kim et al. 2011; Martínez-Máñez and Sancenón 2003). The concentration of a target analyte can be measured in biosamples using this technique (Kim et al. 2011). For instance, Nolan and Lippard (2008) investigated the detection of mercury ion with sufficient selectivity. By monitoring the fluorescence intensity changes, Pb (Lead) is detected in a microfluidic channel where the surface is functionalized with a fluorophore (Basabe-Desmots et al. 2004). By using rhodamine derivatives, chemosensors can be designed for metal ion detection (Kim et al. 2008a). Although rhodamine derivatives are non-fluorescent, the fluorescence emission is provided by the corresponding spirolactam (Yang et al. 2005). Mela et al. (2005) coated the surface of a microfluidic network with rhodamine B and utilized fluorescent microscopy techniques for local pH measurements. Chang et al. (2017) used pH-sensitive dye pHrodo[®] Red (Life Technologies, Carlsbad, CA), to study dissolution of CO_2 in water during a drainage process in a porous micromodel. Fluorescein is another water-soluble pH-sensitive dye whose fluorescence intensity increases with pH of the solution in the pH range of $\sim 4\text{--}8$ (Doughty 2010; Martin and Lindqvist 1975).

3.4 Microscopic Particle Image Velocimetry (Micro-PIV)

Particle image velocimetry (PIV) is a particle-based, nondestructive, optical diagnostic technique for fluid velocity measurement (Adrian and Westerweel 2011). In this technique, fluid is tagged with tracer particles that, when subjected to laser, can illuminate and is then imaged at two time instants separated by a set time delay, Δt . The image is subdivided into small interrogation windows (IW) that contain typically ~ 10 particles. The average displacement of particles ($\Delta\vec{x}$) in each IW can be obtained by cross-correlation analysis between the two image frames. Consequently, $\Delta\vec{x}/\Delta t$ yields the average velocity vector, \vec{u} , of particles in that IW. Hence, each image pair yields one velocity vector field, whose spatial resolution is determined by the size of the IW. A variant of PIV that is tailored for flow diagnostics at the microscale is microscopic particle image velocimetry (micro-PIV) (Meinhart et al. 1999; Santiago et al. 1998). Numerous factors must be considered to produce reasonable velocity measurements. These factors include: illumination method, tracer particle density and size, camera sensor versus particle diameter and chemical interactions.

Due to geometrical limitation, it is not possible to generate a light sheet in microfluidic applications (as is customary in standard PIV); thus, volume illumination is employed where particles in the entire depth of the microfluidic device are illuminated. Consequently, out-of-focus particles take part in the cross-correlation function that is used to determine average particle displacement in an IW (Olsen and Adrian 2000). Moreover, to suppress the background scattered light and increase the signal-to-noise ratio in PIV images, fluorescent particles are used, allowing long-pass filtering of the scattered light. The ideal illumination source for PIV application is a pulsed laser that delivers an intense pulse of energy over a very short period of time (for instance, ~ 10 ns for Nd:YAG lasers). The short pulse of the laser ensures that the particles are frozen in the image, and no streaking occurs from the movement of particles during exposure. The particles dispersed in the fluid phase(s) acting as tracers must have specific properties to faithfully follow the fluid flow. First, the particles' density should (nearly) match that of the fluid to eliminate gravity/buoyancy driven motion. Also, for particles to follow rapid flow acceleration and/or decelerations, the Stokes number, which represents the tracer particle typical response time to flow, should be very small (Kazemifar et al. 2015). Moreover, the particle diameter must be 10^1 – 10^2 times smaller than the smallest channel dimension to avoid blocking effects. However, with small particles, displacement of the tracer particles due to Brownian motion must be considered (Santiago et al. 1998). Other sources of error in determining average displacement of particles from the cross-correlation function pertain to the particle image diameter and resolution of the camera sensor (Christensen 2004; Westerweel 1997). Lastly, the material of the tracer particle should be considered, which is typically a polymer. Thus, depending on the fluids, the physical and chemical compatibility of the polymer must be considered. This is particularly important in studies with supercritical CO_2 (Kazemifar et al. 2015), which is a strong solvent and can cause polymer swelling (Hilic et al. 2001; Rindfleisch et al. 1996; Sato et al. 1999; Webb and Teja 1999). Further details on the theory and practice of this technique are provided in (Adrian and Westerweel 2011), Raffel et al. (2013) and Tropea et al. (2007).

3.5 Raman Spectroscopy

Raman spectroscopy detects molecule-specific information at the microscale by measuring the vibrational modes of molecules (Chrimes et al. 2013). Details on Raman spectroscopy are explained in Chrimes et al. (2013). Raman coupled with microfluidic experiments could

provide information on miscible and immiscible fluids, such as identifying chemical pathways and structures, understanding intrinsic kinetics and thermodynamics and improving the accuracy of mass transport coefficients. Several studies have utilized Raman spectroscopy with microfluidic devices. For instance, Raman spectroscopy can be used to validate the presence of relevant rock minerals on geomaterial microfluidic devices (Lee Seung et al. 2016; Wang et al. 2017). In addition, Raman was also used to study the polymorphs of calcite during precipitation caused by acid (Singh et al. 2015; Yoon et al. 2012), which is one of the fundamental processes in subsurface engineering. Others have used Raman spectroscopy to study the CO₂ solubility in water and brine (Guo et al. 2014, 2015; Liu et al. 2012; Lu et al. 2013; Morais et al. 2015). The Raman spectra obtained from microscopic imaging provide a small cross section of the sample. This is because the light spot for each pixel (generally $0.3 \times 0.3 \mu\text{m}^2$), which refers to the number of molecules in the spot, is also small. This is considered as one of the drawbacks of Raman spectroscopy. Kawata et al. (2017) and Deckert et al. (2015) discuss more about Raman spectra resolution and how to overcome the challenges associated with Raman spectroscopy.

4 Applications of Microfluidics

Using microfluidics for visualizing flow and transport in porous media is relevant to several engineering applications, particularly in energy-related applications (such as hydrocarbon recovery processes), and geological CO₂ sequestration. Here, the focus is on understanding a specific mechanism(s) and/or the generation of data to provide spatial and temporal concentrations/velocities used for validating numerical codes. Microfluidics is also relevant in biomedical fields, such as tissue engineering and cell sorting to engineer a specific application by controlling a particular process and/or generating a particular environment necessary for tissue development. The following subsections discuss recent advancements and applications of microfluidics within these fields.

4.1 Hydrocarbon Recovery

Enhanced oil recovery (EOR) is a broad range of processes that aims to improve oil recovery (Alagorni et al. 2015; Lake 2014). EOR processes ultimately deal with the flow and transport of chemical species and the resulting phase behavior in porous media. Microfluidic devices can serve as a good platform for assessing pore-scale chemical or thermal recovery processes. These devices can be adjusted to accommodate a testing reservoir fluid at reservoir conditions. In this section, we summarize a few selected studies that have used microfluidics for investigating EOR methods.

Low-salinity water (LSW) flooding denotes injection of diluted brine concentrations to increase oil recovery. Morin et al. (2016) introduced a novel microfluidic device to assess the effects of chemically mediated interfacial properties between oil and brine upon snap-off at the pore level. The microfluidic device formed oil drops through extensional flows and allowed the aging of crude oil against brines of different salinities, hence assessing the role of salinity in snap-off, i.e., oil droplet formation. Low-salinity brine was found to result in the preferential development of dynamic interfacial viscoelasticity, thereby suppressing pore-level snap-off events. Bartels et al. (2016) and Bartels et al. (2017) used clay-coated micromodels to investigate the low-salinity effect and its dependence on crude oil properties, presence of clay particles and aging. Amirian et al. (2017) utilized the approach, proposed

by Song and Kovscek (2015) to deposit clay particles into micromodels and visualized the micro-mechanism of displacement under LSW injection.

The effect of surfactant additives was also studied using microfluidics (Alzahid et al. 2019; de Haas et al. 2013; He et al. 2015, 2017; Nguyen et al. 2015). Yadali Jamaloei and Kharat (2009) utilized a low-concentration surfactant solution in both water- and oil-wet glass micromodels. Different events were observed in the two micromodels. Oil-wet micromodels showed water-in-oil emulsions, which is not preferable for EOR. Water-wet micromodels displayed bridging between pores, and deformation of the residual oil, which is favorable in EOR processes. Pei et al. (2013) visualized the displacement mechanism of emulsions created from alkaline flooding (Fig. 7b). Dong et al. (2012) also conducted a microfluidic approach to studying the displacement mechanism of alkaline flooding in heavy oil. In their study, two events were observed: (1) in situ water-in-oil emulsion formation and partial change in wettability and (2) oil-in-water emulsion occurred only when adding a surfactant solution, which resulted in the mixing of heavy oil in the water phase. Unsal et al. (2016) studied the dynamic formation of micro-emulsion in situ by co-injecting decane and surfactant solution (at a specific concentration) into a *T*-junction capillary geometry at different salinities and flow rates (Fig. 7a). They utilized Nile Red, a unique solvatochromic dye, which allowed the micro-emulsion formation to be visualized using fluorescent microscopy. Lastly, Sedaghat et al. (2016) used several glass-etched micromodels with different fracture arrangements. They investigated the effect of fracture characteristics (length, orientation and quantity of fractures) and ASP slug compositions on heavy oil recovery.

Thermal EOR mechanisms, such as steam-assisted gravity drainage (SAGD), are mainly employed for heavy oil recovery. Conventional SAGD and hybrid SAGD processes (pentane and hexane additives) were thoroughly investigated by researchers using glass micromodel (Mohammadzadeh and Chatzis 2016; Mohammadzadeh et al. 2010). Their visualization led to in-depth understanding of micro-pore flow, and residual oil trapping mechanisms in SAGD, including (i) layered drainage flow perpendicular to the nominal oil–gaseous mixture interface and (ii) occurrence of both water-in-oil and solvent-in-water emulsions at the interface. Other pore-scale phenomena have also been observed, such as entrapment of steam and condensation, and liquid film snap-off. Sinton's laboratory introduced a microfluidic network that represented a realistic model of a typical SAGD, which was saturated with bitumen and the relevant reservoir conditions and pore sizes (de Haas et al. 2013). They achieved high-resolution visualization by using the ability of native bitumen to fluoresce in order to assess the alkaline additive (Fig. 7c). The additive significantly reduced the size of oil-in-water emulsions, and the corresponding recovery was improved by ~50% during SAGD. As a further step for alkaline additive screening, infrared and optical pore-scale imaging of the SAGD process using different alkaline additives were analyzed using the same micromodel (Syed et al. 2016). Using a combination of microscale flow and high-resolution temperature analysis can provide valuable insights into pore-scale phenomena, specifically the interrelationships between temperature drop at the steam chamber interface, drainage modes and recovery during SAGD. In another attempt, alcohol- and alkaline-based elements as evolving additives to improve the performance of SAGD were tested by pore-scale visualization in order to differentiate mechanisms associated with each alcohol and alkaline additive (Kim et al. 2017). It was concluded that although alcohol slightly improved the growth of steam, whereas a 10% expansion of steam was achieved by alkaline and improved recovery.

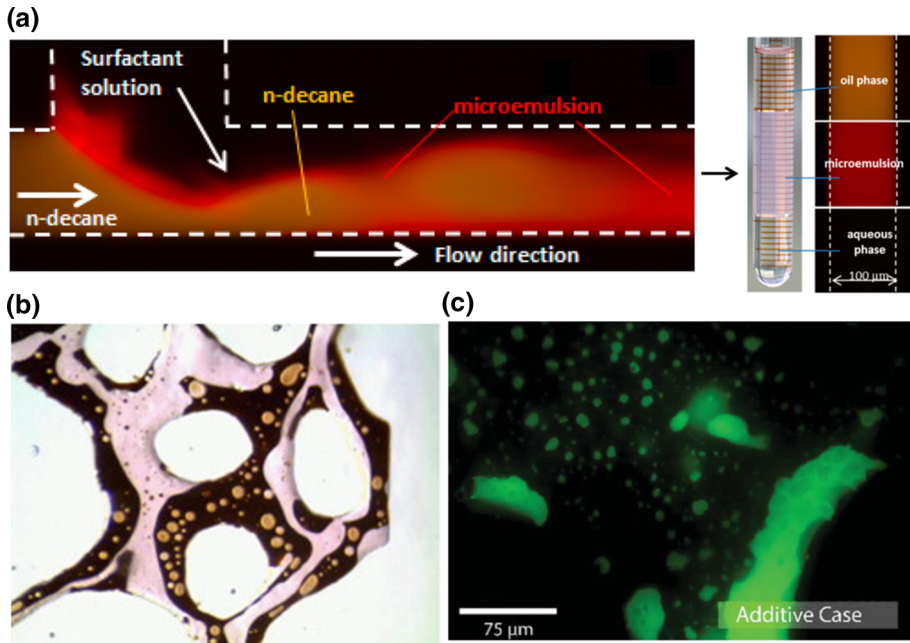


Fig. 7 The formation of emulsion systems. **a** Top view of a *T*-junction during the co-injection of surfactant solution and colored decane under fluorescent light, highlighting the micro-emulsion formation at optimum salinity during continuous flow. Black is an aqueous phase; red is micro-emulsion; and brown is decane. Reproduced with permission from Unsal et al. (2016). **b** With and without emulsions after alkaline flooding. Reproduced with permission from Pei et al. (2013). **c** With and without emulsions after steam-assisted gravity drainage (oil shown in green and water in black). Reproduced with permission de Haas et al. (2013)

4.2 CO₂ Sequestration

Carbon capture and sequestration (CCS) is where CO₂ is taken from the flue gas stream of large stationary greenhouse gas emitters (e.g., fossil fuel power plants) and then compressed and transported for storage in geological formations. This technology has received increased attention due to concerns about the effects of CO₂ on climate change and global warming (Haszeldine 2009; Pacala and Socolow 2004; White et al. 2003). Saline aquifers are among the most promising candidates as storage sites, in which pressurized CO₂ is injected into brine-saturated rock formations for permanent storage (Bachu 2000; Huppert and Neufeld 2014; Nordbotten et al. 2005). However, our understanding of the fate of injected CO₂ and its migration is still lacking as numerical models cannot fully capture the spatiotemporal evolution of injected CO₂ plumes. In this regard, microfluidic devices and micromodels are potent tools that can help us better understand CCS-relevant flow, transport and chemical processes at the pore scale.

At typical pressures and temperatures in a saline aquifer (80+ bar, 30+ °C), CO₂ exists as a supercritical fluid, i.e., pressure and temperature are beyond the critical point of CO₂ at 74 bar and 31 °C. Under these conditions, CO₂ and water have limited mutual solubility. As a reference, the solubility of CO₂ in deionized water at 297 K increases with pressure until it levels at approximately 2.5% by mole (6.1% by mass) beyond 7 MPa. On the other hand, the solubility of water in CO₂ at CCS-relevant pressures and temperatures is approximately one

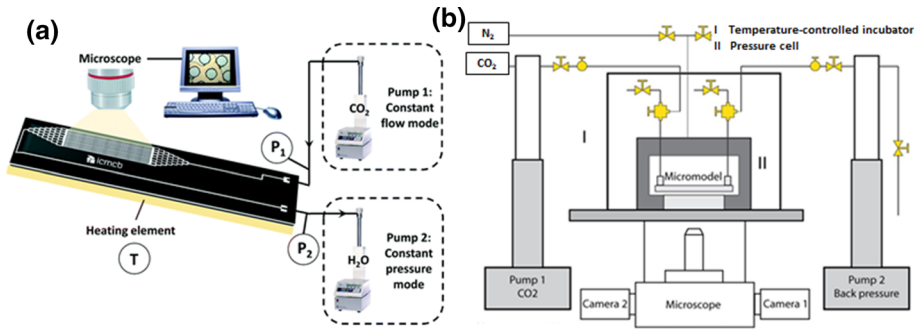


Fig. 8 Schematic of an experimental setup of a high-pressure micromodel. **a** CO₂ injection in a water-saturated pore network under identical geological conditions ($25 < T$ (°C) < 75 and $4.5 < p$ (MPa) < 8). Reproduced with permission from Morais et al. (2016). **b** Multiphase flow of liquid/supercritical CO₂ and water through a porous micromodel from below. Adapted with permission from (Kazemifar et al. 2015)

order of magnitude less than that of CO₂ in water, and it is 0.3–0.4% by mole (0.12–0.16% by mass) (Jacob and Saylor 2016; King et al. 1992; Wiebe and Gaddy 1940). In general, solubility of CO₂ in water increases with pressure and decreases with both temperature and the salinity of water/brine. Another significance of the critical point is that, in its vicinity, thermophysical properties, e.g., viscosity and diffusivity, of fluids become very sensitive to changes in pressure and temperature (Kazemifar and Kyritsis 2014). Thus, any experimental apparatus must be designed to provide precise control over pressure and temperature (Fig. 8). During injection, due to the lower viscosity of the invading CO₂ phase with respect to the resident brine phase, the advancing CO₂–water displacement front is unstable and exhibits a phenomenon referred to as *fingering*. This phenomenon can affect the displacement patterns and spatial distribution of fluid phases in a porous medium, and it has been studied extensively in the context of immiscible displacement in porous media (Homsy 1987; Lenormand et al. 1988; Zhao et al. 2016). Figure 8 illustrates experimental setups for CO₂ injection in water-saturated pore networks at reservoir condition.

For visualizing the flow in a multiphase immiscible system, such as water and liquid/supercritical CO₂, the fluorescent dye should ideally be soluble in only one of the two fluid phases. One of the few dyes satisfying this requirement is Coumarin 153 (C153), which is soluble in CO₂ but nearly insoluble in water. The emission/absorption spectra of C153 (Biswas et al. 1999; Kim et al. 2012a) and its solubility (Hae Choi et al. 1998; Shiota and Castner 2000) in CO₂ and other solvents have been documented in the literature. Numerous researchers (Chang et al. 2016; Chen et al. 2017; Fakhari et al. 2018; Kazemifar et al. 2015, 2016; Li et al. 2017; Wang et al. 2013c; Zhang et al. 2011) have used C153 to visualize liquid/supercritical CO₂ in CCS-relevant studies. Zhang et al. (2011) studied the steady-state distribution of fluid phases in a dual-permeability homogeneous micromodel during CO₂ drainage. Wang et al. (2013c) studied the steady-state distribution and displacement patterns resulting from different fingering regimes in a homogeneous micromodel during CO₂ drainage. Kazemifar et al. (2015, 2016) combined fluorescence microscopy and micro-PIV to simultaneously visualize CO₂ and record the velocity field in the aqueous phase during a drainage process in a homogeneous micromodel. They observed flow in thin water films and shear-induced recirculation in trapped water ganglia as evidenced by the motion of 1- μ m tracer particles dispersed in the aqueous phase. Li et al. (2017) applied the same technique (fluorescence microscopy and micro-PIV) in a heterogeneous micromodel, using the velocity

vector field to quantify the zone of influence during Haines jump events. Fakhari et al. (2018) and Chen et al. (2017) performed coordinated lattice Boltzmann method (LBM) simulations and experiments using fluorescence high-speed imaging, to study the spatiotemporal evolution of supercritical (sc)CO₂ displacement of water in a heterogeneous micromodel. Chang et al. (2016) studied the reduction in CO₂ saturation during imbibition in a micromodel, and they calculated average mass transfer from CO₂ to the aqueous phase. Other water-soluble dyes have also been used in CCS-related studies. Zuo et al. (2013) used fluorescein and Xu et al. (2017) used rhodamine B to study depressurization-induced exsolution of CO₂ from water in micromodels. Buchgraber et al. (2012) used a general-purpose UV dye to study residual and capillary trapping of CO₂ during drainage and imbibition processes in a micromodel. Zheng et al. (2017) used food coloring to tag brine in drainage experiments with CO₂ under liquid, gaseous and supercritical conditions.

Imaging can be carried out even without a fluorescent dye, using bright-field imaging, although with a lower signal-to-noise ratio. In this configuration, CO₂–water interfaces are visible due to their different refractive indices, and depending on the illumination source and imaging spectrum, the two fluid phases may have different signal intensity. In addition, information such as wetting properties or flow direction can be used to identify the fluid phases (Cao et al. 2016; Hu et al. 2017a, b; Jafari and Jung 2017; Kim et al. 2012c; Morais et al. 2016; Qin et al. 2017). Kim et al. (2012c) studied the changes in wettability of a glass micromodel due to exposure to scCO₂ and brine with different salinities. Cao et al. (2016) studied the effect of contact angle and salinity on displacement patterns in CO₂ drainage, and they compared the results with pore network numerical simulations. Morais et al. (2016) used high-speed imaging to resolve dynamic displacement patterns and evolution of CO₂ saturation for various subcritical and supercritical p – T combinations. Hu et al. (2017a) studied the effects of contact angle and flow rate on displacement patterns during CO₂ drainage, and they compared experimental results with numerical simulations solving the Navier–Stokes equations. Hu et al. (2017b) studied the effect of contact angle on spatial distribution and morphology of the trapped CO₂ phase during water imbibition for different flow rates. Jafari and Jung (2017) used micromodels to measure static as well as advancing and receding dynamic contact angles in a CO₂/water/glass system. Qin et al. (2017) studied flow of liquid CO₂ and water in a micro- T -junction, and Sell et al. (2013) measured diffusivity of CO₂ in water and 0–5 M NaCl solution using fluorescein at 26 °C and 5–50 bar.

4.3 Biomedical Sciences

Microfluidics can revolutionize current practices in cell biology (Paguirigan and Beebe 2008), in vitro cell culture studies (Barisam et al. 2017), pathophysiology (Wang et al. 2013b), biochemistry (Ohno et al. 2008), drug delivery (Nguyen et al. 2013), nanoparticle deposition (Moghadas et al. 2017b), oncology (Kashaninejad et al. 2016), assisted reproductive technology (Kashaninejad et al. 2018), hematology (Myers et al. 2012), immunology and antibody screening (Seah et al. 2017) and pharmacology (Delamarche et al. 2013). For instance, microfluidic devices can provide an in vivo-like microenvironment to culture cells in a dynamic and perfusion-based manner. Coupled with concentration gradient generators, microfluidic cell culture devices can facilitate high-throughput and high-content drug screening, thus opening a new era in personalized medicine. For cancer treatment, microfluidic platforms have shown a great promise in 3D tumor spheroid formation and culture (Moshksayan et al. 2018). At a single-cell level, microfluidic devices enable a versatile platform to address fundamental questions in biology. Droplet- and valve-based microfluidic devices

realize highly efficient and compartmentalized platforms to study individual cells, including the interaction of T-cell and B-cell receptors (Seah et al. 2018). The unique features of two commonly used formats of microfluidics, i.e., continuous-flow microfluidics or droplet-based microfluidics, in liquid handling can automate sophisticated bioassay protocols and facilitate mixing and separation of various biomedical samples for diagnostics and treatment (Gomez 2013; Nguyen et al. 2017; Sackmann et al. 2014). Proposed by Whiteside's group at Harvard University in 2009, microfluidic paper-based analytical devices (μ PADs) are another format of microfluidics that can be used for diagnostic purposes (Martinez et al. 2009). They meet the ASSURED (affordable, sensitive, specific, user-friendly, rapid and robust, equipment-free and deliverable to end-users) criteria of World Health Organization and can be used as portable point-of-care diagnostic devices in resource-limited settings.

For tissue engineering and regenerative medicine, microfluidic cell culture bioreactors have also progressed rapidly. Accordingly, another format of microfluidic systems in biomedical science named as organ-on-a-chip has emerged (Morales et al. 2012). Organ-on-a-chip devices with a semipermeable porous membrane, which was discussed previously, have provided a platform that can bridge the gap between animal studies and in vitro cell culture models (Bhatia and Ingber 2014; Huh et al. 2013). These membranes have been used in various organ-on-a-chip platforms for disease modeling and drug screening (Huh et al. 2011). These platforms include lung-on-a-chip (Huh et al. 2010), gut-on-a-chip (Kim et al. 2012b), liver-on-a-chip (Prodanov et al. 2016), kidney-on-a-chip (Nieskens and Wilmer 2016), blood-brain barrier-on-a-chip (van der Helm et al. 2016) and placenta-on-a-chip (Lee et al. 2016).

Other than organ-on-a-chip, membrane-based microfluidic devices can be used in cell/particle sorting by implementing strategies of size-based filtration. Efficient particle/cell sorting is an essential step in most clinical, biological and industrial processes. To this end, both active and passive techniques can be used. Although the separation efficiency and selectivity can be better controlled using active techniques, these techniques require external forces that compromise the portability and simplicity of the device. Among various passive techniques, size-based filtration using isoporous membranes embedded in a microfluidic device have attracted significant attention. These devices have several applications including emulsion separation (Vladislavjević et al. 2012), drug delivery (Yang et al. 2010), water purification (Warkiani et al. 2011) and pathogen detection for food safety (Yoon and Kim 2012). Both in situ and off-chip techniques can be used to fabricate and integrate these membranes into microfluidic devices. Although in situ techniques such as femtosecond laser multi-foci parallel microfabrication (Xu et al. 2016) are elegant and can significantly reduce production time, their poor controllability over membrane pore size and difficulty in precisely positioning the membrane limit their application.

Size-based filtration using membrane-based microfluidics can be used for cancer diagnostics (Dong et al. 2013). Of particular interest is the application of minimally invasive techniques to detect cancer biomarkers in the blood known as liquid biopsy (Zhang et al. 2017). Among cancer biomarkers, circulating tumor cells (CTCs) proved to be a better candidate for diagnostic and prognostic of cancer (Warkiani et al. 2014a). Accordingly, using microfluidic devices can offer significant advantages for label-free detection of viable CTCs from peripheral blood (Warkiani et al. 2014b). To this end, size-based filtration using a porous membrane integrated inside a microfluidic device is a practical approach. The membrane used for such a device should be highly porous with precise control over the pore size. Silicon-based membranes that are fabricated using photolithography were among the first membranes which met the necessary conditions for efficient CTCs detection (Lim et al. 2012). Fan et al. (2015) used water-dissolvable polyvinyl alcohol (PVA) as supporting (and sacrificial) layer for PDMS soft lithography to fabricate a thin and highly porous PDMS membrane. As shown

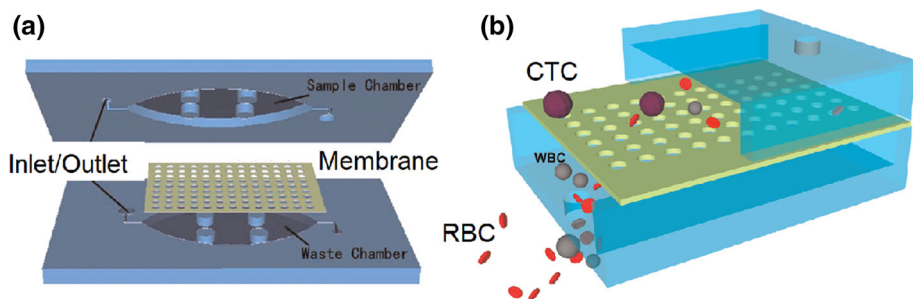


Fig. 9 Schematic of membrane-based microfluidic devices used to isolate CTCs. **a** Porous membrane sandwiched between sample channel and waster channel. **b** Illustration of sized-based filtration method to isolate CTCs from RBCs and WBCs. Reproduced with permission from Fan et al. (2015)

in Fig. 9, the membrane was then used inside a microfluidic device to separate CTCs from white blood cells (WBCs) and red blood cells (RBCs). They reported a capture efficiency of more than 90% using this technique.

To improve the release efficiency of the captured CTCs for further molecular analysis, Kim et al. (2016) used a releasing agent, poly(ethylene glycol) (PEG), on the SU8 microfilter. They showed over 20% improvement in releasing the captured CTCs from the whole blood sample. Kang et al. (2017) fabricated a photosensitive polymer-based microfilter and attached the filter to a syringe to rapidly isolate viable CTCs. They reported a CTC capture efficiency of over 75% from the whole blood samples with over 80% viability. Nevertheless, the efficiency of microfiltration-based CTC isolation techniques is highly dependent on the pore size, and it is limited to CTCs larger than the pore size (Zhang et al. 2016).

5 Future Directions

The development of microfluidics techniques is continually enhancing biological, medical, environmental and engineering technologies in many aspects. Samples can be prepared and analyzed at low volumes to replace heavy, large and expensive equipment and manual processing. Based on the extensive knowledge in microfluidic techniques, chips with specific applications can be designed, fabricated and commercialized. During the past two decades, the commercialization of microfluidics in biomedical science has been rapidly growing and on-a-chip devices have been introduced to the market for many techniques including genome sequencing and in vitro diagnostics (Volpatti and Yetisen 2014). In the oil and gas industry, lab-on-a-chip devices are also advancing, such as the commercialization of a microfluidic device for the measurement of asphaltene content in crude oil (Sieben et al. 2013). Other companies are producing and commercializing miniaturized analytical devices for various applications (Haber 2006). These applications will reduce the cost and time for the fabrication of microfluidic devices and thus increase the adoption of this technology for industrial applications. In particular, new opportunities in automation and rapid analysis or screening procedures for a variety of different engineering applications are a promising way forward.

We need to combine and integrate recent advances and innovations from various disciplines in biomedical science, chemistry, hydrology and petroleum engineering, which can be merged for the production of fully integrated and/or functionalized devices. For instance, developments in surface functionalization, chemical processes and catalyst performance

from chemistry and biomedical sciences could be important for developing microfluidic chips with the surface wetting properties required to study a given EOR process. In addition, the development of geomaterial chips could be utilized for etching biomedical scaffoldings for depositing cells. Last, membrane technologies for advanced sorting and filtration in the biomedical sciences are also largely important for water treatment processes and/or potential separation of crude oil components for processing and/or analytical analyses. Microfluidics can be implemented in order to address engineering problems that lack conventional setups for observation, diagnostic, or analysis. Cooperation of academics and industrial companies will play an important role in the identification of potential objectives in which microfluidics can help to address them. Other than commercializing microfluidic devices, advanced visualization and analysis setups offered by microfluidics can provide new insights into unknown mechanisms that occur in porous media. They can facilitate the analysis of simulation capabilities where multiple phases and components are being transported with unique equations of state and/or where standard assumptions of local equilibrium can no longer be applied. The future of microfluidic studies is indeed an exciting area of research and will remain as an essential tool for porous media studies and engineering applications.

References

- Adrian, R.J., Westerweel, J.: Particle Image Velocimetry. Cambridge University Press, Cambridge (2011)
- Ahmed, F.E., Lalia, B.S., Hashaikh, R.: A review on electrospinning for membrane fabrication: challenges and applications. *Desalination* **356**, 15–30 (2015)
- Alagorni, A.H., Yaacob, Z., Nour, A.H.: An overview of oil production stages: enhanced oil recovery techniques and nitrogen injection. *Int. J. Environ. Sci. Dev.* **6**(9), 693–701 (2015)
- Albani, J.R.: Structure and Dynamics of Macromolecules: Absorption and Fluorescence Studies. Elsevier, Amsterdam (2011)
- Albaugh, K.B.: Electrode phenomena during anodic bonding of silicon to sodium borosilicate glass. *J. Electrochem. Soc.* **138**(10), 3089–3094 (1991)
- Alzahid, Y., et al.: Alkaline surfactant polymer flooding: what happens at the pore scale? In: SPE Europec Featured at 79th EAGE Conference and Exhibition. Society of Petroleum Engineers (2017)
- Alzahid, Y.A., et al.: Functionalisation of polydimethylsiloxane (PDMS)—microfluidic devices coated with rock minerals. *Sci. Rep.* **8**(1), 15518 (2018)
- Alzahid, Y.A., Mostaghimi, P., Walsh, S.D.C., Armstrong, R.T.: Flow regimes during surfactant flooding: the influence of phase behaviour. *Fuel* **236**, 851–860 (2019)
- Amirian, T., Haghghi, M., Mostaghimi, P.: Pore scale visualization of low salinity water flooding as an enhanced oil recovery method. *Energy Fuels* **31**, 13133–13143 (2017)
- Anbari, A., et al.: Microfluidic model porous media: fabrication and applications. *Small* **14**(18), 1703575 (2018)
- Armstrong, R.T., Berg, S.: Interfacial velocities and capillary pressure gradients during Haines jumps. *Phys. Rev. E* **88**(4), 043010 (2013)
- Atencia, J., Beebe, D.: Controlled microfluidic interfaces. *Nature* **437**, 648–655 (2005)
- Bachu, S.: Sequestration of CO₂ in geological media: criteria and approach for site selection in response to climate change. *Energy Convers. Manag.* **41**(9), 953–970 (2000)
- Barisam, M., Saidi, M., Kashaninejad, N., Vadivelu, R., Nguyen, N.-T.: Numerical simulation of the behavior of toroidal and spheroidal multicellular aggregates in microfluidic devices with microwell and U-shaped barrier. *Micromachines* **8**(12), 358 (2017)
- Bartels, W.-B., et al.: Oil configuration under high-salinity and low-salinity conditions at pore scale: a parametric investigation by use of a single-channel micromodel. *SPE J.* **22**(05), 1362–1373 (2017)
- Bartels, W.B., et al.: Low salinity flooding (LSF) in sandstones at pore scale: micro-model development and investigation. In: SPE Annual Technical Conference and Exhibition. Society of Petroleum Engineers, p. 17, Dubai (2016)
- Basabe-Desmots, L., et al.: A simple approach to sensor discovery and fabrication on self-assembled monolayers on glass. *J. Am. Chem. Soc.* **126**(23), 7293–7299 (2004)

- Berkowski, K.L., Plunkett, K.N., Yu, Q., Moore, J.S.: Introduction to photolithography: preparation of microscale polymer silhouettes. *J. Chem. Educ.* **82**(9), 1365 (2005)
- Bhatia, S.N., Ingber, D.E.: Microfluidic organs-on-chips. *Nat. Biotechnol.* **32**(8), 760–772 (2014)
- Biswas, R., Lewis, J.E., Maroncelli, M.: Electronic spectral shifts, reorganization energies, and local density augmentation of Coumarin 153 in supercritical solvents. *Chem. Phys. Lett.* **310**, 485–494 (1999)
- Booth, R., Kim, H.: Characterization of a microfluidic in vitro model of the blood–brain barrier (μ BBB). *Lab Chip* **12**(10), 1784–1792 (2012)
- Bowden, S.A., Tanino, Y., Akamairo, B., Christensen, M.: Recreating mineralogical petrographic heterogeneity within microfluidic chips: assembly, examples, and applications. *Lab Chip* **16**(24), 4677–4681 (2016)
- Brian, J.K., Ellis, M.: Review of polymer MEMS micromachining. *J. Micromech. Microeng.* **26**(1), 013001 (2016)
- Britt, L.K., Schoeffler, J.: *The Geomechanics of a Shale Play: What Makes a Shale Prospective*. Society of Petroleum Engineers, New York (2009)
- Buchgraber, M., Kovscek, A.R., Castanier, L.M.: A study of microscale gas trapping using etched silicon micromodels. *Transp. Porous Media* **95**(3), 647–668 (2012)
- Cao, S.C., Dai, S., Jung, J.: Supercritical CO₂ and brine displacement in geological carbon sequestration: micromodel and pore network simulation studies. *Int. J. Greenhouse Gas Control* **44**(6), 104–114 (2016)
- Chang, C., et al.: Pore-scale supercritical CO₂ dissolution and mass transfer under imbibition conditions. *Adv. Water Resour.* **92**(March), 142–158 (2016)
- Chang, C., Zhou, Q., Oostrom, M., Kneafsey, T.J., Mehta, H.: Pore-scale supercritical CO₂ dissolution and mass transfer under drainage conditions. *Adv. Water Resour.* **100**, 14–25 (2017)
- Chapman, E.M., Yang, J., Crawshaw, J.P., Boek, E.S.: Pore scale models for imbibition of CO₂ analogue fluids in etched micro-model junctions using micro-fluidic experiments and direct flow calculations. *Energy Proc.* **37**, 3680–3686 (2013)
- Chen, Y.: Nanofabrication by electron beam lithography and its applications: a review. *Microelectron. Eng.* **135**, 57–72 (2015)
- Chen, Y., Li, Y., Valocchi, A.J., Christensen, K.T.: Lattice Boltzmann simulations of liquid CO₂ displacing water in a 2D heterogeneous micromodel at reservoir pressure conditions. *J. Contam. Hydrol.* **53**, 6178–6196 (2017)
- Chrimes, A.F., Khoshmanesh, K., Stoddart, P.R., Mitchell, A., Kalantar-zadeh, K.: Microfluidics and Raman microscopy: current applications and future challenges. *Chem. Soc. Rev.* **42**(13), 5880–5906 (2013)
- Christensen, K.: The influence of peak-locking errors on turbulence statistics computed from PIV ensembles. *Exp. Fluids* **36**(3), 484–497 (2004)
- Datta, S., Chiang, H., Ramakrishnan, T.S., Weitz, D.: Spatial fluctuations of fluid velocities in flow through a three-dimensional porous medium. *Phys. Rev. Lett.* **111**, 064501 (2013)
- Datta, S.S., Dupin, J.-B., Weitz, D.A.: Fluid breakup during simultaneous two-phase flow through a three-dimensional porous medium. *Phys. Fluids* **26**(6), 062004 (2014)
- Davies, M.J., Marques, M.P.C., Radhakrishnan, A.N.P.: Chapter 2 Microfluidics Theory in Practice, Microfluidics in Detection Science: Lab-on-a-chip Technologies, pp. 29–60. The Royal Society of Chemistry, New York (2015)
- de Haas, T.W., Fadaei, H., Guerrero, U., Sinton, D.: Steam-on-a-chip for oil recovery: the role of alkaline additives in steam assisted gravity drainage. *Lab Chip* **13**(19), 3832–3839 (2013)
- Deckert, V., et al.: Spatial resolution in Raman spectroscopy. *Faraday Discuss.* **177**, 9–20 (2015)
- Delamarque, E., Tonna, N., Lovchik, R.D., Bianco, F., Matteoli, M.: Pharmacology on microfluidics: multimodal analysis for studying cell–cell interaction. *Curr. Opin. Pharmacol.* **13**(5), 821–828 (2013)
- Dong, M., Liu, Q., Li, A.: Displacement mechanisms of enhanced heavy oil recovery by alkaline flooding in a micromodel. *Particuology* **10**(3), 298–305 (2012)
- Dong, Y., et al.: Microfluidics and circulating tumor cells. *J. Mol. Diagn.* **15**(2), 149–157 (2013)
- Doughty, M.J.: pH dependent spectral properties of sodium fluorescein ophthalmic solutions revisited. *Ophthalmic Physiol. Opt.* **30**(2), 167–174 (2010)
- Fakhari, A., Li, Y., Bolster, D., Christensen, K.T.: A phase-field lattice Boltzmann model for simulating multiphase flows in porous media: application and comparison to experiments of CO₂ sequestration at pore scale. *Adv. Water Resour.* **114**, 119–134 (2018)
- Fan, X., et al.: A microfluidic chip integrated with a high-density PDMS-based microfiltration membrane for rapid isolation and detection of circulating tumor cells. *Biosens. Bioelectron.* **71**, 380–386 (2015)
- Franssila, S.: *Introduction to Microfabrication*. Wiley (2010)
- Friend, J., Yeo, L.: Fabrication of microfluidic devices using polydimethylsiloxane. *Biomicrofluidics* **4**(2), 026502 (2010)
- Gerami, A., et al.: Microscale insights into gas recovery from bright and dull bands in coal. *J. Petrol. Sci. Eng.* **172**, 373–382 (2018)

- Gerami, A., et al.: Coal-on-a-chip: visualizing flow in coal fractures. *Energy Fuels* **31**(10), 10393–10403 (2017)
- Gerami, A., Mostaghimi, P., Armstrong, R.T., Zamani, A., Warkiani, M.E.: A microfluidic framework for studying relative permeability in coal. *Int. J. Coal Geol.* **159**, 183–193 (2016)
- Giboz, J., Copponnex, T., Mélé, P.: Microinjection molding of thermoplastic polymers: a review. *J. Micromech. Microeng.* **17**(6), R96 (2007)
- Godinez-Brizuela, O.E., Karadimitriou, N.K., Joekar-Niasar, V., Shore, C.A., Ostrom, M.: Role of corner interfacial area in uniqueness of capillary pressure-saturation- interfacial area relation under transient conditions. *Adv. Water Resour.* **107**, 10–21 (2017)
- Gomez, F.A.: The future of microfluidic point-of-care diagnostic devices. *Bioanalysis* **5**(1), 1–3 (2013)
- Gravesen, P., Branebjerg, J., Jensen, O.S.: Microfluidics—a review. *J. Micromech. Microeng.* **3**(4), 168 (1993)
- Guckenberger, D.J., de Groot, T.E., Wan, A.M.D., Beebe, D.J., Young, E.W.K.: Micromilling: a method for ultra-rapid prototyping of plastic microfluidic devices. *Lab Chip* **15**(11), 2364–2378 (2015)
- Gunda, N.S., Bera, B., Karadimitriou, N.K., Mitra, S.K., Hassanizadeh, S.M.: Reservoir-on-a-chip (ROC): a new paradigm in reservoir engineering. *Lab Chip* **11**(22), 3785–3792 (2011)
- Guo, H., et al.: Quantitative Raman spectroscopic investigation of geo-fluids high-pressure phase equilibria: part I. Accurate calibration and determination of CO₂ solubility in water from 273.15 to 573.15 K and from 10 to 120 MPa. *Fluid Phase Equilib.* **382**, 70–79 (2014)
- Guo, H., Huang, Y., Chen, Y., Zhou, Q.: Quantitative Raman spectroscopic measurements of CO₂ solubility in NaCl solution from (273.15 to 473.15) K at $p = (10.0, 20.0, 30.0, \text{ and } 40.0)$ MPa. *J. Chem. Eng. Data* **61**(1), 466–474 (2015)
- Haber, C.: Microfluidics in commercial applications; an industry perspective. *Lab Chip* **6**(9), 1118–1121 (2006)
- Hae Choi, Y., et al.: Effect of functional groups on the solubilities of coumarin derivatives in supercritical carbon dioxide. *Chromatographia* **47**(1–2), 93–97 (1998)
- Haerberle, S., Zengerle, R.: Microfluidic platforms for lab-on-a-chip applications. *Lab Chip* **7**(9), 1094–1110 (2007)
- Haszeldine, R.S.: Carbon capture and storage: how green can black be? *Science (New York)* **325**(5948), 1647–1652 (2009)
- He, K., Xu, L., Gao, Y., Yin, X., Neeves, K.B.: Evaluation of surfactant performance in fracturing fluids for enhanced well productivity in unconventional reservoirs using rock-on-a-Chip approach. *J. Petrol. Sci. Eng.* **135**, 531–541 (2015)
- He, K., Xu, L., Kenzhekhanov, S., Yin, X., Neeves, K.B.: A Rock-on-a-Chip Approach to Study Fluid Invasion and Flowback in Liquids-Rich Shale Formations. Society of Petroleum Engineers, London (2017)
- Hematpour, H., Mardi, M., Edalatkhah, S., Arabjamaloei, R.: Experimental study of polymer flooding in low-viscosity oil using one-quarter five-spot glass micromodel. *Pet. Sci. Technol.* **29**(11), 1163–1175 (2011)
- Hilic, S., Boyer, S.V.A.E., AlAH, Pádua, Grolier, J.P.E.: Simultaneous measurement of the solubility of nitrogen and carbon dioxide in polystyrene and of the associated polymer swelling. *J. Polym. Sci. Part B: Polym. Phys.* **39**(17), 2063–2070 (2001)
- Homsy, G.M.: Viscous fingering in porous media. *Annu. Rev. Fluid Mech.* **19**(1), 271–311 (1987)
- Hu, R., Wan, J., Kim, Y., Tokunaga, T.K.: Wettability effects on supercritical CO₂-brine immiscible displacement during drainage: pore-scale observation and 3D simulation. *Int. J. Greenhouse Gas Control* **60**, 129–139 (2017a)
- Hu, R., Wan, J., Kim, Y., Tokunaga, T.K.: Wettability Impact on Supercritical CO₂ Capillary Trapping: Pore-Scale Visualization and Quantification. Water Resources Research, London (2017b)
- Huh, D., Hamilton, G.A., Ingber, D.E.: From 3D cell culture to organs-on-chips. *Trends Cell Biol.* **21**(12), 745–754 (2011)
- Huh, D., et al.: Microfabrication of human organs-on-chips. *Nat. Protoc.* **8**(11), 2135–2157 (2013)
- Huh, D., et al.: Reconstituting organ-level lung functions on a chip. *Science* **328**(5986), 1662–1668 (2010)
- Huppert, H.E., Neufeld, J.A.: The fluid mechanics of carbon dioxide sequestration. *Annu. Rev. Fluid Mech.* **46**(1), 255–272 (2014)
- Iliescu, C., Taylor, H., Avram, M., Miao, J., Franssila, S.: A practical guide for the fabrication of microfluidic devices using glass and silicon. *Biomicrofluidics* **6**(1), 016505–016505-16 (2012)
- Jacob, R., Saylor, B.Z.: CO₂ solubility in multi-component brines containing NaCl, KCl, CaCl₂ and MgCl₂ at 297 K and 1–14MPa. *Chem. Geol.* **424**, 86–95 (2016)
- Jafari, M., Jung, J.: Direct measurement of static and dynamic contact angles using a random micromodel considering geological CO₂ sequestration. *Sustainability* **9**(12), 2352 (2017)
- Jahanshahi, A., Salvo, P., Vanfleteren, J.: PDMS selective bonding for the fabrication of biocompatible all polymer NC microvalves. *J. Microelectromech. Syst.* **22**(6), 1354–1360 (2013)

- Jiang, C., Tsukruk, V.V.: Freestanding nanostructures via layer-by-layer assembly. *Adv. Mater.* **18**(7), 829–840 (2006)
- Kalkandjiev, K., Gutzweiler, L., Welsche, M., Zengerle, R., Koltay, P.: A novel approach for the fabrication of all-polymer microfluidic devices. In: 2010 IEEE 23rd International Conference on Micro Electro Mechanical Systems (MEMS), pp. 1079–1082. IEEE (2010)
- Kang, Y.-T., Doh, I., Byun, J., Chang, H.J., Cho, Y.-H.: Label-free rapid viable enrichment of circulating tumor cell by photosensitive polymer-based microfilter device. *Theranostics* **7**(13), 3179 (2017)
- Karadimitriou, N.K., Hassanizadeh, S.M.: A review of micromodels and their use in two-phase flow studies. *Vadose Zone J.* **11**(3), 85 (2012)
- Karadimitriou, N.K., Hassanizadeh, S.M., Joekar-Niasar, V., Kleingeld, P.J.: Micromodel study of two-phase flow under transient conditions: quantifying effects of specific interfacial area. *Water Resour. Res.* **50**(10), 8125–8140 (2014)
- Karadimitriou, N.K., Joekar-Niasar, V., Hassanizadeh, S.M., Kleingeld, P.J., Pyrak-Nolte, L.J.: A novel deep reactive ion etched (DRIE) glass micro-model for two-phase flow experiments. *Lab Chip* **12**(18), 3413–3418 (2012)
- Karadimitriou, N.K., et al.: On the fabrication of PDMS micromodels by rapid prototyping, and their use in two-phase flow studies. *Water Resour. Res.* **49**(4), 2056–2067 (2013)
- Kashaninejad, N., et al.: Organ-tumor-on-a-chip for chemosensitivity assay: a critical review. *Micromachines* **7**(8), 130 (2016)
- Kashaninejad, N., Shiddiky, M.J.A., Nguyen, N.-T.: Advances in microfluidics-based assisted reproductive technology: from sperm sorter to reproductive system-on-a-chip. *Advanced Biosystems* **2**(1), 1700197 (2018)
- Kawata, S., Ichimura, T., Taguchi, A., Kumamoto, Y.: Nano-Raman scattering microscopy: resolution and enhancement. *Chem. Rev.* **117**(7), 4983–5001 (2017)
- Kazemifar, F., Blois, G., Kyritsis, D.C., Christensen, K.T.: A methodology for velocity field measurement in multiphase high-pressure flow of CO₂ and water in micromodels. *Water Resour. Res.* **51**(4), 3017–3029 (2015)
- Kazemifar, F., Blois, G., Kyritsis, D.C., Christensen, K.T.: Quantifying the flow dynamics of supercritical CO₂–water displacement in a 2D porous micromodel using fluorescent microscopy and microscopic PIV. *Adv. Water Resour.* **95**, 352–368 (2016)
- Kazemifar, F., Kyritsis, D.C.: Experimental investigation of near-critical CO₂ tube-flow and Joule-Thompson throttling for carbon capture and sequestration. *Exp. Therm. Fluid Sci.* **53**, 161–170 (2014)
- Kim, D., et al.: Reaction-based two-photon probes for in vitro analysis and cellular imaging of monoamine oxidase activity. *Chem. Commun.* **48**(54), 6833–6835 (2012a)
- Kim, H.J., Huh, D., Hamilton, G., Ingber, D.E.: Human gut-on-a-chip inhibited by microbial flora that experiences intestinal peristalsis-like motions and flow. *Lab Chip* **12**(12), 2165–2174 (2012b)
- Kim, Y., Wan, J., Kneafsey, T.J., Tokunaga, T.K.: Dewetting of silica surfaces upon reactions with supercritical CO₂ and brine: pore-scale studies in micromodels. *Environ. Sci. Technol.* **46**(7), 4228–4235 (2012c)
- Kim, H.N., Lee, M.H., Kim, H.J., Kim, J.S., Yoon, J.: A new trend in rhodamine-based chemosensors: application of spirolactam ring-opening to sensing ions. *Chem. Soc. Rev.* **37**(8), 1465–1472 (2008a)
- Kim, P., Kwon, K.W., Park, M.C., Lee, S.H., Kim, S.M., Suh, K.Y.: Soft lithography for microfluidics: a review. *Biochip J.* **2**(1), 1–11 (2008b)
- Kim, H.N., et al.: Rhodamine hydrazone derivatives as Hg²⁺ + selective fluorescent and colorimetric chemosensors and their applications to bioimaging and microfluidic system. *Analyst* **136**(7), 1339–1343 (2011)
- Kim, Y.J., Kang, Y.-T., Cho, Y.-H.: Poly(ethylene glycol)-modified tapered-slit membrane filter for efficient release of captured viable circulating tumor cells. *Anal. Chem.* **88**(16), 7938–7945 (2016)
- Kim, M., Abedini, A., Lele, P., Guerrero, A., Sinton, D.: Microfluidic pore-scale comparison of alcohol- and alkaline-based SAGD processes. *J. Petrol. Sci. Eng.* **154**, 139–149 (2017)
- King, M.B.B., Mubarak, A., Kim, J.D.D., Bott, T.R.R.: The mutual solubilities of water with supercritical and liquid carbon dioxides. *J. Supercrit. Fluids* **5**(4), 296–302 (1992)
- Kjeang, E., Djilali, N., Sinton, D.: Microfluidic fuel cells: a review. *J. Power Sour.* **186**(2), 353–369 (2009)
- Laerme, F., Schilp, A., Funk, K., Offenbergh, M.: Bosch deep silicon etching: improving uniformity and etch rate for advanced MEMS applications. In: 12th IEEE International Conference on Micro Electro Mechanical Systems, 1999. MEMS'99, pp. 211–216. IEEE (1999)
- Lake, L.W.: *Enhanced Oil Recovery*. Prentice Hall, Englewood Cliffs (2014)
- Le-The, H., et al.: Large-scale fabrication of free-standing and sub-[small mu]m PDMS through-hole membranes. *Nanoscale* **10**(16), 7711–7718 (2018)
- Lee, J.S., et al.: Placenta-on-a-chip: a novel platform to study the biology of the human placenta. *J. Matern. Fetal Neonatal Med.* **29**(7), 1046–1054 (2016)

- Lee Seung, G., Lee, H., Gupta, A., Chang, S., Doyle Patrick, S.: Site-selective in situ grown calcium carbonate micromodels with tunable geometry, porosity, and wettability. *Adv. Func. Mater.* **26**(27), 4896–4905 (2016)
- Lei, K.F.: Chapter 1 Materials and Fabrication Techniques for Nano- and Microfluidic Devices, *Microfluidics in Detection Science: Lab-on-a-chip Technologies*, pp. 1–28. The Royal Society of Chemistry, New York (2015)
- Leis, A.P., Schlicher, S., Franke, H., Strathmann, M.: Optically transparent porous medium for nondestructive studies of microbial biofilm architecture and transport dynamics. *Appl. Environ. Microbiol.* **71**(8), 4801–4808 (2005)
- Lenormand, R., Touboul, E., Zarcone, C.: Numerical models and experiments on immiscible displacements in porous media. *J. Fluid Mech.* **189**, 165–187 (1988)
- Li, X., Wu, N., Rojanasakul, Y., Liu, Y.: Selective stamp bonding of PDMS microfluidic devices to polymer substrates for biological applications. *Sens. Actuators A* **193**, 186–192 (2013)
- Li, Y., Kazemifar, F., Blois, G., Christensen, K.T.: Micro-PIV measurements of multiphase flow of water and liquid CO₂ in 2-D heterogeneous porous micromodels. *Water Resour. Res.* **53**(7), 6178–6196 (2017)
- Lim, L.S., et al.: Microsieve lab-chip device for rapid enumeration and fluorescence in situ hybridization of circulating tumor cells. *Lab Chip* **12**(21), 4388–4396 (2012)
- Liu, N., Aymonier, C., Lecoutre, C., Garrabos, Y., Marre, S.: Microfluidic approach for studying CO₂ solubility in water and brine using confocal Raman spectroscopy. *Chem. Phys. Lett.* **551**, 139–143 (2012)
- Liu, M., Shabaninejad, M., Mostaghimi, P.: Impact of mineralogical heterogeneity on reactive transport modelling. *Comput. Geosci.* **104**(Supplement C), 12–19 (2017)
- Lu, C., Lee, L.J., Juang, Y.J.: Packaging of microfluidic chips via interstitial bonding technique. *Electrophoresis* **29**(7), 1407–1414 (2008)
- Lu, W., Guo, H., Chou, I.M., Burruss, R.C., Li, L.: Determination of diffusion coefficients of carbon dioxide in water between 268 and 473 K in a high-pressure capillary optical cell with in situ Raman spectroscopic measurements. *Geochim. Cosmochim. Acta* **115**, 183–204 (2013)
- Madou, M.J.: *Fundamentals of Microfabrication: The Science of Miniaturization*. CRC Press, Boca Raton (2002)
- Mahoney, S.A., Rufford, T.E., Dmyterko, A.S.K., Rudolph, V., Steel, K.M.: The effect of rank and lithotype on coal wettability and its application to coal relative permeability models. In: *SPE Asia Pacific Unconventional Resources Conference and Exhibition, Brisbane*
- Mahoney, S.A., et al.: The effect of rank, lithotype and roughness on contact angle measurements in coal cleats. *Int. J. Coal Geol.* **179**, 302–315 (2017)
- Martin, M.M., Lindqvist, L.: The pH dependence of fluorescein fluorescence. *J. Lumin.* **10**(6), 381–390 (1975)
- Martínez-Mañez, R., Sancenón, F.: Fluorogenic and chromogenic chemosensors and reagents for anions. *Chem. Rev.* **103**(11), 4419–4476 (2003)
- Martinez, A.W., Phillips, S.T., Whitesides, G.M., Carrillo, E.: Diagnostics for the developing world: microfluidic paper-based analytical devices. *Anal. Chem.* **82**(1), 3–10 (2009)
- McDonald, J.C., et al.: Fabrication of microfluidic systems in poly(dimethylsiloxane). *Electrophoresis* **21**(1), 27–40 (2000)
- Meinhart, C.D., Wereley, S.T., Santiago, J.G.: PIV measurements of a microchannel flow. *Exp. Fluids* **27**(5), 414–419 (1999)
- Mela, P., et al.: Monolayer-functionalized microfluidics devices for optical sensing of acidity. *Lab Chip* **5**(2), 163–170 (2005)
- Moebius, F., Or, D.: Interfacial jumps and pressure bursts during fluid displacement in interacting irregular capillaries. *J. Colloid Interface Sci.* **377**(1), 406–415 (2012)
- Moebius, F., Or, D.: Pore scale dynamics underlying the motion of drainage fronts in porous media. *Water Resour. Res.* **50**(11), 8441–8457 (2014)
- Moghadas, H., Saidi, M.S., Kashaninejad, N., Kiyoumarsioskouei, A., Nguyen, N.-T.: Fabrication and characterization of low-cost, bead-free, durable and hydrophobic electrospun membrane for 3D cell culture. *Biomed. Microdevice* **19**(4), 74 (2017a)
- Moghadas, H., Saidi, M.S., Kashaninejad, N., Nguyen, N.-T.: Challenge in particle delivery to cells in a microfluidic device. *Drug Deliv. Transl. Res.* (2017b). <https://doi.org/10.1007/s13346-017-0467-3>
- Moghadas, H., Saidi, M.S., Kashaninejad, N., Nguyen, N.-T.: A high-performance polydimethylsiloxane electrospun membrane for cell culture in lab on a chip. *Biomicrofluidics* **12**(2), 024117 (2018)
- Mohammadzadeh, O., Chatzis, I.: Analysis of the heat losses associated with the SAGD visualization experiments. *J. Petrol. Explor. Prod. Technol.* **6**(3), 387–400 (2016)
- Mohammadzadeh, O., Rezaei, N., Chatzis, I.: Pore-level investigation of heavy oil and Bitumen recovery using solvent-aided steam assisted gravity drainage (SA-SAGD) process. *Energy Fuels* **24**(12), 6327–6345 (2010)

- Moraes, C., Mehta, G., Leshner-Perez, S.C., Takayama, S.: Organs-on-a-chip: a focus on compartmentalized microdevices. *Ann. Biomed. Eng.* **40**(6), 1211–1227 (2012)
- Morais, S., Diouf, A., Lecoutre, C., Bernard, D., Garrabos, Y., Marre, S.: Geological labs on chip—new tools for investigating key aspects of CO₂ geological storage. In: *The Third Sustainable Earth Sciences Conference and Exhibition* (2015)
- Morais, S., et al.: Monitoring CO₂ invasion processes at the pore scale using geological labs on chip. *Lab Chip* **16**(18), 3493–3502 (2016)
- Morin, B., Liu, Y., Alvarado, V., Oakey, J.: A microfluidic flow focusing platform to screen the evolution of crude oil-brine interfacial elasticity. *Lab Chip* **16**(16), 3074–3081 (2016)
- Moshksayan, K., et al.: Spheroids-on-a-chip: recent advances and design considerations in microfluidic platforms for spheroid formation and culture. *Sens. Actuators B Chem.* **263**, 151–176 (2018)
- Myers, D.R., et al.: Endothelialized microfluidics for studying microvascular interactions in hematologic diseases. *J. Vis. Exp. (JoVE)* **64**, 3958 (2012)
- Nan, Z., et al.: Manufacturing microstructured tool inserts for the production of polymeric microfluidic devices. *J. Micromech. Microeng.* **25**(9), 095005 (2015)
- Nguyen, C., Kothamasu, R., He, K., Xu, L.: Low-Salinity Brine Enhances Oil Production in Liquids-Rich Shale Formations. Society of Petroleum Engineers, London (2015)
- Nguyen, N.-T., Hejazian, M., Ooi, C.H., Kashaninejad, N.: Recent advances and future perspectives on microfluidic liquid handling. *Micromachines* **8**, 186 (2017)
- Nguyen, N.-T., Shaegh, S.A.M., Kashaninejad, N., Phan, D.-T.: Design, fabrication and characterization of drug delivery systems based on lab-on-a-chip technology. *Adv. Drug Deliv. Rev.* **65**(11–12), 1403–1419 (2013)
- Nieskens, T.T., Wilmer, M.J.: Kidney-on-a-chip technology for renal proximal tubule tissue reconstruction. *Eur. J. Pharmacol.* **790**, 46–56 (2016)
- Nolan, E.M., Lippard, S.J.: Tools and tactics for the optical detection of mercuric ion. *Chem. Rev.* **108**(9), 3443–3480 (2008)
- Nordbotten, J.M., Celia, M.A., Bachu, S.: Injection and storage of CO₂ in deep saline aquifers: analytical solution for CO₂ plume evolution during injection. *Transp. Porous Media* **58**(3), 339–360 (2005)
- Oh, Y.S., Jo, H.Y., Ryu, J.-H., Kim, G.-Y.: A microfluidic approach to water–rock interactions using thin rock sections: Pb and U sorption onto thin shale and granite sections. *J. Hazard. Mater. B* **324**, 373–381 (2017)
- Ohno, K.I., Tachikawa, K., Manz, A.: Microfluidics: applications for analytical purposes in chemistry and biochemistry. *Electrophoresis* **29**(22), 4443–4453 (2008)
- Olsen, M.G., Adrian, R.J.: Out-of-focus effects on particle image visibility and correlation in microscopic particle image velocimetry. *Exp. Fluids* **29**(7), S166–S174 (2000)
- Pacala, S., Socolow, R.: Stabilization wedges: solving the climate problem for the next 50 years with current technologies. *Science* **305**(5686), 968–972 (2004)
- Paguirigan, A.L., Beebe, D.J.: Microfluidics meet cell biology: bridging the gap by validation and application of microscale techniques for cell biological assays. *BioEssays* **30**(9), 811–821 (2008)
- Pei, H., Zhang, G., Ge, J., Jin, L., Ma, C.: Potential of alkaline flooding to enhance heavy oil recovery through water-in-oil emulsification. *Fuel* **104**, 284–293 (2013)
- Pensabene, V., et al.: Ultrathin polymer membranes with patterned, micrometric pores for organs-on-chips. *ACS Appl. Mater. Interfaces* **8**(34), 22629–22636 (2016)
- Porter, M.L., et al.: Fundamental Investigation of Gas Injection in Microfluidic Shale Fracture Networks at Geologic Conditions. American Rock Mechanics Association, New York (2015a)
- Porter, M.L., et al.: Geo-material microfluidics at reservoir conditions for subsurface energy resource applications. *Lab Chip* **15**, 4044–4053 (2015b)
- Prodanov, L., et al.: Long-term maintenance of a microfluidic 3D human liver sinusoid. *Biotechnol. Bioeng.* **113**(1), 241–246 (2016)
- Qin, N., Wen, J.Z., Ren, C.L.: Highly pressurized partially miscible liquid–liquid flow in a micro-*T*-junction. *I. Exp. Obser. Phys. Rev. E* **95**(4), 043110 (2017)
- Raffel, M., Willert, C.E., Wereley, S.T., Kompenhans, J.: *Particle Image Velocimetry: A Practical Guide*. Springer, Berlin (2013)
- Rangel-German, E., Kovscek, A.: A micromodel investigation of two-phase matrix-fracture transfer mechanisms. *Water Resour. Res.* **42**(3), 1 (2006)
- Rindfleisch, F., DiNoia, T.P., McHugh, M.A.: Solubility of polymers and copolymers in supercritical CO₂. *J. Phys. Chem.* **100**(38), 15581–15587 (1996)
- Rodríguez, S.J., Bishop, P.L.: Three-dimensional quantification of soil biofilms using image analysis. *Environ. Eng. Sci.* **24**(1), 96–103 (2007)
- Sackmann, E.K., Fulton, A.L., Beebe, D.J.: The present and future role of microfluidics in biomedical research. *Nature* **507**(7491), 181–189 (2014)

- Santiago, J.G., Wereley, S.T., Meinhart, C.D., Beebe, D.J., Adrian, R.J.: A particle image velocimetry system for microfluidics. *Exp. Fluids* **25**(4), 316–319 (1998)
- Sato, Y., et al.: Solubilities and diffusion coefficients of carbon dioxide and nitrogen in polypropylene, high-density polyethylene, and polystyrene under high pressures and temperatures. *Fluid Phase Equilib.* **162**(1–2), 261–276 (1999)
- Schmidt, M.A.: Wafer-to-wafer bonding for microstructure formation. *Proc. IEEE* **86**(8), 1575–1585 (1998)
- Schwartz, G., Schaible, P.: Reactive ion etching of silicon. *J. Vac. Sci. Technol.* **16**(2), 410–413 (1979)
- Seah, Y.F.S., Hu, H., Merten, C.A.: Microfluidic single-cell technology in immunology and antibody screening. *Mol. Aspects Med.* **59**, 47–61 (2017)
- Seah, Y.F.S., Hu, H., Merten, C.A.: Microfluidic single-cell technology in immunology and antibody screening. *Mol. Aspects Med.* **59**, 47–61 (2018)
- Sedaghat, M., Mohammadzadeh, O., Kord, S., Chatzis, I.: Heavy oil recovery using ASP flooding: a pore-level experimental study in fractured five-spot micromodels. *Can. J. Chem. Eng.* **94**(4), 779–791 (2016)
- Sell, A., Fadaei, H., Kim, M., Sinton, D.: Measurement of CO₂ diffusivity for carbon sequestration: a microfluidic approach for reservoir-specific analysis. *Environ. Sci. Technol.* **47**(1), 71–78 (2013)
- Shirota, H., Castner Jr., E.W.: Solvation in highly nonideal solutions: a study of aqueous 1-propanol using the coumarin 153 probe. *J. Chem. Phys.* **112**(5), 2367 (2000)
- Shiu, P.P., Knopf, G.K., Ostojic, M., Nikumb, S.: Rapid fabrication of tooling for microfluidic devices via laser micromachining and hot embossing. *J. Micromech. Microeng.* **18**(2), 025012 (2008)
- Sieben, V., Kharrat, A.M., Mostowfi, F.: Novel measurement of asphaltene content in oil using microfluidic technology. In: SPE Annual Technical Conference and Exhibition. Society of Petroleum Engineers, New Orleans (2013)
- Silverio, V., de Freitas, S.C.: *Microfabrication Techniques for Microfluidic Devices, Complex Fluid-Flows in Microfluidics*, pp. 25–51. Springer, Berlin (2018)
- Singh, R., et al.: Real rock-microfluidic flow cell: a test bed for real-time in situ analysis of flow, transport, and reaction in a subsurface reactive transport environment. *J. Contam. Hydrol.* **204**, 28–39 (2017)
- Singh, R., et al.: Metabolism-induced CaCO₃ biomineralization during reactive transport in a micromodel: implications for porosity alteration. *Environ. Sci. Technol.* **49**(20), 12094–12104 (2015)
- Sinton, D.: Energy: the microfluidic frontier. *Lab Chip* **14**(17), 3127–3134 (2014)
- Song, W., de Haas, T.W., Fadaei, H., Sinton, D.: Chip-off-the-old-rock: the study of reservoir-relevant geological processes with real-rock micromodels. *Lab Chip* **14**(22), 4382–4390 (2014)
- Song, W., Kovscek, A.R.: Functionalization of micromodels with kaolinite for investigation of low salinity oil-recovery processes. *Lab Chip* **15**(16), 3314–3325 (2015)
- Song, W., Kovscek, A.R.: Direct visualization of pore-scale fines migration and formation damage during low-salinity waterflooding. *J. Nat. Gas Sci. Eng.* **34**, 1276–1283 (2016)
- Stephan, K., et al.: Fast prototyping using a dry film photoresist: microfabrication of soft-lithography masters for microfluidic structures. *J. Micromech. Microeng.* **17**(10), N69 (2007)
- Stevenson, J.T.M., Gundlach, A.M.: The application of photolithography to the fabrication of microcircuits. *J. Phys. E: Sci. Instrum.* **19**(9), 654 (1986)
- Syed, A.H., et al.: A combined method for pore-scale optical and thermal characterization of SAGD. *J. Petrol. Sci. Eng.* **146**, 866–873 (2016)
- Tan, S.H., Nguyen, N.-T., Chua, Y.C., Kang, T.G.: Oxygen plasma treatment for reducing hydrophobicity of a sealed polydimethylsiloxane microchannel. *Biomicrofluidics* **4**(3), 032204 (2010)
- Tanino, Y., Zacarias-Hernandez, X., Christensen, M.: Oil/water displacement in microfluidic packed beds under weakly water-wetting conditions: competition between precursor film flow and piston-like displacement. *Exp. Fluids* **59**(2), 35 (2018)
- Trietsch, S.J., Hankemeier, T., van der Linden, H.J.: Lab-on-a-chip technologies for massive parallel data generation in the life sciences: a review. *Chemometr. Intell. Lab. Syst.* **108**(1), 64–75 (2011)
- Tropea, C., Yarin, A.L., Foss, J.F.: *Springer Handbook of Experimental Fluid Mechanics*. Springer, Berlin (2007)
- Tsao, C.-W., DeVoe, D.L.: Bonding of thermoplastic polymer microfluidics. *Microfluid. Nanofluid.* **6**(1), 1–16 (2009)
- Unsal, E., Broens, M., Armstrong, R.T.: Pore scale dynamics of microemulsion formation. *Langmuir* **32**(28), 7096–7108 (2016)
- van der Helm, M.W., van der Meer, A.D., Eijkel, J.C., van den Berg, A., Segerink, L.I.: Microfluidic organ-on-chip technology for blood-brain barrier research. *Tissue Barriers* **4**(1), e1142493 (2016)
- Verpoorte, E., De Rooij, N.F.: Microfluidics meets MEMS. *Proc. IEEE* **91**(6), 930–953 (2003)
- Vladisavljević, G.T., Kobayashi, I., Nakajima, M.: Production of uniform droplets using membrane, microchannel and microfluidic emulsification devices. *Microfluid. Nanofluid.* **13**(1), 151–178 (2012)

- Volpatti, L.R., Yetisen, A.K.: Commercialization of microfluidic devices. *Trends Biotechnol.* **32**(7), 347–350 (2014)
- Wang, W., Chang, S., Gizzatov, A.: Toward reservoir-on-a-chip: fabricating reservoir micromodels by in situ growing calcium carbonate nanocrystals in microfluidic channels. *ACS Appl. Mater. Interfaces* **9**(34), 29380–29386 (2017)
- Wang, X., Ding, B., Li, B.: Biomimetic electrospun nanofibrous structures for tissue engineering. *Mater. Today* **16**(6), 229–241 (2013a)
- Wang, Y., et al.: Application of microfluidic technology for studying islet physiology and pathophysiology. *Micro Nanosyst.* **5**(3), 216–223 (2013b)
- Wang, Y., et al.: Experimental study of crossover from capillary to viscous fingering for supercritical CO₂–water displacement in a homogeneous pore network. *Environ. Sci. Technol.* **47**(1), 212–218 (2013c)
- Warkiani, M.E., et al.: Capturing and recovering of *Cryptosporidium parvum* oocysts with polymeric micro-fabricated filter. *J. Membr. Sci.* **369**(1), 560–568 (2011)
- Warkiani, M.E., et al.: Slanted spiral microfluidics for the ultra-fast, label-free isolation of circulating tumor cells. *Lab Chip* **14**(1), 128–137 (2014a)
- Warkiani, M.E., et al.: An ultra-high-throughput spiral microfluidic biochip for the enrichment of circulating tumor cells. *Analyst* **139**(13), 3245–3255 (2014b)
- Webb, K.F., Teja, A.S.: Solubility and diffusion of carbon dioxide in polymers. *Fluid Phase Equilib.* **158–160**(1), 1029–1034 (1999)
- Westerweel, J.: Fundamentals of digital particle image velocimetry. *Meas. Sci. Technol.* **8**(12), 1379 (1997)
- White, C.M., et al.: Separation and capture of CO₂ from large stationary sources and sequestration in geological formations—coalbeds and deep saline aquifers separation and capture of CO₂ from large stationary sources and sequestration in geological formations—coalbeds. *J. Air Waste Manag. Assoc.* **53**(6), 645–715 (2003)
- Whitesides, G.: The origins and the future of microfluidics. *Nature* **442**, 368–373 (2006a)
- Whitesides, G.M.: The origins and the future of microfluidics. *Nature* **442**(7101), 368–373 (2006b)
- Wiebe, R., Gaddy, V.L.: The solubility of carbon dioxide in water at various temperatures from 12° to 40° and at pressures to 500 atmospheres. *Critical phenomena.* *J. Am. Chem. Soc.* **62**(4), 815–817 (1940)
- Wong, I., Ho, C.-M.: Surface molecular property modifications for poly(dimethylsiloxane)(PDMS) based microfluidic devices. *Microfluid. Nanofluid.* **7**(3), 291–306 (2009)
- Wu, B., Kumar, A., Pamarthy, S.: High aspect ratio silicon etch: a review. *J. Appl. Phys.* **108**(5), 9 (2010)
- Xu, B., et al.: High efficiency integration of three-dimensional functional microdevices inside a microfluidic chip by using femtosecond laser multifoci parallel microfabrication. *Sci. Rep.* **6**, 19989 (2016)
- Xu, R., Li, R., Huang, F., Jiang, P.: Pore-scale visualization on a depressurization-induced CO₂ exsolution. *Sci. Bull.* **62**, 795–803 (2017)
- Xu, W., Ok, J.T., Xiao, F., Neeves, K.B., Yin, X.: Effect of pore geometry and interfacial tension on water-oil displacement efficiency in oil-wet microfluidic porous media analogs. *Phys. Fluids* **26**(9), 093102 (2014)
- Yadali Jamaloei, B., Kharrat, R.: Analysis of microscopic displacement mechanisms of dilute surfactant flooding in oil-wet and water-wet porous media. *Transp. Porous Media* **81**(1), 1 (2009)
- Yang, S.-Y., et al.: Single-file diffusion of protein drugs through cylindrical nanochannels. *ACS Nano* **4**(7), 3817–3822 (2010)
- Yang, Y.-K., Yook, K.-J., Tae, J.: A rhodamine-based fluorescent and colorimetric chemodosimeter for the rapid detection of Hg²⁺ ions in aqueous media. *J. Am. Chem. Soc.* **127**(48), 16760–16761 (2005)
- Yaozhong, Z., Jea-Hyeoung, H., Likun, Z., Mark, A.S., Junghoon, Y.: Soft lithographic printing and transfer of photosensitive polymers: facile fabrication of free-standing structures and patterning fragile and unconventional substrates. *J. Micromech. Microeng.* **24**(11), 115019 (2014)
- Yoon, H., Valocchi, A.J., Werth, C.J., Dewers, T.: Pore-scale simulation of mixing-induced calcium carbonate precipitation and dissolution in a microfluidic pore network. *Water Resour. Res.* **48**(2), W02524 (2012)
- Yoon, J.-Y., Kim, B.: Lab-on-a-chip pathogen sensors for food safety. *Sensors* **12**(8), 10713–10741 (2012)
- Zarikos, I.M., Hassanizadeh, S.M., van Oosterhout, L.M., van Oordt, W.: *Manufacturing a Micro-model with Integrated Fibre Optic Pressure Sensors.* Transport in Porous Media, New York (2018)
- Zevi, Y., Dathe, A., McCarthy, J.F., Richards, B.K., Steenhuis, T.S.: Distribution of colloid particles onto interfaces in partially saturated sand. *Environ. Sci. Technol.* **39**(18), 7055–7064 (2005)
- Zhang, C., Oostrom, M., Grate, J.W., Wietsma, T.W., Warner, M.G.: Liquid CO₂ displacement of water in a dual-permeability pore network micromodel. *Environ. Sci. Technol.* **45**(17), 7581–7588 (2011)
- Zhang, J., Chen, K., Fan, Z.H.: Chapter one-circulating tumor cell isolation and analysis. In: Makowski, G.S. (ed.) *Advances in Clinical Chemistry*, pp. 1–31. Elsevier, Amsterdam (2016)
- Zhang, Q., Karadimitriou, N.K., Hassanizadeh, S.M., Kleingeld, P.J., Imhof, A.: Study of colloids transport during two-phase flow using a novel polydimethylsiloxane micro-model. *J. Colloid Interface Sci.* **401**, 141–147 (2013)

- Zhang, W., et al.: Liquid biopsy for cancer: circulating tumor cells, circulating free DNA or exosomes? *Cell. Physiol. Biochem.* **41**(2), 755–768 (2017)
- Zhang, Y., Sanati-Nezhad, A., Hejazi, S.: Geo-material surface modification of microchips using layer-by-layer (LbL) assembly for subsurface energy and environmental applications. *Lab Chip* **18**(2), 285–295 (2018)
- Zhao, B., MacMinn, C.W., Juanes, R.: Wettability control on multiphase flow in patterned microfluidics. *Proc. Natl. Acad. Sci.* **113**(37), 10251–10256 (2016)
- Zheng, X., Mahabadi, N., Yun, T.S., Jang, J.: Effect of capillary and viscous force on CO₂ saturation and invasion pattern in the microfluidic chip. *J. Geophys. Res. Solid Earth* **122**(3), 1634–1647 (2017)
- Zuo, L., Zhang, C., Falta, R.W., Benson, S.M.: Micromodel investigations of CO₂ exsolution from carbonated water in sedimentary rocks. *Adv. Water Resour.* **53**(6), 188–197 (2013)

Publisher's Note Springer Nature remains neutral with regard to jurisdictional claims in published maps and institutional affiliations.

Statement of Authorship

Title of Paper	Functionalisation of Polydimethylsiloxane (PDMS)-Microfluidic Devices coated with Rock Minerals
Publication Status	<input checked="" type="checkbox"/> Published <input type="checkbox"/> Accepted for Publication <input type="checkbox"/> Submitted for Publication <input type="checkbox"/> Unpublished and Unsubmitted work written in manuscript style
Publication Details	Alzahid, Y. A., Mostaghimi, P., Gerami, A., Singh, A., Privat, K., Amirian, T., & Armstrong, R. T. (2018). Functionalisation of Polydimethylsiloxane (PDMS)-Microfluidic Devices coated with Rock Minerals. Scientific reports, 8(1), 15518.

Co-Author

Name of Co-Author (Candidate)	Tammy Amirian		
Contribution to the Paper	Critically revised the manuscript and helped with interpretation of data.		
Overall percentage (%)	10%		
Signature		Date	27/03/19

Co-Author Contributions

By signing the Statement of Authorship, each author certifies that:

- the candidate's stated contribution to the publication is accurate (as detailed above);
- permission is granted for the candidate to include the publication in the thesis; and
- The sum of all co-author contributions is equal to 100% less the candidate's stated contribution.

Name of Co-Author	Yara Alzahid		
Contribution to the Paper	Designed the research work. Constructed the experimental apparatus and conducted the experiments. Conducted data analysis. Wrote the manuscript with input from all other authors.		
Signature		Date	11/4/2019

Name of Co-Author	Peyman Mostaghimi		
Contribution to the Paper	Critically revised the manuscript and helped with interpretation of data.		
Signature		Date	27/3/19

Name of Co-Author	Alireza Gerami		
Contribution to the Paper	Constructed the experimental apparatus and conducted the experiments. Conducted data analysis.		
Signature		Date	27/03/2019

Name of Co-Author	Ankita Singh		
Contribution to the Paper	Constructed the experimental apparatus and conducted the experiments. Conducted data analysis.		
Signature		Date	27/3/2019

Please cut and paste additional co-author panels here as required.

Name of Co-Author	Karen Privat		
Contribution to the Paper	Constructed the experimental apparatus and conducted the experiments.		
Signature		Date	

Name of Co-Author	Ryan Armstrong		
Contribution to the Paper	Designed the research work. Constructed the experimental apparatus and conducted the experiments. Conducted data analysis. Wrote the manuscript with input from all other authors. Critically revised the manuscript and helped with interpretation of data.		
Signature		Date	27-3-19

Statement of Authorship

Title of Paper	Functionalisation of Polydimethylsiloxane (PDMS)-Microfluidic Devices coated with Rock Minerals
Publication Status	<input checked="" type="checkbox"/> Published <input type="checkbox"/> Accepted for Publication <input type="checkbox"/> Submitted for Publication <input type="checkbox"/> Unpublished and Unsubmitted work written in manuscript style
Publication Details	Alzahid, Y. A., Mostaghimi, P., Gerami, A., Singh, A., Privat, K., Amirian, T., & Armstrong, R. T. (2018). Functionalisation of Polydimethylsiloxane (PDMS)-Microfluidic Devices coated with Rock Minerals. Scientific reports, 8(1), 15518.

Co-Author

Name of Co-Author (Candidate)	Tammy Amirian		
Contribution to the Paper	Critically revised the manuscript and helped with interpretation of data.		
Overall percentage (%)	10%		
Signature		Date	

Co-Author Contributions

By signing the Statement of Authorship, each author certifies that:

- i. the candidate's stated contribution to the publication is accurate (as detailed above);
- ii. permission is granted for the candidate to include the publication in the thesis; and
- iii. The sum of all co-author contributions is equal to 100% less the candidate's stated contribution.

Name of Co-Author	Yara Alzahid		
Contribution to the Paper	Designed the research work. Constructed the experimental apparatus and conducted the experiments. Conducted data analysis. Wrote the manuscript with input from all other authors.		
Signature		Date	

Name of Co-Author	Peyman Mostaghimi		
Contribution to the Paper	Critically revised the manuscript and helped with interpretation of data.		
Signature		Date	

Name of Co-Author	Alireza Gerami		
Contribution to the Paper	Constructed the experimental apparatus and conducted the experiments. Conducted data analysis.		
Signature		Date	


Name of Co-Author	Ankita Singh		
Contribution to the Paper	Constructed the experimental apparatus and conducted the experiments. Conducted data analysis.		
Signature		Date	

Please cut and paste additional co-author panels here as required.

Name of Co-Author	Karen Privat		
Contribution to the Paper	Constructed the experimental apparatus and conducted the experiments.		
Signature		Date	4/4/19

Name of Co-Author	Ryan Armstrong		
Contribution to the Paper	Designed the research work. Constructed the experimental apparatus and conducted the experiments. Conducted data analysis. Wrote the manuscript with input from all other authors. Critically revised the manuscript and helped with interpretation of data.		
Signature		Date	

SCIENTIFIC REPORTS



OPEN

Functionalisation of Polydimethylsiloxane (PDMS)-Microfluidic Devices coated with Rock Minerals

Yara A. Alzahid¹ , Peyman Mostaghimi¹, Alireza Gerami¹, Ankita Singh¹, Karen Privat² , Tammy Amirian³ & Ryan T. Armstrong¹

Fluid flow in porous rocks is commonly capillary driven and thus, dependent on the surface characteristics of rock grains and in particular the connectivity of corners and crevices in which fluids reside. Traditional microfluidic fabrication techniques do not provide a connected pathway of crevices that are essential to mimic multiphase flow in rocks. Here, geo-material microfluidic devices with connected pathways of corners and crevices were created by functionalising Polydimethylsiloxane (PDMS) with rock minerals. A novel fabrication process that provides attachment of rock minerals onto PDMS was demonstrated. The geo-material microfluidic devices were compared to carbonate and sandstone rocks by using energy dispersive X-ray spectroscopy, scanning electron microscopy (SEM), contact angle measurements, and a surface profilometer. Based on SEM coupled with energy-dispersive X-ray spectrometry (SEM-EDS) analyses, roughness measurements, contact angle, wettability, and roughness were comparable to real rocks. In addition, semivariograms showed that mineral deposition across the different geo-material devices was nearly isotropic. Lastly, important multiphase flow phenomena, such as snap-off and corner flow mechanisms, equivalent to those occurring in reservoir rocks have been visualised. The presented approach can be used to visualise rock-fluid interactions that are relevant to subsurface engineering applications, such as hydrocarbon recovery and CO₂ sequestration.

Multiphase flow is relevant to several industrial fields, such as geologic CO₂ sequestration^{1–4}, enhanced oil recovery^{5–7}, hydrology^{8,9} and fuel cells¹⁰. Wettability, which is the preference of a fluid to a solid, is a key parameter that influences multiphase flow in porous media^{11–15}. Wettability of surfaces is commonly quantified through contact angle (θ) measurements where $\theta < 90^\circ$ corresponds to water-wet surfaces and $\theta > 90^\circ$ corresponds to oil-wet surfaces^{11,16}. Flow mechanisms that occur between rock grains are highly dependent on wettability, such as snap-off¹⁷ and corner flow¹⁸, and are of particular interest for carbon capture and storage¹⁹ and enhanced oil recovery technologies^{5–7}. Hence, visualising these processes in an environment similar to that of rock grains that provides contact angles and flow mechanisms equivalent to those found in reservoir rocks is essential to the design of any microfluidic device and the subsequent study of the fundamental physics that occur within the space between rock grains.

Snap-off and corner flow are responsible for disconnection and trapping of hydrocarbons and/or CO₂. Snap-off occurs when a droplet of non-wetting phase (typically oil or gas) disconnects, leading to the trapping of that phase (Fig. 1). The basic physics of snap-off was first described by Rayleigh²⁰. Flow instabilities arise due to geometrical changes, resulting in differences of capillary pressure. For a jet, as described by Rayleigh²⁰, with a given wavelength, regions of constriction develop, leading to higher capillary pressures than adjacent regions. This high capillary pressure causes fluids to flow away from the constriction eventually resulting in the collapse of an interface. For a porous media, a similar situation occurs when an oil droplet spans many pores.

¹School of Minerals and Energy Resources Engineering, The University of New South Wales, Sydney, NSW, 2052, Australia. ²Electron Microscope Unit, The University of New South Wales, Sydney, NSW, 2052, Australia. ³Australian School of Petroleum, Faculty of Engineering, Computer and Mathematical Sciences, The University of Adelaide, Adelaide, SA, 5000, Australia. Correspondence and requests for materials should be addressed to R.T.A. (email: Ryan.armstrong@unsw.edu.au)

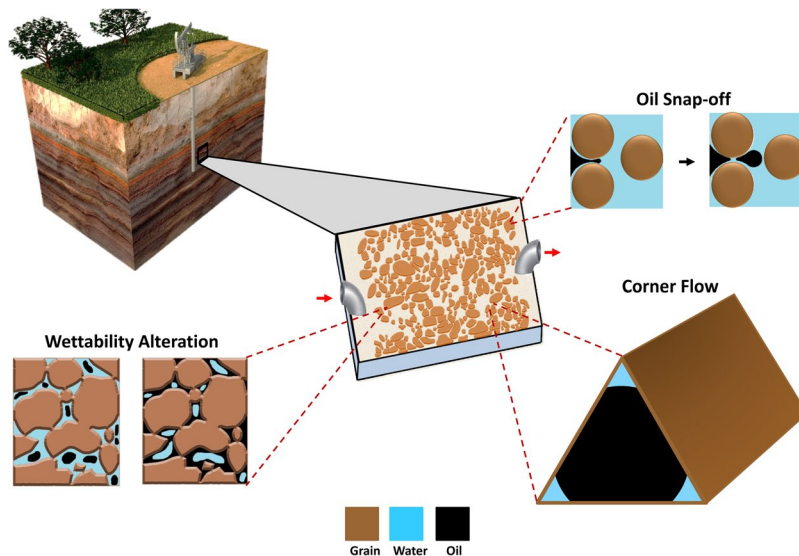


Figure 1. Geo-material microfluidic chip (centred) and its applications/features. This figure highlights the ability to re-create the reservoir rock environment, due to the added minerals on the grains and pore space of the microfluidic platform. This type of microfluidics devices can capture several important rock/fluid features, including: corner flow, wetting conditions (oil or water-wet), and snap-off.

The leading and trailing ends of the oil droplet have a given capillary pressure, while the pore throat constriction between pores can result in a larger capillary pressure due to the swelling of a wetting film in the neck region. Hence, the formation of snap-off is also largely dependent on the specific pore geometry, i.e. pore-wall curvature, and pressures in the wetting and nonwetting phases^{21,22}. For a complete water-wet environment ($\theta = 0$), and at capillary-dominated flow regime, snap-off favours a large aspect ratio (pore radius/ throat radius) during an imbibition process, such as water flooding^{5,23–25}. In pores of rocks with complex pore geometry, snap-off is controlled by corner flow (Fig. 1), which is the advancement of the wetting phase through connected water films that cover the water-wet grains. This mechanism was proposed by Ransohoff, *et al.*²⁶ as the quasi-static snap-off criterion, which predicts non-wetting phase snap-off within a smoothly constricted noncircular capillary.

In water-wet rocks, thin films of water cover the surfaces of grains and extend across adjacent grains. These films influence immiscible displacement. For example, in enhanced oil recovery processes and during imbibition, water is known to flow in the pore space via the wetting films ahead of the advancing meniscus, bridging across the pore space containing oil, which creates the possibility for snap-off events and influences the order in which pores are saturated. Pore network models are often used to demonstrate the importance of corner flow during immiscible displacement²⁷. Other parameters such as aspect ratio²⁸, flow rate²⁹, contact angles^{7,30} and dimensionless parameters (such as capillary number and viscosity ratio)^{28,31–35} have also been investigated using pore-network models. Pore network models that do not account for corner flow provide significantly different results than models that allow for the wetting phase to reside in the corners of the network³¹. Therefore, when considering idealised geometries for experiments, it is essential to consider systems that support the natural mechanisms of porous media flow.

Throughout the past few decades, microfluidic devices with porous media patterns representing porous rock have been used to study fluid flow for subsurface engineering^{6,36–39}. Images or 3D models of actual porous rock can be generated using micro-computed tomography (micro-CT), focused ion beam-scanning electron microscope (FIB-SEM) or nuclear magnetic resonance (NMR)^{36,40–42} methods. These images can then be transformed to a microfluidic chip using standard photolithography or soft photolithography⁴². Karadimitriou and Hassanizadeh⁴³ summarise microfabrication methods for micromodels and the history of their usage in soil science and petroleum research, particularly enhanced oil recovery (EOR)^{6,36,38,44–46}. However, microfluidic models generally do not allow for the connectivity of corners and crevices due to their 2D nature, in addition to their lack of roughness, which can limit the type of flow processes that occur during immiscible displacement experiments.

Several fabrication methods for geo-material chips have been proposed to produce microfluidics devices that mimic real rock. Song, *et al.*³⁷ developed an approach to study acid injection in carbonate formation by etching microfluidics channels into a natural calcite rock, which required multiple pre-processing steps. Song and Kovscek⁴⁷ developed a method to create a functionalised 2D silicon micromodel with pore surfaces coated mainly with kaolinite clay, which allows for the study of fluid–solid interactions. In addition, these authors published another paper describing the use of their functionalised microfluidic platform to study the response of clay to low salinity brine injection⁴⁸. Other microfluidic device modifications that aid in representing real rock include altering the wettability of the porous network. Lee, *et al.*⁴⁹ developed a novel method termed “Stop-Flow-Lithography (SFL)” to fabricate microfluidics devices with controlled wetting properties in a single lithographic step. They showed immiscible fluid displacement in single pore bodies with varying wetting properties. Porter, *et al.*⁵⁰ developed a novel fabrication method whereby fractures are etched into thin sections of different rock types (shale,

sandstone, and siltstone) by a custom-built femtosecond laser direct-write (LDW) system. Similarly, Gerami, *et al.*⁵¹ presented a coal geo-material microfluidic chip that was fabricated by etching a fracture pattern into a coal surface using three-dimensional laser micromachining. Wang, *et al.*⁵² demonstrated a novel way to coat a controlled thickness of calcite (CaCO₃) nanocrystal layer onto a simple glass microfluidic channel. This process was achieved by converting the inner surface of the microfluidic silica channels to CaCO₃ through numerous chemical surface modifications to functionalise the glass surface to grow a CaCO₃ nanocrystal layer. Singh, *et al.*⁵³ used another approach to design a microfluidic device of a sandstone rock called “Real Rock Microfluidic Flow Cell” (RRMFC). They mounted a thin section (500 μm) of a sandstone rock between two covers that were bonded via a plasma generator. Lastly, another approach taken by Zhu and Papadopoulos⁵⁴ demonstrated two-phase flow in transparent miniature packed beds with rough grains and analysed the effect of roughness on flow.

Traditionally, core-flooding experiments are conducted to establish the wettability, capillary pressure data, relative permeability curves, and oil recovery for a given reservoir rock sample⁵². With different geo-material microfluidics, or rock-on-a-chip methods, oil recovery can be measured and pore-scale mechanisms (on the order of micrometres) can be captured. EOR mechanisms such as chemical or low salinity can be tested prior to core scale experiments to study a wide range of the parameter space necessary to understand pore-scale oil recovery mechanisms and/or evaluate screening criteria for particular EOR applications. This can guide the planning and assessment of core floods and/or illustrate if a given EOR mechanism could suppress oil snap-off, enhance dissolution and/or cause fines migration for a given set of flooding conditions.

The aforementioned fabrication methods of geo-material microfluidics devices involve several pre-processing and complex fabrication steps, in addition to the use of expensive machines and/or packed grains that obstruct visualisation. In addition, the previous works have not provided evidence that the essential pore-scale flow mechanism of corner flow leading to snap-off actually occur in the fabricated geo-material chips. We propose a simple process for functionalising the pore space of PDMS microfluidic chips with rock minerals and controlled wetting conditions, which allows for snap-off and corner flow mechanisms to occur. The resulting geo-material microfluidic device allows for direct visualisation and understanding of rock-fluid interactions in oil reservoirs during any type of flooding. We describe the coating of PDMS microfluidic chips with the following materials: (1) quartz and kaolinite to represent sandstone⁵⁵ formations, and (2) calcite to represent carbonate formations⁵⁶. We characterise the surface composition, roughness, wettability, and uniformity of the functionalised PDMS models and compare them with reservoir rock samples. Lastly, we conduct water flooding experiments to study the resulting pore-scale flow mechanisms and conclude that many of the well-established mechanisms important for porous media flow are captured by the microfluidic device due to the wettability and connectivity of corners and crevices added by the geo-material coating process.

Results and Discussion

PDMS Surface modifications for generating geo-material microfluidic chips. The process of treating PDMS with oxygen plasma is well-understood^{57–59}. On exposure to oxygen plasma, silanol groups (Si–OH) are added to replace –CH₃ on the PDMS structure, which comprises of –O–Si(CH₃)₂– repetition units prior to plasma treatment. The Si–OH groups are then able to bond with other functional groups, such as –OH, –COOH, and ketone, when the two surfaces are brought into contact^{57–61} as depicted in Fig. 2. Plasma treatment of PDMS is crucial to functionalise the surface for depositing sandstone and carbonate mineral mixtures. In the quartz and kaolinite suspension, the presence of silicate oxygen groups in the quartz and kaolinite and hydrogen groups along the edge of the kaolinite particles are the main active groups that bond with silanol groups on the PDMS surface. Both oxygen atoms and hydroxyl groups in the quartz and kaolinite suspension can hydrogen bond with the hydroxyl groups at the ends of the PDMS chain. As for the calcite mixture, due to its suspension in water, the hydroxyl groups and calcium ions can also bond with silanol groups on the PDMS. Figure 2 highlights the bonding of chemical structures for both the sandstone and calcite suspensions with silanol groups present on the PDMS surface. Further details on fabrication are discussed in the Methods section.

Minerals Coating Characterisation. To characterise the functionalised PDMS surface, we used semivariograms to study the spatial arrangements of the deposited minerals and compared SEM-EDS measurements to equivalent measurements taken from reservoir rock samples. The semivariograms in Fig. 3a and b illustrate the average semivariance of the mineral deposition for both sandstone and carbonate PDMS chips, respectively for a lag distance of up to 50-pixel values (333.34 μm, scale of 0.15 pixels/μm) in both the horizontal (0°) and vertical (90°) directions. The semivariances in both samples show the expected trend of increasing semivariance with increased lag distance. The semi-variances increase with pixel distance (or lag distance) because pixels adjacent to each other are more correlated to each other than pixels far apart. The error bars in Fig. 3a and b indicate the variation in average semivariances for a lag distance of 3, 10, 20, 30 and 50 pixels for the minerals deposited on three independent sandstone and carbonate chips. For sandstone (Fig. 3a), the error bars demonstrate that there were measurable differences in the horizontal and vertical directions. This occurred because the measured variance between tested locations on the PDMS sandstone chip are relatively small resulting in narrow error bars. Conversely, the error bars for mineral deposition in the case of carbonate (Fig. 3b) are wider, which demonstrates that the variation between independent samples was greater than that for the sandstone PDMS chip. Therefore, for the carbonate PDMS chip, there were no measurable differences in the semivariances in the horizontal (0°) and vertical (90°) directions. Overall, for both sandstone and carbonate depositions, the semivariances in the horizontal (0°), and vertical (90°) directions are similar suggesting that the deposition was nearly isotropic. Isotropic deposition is an important factor for mineral deposition since wetting films are likely to be established in the deposited minerals and a directional bias of wetting films could influence experimental results.

The surface roughness data of the geo-material chips are calculated and compared to roughness values measured for carbonate and sandstone rocks. The data are obtained from the surface height profiles of multiple

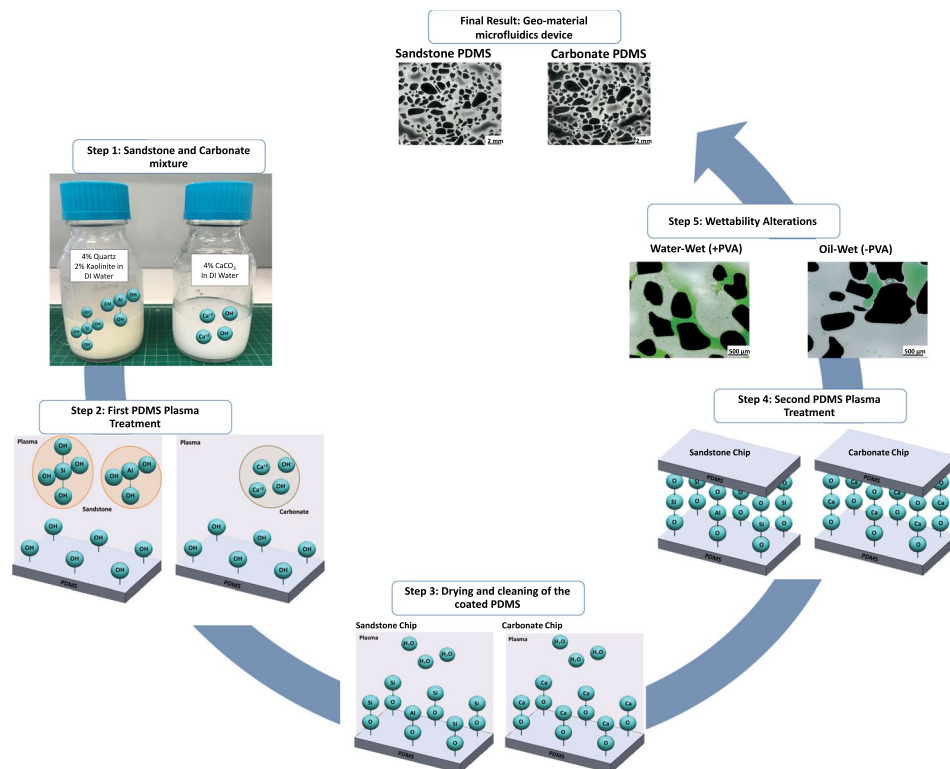


Figure 2. The workflow for fabrication of the geo-material PDMS microfluidics device. The sandstone and carbonate mixtures are first prepared by mixing quartz and kaolinite in DI water, and calcite in DI water, respectively. When mixing quartz and kaolinite with DI water, it mainly results in soluble silica (SiOH_4), also referred to as silicic acid, and kaolinite gibbsite (AlOH_3). As for the calcite mixture, the calcium carbonate does not mix well with water, as it rapidly separates when left stagnant, however, some calcium ions separate and can attach with silanol group in subsequent steps. When the two PDMS slides with the porous media are exposed to oxygen plasma, it attaches silanol groups on the PDMS surface, rendering it water-wet temporarily, these silanol groups then bond with the silicic acid and kaolinite gibbsite in the sandstone mixture, creating very strong siloxane bond and Al-O-Si bonds. As for the calcium hydroxide, it also attaches to the silanol groups. Then, both chips are air-dried and cleaned with Ethanol. After ensuring the pillars in the PDMS chips are clean, the PDMS with the deposited materials and PDMS slabs (covers) undergo a second plasma treatment, creating additional SiOH groups on both PDMS slides, and immediately put in conformal contact, which results in a sealed geo-material PDMS chip. Wettability alterations can then be made by adding 1% PVA solution immediately after the second plasma treatment, which makes the geo-material water-wet. Without PVA treatment the geo-material PDMS device is oil-wet.

locations on each sample. In total, 15 locations of roughness measurements for carbonate PDMS and rock, 21 locations for sandstone PDMS and 19 locations for sandstone rock are collected. The results indicate similar roughness data for the pore surfaces of the fabricated chips and the real rock surfaces. For instance, only 9.9% variation exists between the roughness of the sandstone PDMS chip and sandstone rock. For the carbonate coated chip the variation of roughness from the real rock is 14.7%. The box plot in Fig. 3c confirms similar roughness data for the pore surfaces of the fabricated chips and the rock surfaces. For both sandstone and carbonate rocks and functionalised PDMS models, the median values (middle lines in the box plots) of roughness are similar. In addition, the roughness of a blank PDMS chip was also evaluated and the roughness data are staunchly different than functionalised PDMS (Fig. 3c). One limitation from this analysis is that these results are only valid for the rocks examined. Different roughness profiles could occur when comparing the functionalised PDMS surface to other sandstone and carbonate rocks.

SEM images of PDMS chips containing mineral depositions (x100) and a higher magnification (x3k) image of the relevant rock slice are present in Fig. 4. Images of the PDMS containing the minerals of interest (Fig. 4a,b,e and f) can be comparable with the rock image (Fig. 4c and g), as the particle morphologies are similar. Furthermore, EDS elemental analysis was performed on the rock slices and PDMS microfluidics chips. Normalised EDS results for the two samples provide comparable results with their respective rock types (Fig. 4d and h). However, the carbonate rock and calcite-PDMS do not exhibit exact elemental spectra in Fig. 4h, due to the presence of silicon in the PDMS backbone. In the case of the calcite-PDMS and limestone rock, the calcium peaks are similar (Fig. 4h). Carbon is present in both rock and geo-material PDMS chips due to the required carbon coating for SEM imaging. Overall, the surface chemistry appears to be similar for the functionalised chips and their reservoir rock equivalents.

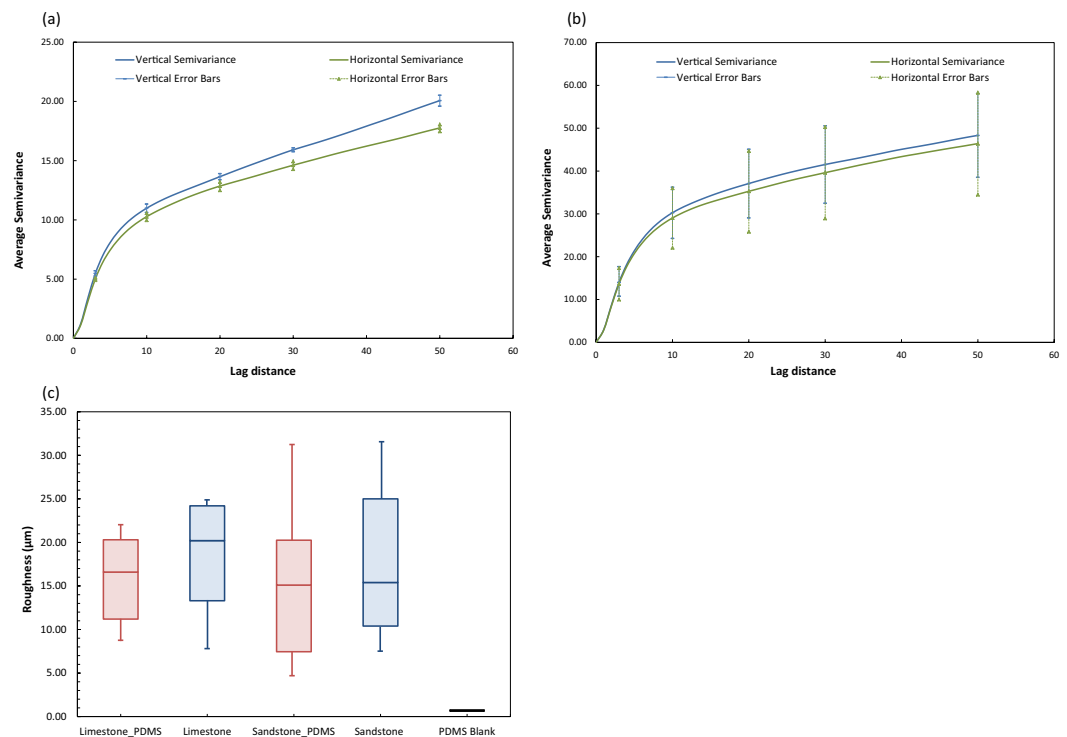


Figure 3. (a) Average semivariance of the sandstone PDMS chip. (b) Average semivariance of the carbonate PDMS chip. The error bars in a and b indicate the variation in average semivariances for a lag distance of 3, 10, 20, 30 and 50 pixel distance for the mineral deposited on three sandstone images and three carbonate images, respectively. (c) Box plot with surface height profile measurements for target areas of $x = 1418 \mu\text{m}$, $y = 1000 \mu\text{m}$ for PDMS coated with carbonate (or limestone) mixture, limestone rock, PDMS coated with the sandstone mixture, sandstone rock and blank PDMS.

Establishment of Surface Wettability. PDMS is strongly oil-wet with contact angles $>100^\circ$ ^{57–59,61,62}. A plasma treated PDMS surface temporarily creates alcoholic hydroxyls (C–OH), silanols (Si–OH), and carboxylic acids (COOH)^{57,59} that render the surface water wet for a limited period of time. As reported in Trantidou, *et al.*⁶¹, applying PVA to a plasma treated PDMS surface creates hydrogen bonds between the PVA molecules and the plasma treated PDMS surfaces. These hydrogen bonds on the PDMS form permanent water-wet surfaces rather than the temporary treatment created by only plasma treatment (Fig. 5). The PDMS surface treatment method developed by Trantidou, *et al.*⁶¹ was applied to our fabricated geo-material chips. Several tests were conducted to understand how the method influences the wettability of PDMS and the deposited minerals. Sandstone, carbonate and un-deposited PDMS chips were treated with PVA immediately after plasma oxidation, as described in Trantidou, *et al.*⁶¹ and imaged after 3 days to eliminate the effect of plasma oxidation. PDMS with and without PVA treatment were first subjected to connate water flooding (green), then decane oil (transparent) and left to equilibrate for 10 minutes. The three chips are shown in Fig. 6. We observe connected thin films of connate water (green) in the geo-material PDMS chips of sandstone and carbonate with PVA treatment (Fig. 6b), which demonstrates that these chips are water wet. Alternatively, without PVA treatment (Fig. 6a), PDMS is highly oil wet in all three conditions. As explained previously, the reason that PVA can alter the wettability of PDMS is that it irreversibly adsorbs onto the hydrophobic polymer films of PDMS, which alters its chemistry by the formation of hydrogen bonds between PVA and the activated PDMS surface⁶¹. As observed in the EDS and SEM results, regions of the functionalised PDMS chips are not completely covered with rock minerals (Fig. 4) and thus, the exposed PDMS still influences the surface wettability.

Trantidou, *et al.*⁶¹ performed a longevity study on their PVA treatment, and the contact angle was stable at $30\text{--}50^\circ$ for 9 days, which confirms the validity of this method and long-term effect of PVA with PDMS. It is also important to note that PVA treatment on the un-deposited PDMS chip showed less connected connate water as compared to the carbonate and sandstone models. This can be attributed to the surface roughness of the geo-material chips, which allows for connate water to exist in the corners and crevices of the chip. The connate water appears to be connected since wetting films in Fig. 6 are seen to extend across grains. This allows for the establishment of connate water films throughout the microfluidic chip. The thin connate water films present for water-wet conditions of the sandstone and carbonate conditions with PVA treatment are essential for visualising pore-scale phenomena in subsurface fluid flow, as demonstrated in the next subsection.

To confirm that PVA treatment of the geo-material PDMS chips does not alter the surface wettability of the deposited grains, we compare contact angles of the rock samples to geo-material PDMS chips with and without PVA. The steps for measuring contact angle are provided in the Methods section. Contact angle measurements in Fig. 7 show that PVA has no effect on the reservoir rock, as the contact angles remain in the same range ($75^\circ\text{--}80^\circ$)

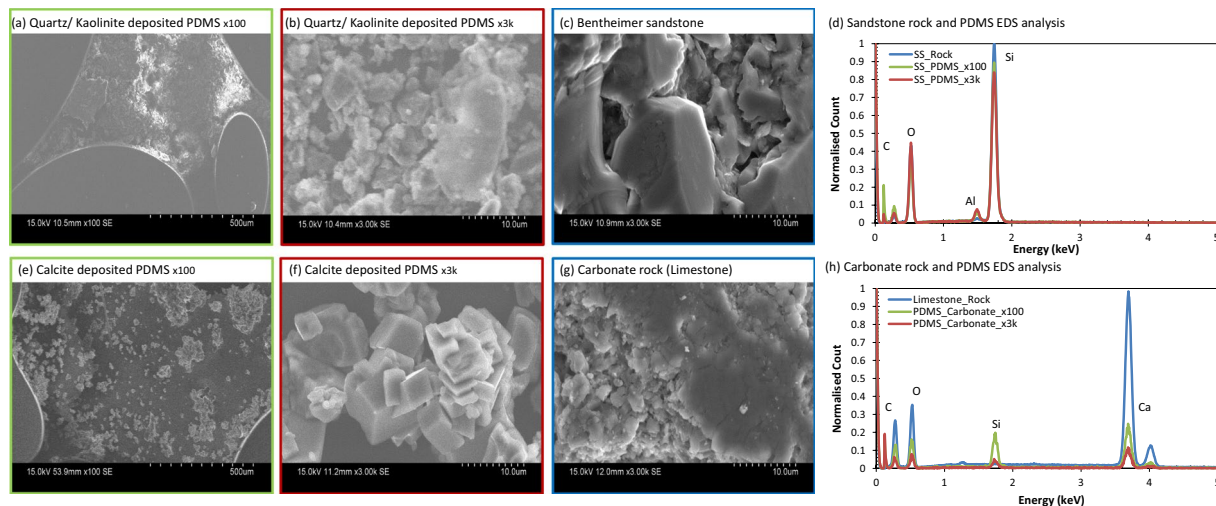


Figure 4. SEM images and EDS analysis of sandstone rock and PDMS (a–c), and carbonate rock and PDMS (e–h). The sandstone and calcite deposited PDMS show similar morphology and compositional analysis compared to their corresponding rocks. The image border colours in (a–c) and (e–g) correspond to the lines present in d and h.

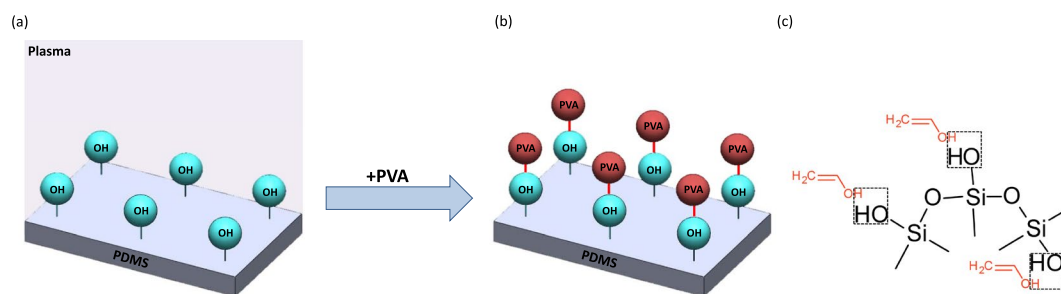


Figure 5. Mechanism of PDMS wettability alteration by adding PVA. (a) shows the PDMS surface following plasma treatment with silanol groups on the surface (Si–OH). (b) shows PVA bonding to the OH groups, and (c) shows the detailed molecular hydrogen bonding between PVA (red) and the PDMS backbone (black). The dashed lines in (c) show the locations of these hydrogen bonds.

with and without PVA treatment. However, the geo-material PDMS chips without PVA show a highly hydrophobic surface ($\theta > 100^\circ$), which demonstrates that the PDMS backbone is influenced by PVA treatment, thereby controlling the contact angle, hence the oil-wet nature of the chips. Conversely, geo-material PDMS chips with PVA treatment show similar contact angle measurements to those present for the reservoir rock samples.

Cassie's equation (Eq. 7) was used to explain the shift in the contact angle in the geo-material PDMS microfluidics devices with and without PVA treatment. Cassie's equation provides an apparent contact angle by considering chemically heterogeneous surfaces with regions that have distinctly different contact angles^{63–65}. For the functionalised PDMS surface, there are regions of exposed PDMS (–PVA or +PVA) and regions of rock minerals. The surface fractions of mineral and exposed PDMS regions are measured from microscope images. The contact angles for these two regions are taken from Fig. 7, as PDMS (–PVA or +PVA) and Ca_{rock} (–PVA) or SS_{rock} (–PVA). From Fig. 7, the contact angle measurements determined from Cassie's equation (yellow) are in agreement with the experimentally measured contact angles in both geo-material microfluidic chips (red). This indicates that the fraction of PDMS present on the surface influences the wettability, especially in the case of no PVA treatment (–PVA).

Flow Visualisation using the Geo-material PDMS chips. With the functionalisation of PDMS with sandstone and carbonate particles, we have established: (1) a geo-chemical environment and roughness profile that is similar to a real rock, and (2) similar wetting profiles, due to the PVA treatment that alters the wettability of PDMS to water-wet but does not alter the geo-material wettability. These factors create a platform for studying the pore-scale flow. In this section, we demonstrate the swelling of connate water wetting films and snap-off in our functionalised chips. Roof¹⁷ describes oil snap-off as the formation of an oil droplet due to oil being pushed through a water-wet constriction into a water-filled pore. Snap-off is strongly dependent on wettability, pore scale geometry, and roughness of the pore–solid interface^{25,26,66}. Figure 8 illustrates the swelling of connate water films (green) when DI water (red) is injected into a functionalised chip at connate water (green) equilibrium. We can observe that the injected water travels within the pre-existing connate water films, leaving oil behind (Fig. 8).

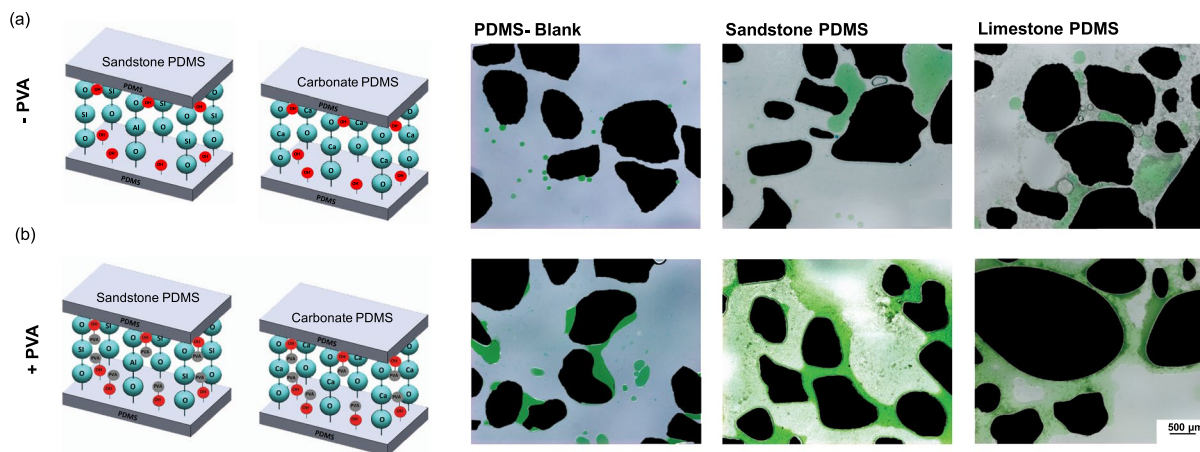


Figure 6. Wetting films during the two cases: (a) without PVA (–PVA), and (b) with PVA (+PVA) treatment. The cartoons on the left illustrate the molecular interactions occurring in each scenario, and the microscope images show the wetting films in each of the three PDMS chips (blank, sandstone and limestone) with and without PVA. Oil is transparent and connate water is green.

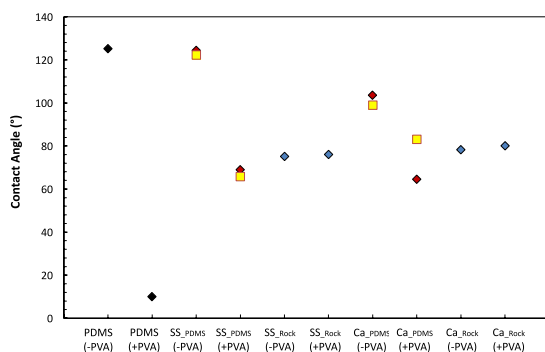


Figure 7. Contact angle measurements of (1) PDMS, (2) the two different geo-material PDMS chips, and (3) their respective rocks without PVA (–PVA) and with PVA (+PVA). The colours of the points correspond to the different materials present. PDMS is shown as black, geo-material PDMS is red, rock slices are blue and Cassie's equation estimates for the geo-material PDMS is yellow.

As previously mentioned, snap-off is highly dependent on the specific pore geometry, i.e. pore-wall curvature, and pressures in the wetting and nonwetting phases^{21,22}. Capillary pressure differences between the leading and tailing ends of an oil droplet and pore necks can be measured directly from microscopic images⁶⁷. In our experiments, time-lapse images were taken in one location while injecting DI water (red). From the collected images, one snap-off event was observed, along with several oil clusters that were a result of previous uncaptured snap-off events, in Fig. 8(b–f). Figure 9 highlights one snap-off event at 0.56 and 0.60 PV, which correspond to before and after snap-off, respectively. Capillary pressures at different locations (throat and pore bodies) are also shown in Fig. 9. For the example snap-off event, capillary pressure in the pore throat region is greater than capillary pressures measured in the leading and tailing ends of the oil droplet. Higher capillary pressure in the pore throat region would cause the oil phase to flow away from the throat constriction and thus, leading to the collapse of an interface, i.e. a snap-off event. Capillary pressures are determined by using the Young Laplace equation, as explained in the Methods section. The two principals of curvatures are measured from the oil interface in the throat and pore bodies as visualised in Fig. 9c. The resulting capillary pressures are reported in Fig. 9d showing that pressure was larger in the throat region than the two pore bodies. This difference in pressure causes snap-off in the throat, as oil flows away from the throat region.

Minerals Attachment Stability of the Geo-material PDMS chips. It is essential to test the stability of the geo-material PDMS chips. In this section, we studied changes between sequential images after flooding the chip with selected fluids. Images are collected after each treatment and segmented to evaluate the amount of deposited minerals. The difference between images is reported as a percent change, as defined in the Methods section. The deposited dry chip (prior to any injection) and brine, decane, and DI water flooding scenarios in 5 different locations across 3 different chips are evaluated. Figure 10 shows the percent change between the initial condition of the geo-material PDMS chip and the subsequent flooding. From Fig. 10, the sandstone chip shows a low change across the different flooding scenarios, with the highest change being 1.1%. An average of 0.4%, 0.6%

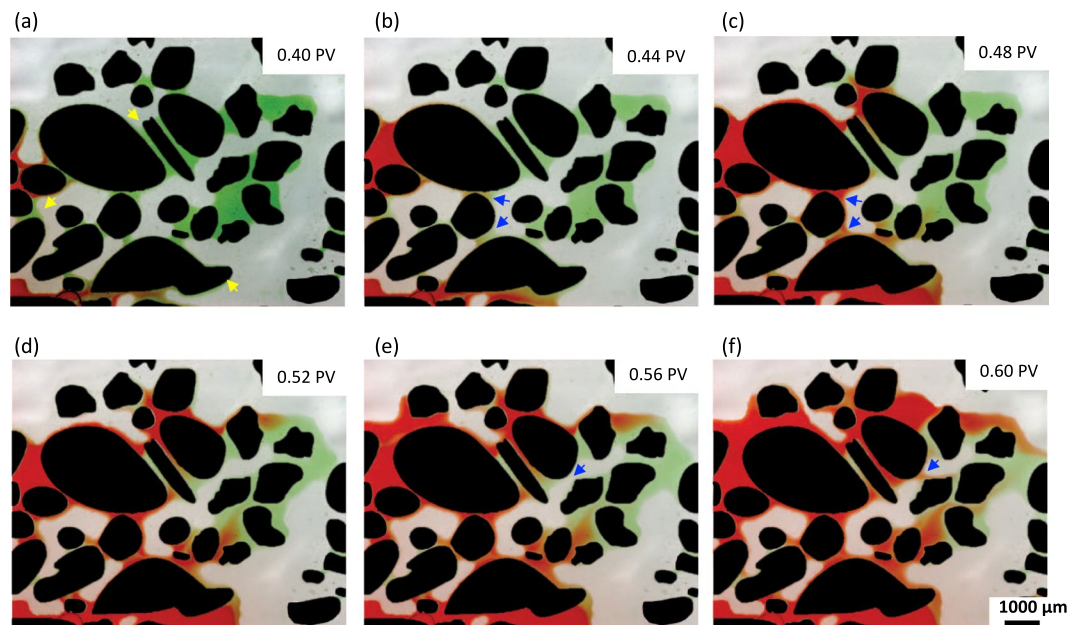


Figure 8. Wetting films of connate water (green) and injected DI water (red) displacing decane (transparent) indicated in yellow arrows and oil snap-off event indicated in blue arrows. From the image, swelling of connate water is observed in (a–c) and one snap-off event is depicted in the blue arrows (e–f).

and 0.7% change between the dry image and connate, decane and DI injections, respectively. For the carbonate PDMS chips, a maximum of 30.9% change between the dry image and the subsequent flooding scenarios was measured. An average of 6.7%, 11.9% and 21.5% change between the dry image and connate, decane and DI injections were measured, respectively. In terms of particle detachment, the calcite mixture appears to detach easier than the sandstone, which is likely due to the strong siloxane bond present between the sandstone mixture and activated PDMS surfaces. The images in Fig. 10c and d provide examples of the highest change in sandstone and carbonate chips (sample 4 and 2, respectively in Fig. 10a and b) to help illustrate what 1.1% and 30.9% change looks like.

Additionally, SEM images before and after flooding are shown for each chip in Fig. 10e and f to help visualise the differences at higher resolution. As it can be depicted, the carbonate geo-material PDMS is not as stable as the sandstone. In addition, roughness measurements before (i.e. dry sample) and after the three consecutive floods were performed on 5 areas in each sample. An average change of 4.8% and 11.9% in roughness was calculated for the sandstone and carbonate geo-material chips, respectively. Overall, the microscope, SEM and roughness measurements demonstrate flooding of geo-material PDMS does show pore-level changes that result from either detachment of minerals from the PDMS surface and/or dissolution of mineral crystals. Similar mechanisms are observed in carbonate and sandstone rocks subjected to low salinity water flooding, where clay fines detach from rock surface, or dissolution of carbonate rock. Since these chips were tested using DI water (no salinity) it is likely that these mechanisms are being observed in our measurements. Both of these mechanisms are proposed oil recovery mechanisms for an enhanced oil recovery technique called low salinity flooding^{68,69}. Further work is needed to relate the observed results in our geo-material PDMS to that observed in carbonate and sandstone rock under low salinity water flooding.

Conclusions

Geo-material microfluidics approaches are essential for the visualisation and understanding of rock–fluid interactions, which are relevant to subsurface engineering applications, such as geologic CO₂ storage, geothermal energy, enhanced oil recovery and hydrology. Thus far, we have demonstrated a simple and rapid fabrication method for a geo-material PDMS microfluidics device. We have evaluated the uniformity of the deposition using semivariograms (Fig. 3a and b), and surface roughness measurements (Fig. 3c). We then, compared our functionalised PDMS devices to their representative rock via SEM-EDS analysis (Fig. 4). From these imaging techniques, we can see that the composition and height profile in both rocks and functionalised PDMS devices are similar and that mineral deposition is nearly isotropic. The establishment of thin films with PVA treatment of the sandstone and carbonate chips (Fig. 8) have shown to be well-connected, particularly in the two PDMS chips with mineral deposition, which demonstrated that water is wetting the pore space.

In addition, we were able to capture the pore-scale flow mechanism of corner flow leading to the snap-off of the nonwetting phase in a controlled wetting environment (Fig. 8). Our fabrication method provides surface roughness and connected corners for thin-film flow. These two multiphase flow mechanisms are important for carbon capture and storage¹⁹ and enhanced oil recovery^{5–7} studies. Lastly, we verify the stability of our fabricated geo-material PDMS chips (Fig. 10) by measuring the similarity of chips before and after flooding with DI water

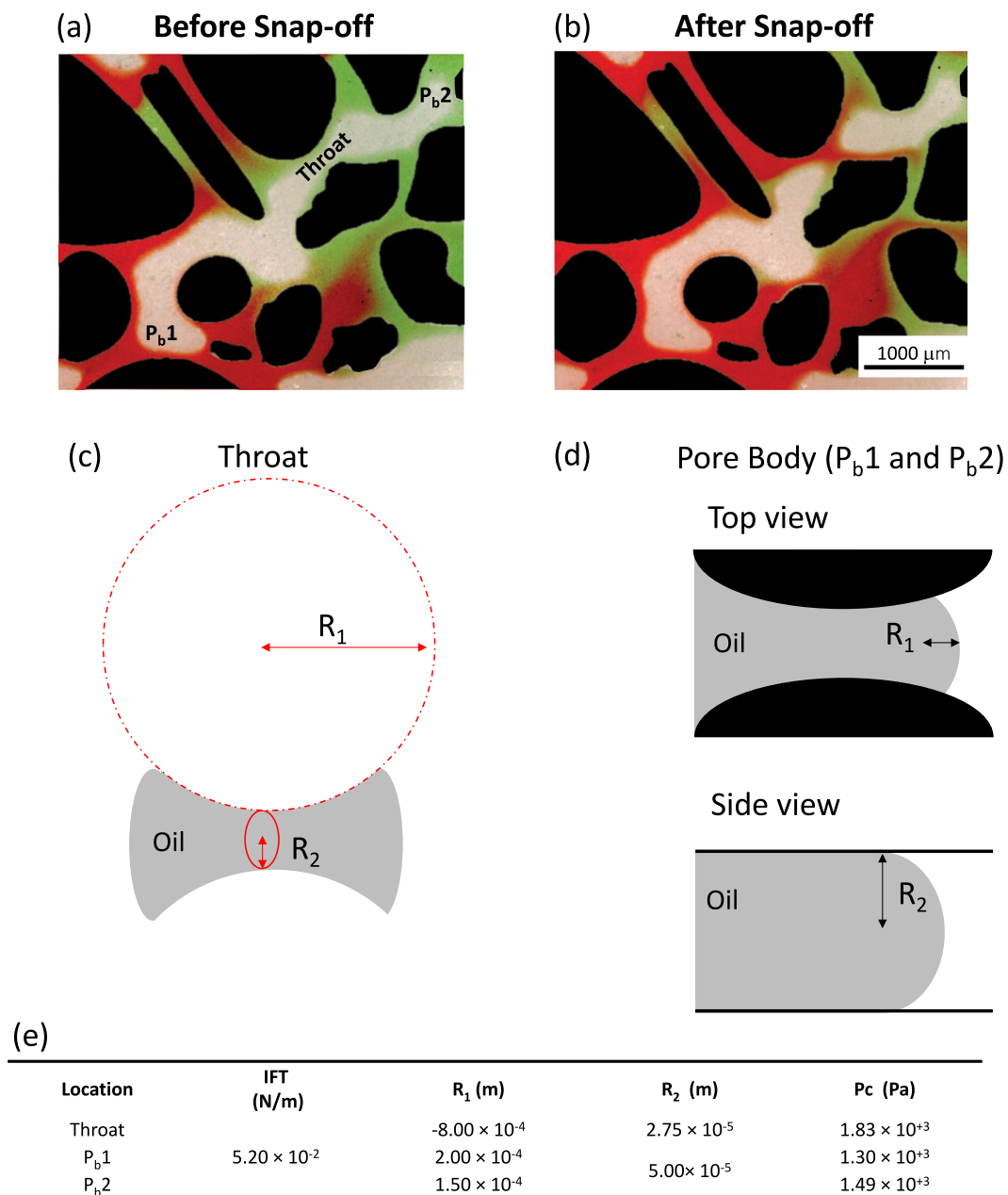


Figure 9. Detailed snap-off event visualisation. (a) Before snap-off event at 0.56 PV. (b) After snap-off at 0.60 PV. (c) R_1 and R_2 measurements taken for throat, and (d) pore bodies (P_b 1 and 2). (e) Capillary pressure measurements at throats and pore bodies (P_b). Grains are present in black, red is DI water, green is connate water, and oil is transparent and/or grey.

and decane. When compared to the dry image of the deposited PDMS chips, the sandstone chip exhibited the highest change being 1.1%, whereas the change in the carbonate PDMS chips was 30.9%. Average roughness measurements and SEM images before and after flooding also confirm that sandstone PDMS chips are more stable than the carbonate PDMS chips. We also acknowledge that pore-level change in the attached geomaterials occur under low salinity water flooding (DI water). Future studies will include visualisation of subsurface engineering related phenomena; such as oil snap-off, enhanced oil recovery and other processes where surface chemistry is highly important, such as CO_2 sequestration, calcite dissolution, surfactant and/or low salinity brine flooding resulting in mineral detachment and migration. Our geo-material PDMS chips can provide a useful platform to answer questions in subsurface and environmental engineering fields, in particular, when fluid-fluid and fluid-rock interactions are highly important.

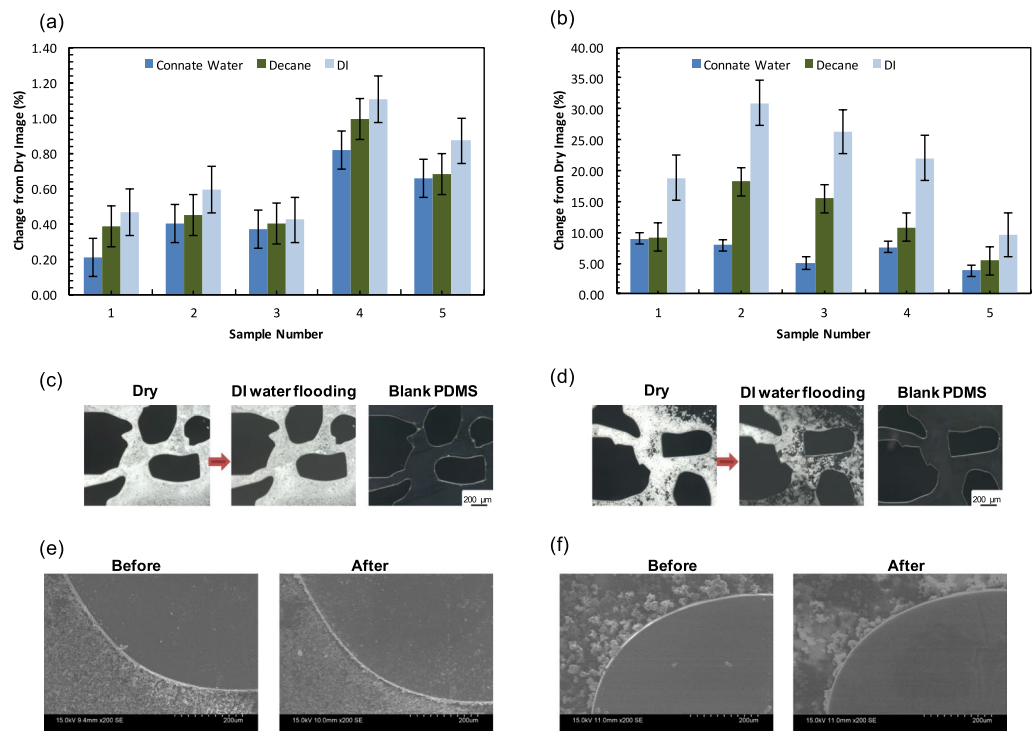
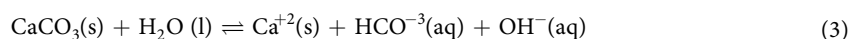
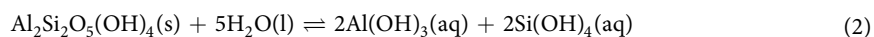


Figure 10. Geo-material stability measurements of (a) sandstone and (b) carbonate PDMS chips. The different injection scenarios (connate water, decane and DI) are compared to the dry image, and the percent change is shown in the column graphs. Error bars indicate the standard error of the mean. (c) and (d) show microscopic images of the highest change in both sandstone (c) and carbonate (d). The images illustrate the change from the dry image (reference) and after DI water flooding, along with a blank PDMS of the same region. As can be seen, minor change is observed in (c), however, the 30.9% change can be clearly visible in (d). Example of SEM images for dry sample (before) and after flooding for (e) sandstone and (f) carbonate.

Methods

Mineral Solution Preparation. To replicate sandstone rock, quartz and kaolinite were chosen as the dominant minerals⁵⁵. For carbonate rock, calcium carbonate (CaCO_3) is the major component⁵². Deionized (DI) water was used to create the following solutions: (1) 4% (w/v) Quartz (silicon dioxide, Sigma-Aldrich) and 2% (w/v) Kaolinite (Kaolin, Imerys minerals, Australia), and (2) 4% (w/v) CaCO_3 (calcium carbonate, Normapur AR). Relatively high fractions of minerals were used to ensure a homogenous deposition on the geo-material PDMS. Solutions were mixed and sonicated (Branson 220) for one hour, as previously described in Song and Kovscek⁴⁷. When mixing sandstone (Eqs 1 and 2) and calcite minerals (Eq. 3) with DI water, the following aqueous dissolutions occur:



Geo-material microfluidics chip fabrication. A random pore network pattern was created in AutoCAD (Version 2017, Autodesk Inc.). The morphology of the pores can be depicted in Fig. 11. The pattern was then transferred into a chrome mask for silicon mould microfabrication using standard lithography techniques, as previously described^{70,71}. The silicon mould was etched using deep reactive ion etching (DRIE) to define the channel features on the wafer to achieve an etch depth of 100 μm . The process of creating the silicon mould was outsourced to the South Australian node of the Australian National Fabrication Facility. This mould was then silanized, coated with de-gassed PDMS (Sylgard 184, Dow Corning Corporation) at ambient conditions and then cured for 4 hours at 65 $^\circ\text{C}$ in-house using a well-known process termed “soft lithography”⁷². The resulting PDMS slice containing the porous media was then peeled off the silicon mould and treated with oxygen plasma (Harrick Plasma Cleaner, NY, USA) for 4 minutes and 15 seconds, and 1 ml of the desired mineral solution was immediately placed on top of the PDMS slice. The PDMS slice was then air-dried and cleaned with ethanol and inspected using a stereo microscope (PSB X2-4, Saxon) to ensure no particles are present in the top of PDMS pillars. Lastly, a blank PDMS cover was bonded to the PDMS slice containing the porous medium with the deposited

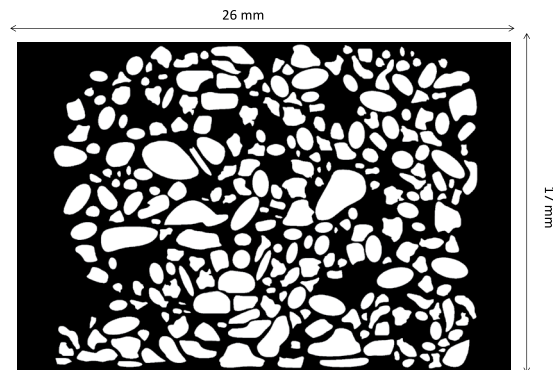


Figure 11. Pore network pattern of the geo-material chip. Black is the pore space and white shows the grains.

mineral via a second plasma treatment. The reason why the PDMS cover is left blank because the silanol groups on the PDMS are required for permanent bonding between the cover and the pillars of the PDMS with minerals. Examining the PDMS prior to the second plasma treatment was crucial for strong bonding of the porous media containing the minerals and the PDMS cover. If some particles were present on the top surface of the PDMS pillars, this would result in weak bonding. Figure 2 summarises the fabrication workflow. The total time needed to fabricate the geo-material PDMS microfluidic chip was 4.5 hours.

Characterisation of the Geo-material Microfluidic system. Semivariograms are used to study spatial arrangement of minerals after deposition. This is done by evaluating the variations in the pixel intensities of the grey-level values across stereo microscope images fabricated chips^{73,74}. The semi-variance $\gamma(h)$ is described as

$$\gamma(h) = \frac{1}{2N(h)} \sum_{i=1}^{N(h)} [Z(x_i) - Z(x_i + h)]^2 \quad (4)$$

where h is the lag distance (or pixel distance), $Z(x_i)$ and $Z(x_i + h)$ are the pixel intensity values in the image, Z at a separation of h and $N(h)$ is the number of pixel pairs at a lag distance, h . The anisotropic nature of an image can be captured by constructing semivariograms in different directions⁷⁵. The semi-variance for different lag distance in both horizontal (0°) and vertical (90°) directions can be calculated. If the semi-variances in these directions are similar, the image is isotropic. To test the isotropic distribution of minerals deposited on the PDMS chips, we conducted semivariogram analysis on three carbonate and three sandstone mineral deposited PDMS chips. Before analysis, images representing the deposited minerals were isolated from the PDMS grains while maintaining their spatial locations to ensure that only the semivariance of deposited minerals are evaluated rather than the PDMS porous pattern. Then, the original 8-bit image was re-quantised to a 6-bit image using uniform quantisation⁷⁶. Lastly, each of these images were cropped to a size of 1600×1600 to ensure that the number of pixel pairs for varying lag distances remained the same in both horizontal (0°) and vertical (90°) directions.

Surface roughness of coated microfluidics chips and their respective rock slices were measured using a 3D laser microscope (VK-X200, Keyence), as previously described in Gerami, *et al.*⁵¹. Rock slices were 30 mm in diameter and 3 mm height thin sections, which were cut using a saw and were put in a vacuum oven at 65°C to dry for 24 hours. It is noteworthy that the rocks were unpolished. The microscope has a resolution of 0.5 nm and 1 nm in the z direction and X-Y plane, respectively. The magnification of the microscope was set at $400\times$ for the measurements. The measured roughness of the geo-material microfluidics devices was compared against slices of their respective rock types. Roughness is measured based on the arithmetic mean roughness, which indicates the average of the absolute value along the reference length⁷⁷. Eq. 5 refers to the average elevation (Z_c), which is the average value of elevation of each curve element (Z_{ti}) on the reference length. Eq. 6 states the average elevation along the X-Y plane, with $Z_{t(xi,yj)}$ as the elevation in the X and Y direction, respectively.

$$Z_c = \frac{1}{m} \sum_{i=1}^m Z_{ti} \quad (5)$$

$$Z_c = \frac{1}{mn} \sum_{i=1}^m \sum_{j=1}^n Z_{t(xi,yj)} \quad (6)$$

where m and n indicate the total number of curved elements in the X and Y directions, respectively.

Lastly, the rock slices and PDMS chips were coated with ~ 20 nm carbon and imaged by scanning electron microscopy (SEM, Hitachi, S-3400N) coupled with energy dispersive X-ray spectroscopy (EDS detector, Bruker X-Flash 5010) analysis at 15 kV. SEM-EDS analysis was done to identify the minerals and elements present on the coated PDMS chip compared to their respective rock types.

Geo-material PDMS Chips Wettability Alterations. To replicate sandstone and carbonate rock properties for the geo-material microfluidic PDMS chip, the wettability conditions must be controlled. PDMS is naturally

oil-wet, and with oxygen plasma exposure it becomes water-wet for a maximum of 2 hours^{59,61}. Trantidou, *et al.*⁶¹ developed a method to modify the wettability of the surface of PDMS to water-wet with the addition of polyvinyl alcohol (PVA) immediately after oxygen plasma. Water-wet sandstone, carbonate and blank PDMS chips were treated with oxygen plasma and put in conformal contact to allow bonding between the sandstone and carbonate chips with the blank PDMS cover. These chips were immediately injected with PVA to fill the entire microfluidic chip via a plastic syringe and left for 10 minutes at room temperature. The PVA was then removed with injecting air in the microfluidic chips and heated to 110°C for 15 minutes. Details on this method is described in Trantidou, *et al.*⁶¹. After PVA treatment, the chips were left for 3 days to eliminate the effect of the oxygen plasma treatment. The chips were then injected with brine of 10% NaCl and 2% (w/v) Green food colour (AmeriColor, Placentia, CA, USA) for multiple pore volumes, followed by decane (Sigma Aldrich, USA) injection to achieve 80–90% oil saturation and left 20 minutes to equilibrate. Images of the sandstone, carbonate and blank PDMS chips were taken after three days with and without PVA treatment using a stereo zoom microscope (Zeiss, Axio Zoom V16) to characterise surface wettability with and without PVA treatment. From the collected microscopic images, the PDMS chips were characterised as either water-wet or oil-wet depending on the pre-dominant fluid (oil or water) surrounding the grains of the PDMS chips.

Contact Angle Measurements. Contact angle measurements were taken on blank PDMS chips and the different geo-material PDMS chips along with their respective rock types with and without PVA treatment. This is done to assess the wettability of the fabricated chip in comparison to their equivalent rock types. The contact angles are for air/DI-water/rock or PDMS chips. A droplet of deionized water was placed on the surface of a sample and contact angle was measured from the collected image using the contact angle plugin for ImageJ⁷⁸. To validate contact angles for the sandstone and carbonate geo-material chips (with and without PVA), the Cassie's equation^{63,64} was used and effective contact angles were measured as

$$\cos\theta_{eff} = f_{Gm} \cos\theta_{Gm} + f_{PDMS} \cos\theta_{PDMS} \quad (7)$$

where θ_{eff} is the effective contact angle, f_{Gm} is the fraction of the geomaterial (minerals) on the PDMS surface, θ_{Gm} contact angle of the geo-material, f_{PDMS} fraction of PDMS and θ_{PDMS} is the PDMS contact angle. Fractions of both PDMS and minerals (f_{PDMS} and f_{Gm} , respectively) were measured based on segmented images of the same PDMS coated mineral surfaces that were used previously for experimental contact angle measurements.

Flow Visualisation. To reproduce fluid distributions within a natural reservoir, the chips were first injected with brine of 10% NaCl (w/v) and 2% green food colour (w/v) (AmeriColor, Placentia, CA, USA), and then decane (Sigma Aldrich, USA) was injected to achieve a 80–90% oil saturation and left 20 minutes to equilibrate. This step establishes connate water saturation within the chip. Then, DI water with 2% red food colour (w/v) (AmeriColor, Placentia, CA, USA) was injected at a capillary number (Ca) of 10^{-5} to replicate water flooding conditions. A high-precision infusion syringe pump (Fusion 100 Infusion, Chemyx, Australia) is used to monitor and control the flow rate (4 $\mu\text{m}/\text{min}$). Optical microscope images were collected using a CCD digital camera (Zeiss, AxioCam 506 colour) coupled with a stereo zoom microscope (Zeiss, Axio Zoom V16) with a size of 2752×2208 pixels. All the experiments were conducted at ambient conditions. The Young-Laplace equation, which relates the mean curvature of the fluid-fluid interface to capillary pressure (P_c) was used to study the snap-off event. Differences in local capillary pressure are known to result in snap-off under specific criteria^{67,79,80}. Capillary pressure (P_c) is calculated as

$$P_c = \sigma \left(\frac{1}{R_1} + \frac{1}{R_2} \right) \quad (8)$$

where σ is interfacial tension (N/m) and R_1 and R_2 are the principal radii of curvatures for the oil/water interface (m). The principal radii of curvature (R_1) of the fluid/fluid interface that is visualised in the focal plan can be directly measured from the image⁶⁷. The second principal radii (R_2) of curvature is estimated based on the form of the interface. If the interface is hyperboloid, then R_2 can be directly measured from the image as half the width of the hyperboloid at its narrowest constriction. For the case of the interfaces at the front and end menisci of an oil cluster, R_2 cannot be directly measured from the collected images and it is assumed to be half of the microfluidics device depth. A similar assumption is made in previous publications^{80–82}. Due to the complexity in measuring contact angle for the functionalised surface, there is no direct way to actually measure the curvature in the plane orthogonal to the focal plane, and thus, we assume complete wetting conditions. This assumption is only an order of magnitude estimate that allows for evaluation of capillary pressure difference over the nonwetting phase.

Minerals Attachment Stability of the Geo-material PDMS chips. To test the stability of the mineral deposition, we measured the degree of mineral detachment from the geo-material chip after sequential flow experiments. Five locations were chosen from three samples of sandstone and carbonate PDMS chips, and imaged using a stereo zoom microscope (Zeiss, Axio Zoom V16) after the following conditions: (1) dry (no prior to injection), which is considered as the reference sample, (2) connate water (10% NaCl (w/v)) injection (3) decane injection, and (4) DI water injection. All the images in the different injection conditions were obtained after 4–5 PV of injected fluid at a rate of 5 $\mu\text{l}/\text{min}$. The samples were dried in a vacuum oven at 65°C for 25 minutes after each injection to obtain a clear image, free of liquid. Images were converted to 8-bit greyscale, which gave a bi-modal histogram of the intensity values that ranged from 0 to 256. An Example histogram is shown in Fig. 12, which displays a clear separation of intensity values between deposited minerals and PDMS.

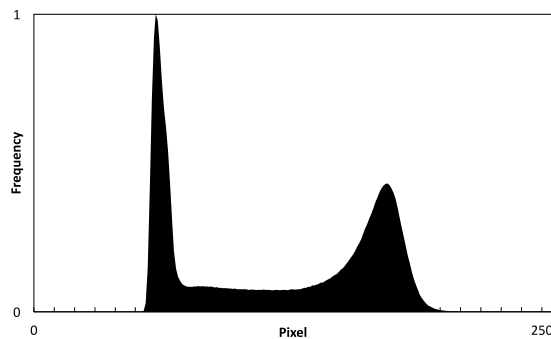


Figure 12. An example histogram of an 8-bit greyscale image used in the stability studies.

The images were then segmented at a unified pixel value of 115 to identify the surface minerals. This value was defined based on the Auto Threshold function in ImageJ, which uses the IsoData method for thresholding⁸³. The sum of pixels was estimated for the entire thresholded image after each flooding using ImageJ. The net percentage change between each flooding scenario and dry image was measured as

$$\% \text{ Change} = \frac{P_{dry} - P_{inj}}{P_{dry}} \times 100 \quad (9)$$

where P_{dry} is the sum of pixel values of the dry geo-material PDMS and P_{inj} is the sum of pixel values in the geo-material PDMS after the different injection scenario. We also provide grey-scale images before and after treatment to illustrate the sensitivity of the calculation presented in Eq. 9. To allow for better quantification and visualisation of the changes occurring from the dry geo-material PDMS and the above-mentioned floods (conate water, decane and DI water), surface roughness was measured (as described previously) and SEM images (Hitachi, S-3400N) were taken for the dry chip and after drying the sample from the final flooding scenario (DI water).

References

1. Pruess, K. & García, J. Multiphase flow dynamics during CO₂ disposal into saline aquifers. *Environmental Geology* **42**, 282–295, <https://doi.org/10.1007/s00254-001-0498-3> (2002).
2. Bromhal, G. S., Neal Sams, W., Jikich, S., Ertekin, T. & Smith, D. H. Simulation of CO₂ sequestration in coal beds: The effects of sorption isotherms. *Chemical Geology* **217**, 201–211, <https://doi.org/10.1016/j.chemgeo.2004.12.021> (2005).
3. Szulczewski, M. L., MacMinn, C. W., Herzog, H. J. & Juanes, R. Lifetime of carbon capture and storage as a climate-change mitigation technology. *Proceedings of the National Academy of Sciences* **109**, 5185–5189 (2012).
4. Kazemifar, F., Blois, G., Kyritsis, D. C. & Christensen, K. T. Quantifying the flow dynamics of supercritical CO₂–water displacement in a 2D porous micromodel using fluorescent microscopy and microscopic PIV. *Advances in Water Resources* **95**, 352–368, <https://doi.org/10.1016/j.advwatres.2015.05.011> (2016).
5. Lake, L. W. *Enhanced oil recovery* (Prentice Hall, 2014).
6. Berejnov, V., Djilali, N. & Sinton, D. Lab-on-chip methodologies for the study of transport in porous media: energy applications. *Lab on a Chip* **8**, 689–693, <https://doi.org/10.1039/B802373P> (2008).
7. Blunt, M. J., Jackson, M. D., Piri, M. & Valvatne, P. H. Detailed physics, predictive capabilities and macroscopic consequences for pore-network models of multiphase flow. *Advances in Water Resources* **25**, 1069–1089, [https://doi.org/10.1016/S0309-1708\(02\)00049-0](https://doi.org/10.1016/S0309-1708(02)00049-0) (2002).
8. Kueper, B. H., Abbott, W. & Farquhar, G. Experimental observations of multiphase flow in heterogeneous porous media. *Journal of Contaminant Hydrology* **5**, 83–95, [https://doi.org/10.1016/0169-7722\(89\)90007-7](https://doi.org/10.1016/0169-7722(89)90007-7) (1989).
9. Parker, J. C. Multiphase flow and transport in porous media. *Reviews of Geophysics* **27**, 311–328, <https://doi.org/10.1029/RG027i003p00311> (1989).
10. Kjeang, E., Djilali, N. & Sinton, D. Microfluidic fuel cells: A review. *Journal of Power Sources* **186**, 353–369, <https://doi.org/10.1016/j.jpowsour.2008.10.011> (2009).
11. Morrow, N. R. Wettability and Its Effect on Oil Recovery, <https://doi.org/10.2118/21621-PA> (1990).
12. Zhao, B., MacMinn, C. W. & Juanes, R. Wettability control on multiphase flow in patterned microfluidics. *Proceedings of the National Academy of Sciences* **113**, 10251–10256 (2016).
13. Mohanty, K. K. & Salter, S. J. In *SPE Annual Technical Conference and Exhibition* (Society of Petroleum Engineers, New Orleans, Louisiana, 1982).
14. Mohanty, K. K. In *SPE Annual Technical Conference and Exhibition* (Society of Petroleum Engineers, San Francisco, California, 1983).
15. Hu, R., Wan, J., Kim, Y. & Tokunaga, T. K. Wettability impact on supercritical CO₂ capillary trapping: Pore-scale visualization and quantification. *Water Resources Research* **53**, 6377–6394, <https://doi.org/10.1002/2017WR020721> (2017).
16. de Gennes, P. G. Wetting: statics and dynamics. *Reviews of Modern Physics* **57**, 827–863 (1985).
17. Roof, J. G. Snap-Off of Oil Droplets in Water-Wet Pores, <https://doi.org/10.2118/2504-PA> (1970).
18. Mohanty, K. K., Davis, H. T. & Scriven, L. E. Physics of Oil Entrapment in Water-Wet Rock, <https://doi.org/10.2118/9406-PA> (1987).
19. Iglauer, S., Paluszny, A., Pentland, C. H. & Blunt, M. J. Residual CO₂ imaged with X-ray micro-tomography. *Geophysical Research Letters* **38**, n/a–n/a, <https://doi.org/10.1029/2011GL049680> (2011).
20. Rayleigh, L. O. The Instability Of Jets. *Proceedings of the London Mathematical Society* **s1-10**, 4–13, <https://doi.org/10.1112/plms/s1-10.1.4> (1878).
21. Lenormand, R., Zarcone, C. & Sarr, A. Mechanisms of the displacement of one fluid by another in a network of capillary ducts. *Journal of Fluid Mechanics* **135**, 337–353 (1983).

22. Geistlinger, H., Ataei-Dadavi, I., Mohammadian, S. & Vogel, H.-J. The impact of pore structure and surface roughness on capillary trapping for 2-D and 3-D porous media: Comparison with percolation theory. *Water Resources Research* **51**, 9094–9111, <https://doi.org/10.1002/2015WR017852> (2015).
23. Chatzis, I., Morrow, N. R. & Lim, H. T. Magnitude and Detailed Structure of Residual Oil Saturation. <https://doi.org/10.2118/10681-PA> (1983).
24. Toledo, P. G., Scriven, L. E. & Davis, H. T. Equilibrium and Stability of Static Interfaces in Biconical Pore Segments, <https://doi.org/10.2118/27410-PA> (1994).
25. Singh, K. *et al.* Dynamics of snap-off and pore-filling events during two-phase fluid flow in permeable media. *Scientific Reports* **7**, 5192, <https://doi.org/10.1038/s41598-017-05204-4> (2017).
26. Ransohoff, T. C., Gauglitz, P. A. & Radke, C. J. Snap-off of gas bubbles in smoothly constricted noncircular capillaries. *AIChE Journal* **33**, 753–765, <https://doi.org/10.1002/aic.690330508> (1987).
27. Constantinides, G. N. & Payatakes, A. C. Effects of Precursor Wetting Films in Immiscible Displacement Through Porous Media. *Transport in Porous Media* **38**, 291–317, <https://doi.org/10.1023/A:1006557114996> (2000).
28. Mogenssen, K. & Stenby, E. H. A Dynamic Two-Phase Pore-Scale Model of Imbibition. *Transport in Porous Media* **32**, 299–327, <https://doi.org/10.1023/A:1006578721129> (1998).
29. Hughes, R. G. & Blunt, M. J. Pore Scale Modeling of Rate Effects in Imbibition. *Transport in Porous Media* **40**, 295–322, <https://doi.org/10.1023/A:1006629019153> (2000).
30. Blunt, M. J. Flow in porous media — pore-network models and multiphase flow. *Current Opinion in Colloid & Interface Science* **6**, 197–207, [https://doi.org/10.1016/S1359-0294\(01\)00084-X](https://doi.org/10.1016/S1359-0294(01)00084-X) (2001).
31. Dias, M. M. & Payatakes, A. C. Network models for two-phase flow in porous media Part 1. Immiscible microdisplacement of non-wetting fluids. *Journal of Fluid Mechanics* **164**, 305–336, <https://doi.org/10.1017/S0022112086002574> (2006).
32. Vizika, O., Avraam, D. G. & Payatakes, A. C. On the Role of the Viscosity Ratio during Low-Capillary-Number Forced Imbibition in Porous Media. *Journal of Colloid and Interface Science* **165**, 386–401, <https://doi.org/10.1006/jcis.1994.1243> (1994).
33. DiCarlo, D. A. Quantitative network model predictions of saturation behind infiltration fronts and comparison with experiments. *Water Resources Research* **42**, n/a–n/a, <https://doi.org/10.1029/2005WR004750> (2006).
34. Nguyen, V. H., Sheppard, A. P., Knackstedt, M. A. & Val Pinczewski, W. The effect of displacement rate on imbibition relative permeability and residual saturation. *Journal of Petroleum Science and Engineering* **52**, 54–70, <https://doi.org/10.1016/j.petrol.2006.03.020> (2006).
35. Blunt, M. J. & Scher, H. Pore-level modeling of wetting. *Physical Review E* **52**, 6387–6403 (1995).
36. Sinton, D. Energy: the microfluidic frontier. *Lab on a Chip* **14**, 3127–3134, <https://doi.org/10.1039/C4LC00267A> (2014).
37. Song, W., de Haas, T. W., Fadaei, H. & Sinton, D. Chip-off-the-old-rock: the study of reservoir-relevant geological processes with real-rock micromodels. *Lab on a Chip* **14**, 4382–4390, <https://doi.org/10.1039/C4LC00608A> (2014).
38. Sinton, D. Microfluidics and Their Macro Applications for the Oil and Gas Industry, <https://doi.org/10.2118/0315-008-TWA> (2015).
39. Karadimitriou, N. K. *et al.* On the fabrication of PDMS micromodels by rapid prototyping, and their use in two-phase flow studies. *Water Resources Research* **49**, 2056–2067, <https://doi.org/10.1002/wrcr.20196> (2013).
40. Mostaghimi, P. *et al.* Cleat-scale characterisation of coal: An overview. *Journal of Natural Gas Science and Engineering* **39**, 143–160, <https://doi.org/10.1016/j.jngse.2017.01.025> (2017).
41. Lifton, V. A. Microfluidics: an enabling screening technology for enhanced oil recovery (EOR). *Lab on a Chip* **16**, 1777–1796, <https://doi.org/10.1039/C6LC00318D> (2016).
42. Kumar Gunda, N. S., Bera, B., Karadimitriou, N. K., Mitra, S. K. & Hassanizadeh, S. M. Reservoir-on-a-Chip (ROC): A new paradigm in reservoir engineering. *Lab on a Chip* **11**, 3785–3792, <https://doi.org/10.1039/C1LC20556K> (2011).
43. Karadimitriou, N. K. & Hassanizadeh, S. M. A Review of Micromodels and Their Use in Two-Phase Flow Studies. *Vadose Zone Journal* **11** (2012).
44. Bowden, S. A., Tanino, Y., Akamairo, B. & Christensen, M. Recreating mineralogical petrographic heterogeneity within microfluidic chips: assembly, examples, and applications. *Lab on a Chip* **16**, 4677–4681, <https://doi.org/10.1039/C6LC01209D> (2016).
45. Joekar-Niasar, V. & Hassanizadeh, S. M. Analysis of Fundamentals of Two-Phase Flow in Porous Media Using Dynamic Pore-Network Models: A Review. *Critical Reviews in Environmental Science and Technology* **42**, 1895–1976, <https://doi.org/10.1080/10643389.2011.574101> (2012).
46. Mahani, H. *et al.* Insights into the Mechanism of Wettability Alteration by Low-Salinity Flooding (LSF) in Carbonates. *Energy & Fuels* **29**, 1352–1367, <https://doi.org/10.1021/ef5023847> (2015).
47. Song, W. & Kovscek, A. R. Functionalization of micromodels with kaolinite for investigation of low salinity oil-recovery processes. *Lab on a Chip* **15**, 3314–3325, <https://doi.org/10.1039/C5LC00544B> (2015).
48. Song, W. & Kovscek, A. R. Direct visualization of pore-scale fines migration and formation damage during low-salinity waterflooding. *Journal of Natural Gas Science and Engineering* **34**, 1276–1283, <https://doi.org/10.1016/j.jngse.2016.07.055> (2016).
49. Lee, H., Lee, S. G. & Doyle, P. S. Photopatterned oil-reservoir micromodels with tailored wetting properties. *Lab on a Chip* **15**, 3047–3055, <https://doi.org/10.1039/C5LC00277J> (2015).
50. Porter, M. L. *et al.* Geo-material microfluidics at reservoir conditions for subsurface energy resource applications. *Lab on a Chip* **15**, 4044–4053, <https://doi.org/10.1039/C5LC00704F> (2015).
51. Gerami, A. *et al.* Coal-on-a-Chip: Visualizing Flow in Coal Fractures. *Energy & Fuels*. <https://doi.org/10.1021/acs.energyfuels.7b01046> (2017).
52. Wang, W., Chang, S. & Gizzatov, A. Toward Reservoir-on-a-Chip: Fabricating Reservoir Micromodels by *in Situ* Growing Calcium Carbonate Nanocrystals in Microfluidic Channels. *ACS Applied Materials & Interfaces* **9**, 29380–29386, <https://doi.org/10.1021/acsami.7b10746> (2017).
53. Singh, R. *et al.* Real rock-microfluidic flow cell: A test bed for real-time *in situ* analysis of flow, transport, and reaction in a subsurface reactive transport environment. *Journal of Contaminant Hydrology* **204**, 28–39, <https://doi.org/10.1016/j.jconhyd.2017.08.001> (2017).
54. Zhu, P. & Papadopoulos, K. D. Visualization and quantification of two-phase flow in transparent miniature packed beds. *Physical Review E* **86**, 046313 (2012).
55. Liu, M., Shabaninejad, M. & Mostaghimi, P. Impact of mineralogical heterogeneity on reactive transport modelling. *Computers & Geosciences* **104**, 12–19, <https://doi.org/10.1016/j.cageo.2017.03.020> (2017).
56. Morse, J. W., Arvidson, R. S. & Lüttge, A. Calcium Carbonate Formation and Dissolution. *Chemical Reviews* **107**, 342–381, <https://doi.org/10.1021/cr050358j> (2007).
57. Bodas, D. & Khan-Malek, C. Hydrophilization and hydrophobic recovery of PDMS by oxygen plasma and chemical treatment—An SEM investigation. *Sensors and Actuators B: Chemical* **123**, 368–373, <https://doi.org/10.1016/j.snb.2006.08.037> (2007).
58. Friend, J. & Ye, L. Fabrication of microfluidic devices using polydimethylsiloxane. *Biomicrofluidics* **4**, 026502, <https://doi.org/10.1063/1.3259624> (2010).
59. Tan, S. H., Nguyen, N.-T., Chua, Y. C. & Kang, T. G. Oxygen plasma treatment for reducing hydrophobicity of a sealed polydimethylsiloxane microchannel. *Biomicrofluidics* **4**, 032204, <https://doi.org/10.1063/1.3466882> (2010).
60. Wong, I. & Ho, C.-M. Surface molecular property modifications for poly(dimethylsiloxane) (PDMS) based microfluidic devices. *Microfluidics and Nanofluidics* **7**, 291–306, <https://doi.org/10.1007/s10404-009-0443-4> (2009).

61. Trantidou, T., Elani, Y., Parsons, E. & Ces, O. Hydrophilic surface modification of PDMS for droplet microfluidics using a simple, quick, and robust method via PVA deposition. *Microsystems & Nanoengineering* **3**, 16091, <https://doi.org/10.1038/micronano.2016.91> <https://www.nature.com/articles/micronano201691#supplementary-information> (2017).
62. Lee, S. J. *et al.* Polymethylhydrosiloxane (PMHS) as a functional material for microfluidic chips. *Journal of Micromechanics and Microengineering* **18**, 025026 (2008).
63. Cassie, A. B. D. Contact angles. *Discussions of the Faraday Society* **3**, 11–16, <https://doi.org/10.1039/DF9480300011> (1948).
64. Swain, P. S. & Lipowsky, R. Contact Angles on Heterogeneous Surfaces: A New Look at Cassie's and Wenzel's Laws. *Langmuir* **14**, 6772–6780, <https://doi.org/10.1021/la980602k> (1998).
65. Marmur, A. & Bittoun, E. When Wenzel and Cassie Are Right: Reconciling Local and Global Considerations. *Langmuir* **25**, 1277–1281, <https://doi.org/10.1021/la802667b> (2009).
66. Geistlinger, H., Ataei-Dadavi, I. & Vogel, H.-J. Impact of Surface Roughness on Capillary Trapping Using 2D-Micromodel Visualization Experiments. *Transport in Porous Media* **112**, 207–227, <https://doi.org/10.1007/s11242-016-0641-y> (2016).
67. Armstrong, R. T. & Berg, S. Interfacial velocities and capillary pressure gradients during Haines jumps. *Physical Review E* **88**, 043010 (2013).
68. Bartels, W.-B., Mahani, H., Berg, S. & Hassanizadeh, S.M. Literature review of low salinity waterflooding from a length and time scale perspective. *Fuel* **236**, 338–353 (2019).
69. Bartels, W.-B. *et al.* Oil Configuration Under High-Salinity and Low-Salinity Conditions at Pore Scale: A Parametric Investigation by Use of a Single-Channel Micromodel. *SPE Journal* **22**(05), 1362–1373 (2017).
70. Alzahid, Y. *et al.* In *SPE Europec featured at 79th EAGE Annual Conference & Exhibition* (Society of Petroleum Engineers, Paris, France, 2017).
71. Gerami, A., Mostaghimi, P., Armstrong, R. T., Zamani, A. & Warkiani, M. E. A microfluidic framework for studying relative permeability in coal. *International Journal of Coal Geology* **159**, 183–193, <https://doi.org/10.1016/j.coal.2016.04.002> (2016).
72. Kim, P. *et al.* Soft lithography for microfluidics: a review (2008).
73. Cohen, W. B., Spies, T. A. & Bradshaw, G. A. Semivariograms of digital imagery for analysis of conifer canopy structure. *Remote Sensing of Environment* **34**, 167–178, [https://doi.org/10.1016/0034-4257\(90\)90066-U](https://doi.org/10.1016/0034-4257(90)90066-U) (1990).
74. van der Sanden, J. J. & Hoekman, D. H. Review of relationships between grey-tone co-occurrence, semivariance, and autocorrelation based image texture analysis approaches. *Canadian Journal of Remote Sensing* **31**, 207–213, <https://doi.org/10.5589/m05-008> (2005).
75. Hohn, M. E. An Introduction to Applied Geostatistics: by Edward H. Isaaks and R. Mohan Srivastava, 1989, Oxford University Press, New York, 561 p., ISBN 0-19-505012-6, ISBN 0-19-505013-4 (paperback), \$55.00 cloth, \$35.00 paper (US). *Computers & Geosciences* **17**, 471–473, [https://doi.org/10.1016/0098-3004\(91\)90055-1](https://doi.org/10.1016/0098-3004(91)90055-1) (1991).
76. Clausi, D. A. Comparison and fusion of co-occurrence, Gabor and MRF texture features for classification of SAR sea-ice imagery. *Atmosphere-Ocean* **39**, 183–194, <https://doi.org/10.1080/07055900.2001.9649675> (2001).
77. Jing, Y., Armstrong, R. T. & Mostaghimi, P. Rough-walled discrete fracture network modelling for coal characterisation. *Fuel* **191**, 442–453, <https://doi.org/10.1016/j.fuel.2016.11.094> (2017).
78. Brugnara, M. *Contact Angle plugin (for ImageJ software)*, <https://imagej.nih.gov/ij/plugins/contact-angle.html> (2006).
79. Rossen, W. R. Theory of mobilization pressure gradient of flowing foams in porous media: I. Incompressible foam. *Journal of Colloid and Interface Science* **136**, 1–16, [https://doi.org/10.1016/0021-9797\(90\)90074-X](https://doi.org/10.1016/0021-9797(90)90074-X) (1990).
80. Pyrak-Nolte, L. J., Nolte, D. D., Chen, D. & Giordano, N. J. Relating capillary pressure to interfacial areas. *Water Resources Research* **44** (2008).
81. Chen, D., Pyrak-Nolte, L. J., Griffin, J. & Giordano, N. J. Measurement of interfacial area per volume for drainage and imbibition. *Water Resources Research* **43**, n/a-n/a, <https://doi.org/10.1029/2007WR006021> (2007).
82. Cheng, J. T., Pyrak-Nolte, L. J., Nolte, D. D. & Giordano, N. J. Linking pressure and saturation through interfacial areas in porous media. *Geophysical Research Letters* **31**, n/a-n/a, <https://doi.org/10.1029/2003GL019282> (2004).
83. Ridler, T. & Calvard, S. Picture Thresholding Using an Iterative Selection Method. *IEEE Transactions on Systems, Man, and Cybernetics* **8**, 630–632, <https://doi.org/10.1109/TSMC.1978.4310039> (1978).

Acknowledgements

Yara Alzahid acknowledges the graduate fellowship provided by Saudi Aramco. The authors also acknowledge the South Australian node of the Australian National Fabrication Facility under the National Collaborative Research Infrastructure Strategy for making the silicon mould and the Microfluidics laboratory at the School of Mechanical and Manufacturing Engineering at UNSW for their support with generating the PDMS micromodels.

Author Contributions

Y.Z. and R.T.A. designed the research work. Y.Z., A.G., A.S. and K.P. constructed the experimental apparatus and conducted the experiments. Y.Z., A.G., A.S. and R.T.A. conducted data analysis. Y.Z. and R.T.A. wrote the manuscript with input from all other authors. R.T.A., P.M. and T.A. critically revised the manuscript and helped with interpretation of data.

Additional Information

Competing Interests: The authors declare no competing interests.

Publisher's note: Springer Nature remains neutral with regard to jurisdictional claims in published maps and institutional affiliations.



Open Access This article is licensed under a Creative Commons Attribution 4.0 International License, which permits use, sharing, adaptation, distribution and reproduction in any medium or format, as long as you give appropriate credit to the original author(s) and the source, provide a link to the Creative Commons license, and indicate if changes were made. The images or other third party material in this article are included in the article's Creative Commons license, unless indicated otherwise in a credit line to the material. If material is not included in the article's Creative Commons license and your intended use is not permitted by statutory regulation or exceeds the permitted use, you will need to obtain permission directly from the copyright holder. To view a copy of this license, visit <http://creativecommons.org/licenses/by/4.0/>.

© The Author(s) 2018